Photoactivatable Iridium(III) Anticancer Complexes

A Thesis Submitted for the Degree of Doctor of Philosophy in Analytical Science

Oliver William Lidbury Carter MChem (Hons), MRSC

Supervisor: Professor Peter J. Sadler, FRS

University of Warwick, Department of Chemistry

February 2023

Table of contents

List of tables

List of figures

Acknowledgements

I would like to thank my supervisor Professor Peter Sadler for giving me the opportunity to pursue a PhD in his lab and his continuous support and guidance since I first started as an MChem student. I would also like to thank the EPSRC and Dr Yingjian (Andy) Xu of Guizhou GoldenKeys High-Tech Materials Co. Ltd. for funding my CASE Award within the Warwick Analytical Science CDT, and the opportunity to visit the company in China in 2019. I'd also like to thank everyone at MAS-CDT for organising my EPSRC funding, as well as running the seminars and annual conferences.

I want to say a massive thank you to Dr Cinzia Imberti for all the amazing help she's given me since joining the group. I like to think she's made me a much better researcher (despite saying I'm cursed), and the regular catch-ups we had through the pandemic are still greatly appreciated. I would also like to thank Dr James Coverdale for all the guidance since my MChem. I've learnt so much and will miss our regular McDonald's trips in between experiments. Massive thanks also to Dr Miguel Gomez Gonzalez (Diamond) for helping with the synchrotron data which was invaluable, and I really appreciate all of the feedback.

To everyone in the Sadler group, thank you for all the chats, help in the lab and feedback at group meetings.

From outside the group, I would like to thank Dr Hannah Bridgewater and Dr Jack Woolley for teaching me how to perform cell work and photophysical experiments, as well as Dr Ian Hands-Portman for confocal expertise.

Massive thanks to all the technicians who have helped me throughout my PhD: Dr Ivan Prokes and Dr Rob Perry for all their help with NMR, and Dr Lijiang Song and Ms Lynette Walsh for answering all my mass spec queries. Thanks to Jason Noone for answering my many IT questions.

I would also like to say a special thanks to Rod Wesson. He's been amazing at fixing all the rotovap issues, building the LED arrays and generally being able to help with anything that went wrong. I'll miss all our music conversations in the corridors!

Finally, to my family and friends, thank you for all your love and support over the last 4 years. PhD life took a pretty dramatic turn in March 2020 and I wouldn't have got through all the COVID lockdowns without your messages and video calls.

Funding

I thank Golden Keys High-Tech Materials Co. Ltd. (贵州金之键高科技材料股份有限公司) and EPSRC *via* MAS-CDT for funding my PhD as a CASE Award.

Declaration

This thesis is submitted to the University of Warwick in support of my application for the degree of Doctor of Philosophy. It has been composed by myself and has not been submitted in any previous application for any degree. The work presented (including data generated and data analysis) was carried out by the author except in the cases outlined below:

Confocal microscopy data was processed by Dr Ian Hands-Portman to determine pixel intensities, as noted in Chapter 4.

Synchrotron data processing was performed by Dr Miguel Gomez Gonzalez at the I14 Beamline, Diamond Light Source, Oxford, UK, as noted in Chapter 5.

Publications

1 Z. Zhu, L. Wei, Y. Lai, **O. W. L. Carter**, S. Banerjee, P. J. Sadler and H. Huang, Photocatalytic glucose-appended bio-compatible Ir(III) anticancer complexes, Dalton Trans., 2022, 51, 10875.

2 **O. W. L. Carter**, Y. Xu and P. J. Sadler, Minerals in biology and medicine, RSC Adv., 2021, 11, 1939. (Review)

3 E. J. Anthony, E. M. Bolitho, H. E. Bridgewater, **O. W. L. Carter**, J. M. Donnelly, C. Imberti *et al.*, Metallodrugs are unique: opportunities and challenges of discovery and development, Chem. Sci., 2020, 11, 12888. (Review)

Abstract

Platinum chemotherapeutics like cisplatin are pivotal in the treatment of cancer. However, platinum drug resistance and undesirable side effects require the development of anticancer agents with different mechanisms of action and better cancer selectivity. Photodynamic therapy and photoactivated chemotherapy use light to activate prodrugs with high spatial resolution, reducing off target effects. Furthermore, since cancer cells overexpress a wide array of membrane proteins, conjugating active complexes to targeting vectors can increase cancer cell selectivity.

In this thesis, glycoconjugated photosensitizers were designed to target the GLUT1 receptor which is typically overexpressed in cancer cells. A series of fourteen photo-stable Ir(III) and Ru(II) glycoconjugates were synthesised. Ir(III) complexes **1**-**10** exhibited phosphorescence from 475-500 nm, with good singlet oxygen quantum yields, whilst Ru(II) complexes **11**-**14** failed to exhibit notable phosphorescence or singlet oxygen production.

The Ir(III) complexes demonstrated low micromolar photoactivity and in-cell singlet oxygen generation. Accumulation in lung cancer cells was unaffected by the sugar bound directly to Ir(III) complexes. However, a dependence on the linker length between glucose and the Ir(III) complex was observed. Co-treatment of cells with a GLUT1 inhibitor reduced the cellular accumulation of glycoconjugate **9** but not of **4**, which differ by a nine-atom linker between the Ir(III) complex and glucose. Complexes were selective for cancer cells and non-toxic towards non-cancerous lung cells at 100 μM.

This thesis also details the in-cell stability and localisation of a novel Pt-Ir complex using synchrotron X-ray techniques. This complex is comprised of an Ir(III) PDT agent conjugated to a Pt(IV) PACT agent, utilising two mechanisms of action upon blue light irradiation. X-ray fluorescence experiments of lung cancer cells treated with Pt-Ir determined the complex photo-decomposed in cells, with the resulting Pt complex localising predominantly in cell nuclei. Intracellular Pt content increased upon irradiation, with ~60% of platinum reduced to Pt(II).

Courses and conferences attended

1 MAS-CDT Conference (Somerset, UK) – June 2019. Poster presentation.

2 MAS-CDT Conference (online) – June 2020. Powerpoint presentation.

3 AEBIN Photochemistry School (online) – September 2020

4 Postgraduate Chemistry Symposium (University of Warwick, UK) – May 2021. Poster presentation.

5 Synchrotron Radiation School (Diamond Light Source, online) – September 2021

6 Postgraduate Research Symposium, Department of Chemistry (University of Warwick, UK) – May 2022. Powerpoint presentation.

Abbreviations

[^{18}F]-FDG	[^{18}F]-Fluorodeoxyglucose
3D	Three dimensional
5-ALA	5-aminolevulinic acid
A2780	Human ovarian carcinoma
A549	Human lung carcinoma
Acetyl-CoA	Acetyl coenzyme A
ADP	Adenosine diphosphate
AEX	Anion-exchange chromatography
ATP	Adenosine triphosphate
bpy	Bipyridine
cps	Counts per second
CT	Computed tomography
CTCL	Cutaneous T-cell lymphoma
CTR1	Copper transporter protein 1
CuAAC	Copper-catalyzed azide-alkyne cycloaddition
DCM	Dichloromethane
DFT	Density functional theory
DLS	Diamond Light Source
DMEM	Dulbecco's Modified Eagle Medium
DMF	Dimethylformamide
DMPU	N,N′-Dimethylpropyleneurea
DMSO	Dimethyl sulfoxide
DNA	Deoxyribonucleic acid
DPC	Differential phase contrast
ECACC	European Collection of Cell Cultures
EDTA	Ethylenediaminetetraacetic acid
EGFR	Epidermal growth factor receptor
eq.	Equivalent
ER	Endoplasmic reticulum
ESI-MS	Electrospray ionisation mass spectrometry
ETC	Electron transport chain
EXAFS	Extended X-ray absorption fine structure

$FADH_2$	Flavin adenine dinucleotide
FDA	Food and Drug Administration (USA)
GLUT	Glucose transporter
GTP	Guanosine triphosphate
HER	Human epidermal growth factor receptor
HMG	High mobility group
HMPA	Hexamethylphosphoramide
HOMO	Highest occupied molecular orbital
HpD	Hematoporphyrin derivative
HPLC	High performance liquid chromatography
HR-ESI-MS	High-resolution electrospray ionisation mass spectrometry
HSA	Human serum albumin
IC_{50}	Half-maximal inhibitory concentration
ICP-MS	Inductively coupled plasma - mass spectrometry
ICP-OES	Inductively coupled plasma - optical emission spectroscopy
ISC	Intersystem crossing
LC	Liquid chromatography
LCF	Linear combination fitting
LED	Light-emitting diode
LUMO	Lowest unoccupied molecular orbital
MAB	Monoclonal antibody
MCF-7	Human breast adenocarcinoma
MCTS	Multicellular tumour spheroids
MLCT	Metal-to-ligand charge transfer
MO	Molecular orbital
MRC5	Human lung fibroblasts (primary, non-cancerous)
MRPs	Multidrug resistance proteins
NADH	Nicotine adenine dinucleotide (reduced)
NER	Nucleotide excision repair
NMIBC	Non-muscle invasive bladder cancer
NMR	Nuclear magnetic resonance
NSCLC	Non-small cell lung cancer
OSCC	Oral squamous cell carcinoma

PACT	Photoactivated chemotherapy
PBS	Phosphate buffered saline
PC3	Human prostate adenocarcinoma
PDT	Photodynamic therapy
PEG	Polyethylene glycol
PET	Positron emission tomography
PPA	Pyropheophorbide a
ppm	Parts per million
ppy	2-phenylpyridine
PS	Photosensitizer
PSMA	Prostate-Specific Membrane Protein
PTFE	Polytetrafluoroethylene
PTT	Photothermal therapy
PUVA	Psoralen + ultraviolet A
RBF	Round bottom flask
RNS	Reactive nitrogen species
ROS	Reactive oxygen species
RPMI	Roswell Park Memorial Institute
SEC	Size-exclusion chromatography
SOSG	Singlet oxygen sensor green
SST	Somatostatin
SSTR	Somatostatin receptor
SUV	Standardised uptake value
TFA	Trifluoroacetic acid
TFA^-	Trifluoroacetate
TKI	Tyrosine kinase inhibitors
TP-PDT	Two-photon photodynamic therapy
UV	Ultraviolet
UV-vis	Ultraviolet-visible
VWD	Variable wavelength detector
XANES	X-ray absorption near-edge structure
XRF	X-ray fluorescence

Chapter 1

Introduction

This thesis details the synthesis, characterisation, and photophysical and biological properties of photoactive iridium(III) and ruthenium(II) anticancer complexes designed to target cancer cells. In addition, a novel dual mode-of-action photoactive Pt-Ir complex developed by the Sadler group is studied by synchrotron X-ray techniques for in-cell stability, localisation, and oxidation state.

1 Introduction

This chapter gives an overall introduction to cancer, cancer metabolism and current cancer treatments, focussing on metal-based chemotherapeutics. Different phototherapies are compared, and photoactive complexes (clinical and in development) are explored. Approaches to targeting cancer cells using conjugated targeting vectors with a view to reducing clinical side-effects are also introduced. Furthermore, synchrotron X-ray fluorescence (XRF) and X-ray absorption near-edge structure (XANES) spectroscopy are described as background for Chapter 5.

1.1 Cancer

Cancer represents a group of diseases generally described as the uncontrolled growth of cells,[1] with over 200 different types of cancer documented.[2] The earliest records of cancer date back to around 1500 BC,[3] yet it remains a prominent health issue to this day.

1.1.1 Cancer incidence and mortality

Analysing trends in cancer incidence in people born in Great Britain between 1930 and 1960, Ahmed *et al*. estimated that over half of all people born after 1960 will be diagnosed with cancer at some point in their lifetime, with lifetime risks slightly higher for men than women.[4] An estimated 10 million people died globally from cancer in 2020, and a further 19.3 million new cases were diagnosed; breast cancer was the most common new cancer diagnosed (11.7%), slightly ahead of lung cancer (11.4%), yet lung cancers accounted for 18% of all cancer deaths.[5] While estimates vary, the vast majority (up to 95%) of cancers are believed to be caused by

environmental factors, *e.g.* diet, tobacco, infection and radiation, with genetic traits considered to contribute to less than 10% of all cases.[6–8]

1.1.2 Hallmarks of cancer

Cancers occur as a result of mutations which lead to greater survival and proliferation.[9] In 2000, Hanahan and Weinberg proposed that cancer could be characterised by six widely accepted hallmarks: self-sufficiency in growth signals, insensitivity to anti-growth signals, evasion of apoptosis, limitless replicative potential, sustained angiogenesis, and tissue invasion and metastasis.[10] These were updated in 2011 to include two further hallmarks (abnormal metabolic pathways and evasion of the immune system) as well as two enabling characteristics (genome instability and inflammation).[11]

A healthy cell typically undergoes apoptosis (programmed cell death) to maintain cell populations or in response to damage.[12,13] Apoptosis can be triggered by intracellular stress signals (intrinsic/mitochondrial pathway) or by extracellular ligands activating cell death receptors on the membrane (extrinsic pathway).[14] This mechanism kills the cell before any harmful mutations can be replicated and allows the organic components to be recycled whilst avoiding damage to surrounding cells.[12]

1.1.3 The Warburg effect

In cells, glucose is metabolised to generate adenosine triphosphate (ATP) as a source of cellular energy.[15] Initially, glycolysis of glucose generates 2 units of pyruvate and 2 units of ATP *via* a multistep mechanism (**Figure 1.1**).[16] The pyruvate molecules then undergo one of two pathways dependent on whether oxygen is present.

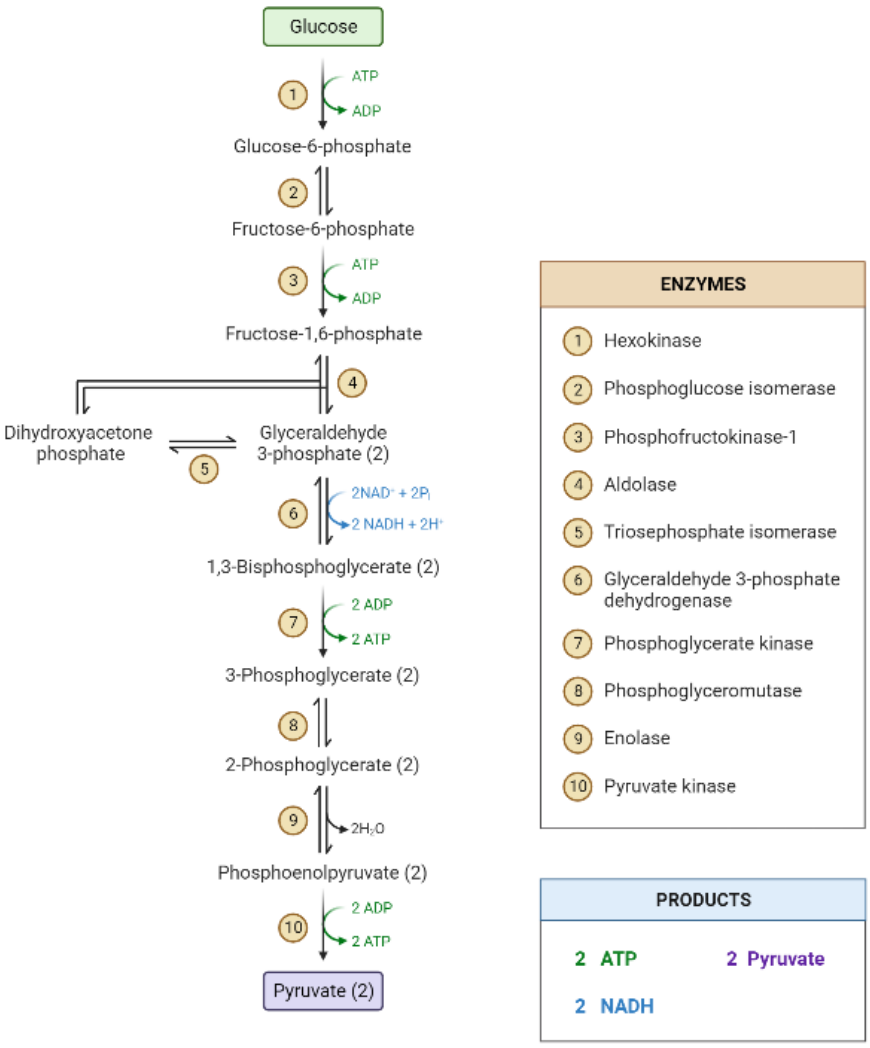

Figure 1.1. Glycolysis pathway detailing the conversion of glucose to pyruvate.[16] Image is a template generated in BioRender.com.

In oxygenated tissue, pyruvate diffuses to mitochondria where it is converted to Acetyl Coenzyme A (Acetyl-CoA), which then enters the Krebs Cycle (**Figure 1.2**).[16,17] This generates carbon dioxide, water, and guanosine triphosphate (GTP), in addition to NADH and $FADH_2$ which enter the Electron Transport Chain (ETC).[18] GTP can be converted to ATP by nucleoside-diphosphate kinase (NDK),[19] and since 2 molecules of pyruvate are formed per glucose molecule, 2 molecules of GTP (and therefore up to 2 molecules of ATP) are produced from the Krebs Cycle. The oxygen dependence of this route is due to the final step of the ETC, where oxygen is reduced to water by cytochrome c oxidase, leading to an electrochemical gradient across the inner mitochondrial membrane. This gradient provides energy to the ATP Synthase enzyme to phosphorylate adenosine diphosphate (ADP) to

synthesise ATP (chemiosmotic coupling).[20] A further 34 molecules of ATP can be generated from the ETC, leading to a total of up to 38 molecules of ATP generated per molecule of glucose in oxygenated tissues.[20]

When not enough oxygen is present, pyruvate is converted to lactate in the cytosol by lactate dehydrogenase in a process called 'anaerobic glycolysis' (**Figure 1.2**).[21] No further molecules of ATP are produced in this case. With only 2 ATP molecules generated from glycolysis, this is far less efficient at creating ATP than the oxidative phosphorylation pathway. However, anaerobic glycolysis occurs up to 100× quicker than the complete oxygen-dependent pathway.[22]

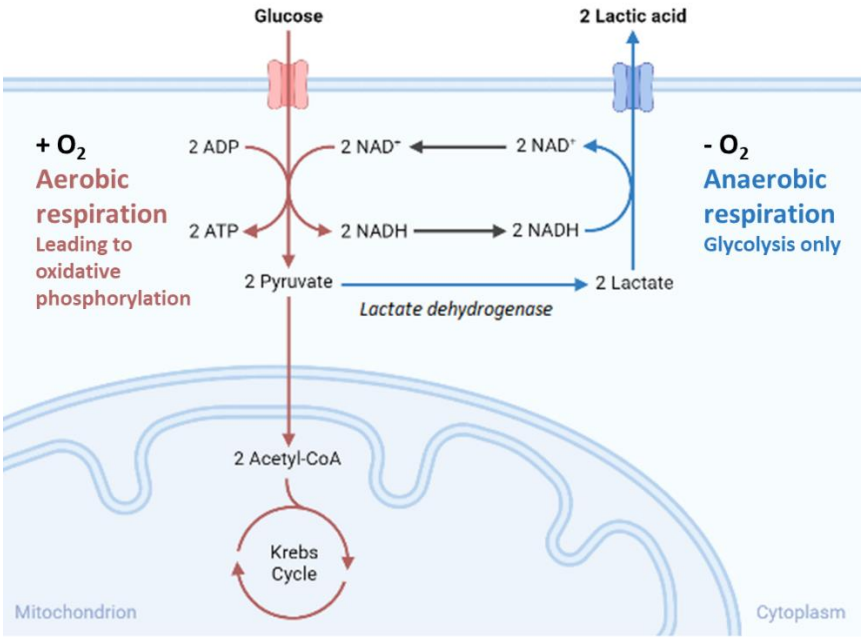

Figure 1.2. Aerobic and anaerobic respiration pathways in healthy cells.[16,21] Image adapted from a template in BioRender.com.

In the 1920s, Otto Warburg recognised that cancer cells consumed glucose at a far greater rate compared to surrounding healthy differentiated tissue, which was mostly converted into lactate despite the presence of oxygen, termed 'aerobic glycolysis'.[23,24] Further studies showed rapidly proliferating cells convert up to 85% of pyruvate into lactate while only 5% undergoes oxidative phosphorylation, with the remaining pyruvate used in other biosynthetic pathways.[25] The phenomenon of cancer cells favouring glycolysis over oxidative phosphorylation even in the

presence of oxygen is known as the Warburg effect, which leads to overexpression of glucose receptors (GLUTs), particularly GLUT1, to meet the increased metabolic demands.[26] High GLUT1 expression has been linked to poor prognosis in a variety of cancers,[27,28] including those of the prostate,[29] breast,[30] and lungs.[31]

1.2 Treatment of cancer

Cancer can be treated in a variety of ways, including:

- Surgery – the removal of solid tumours and cancerous tissue, though highly dependent on the type, stage, and location of the cancer. The earliest use of surgery to treat cancer dates back to ancient Egypt.[32]
- Radiotherapy – gamma rays are used to induce DNA damage in cancer cells, leading to cell death. Radiation has been used in the treatment of cancer since the late 19th century.[33]
- Chemotherapy – the use of chemical compounds to kill cancer cells, originating with nitrogen mustards in the 1930s.[34]
- Immunotherapy – modulating a person's immune response, including by use of vaccines and monoclonal antibodies, in order to prevent and treat cancer.[35,36] First used in 1891 by William Coley, using *Streptococcus pyogenes* and *Serratia marcescens* to treat sarcoma patients.[36]
- Endocrine/hormone therapy – modulation of hormone levels to disrupt the growth of hormone-sensitive cancers, such as those of the prostate and breast.[37]

Surgery and radiotherapy were the main treatment methods up until the 1960s, when chemotherapeutics started to be employed in adjuvant therapy with surgery and radiotherapy.[34] In the UK, 28% of cancers diagnosed between 2013 and 2016 were treated with chemotherapy (alone or in combination with other treatments),[38] and roughly half of all chemotherapy treatments use some form of platinum drug.[39]

1.2.1 Cisplatin and platinum drugs

Transition metal complexes have played a crucial role in the treatment of cancer since the discovery of the anticancer effects of cisplatin (*cis*-$[PtCl_2(NH_3)_2]$).

Cisplatin was originally synthesised in 1844 as Peyrone's salt, though its structure wasn't elucidated until 1893.[40] In 1965, Rosenberg discovered that electrolysis products from a platinum electrode inhibited cell division in *E. coli*, with the bacteria forming long filaments.[41] Further work on bacteria was conducted with metal complexes in groups 8-10, with cisplatin tested directly on *E. coli* in 1966.[42,43] It wasn't until 1969 that the anticancer activity of cisplatin (and other platinum complexes) was observed in leukaemia in mice.[44] Trials in humans came shortly after in 1971, with FDA approval in 1978 for the treatment of ovarian and bladder cancer under the brand name Platinol®.[45] Since then, cisplatin has been used clinically in the treatment of various other cancers, including head and neck, lung, and testicular cancers.[40] However, cisplatin is known to cause a wide array of side effects, including nephrotoxicity, neurotoxicity, myelosuppression, immunosuppression, and nausea/vomiting.[46]

Second generation platinum complexes were designed to circumvent the side effects observed in patients treated with cisplatin. Carboplatin, a cisplatin analogue with a bidentate carboxylate ligand in place of the two chlorides, was approved by the FDA in 1989 due to its reduced nephrotoxicity. Oxaliplatin gained FDA approval in 2004 for the treatment of colorectal cancers in combination with 5-fluorouracil.[47] Nedaplatin, lobaplatin and heptaplatin have been approved in Japan, China, and South Korea, respectively (**Figure 1.3**).[39] Further platinum complexes have been studied, including satraplatin, developed as the first orally-active Pt complex (others are given intravenously), and picoplatin, though both failed in Phase III clinical trials.[48,49]

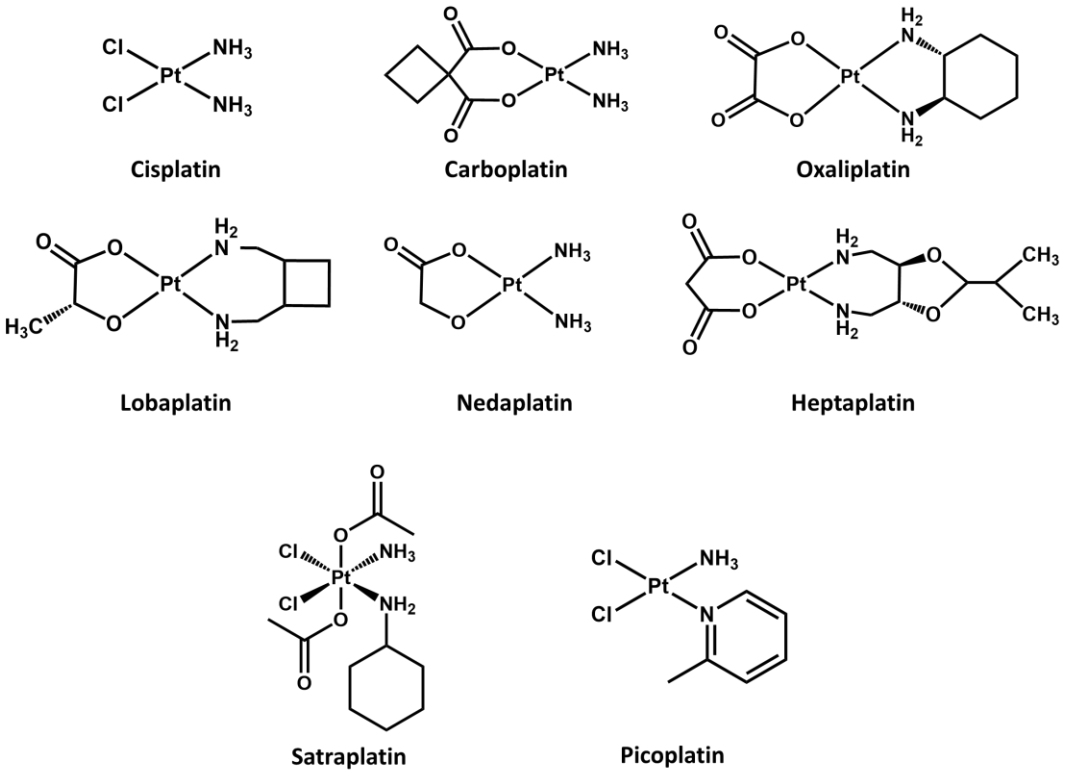

Figure 1.3. Structures of eight platinum-based chemotherapeutics that are either clinically approved or have undergone clinical trials for the treatment of cancer.

Cisplatin exists as the neutral dichlorido species in blood as the chloride concentration is high (~100 mM).[50] It then enters the cell either through transporters such as copper transporter CTR1 or passive diffusion. Intracellular chloride concentrations are far lower,[51] facilitating stepwise hydrolysis to form the aqua and di-aqua species, which can then go on to form DNA adducts (**Figure 1.4**).[52] The di-aqua species binds to the N7 position of purine bases (guanine, G, and adenine, A), typically forming 1,2-intrastrand cross-links (65% G-G, 25% A-G), with 1,3-intrastrand, 1,2-interstrand and monofunctional adducts accounting for the remaining 10%.[53] Interestingly, only 1% of intracellular cisplatin reacts with DNA.[54] High mobility group (HMG) proteins then bind to these Pt-DNA adducts, inhibiting DNA repair by nucleotide excision repair (NER) proteins,[55] leading to cell death by apoptosis and necrosis.[56] Carboplatin works *via* the same mechanism, forming essentially the same DNA adducts as cisplatin but at a 10-fold slower rate.[45] Interestingly, oxaliplatin also forms DNA adducts, though the importance of these adducts has been questioned; Oxaliplatin does not activate a DNA damage response, instead it causes ribosome biogenesis stress, though this may be caused

by binding to DNA.[57] Importantly, none of these platinum complexes are targeted to cancer cells.

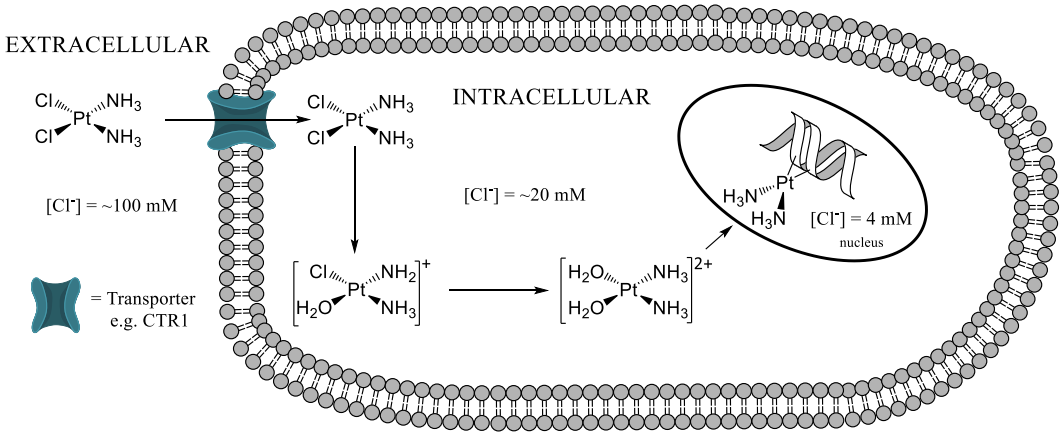

Figure 1.4. Mechanism of action of cisplatin. Adapted from references.[45,58]

1.2.2 Platinum drug resistance

A major drawback of platinum chemotherapeutics is resistance. Cancer cells can be intrinsically resistant to platinum treatments, for example due to high expression of multidrug resistance proteins (MRPs).[59] However, they may also acquire resistance after exposure to platinum drugs, leading to less effective treatment and increased patient mortality. Acquired resistance can be caused by several mechanisms, including:

- Reduced cellular accumulation by either reducing influx (*e.g.* by decreasing CTR1 expression) or enhancing efflux pathways.[60–62]
- Deactivation by binding to proteins such as glutathione and metallothionein.[59,63]
- Increased DNA repair such as NER and mismatch repair.[63,64]

Cancers that acquire resistance to cisplatin are typically cross-resistant with carboplatin due to their similar mechanisms of action.[65] In addition, cross-resistance has also been observed with oxaliplatin, though to differing extents dependent on the level of resistance to cisplatin.[66] As such, it is imperative to develop novel anticancer agents that circumvent platinum resistance.

1.2.3 Transition metal anticancer complexes

Non-platinum transition metal chemotherapeutics have been designed with novel mechanisms of action in order to avoid Pt resistance. Notably, Ru(III) complexes NAMI-A, KP1019 and KP1339/BOLD-100 (**Figure 1.5**) all entered clinical trials for the treatment of various cancers.[67]

NAMI-A, [*trans*-$RuCl_4$(dmso)(imidazole)]$^-$ with an imidazolium counter ion, has mostly antimetastatic activity, with little cytotoxic activity. The majority of NAMI-A localises extracellularly or on the cell membrane, with no apparent involvement of nuclear DNA. NAMI-A was the first Ru drug tested in humans, entering Phase I clinical trials in 1999 for the treatment of non-small cell lung cancer (NSCLC),[67] followed by Phase I/II clinical trials in combination with gemcitabine for use in patients after first line treatment. However, NAMI-A/gemcitabine treatment was found to be less active than gemcitabine alone and was only moderately tolerated.[68]

KP1019 and KP1339 (also called BOLD-100) are both based on the [*trans*-$RuCl_4(indazole)_2]^-$ anion, with an indazolium and sodium cation, respectively. KP1019/KP1339 is significantly more stable towards aquation than NAMI-A, leading to a dramatic difference in uptake profiles. KP1019/KP1339 enters the cytosol, interacting with proteins resulting in ROS and endoplasmic reticulum stress, rather than direct DNA damage.[69] Phase I studies on KP1019 contained patients with varying solid tumours, including tumours in the bladder, eye, colon, and tongue. A maximum tolerated dose of KP1019 could not be determined due to low solubility,[70] so a larger Phase I trial was performed using the sodium salt KP1339.[67] Phase Ib/IIa clinical trials of BOLD-100 in combination with FOLFOX are currently ongoing for the treatment of advanced solid colorectal, pancreatic and gastric tumours, expected to finish in December 2023 (NCT04421820).[71] An interim report has stated the combination "is well-tolerated with no clinically significant safety findings".[72]

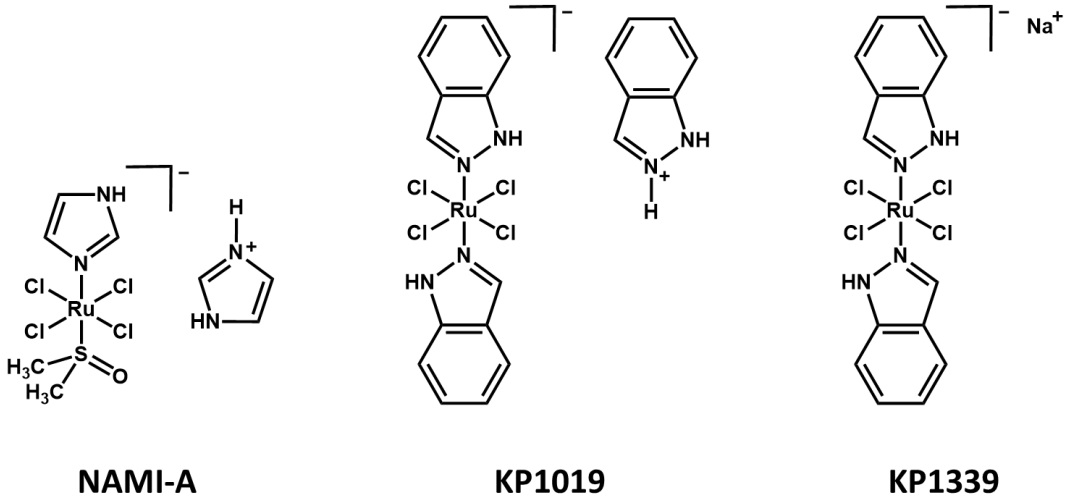

Figure 1.5. Structures of clinically trialled ruthenium(III) complexes NAMI-A, KP1019 and KP1339 (BOLD-100).

To the best of my knowledge, no other transition metal complexes have been investigated in clinical trials for standard chemotherapeutic cancer treatment (*i.e.* excluding radioactive and photoactive complexes).[73] However, Os analogues of NAMI-A and KP1019/KP1339 have been extensively studied.[74,75] In addition, considerable research has gone into metal half-sandwich complexes, especially FY26 (osmium)[76–79] and RAPTA-C (ruthenium) shown in **Figure 1.6**.[80–83]

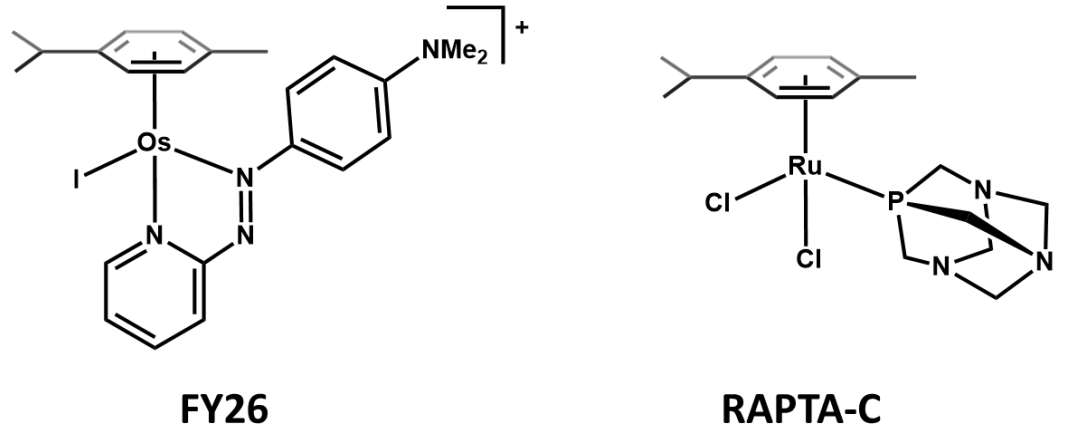

Figure 1.6. Structures of half-sandwich complexes FY26 and RAPTA-C.

1.3 Targeting cancer cells

Side effects caused by cisplatin and other clinically used chemotherapeutics are caused by cytotoxic agents damaging healthy cells, as the complexes are not selective for cancer cells. A major strategy employed to increase specificity towards cancer cells is to target membrane proteins that are either specific to or greatly overexpressed on the cells of interest. Targeting membrane proteins can be achieved by conjugation of active drugs to a variety of vectors, ranging from antibodies and their fragments, to peptides, and simple monosaccharides. Several membrane proteins are already clinically established targets, such as epidermal growth factor receptors, prostate-specific membrane protein, and glucose transporters.

Epidermal growth factor receptors (EGFR) are a family of transmembrane receptor tyrosine kinases consisting of four receptors: EGFR (HER1), HER2, HER3 and HER4 (also known as ErbB1-4, respectively). EGFR drives tumorigenesis and is overexpressed in a multitude of cancers, including head and neck, breast, ovarian, lung, and colorectal cancer, and is associated with poor prognosis and drug resistance.[84] Tyrosine kinase inhibitors (TKIs) such as gefitinib and erlotinib have been employed to inactivate EGFR signalling, as well as monoclonal antibodies (MABs) such as cetuximab and panitumumab.[85] HER2 overexpression also drives tumorigenicity, and is implicated in fast-tracking oncogenicity, since breast cancers overexpressing HER2 emerge at an earlier age. In addition to breast cancer, HER2 can also be overexpressed in other cancers such as gastric, ovarian and lung.[86]

The integral membrane protein Prostate-Specific Membrane Protein (PSMA) is found in all prostate tissues, and often with increased expression in cancerous tissues. Targeting prostate cancer with radionuclides has been achieved by conjugation to anti-PSMA antibodies, notably in the case of FDA approved ProstaScint® - ^{111}In-labelled capromab pendetide for single photon emission computed tomography (SPECT) imaging.[87] PSMA has also been targeted with urea-based PSMA ligands based on glutamate-urea-lysine such as PSMA 617, labelled with ^{68}Ga, ^{177}Lu or ^{225}Ac.[88]

The GLUT family of membrane proteins, also known as the solute carrier 2 family, transport glucose and other monosaccharides across the cell membrane. The most commonly studied transporter, GLUT1, is a ubiquitously distributed high affinity

glucose transporter responsible for the basal glucose uptake with high expression at the blood-brain barrier. It is overexpressed in a variety of cancers, including breast, lung, cervix and prostate.[89] [^{18}F]-Fluorodeoxyglucose ([^{18}F]-FDG, **Figure 1.7**) is a radiolabelled glucosyl imaging agent clinically used in positron emission tomography (PET) to detect cancers due to its uptake *via* GLUT1 and other overexpressed sugar transporters.[90] Conjugation of glucose to exploit GLUT1 overexpression has been studied widely. For example, a 5000-fold increase in activity for 2-Glu-SNAP, a glucose conjugate of S-nitroso-N-acetyl-penicillamine (SNAP), was attributed to the enhanced tumour selectivity of the glycoconjugate.[91]

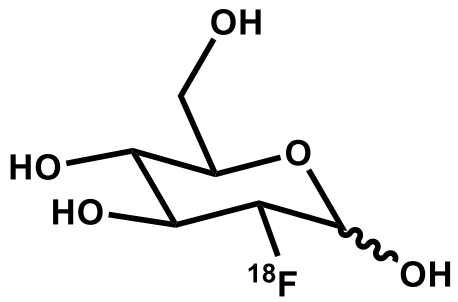

Figure 1.7. Structure of 2-deoxy-2-[^{18}F]-fluoroglucose ([^{18}F]-FDG).

1.4 Phototherapies

Selectivity can also be achieved by the activation of inactive pro-drugs in cancer cells using visible light. Phototherapies are in three main branches: photodynamic therapy (PDT), photoactivated chemotherapy (PACT), and photothermal therapy (PTT). PTT is beyond the scope of this thesis and will not be discussed here, but a summary of recent developments in PTT can be found in the review by Lu *et al.*[92] The wavelength of the irradiation source is vital to all phototherapies. Photons must have sufficient energy to excite the photosensitizer, however, tissue penetration increases at longer wavelengths (**Figure 1.8**). The 'therapeutic window' of wavelengths from 600-800 nm is considered ideal for phototherapeutic treatment since it uses relatively low energy which is more penetrating than UV and blue light.[93]. Tissue penetration depths decrease beyond the therapeutic window from around 1000 nm due to absorption by water.[94]

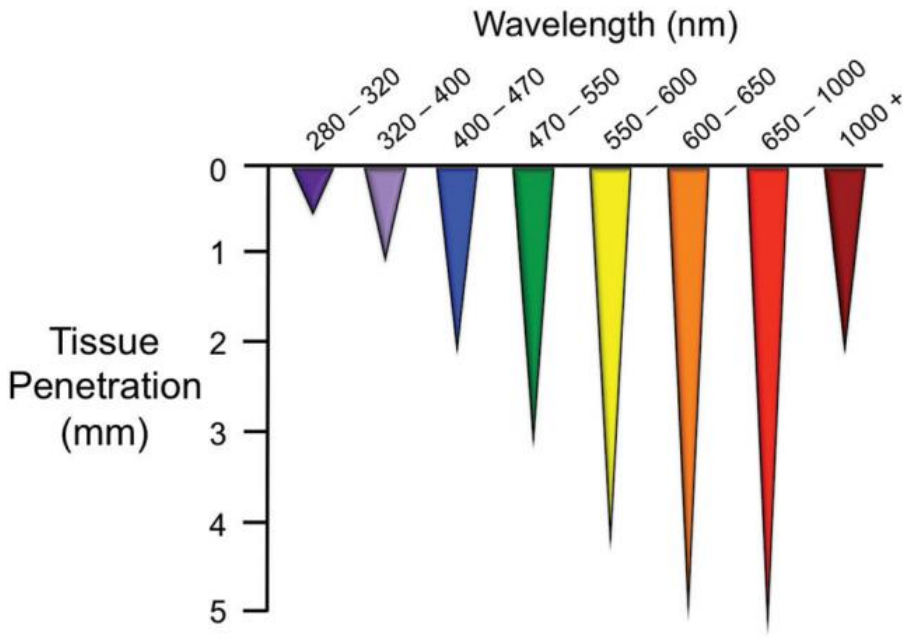

Figure 1.8. Tissue penetration depth of light at different wavelengths. Reproduced from reference 95 with permission from the Royal Society of Chemistry.[95]

1.4.1 Photodynamic therapy

Photodynamic therapy (PDT) is an approved treatment of many pre-cancerous conditions such as actinic keratoses,[96] Barrett's oesophagus,[97] and Bowen's disease,[98] as well as oesophageal, lung, and head and neck cancers.[99] For these treatments, an inactive photosensitizer (PS) is administered and allowed to accumulate in the tumour before being irradiated with a suitable wavelength of light. The period between administering the drug and photoactivation is known as the drug to light interval.

For low-spin d^6 metal coordination complexes (*e.g.* Re(I), Ru(II), Os(II), Ir(III)) with π-acceptor ligands, the absorption of a photon (or multiple photons) leads to metal-to-ligand charge transfer (MLCT), formally oxidising the metal as an electron is promoted from a metal-based t_{2g} orbital to a more ligand-based π* orbital. These complexes have singlet ground states so can typically only be excited to a singlet excited state due to Hund's selection rules, however, spin-orbit coupling causes mixing of excited states which enhances deactivation by spin-forbidden intersystem crossing (ISC) to a lower-energy triplet state in molecules with heavy atoms (heavy atom effect) and allows emission from a ^{3}MLCT state back to the ground state (**Figure 1.9).**[100] The ^{3}MLCT excited states are long-lived (up to milliseconds)[101]

due to the transition back to the ground state being spin-forbidden, giving the PS time to react with other molecules.

In Type I PDT, electron transfer to biological substrates can produce radicals which go on to react with oxygen to generate reactive oxygen species (ROS), regenerating the ground state PS in the process. However, the triplet state can also react directly with ground state triplet oxygen ($^3O_2$) *via* energy transfer to form singlet oxygen ($^1O_2$) in the tumour microenvironment (Type II).[102,103] Singlet oxygen is very reactive, with intracellular lifetimes typically ≤ 3 μs and reacting within 200 nm of where it was generated.[103–105] Both these mechanisms can lead to cell death by necrosis and apoptosis; however, they are oxygen dependent which results in weaker effects in the hypoxic environment commonly found in tumours.[106] Type II processes typically dominate the cytotoxic effects observed for clinically used PSs.[107] Since PDT is catalytic (in theory the PS is regenerated), doses required for treatment can be reduced when compared to traditional chemotherapeutics. The ability of PDT to damage cancer cells in unusual ways and release damage-associated molecules into circulation may also provide a basis for an immunogenic response.[108]

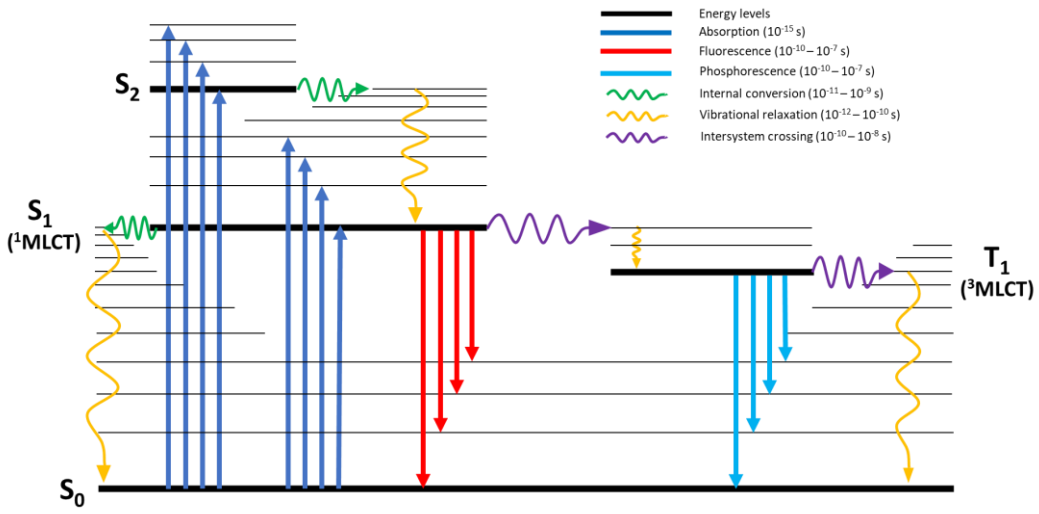

Figure 1.9. Jablonski diagram, adapted from https://www.edinst.com/us/blog/jablonski-diagram/ (Accessed December 2022).

Clinical Type II photosensitizers are typically porphyrin- or tetrapyrrole-based (**Figure 1.10**), such as hematoporphyrin derivative (HpD, a complex mixture of

porphyrins), porfimer sodium (Photofrin®) and 5-aminolevulinic acid (5-ALA). Whilst 5-ALA does not contain a porphyrin or tetrapyrrole itself, it is metabolised specifically in cancer cells to form Protoporphyrin IX.[109] In addition, an anti-EGFR antibody conjugate of porphyrin-based IR700 has undergone Phase I/IIa clinical trials for the targeted treatment of recurrent head and neck squamous cell carcinoma.[110]

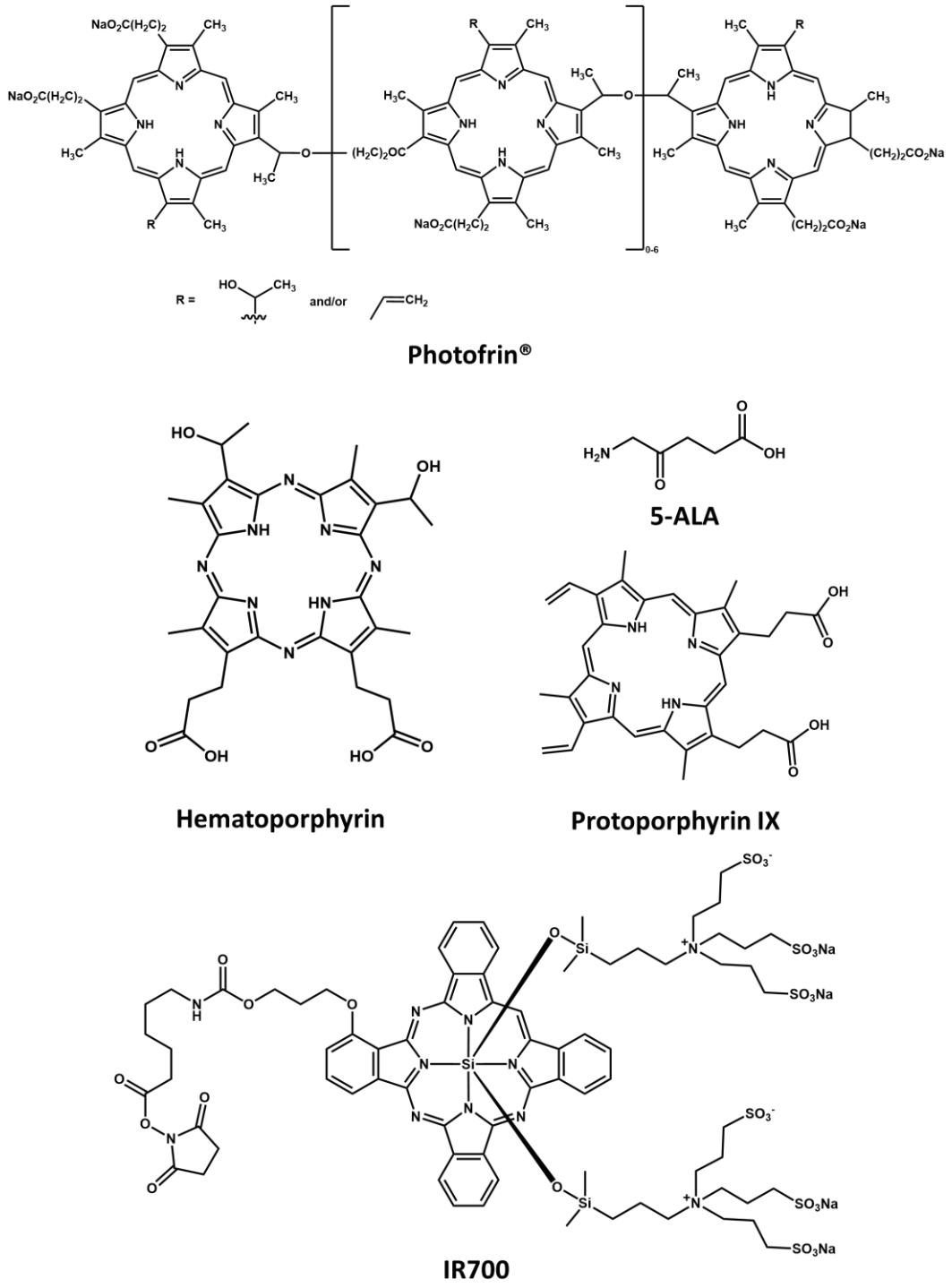

Figure 1.10. Structures of clinically approved photosensitizers. HpD is not shown as it is a complex mixture of porphyrins.

Complexes containing heavy transition metals such as iridium, ruthenium and osmium are attractive as Type II photosensitizers due to their spin-orbit coupling, increasing the amount of intersystem crossing leading to a more populated triplet state. In addition, metal complexes can have high singlet oxygen quantum yields (a

measure of the efficiency of converting ground state oxygen into singlet oxygen after absorption of a photon).

A variety of metal photosensitizers, although typically porphyrin/tetrapyrrole-based, have been investigated clinically **(Figure 1.11**). The aluminium phthalocyanine complex Photosens® has been approved in Russia,[111] and the palladium complex Tookad®-soluble is approved for the treatment of prostate cancer in Israel, Mexico and some European countries including the UK and Germany. Interestingly, Tookad®-soluble generates superoxide ($O_2^{\cdot-}$) and hydroxide radicals ($HO^{\cdot}$) through Type I photoreactions exclusively.[112] Metal compounds with tetrapyrrole-like ligands, motexafin lutetium and rostaporfin (tin), have also been in clinical trials. Ru(II) complex TLD-1433 has completed Phase I and II clinical trials in non-muscle invasive bladder cancer (NMIBC), becoming the first non-pyrrole-based metal photosensitizer to enter clinical trials.

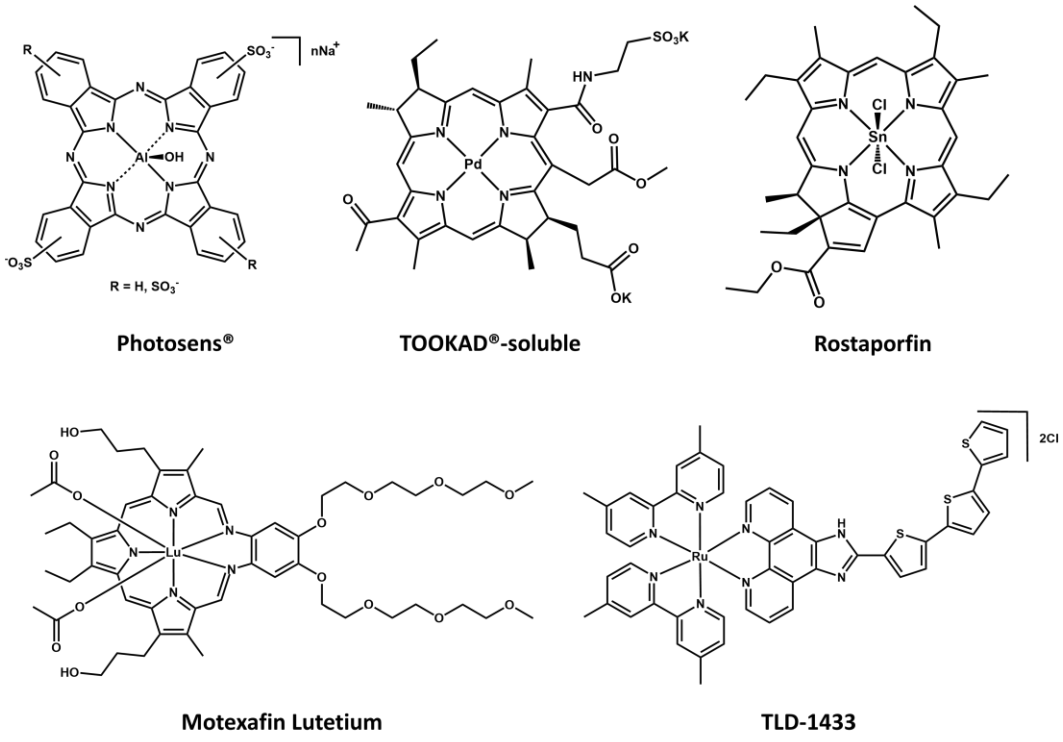

Figure 1.11. Metal-based photosensitizers. Clinically approved: Photosens®, TOOKAD®-soluble. Clinical trials: Rostaporfin, Motexafin Lutetium, TLD-1433.

Since the triplet state must be populated for singlet oxygen to be generated, phosphorescence is also possible from many photosensitisers. This has been observed with many Ir(III), Ru(II) and Os(II) complexes, leading to potential diagnostic applications.[113] Compounds that may act as both therapeutic and diagnostic agents have been termed 'theranostic' agents. This allows for the delineation of tumour locations and margins for the optimal spatial resolution of the phototherapy, in addition to increasing temporal resolution by determining the optimal interval between administering the drug and irradiation (the time with greatest tumour uptake).

1.4.2 Iridium(III) photosensitizers for PDT

Cyclometalated iridium(III) complexes in particular have been investigated as they exhibit high photostability and large Stokes shifts, therefore minimising the effects of self-quenching. In addition to this, the heavy metal centre favours fast singlet-to-triplet intersystem crossing giving a long excited triplet state lifetime, leading to phosphorescence which allows for time-resolved detection.[114] Singlet oxygen quantum yields are typically 50-90%,[115] highlighting their potential as Type II photosensitizers, whilst the ligands on cyclometalated Ir(III) PDT agents can also be tuned in order to target specific subcellular locations (*e.g.* mitochondria, lysosomes).[116] Ir(III) PDT agents based on the $[Ir(C\hat{}N)_2(N\hat{}N)]^+$ scaffold have been studied extensively, as detailed in the recent review by Kar *et al*.[117]

Cyclometalated Ir(III) compounds bearing tridentate ligands have also been investigated. $[Ir(L)(ppy)Cl](PF_6)$ (L1 = 2,6-bis(2-benzimidazolyl)pyridine, L2 = 2,6-bis(1-methyl-benzimidazol-2-yl) pyridine, **Figure 1.12a**), which induced apoptosis by caspase activation after 425 nm irradiation generated ROS in cancer cells. The L1 complex was determined to have a pH-dependent $^1O_2$ yield which damaged lysosomes, whilst the L2 complex impaired mitochondrial function.[118]

The Ir(III) complex $[Ir(ttpy)(pq)Cl]PF_6$ (ttpy = 4′-(p-tolyl)-2,2′:6′,2″-terpyridine, pq = 3-phenylisoquinoline, **Figure 1.12b**) containing the tridentate ttpy ligand was phototoxic in both hypoxic and normoxic cells due to an oxygen-independent mechanism of action.[119] In normoxia, irradiation led to the photocatalytic oxidation of NADH to $NAD^{\cdot}$ radicals *via* the generation of superoxide radicals, whilst the

reduction of cytochrome c was observed under hypoxia. The complex exhibited excellent photocytotoxicity in cancer cells across 2D and 3D cultures, with photo-IC_{50} values below 3 μM in both normoxic and hypoxic conditions.

In addition to use as PDT agents, the generation of the triplet state also allows Ir(III) complexes to act as phosphorescent probes. This has led to many studies into their use as theranostic agents. For example, Redrado *et al*. synthesised a series of Ir(III) complexes suitable for in cell tracking upon 405 nm irradiation, with excellent photocytotoxicity (photo-IC_{50} = 180-400 nM) upon 470 nm irradiation. Furthermore, an Ir-acridine complex (**Figure 1.12c**) exhibited different emission spectra upon irradiation at different wavelengths: 374-400 nm light led to emission attributed to the acridine chromophore (~430 nm), whilst wavelengths outside of this range (*i.e*. below 374 nm or above 400 nm) led to emission from the Ir fragment (~525 nm).[120] Therefore, the irradiation wavelength used to track the complex in cells can differ from the irradiation wavelength used for therapeutic activation.

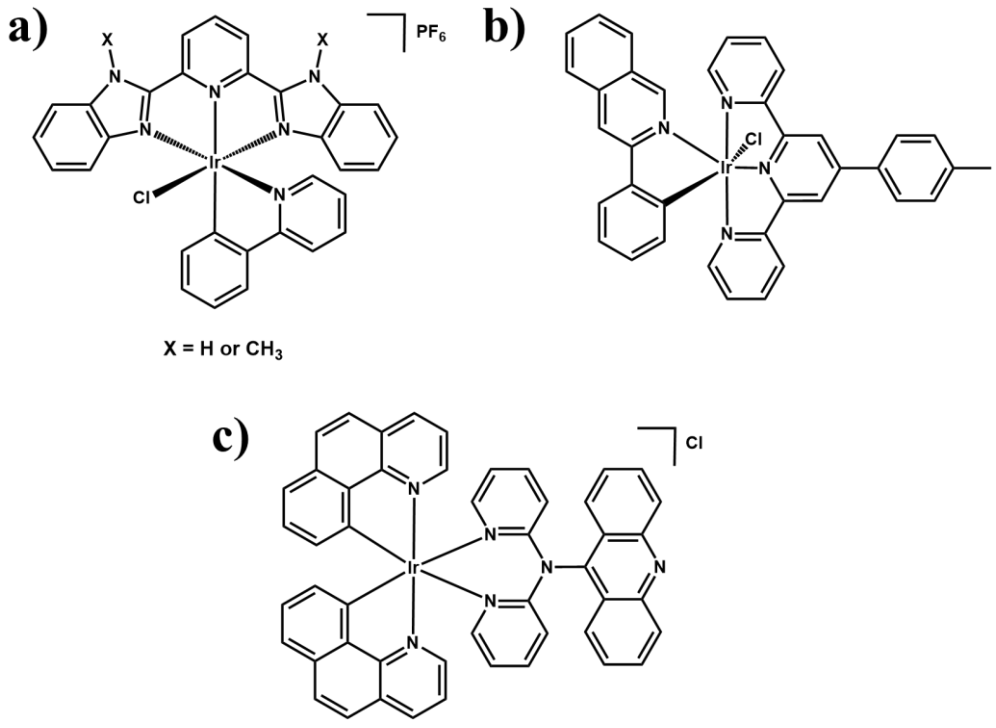

Figure 1.12. Structures of a) [Ir(L)(ppy)Cl](PF$_6$), b) [Ir(ttpy)(pq)Cl]PF$_6$, and c) Ir-acridine.

Ir(III) complexes have also been studied for their phosphorescence properties alone, with no research into their use for PDT. Liu *et al.* developed Ir(III) complexes to probe for cyclooxygenase-2 (overexpressed in a variety of cancer cells), with complexes exhibiting high specificity for cancer cells with low cytotoxicity.[121] Meanwhile, Ir(III)-oligoarginine complexes targeting vascular endothelial cells have been designed as probes for *in vivo* microvascular imaging.[122] In addition, the conjugation of chelators has led to the development of phosphorescent biological metal ion sensors,[123] further highlighting the excellent potential of cyclometalated Ir(III) complexes as both PDT and diagnostic agents.

1.4.3 PDT resistance and side effects

PDT resistance has so far only been observed *in vitro*, typically through altered influx/efflux as seen for non-photoactivatable drugs, and the extent of resistance is usually lower than seen for common chemotherapies in drug-resistant cell lines.[124,125] However, an increase of antioxidant enzymes and activation of heat shock proteins has led to increased inactivation of toxic species (*i.e.* ROS) in cells.[124] Currently, side effects of PDT include long-term skin photosensitivity (up to 3 months with Photofrin® treatment) due to photosensitizers accumulating in skin tissue.[126] Cancer-targeted photosensitizers may reduce such side effects due to less accumulation in healthy tissues.

1.4.4 Photoactivated chemotherapy

Photoactivated chemotherapy (PACT) is an oxygen-independent process that utilises light to activate otherwise inert compounds with a variety of mechanisms of action, with the potential to be more effective than PDT in hypoxic environments.[127]

In a clinical context, PACT is less developed than PDT. Whilst no metal-based compounds are currently approved for clinical use or in clinical trials, psoralen (**Figure 1.13**), an organic PACT agent structurally similar to coumarin, is clinically used in PUVA (psoralen + ultraviolet A) therapy to treat cutaneous T-cell lymphoma (CTCL) and other conditions.[128] However, long-term treatment with psoralen has been linked with higher rates of skin cancer.[129]

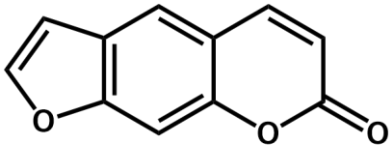

Psoralen

Figure 1.13. Structure of psoralen, used in PUVA.

Metal complexes have been explored as PACT agents due to their ability to generate active species in a variety of ways, including photoinduced electron transfer, photo-substitution, bioactive ligand release and ligand photocleavage.[127] In particular, Pt(IV) complexes have been explored as prodrugs to release cytotoxic Pt(II) agents and azide radicals upon irradiation.[130]

The novel mechanisms of action of Pt(IV) prodrugs have the possibility to overcome cisplatin resistance, and their selective activation has the potential to minimise side effects.[131] A series of diazido Pt(IV) photoactivatable prodrugs developed by Shi *et al*. exhibited low toxicity and high stability in the dark, combined with potent visible-light photocytotoxicity, making them good candidates for PACT.[131] Zhu *et al*. recently reported phorbiplatin – a novel platinum agent with an oxaliplatin scaffold.[132] Phorbiplatin is inert in the dark, but irradiation with red light leads to the formation of the Pt-conjugated pyropheophorbide a (PPA) anion, which dissociates to form oxaliplatin and PPA, inducing DNA damage and ROS generation, respectively, and resulting in *ca.* 1800× higher toxicity to breast cancer cells *in vitro* and 58× higher toxicity *in vivo* than the frontline chemotherapeutic oxaliplatin alone.[132] More recently, Gabbiani *et al.* developed a Pt(IV) complex bearing a tridentate terpyridine-based ligand with good dark stability that undergoes flavin-catalysed photoreduction upon 460 nm irradiation, however, *in vitro* studies are yet to be reported.[133] Other metal complexes have also been studied for applications in PACT, including Re(I) tricarbonyl complexes,[134] Ru(III) bisquinoline chelates,[135] and Os(II) half-sandwich complexes.[136]

1.4.5 PDT *vs.* PACT

Whilst both PDT and PACT both require a suitable wavelength for activation, their mechanisms of action differ greatly. Since PACT does not require oxygen for successful photocytotoxicity, it has in principle a great advantage over PDT in hypoxic environments. However, PDT is a much more clinically established modality, especially when considering the use of metal-based therapies. In addition, PDT photosensitizers must be photostable, in contrast to the deliberate photodissociation required from PACT agents. Therefore, PACT agents are likely to require further studies on their photodecomposition products and the nature of their interactions in biological settings, which may hinder their clinical development.

1.5 Cancer-targeted photosensitizers

Combining the spatial targeting of PDT with the targeting capabilities of bioconjugates has led to the development of cancer-targeted photosensitizers. For example, IR700 Dye (**Figure 1.10**) conjugated to cetuximab, a clinically used EGFR inhibitor, is currently in Phase III clinical trials for recurrent head/neck cancers (ASP-1929; NCT03769506).[137] IR700-conjugates with antibodies, nanobodies, and fragment antigen-binding regions targeted to a variety of receptors including EGFR, HER2, and PSMA have been reviewed by Tomé *et al.*[138] A structurally similar silicon phthalocyanine uses erlotinib for EGFR targeting and a methyl sulfonamide fragment designed to target the endoplasmic reticulum (ER) once internalised. The complex exhibited a low nanomolar photoactivated (λ = 670 nm) IC_{50} in EGFR-expressing cancer cells and was confirmed to localise in the ER by confocal microscopy, whilst analogues without the ER-targeting fragment were found in the mitochondria.[139]

In addition to these silicon phthalocyanine complexes, heavy metal complexes have been conjugated to targeting vectors in attempts to increase selectivity towards cancer cells (**Figure 1.14**). Weil *et al*. designed a relatively photostable Ru(II)-somatostatin (SST) conjugate to target cancer cells that overexpress somatostatin receptor subtype 2 (SSTR2).[140] The Ru-SST complex generates singlet oxygen and is internalised by cells *via* SSTR2. Although no data in healthy cell lines were

reported and the excitation wavelength is outside of the therapeutic window, blue light irradiation ($\lambda = 470$ nm) caused 23× greater activity in A549 lung cancer cells, potentially due to efficient internalisation.[140] More recently, Gasser *et al*. developed two Ru(II) polypyridyl complexes designed to target the gastrin-releasing peptide receptor (frequently overexpressed in cancer cells) by conjugation to bombesin.[141] Interestingly, bioconjugation did not lead to increased selectivity for cancer cells, however, the bioconjugates were less toxic in the dark than the parent complex, resulting in higher phototoxicity indexes.

Human serum albumin (HSA) can act as a delivery system for cancer drugs.[142] Zhang *et al.* therefore developed a novel Ir-HSA conjugate with ≤ 5 μM photo-IC_{50} values in multiple cancer cell lines, leading to phototoxicity indexes of between 40 and 60.[143]

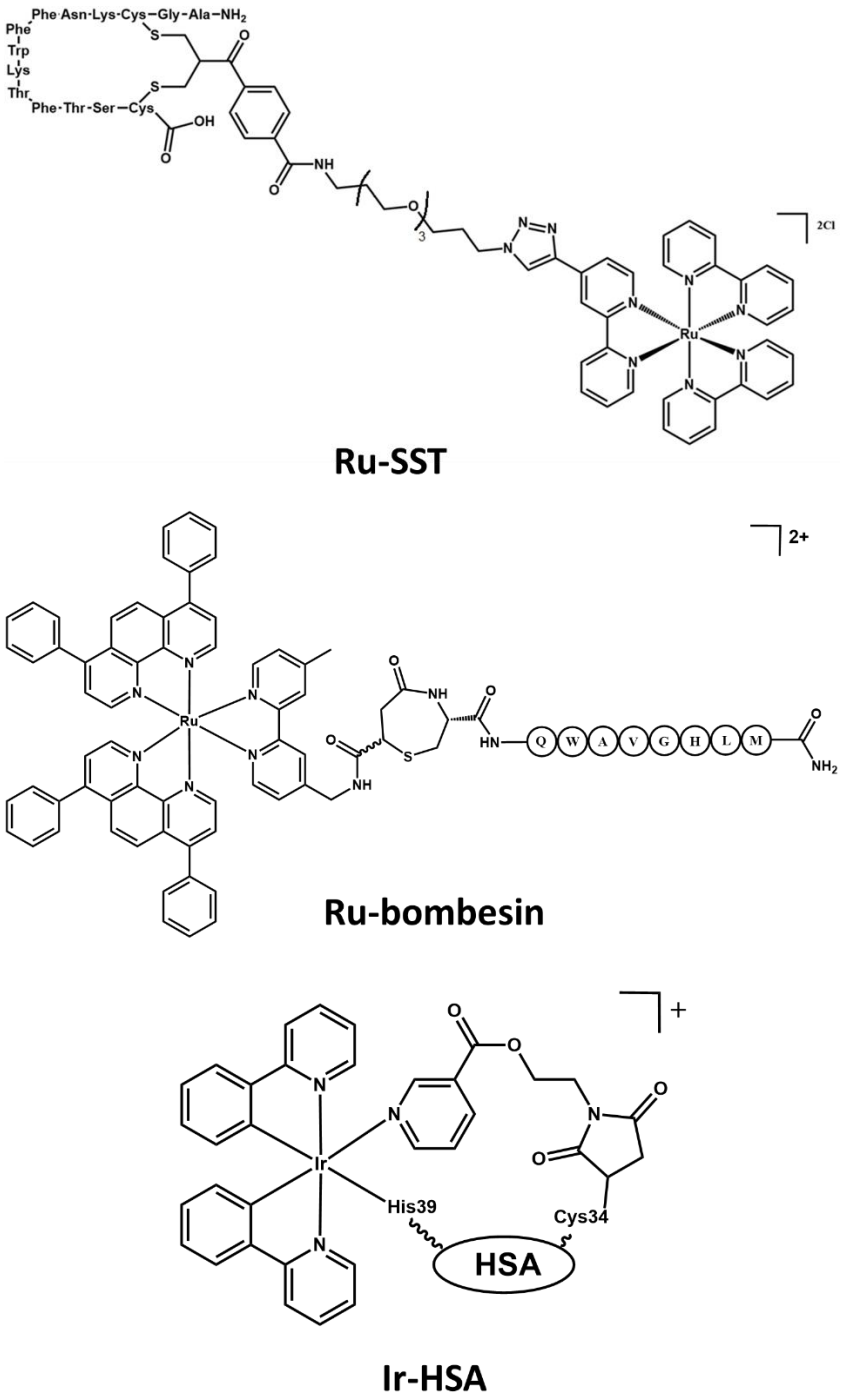

Figure 1.14. Structures of Ru-SST conjugate, Ru-bombesin conjugate, and Ir-albumin conjugate.

Conjugating PDT photosensitizers to EGFR targeting agents is one of the most common forms of targeting for photosensitizers. Several antibodies and inhibitors (*e.g.*, cetuximab, panitumumab, erlotinib, gefitinib) are clinically approved, so such conjugation may improve the chance of clinical approval over conjugates with non-clinically approved targeting vectors. However, Robinson *et al*. have warned that

EGFR density is not the only factor determining the effectiveness of anti-EGFR PSs, as intrinsic biological properties differ between cell lines which can lead to differences in cell death mechanisms.[144]

1.5.1 GLUT-targeting photosensitizers

GLUT1 is typically overexpressed in cancer cells, causing far greater glucose uptake than in healthy cells.[145] This increased glucose metabolism has been exploited clinically with the radiotracer [^{18}F]-FDG (**Figure 1.7**), a glucose analogue used in PET to determine the location and size of tumours. On this basis, the attachment of glucose to active complexes (glycoconjugation) has been explored as an approach for increasing selectivity towards cancer cells.

Several glycoconjugated photosensitizers have been investigated for GLUT1 targeting (**Figure 1.15**). The third-generation photosensitizer G-chlorin was synthesized by conjugating four glucose molecules to the photosensitizer chlorin, which showed 20-50 times more cytotoxicity than second-generation talaporfin in gastric and colon cancers.[146] Glycosylated zinc(II) phthalocyanines were reported to produce $^1O_2$ quantum yields of *ca*. 65% upon 670 nm irradiation, with irradiated IC_{50} values between 10 and 41 nM in MCF-7 breast cancer cells due to their high cellular uptake, caused by the overexpression of GLUT1.[147] Pyropheophorbide 2-deoxyglucosamide is another photosensitizer designed to target glucose transporters. The compound was shown to cause selective mitochondrial damage after irradiation in a 9L glioma rat model and did not affect surrounding tissues that were not irradiated.[148] Interestingly, a range of GLUT-targeting Ir(III) probes were developed by Law *et al.*, but these were not studied for their phototoxicity.[149]

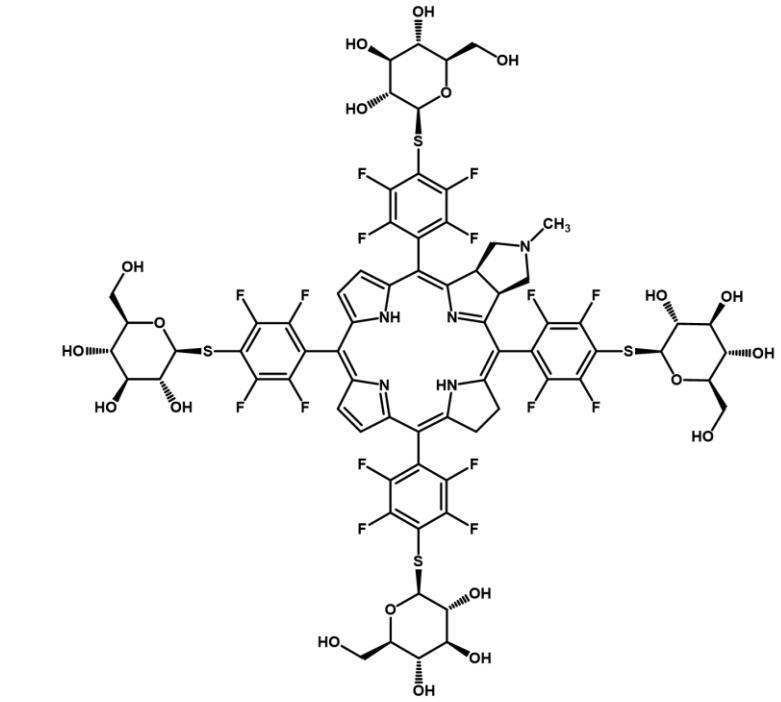

G-chlorin

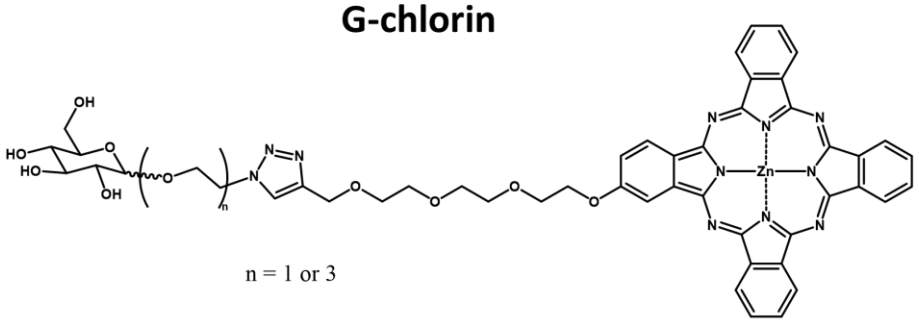

Glycosylated Zn phthalocyanine

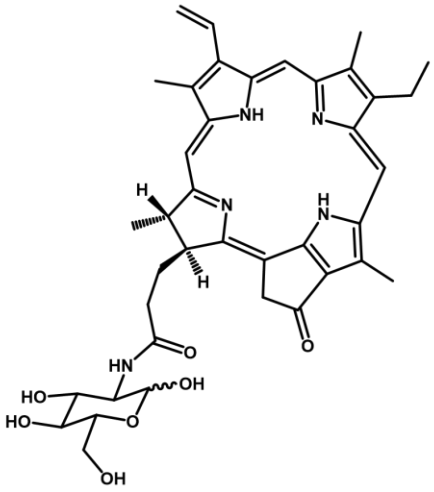

Pyropheophorbide 2-deoxyglucosamide

Figure 1.15. Structures of G-chlorin, glycosylated Zn phthalocyanines, and pyropheophorbide 2-deoxyglucosamide.

1.6 Synchrotron radiation

Synchrotron radiation is the energy emitted by a charged particle travelling at close to the speed of light when deviated from its path under the effect of a magnetic field.[150] At the UK's national synchrotron facility, Diamond Light Source (DLS), electrons are accelerated to nearly the speed of light using a linear accelerator (linac) and booster synchrotron. The electrons then enter the large storage ring, comprised of 24 straight sections with bending magnets to change their path. At these points, synchrotron radiation is emitted and channelled into the beamlines, with energies ranging from 0.6 meV up to 150 keV.[151]

X-rays have been used at DLS to study metal anticancer complexes in a variety of ways. For example, hard X-ray studies (2-100 keV) have been used to determine the stability of brominated osmium complexes in cancer cells,[152] whilst soft X-rays (0.1-2 keV) have been used to determine changes at the subcellular level in response to photoactivated iridium complexes.[153]

This thesis investigates the stability and accumulation of a bimetallic PDT-PACT complex in lung cancer cells using X-ray fluorescence, as well as determining the platinum oxidation state using X-ray absorption near-edge structure spectroscopy. Experiments were performed at the I14 beamline, which generates hard X-rays in the 5-23 keV range.

1.6.1 X-ray fluorescence spectroscopy

X-ray fluorescence (XRF) spectroscopy is a technique used to determine the elemental composition of a sample. High energy (hard) X-rays are used to bombard the sample, with sufficient energy to eject a low-energy core electron from the inner (K/L) shells (**Figure 1.16a**). The 'hole' left by the ejected electron is then filled by an electron in a higher energy orbital, releasing a photon with the energy equivalent to the difference in energy between the two quantum states (**Figure 1.16b**). The energy of the photon released differs for every element. Therefore, each element has a unique X-ray fluorescence spectrum, allowing for the determination of the elements present in a sample. These can be determined at concentrations as low as 100 ppb.

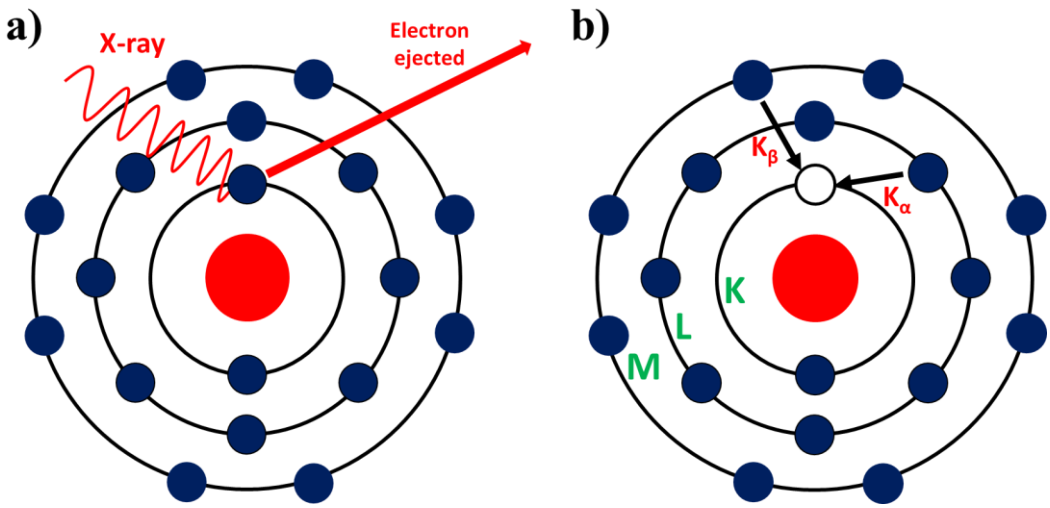

Figure 1.16. Principle of X-ray fluorescence. A) High energy X-rays eject a low energy core electron. B) The hole left by the ejected electron is filled by a higher energy electron, leading to emission of a photon (K_α/K_β).

For each atom, the shells are labelled K, L, and M with increasing energy (**Figures 1.16 and 1.17**). Since it is possible to achieve multiple emissions from the same element, emissions are labelled based on the electron's original shell and the shell of the hole it is filling. For example, a hole formed in the K-shell and filled by an electron from the L-shell would be a primary emission, labelled K_α, whilst the same hole filled by an M-shell electron would be a secondary emission, labelled K_β (**Figure 1.17**). Synchrotron XRF allows for the detection of multiple elements simultaneously. Therefore, using an incident energy greater than the highest electron binding energy of elements in the sample allows for the observation of all X-ray fluorescence in the sample, giving a full elemental composition. Electron binding energies of endogenous elements as well as those of Pt and Ir are summarised in **Appendix Table A1**.

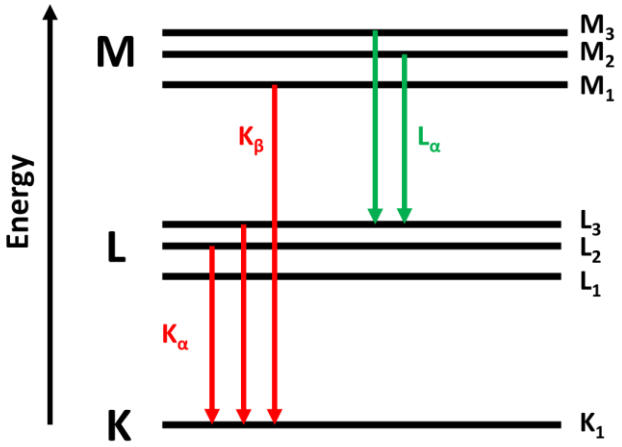

Figure 1.17. K_α, K_β and L_α emissions, where α emissions are from electrons one shell higher in energy, and β emissions from electrons two shells higher in energy. Adapted from reference.[154]

XRF can be used to probe the in-cell stability of complexes by correlating the positions of the metal centre with other exogenous elements in the structure, as well as to determine intracellular localisation, co-localisation with endogenous elements, and total intracellular content of exogenous elements. This has been demonstrated previously in cancer cells treated with heavy metal complexes, including those of platinum,[155] iridium,[156] osmium,[77,157] and ruthenium.[158] The I14 beamline does not currently have the facilities for cryogenic samples, so cells must be cryo-fixed and freeze-dried before analysis.

1.6.2 X-ray absorption near-edge structure spectroscopy

X-ray absorption near-edge structure (XANES) spectroscopy is a type of X-ray absorption spectroscopy (XAS) using a scanned energy range to determine the oxidation state of an atom. A 'jump' (edge) is observed in the absorption profile when X-rays are absorbed, followed by a unique fingerprint. In an X-ray absorption spectrum, the XANES region refers to the 'edge-jump' (from 30 eV pre-edge to 50 eV after the edge), whereas the EXAFS region refers to the fingerprint region >50 eV (**Figure 1.18**).

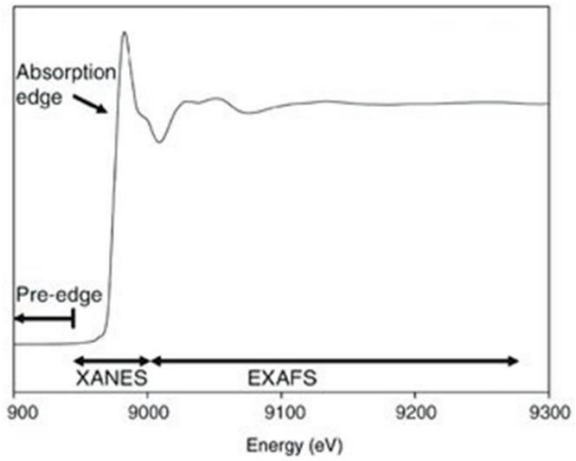

Figure 1.18. Representative X-ray absorption spectrum with XANES and EXAFS regions labelled. Adapted from reference.[159]

XANES has been widely used in the analysis of heavy metal anticancer complexes. Previously, Sadler *et al.* probed the oxidation state of an organo-osmium complex in ovarian cancer cells, whilst Hambley *et al.* have investigated Pt(IV) anticancer pro-drugs such as those based on cisplatin and transplatin in ovarian and colorectal cancer cells.[160–162] Furthermore, clinically trialled ruthenium complexes KP1019, KP1339, and NAMI-A have been studied by XANES, including in tissues of tumour-bearing mice.[67,163,164]

1.7 Research aims

This thesis explores new approaches to the development of Ir(III) photosensitizers for cancer treatment, focussing on 1) the development of novel Ir(III) glycoconjugates which combine the spatial targeting of PDT with the cellular targeting of glucose receptors, and 2) the use of innovative synchrotron techniques to study the mechanism of action of an iridium-platinum based PDT-PACT agent. The content of the three results chapters is summarised as below.

- **Photophysical properties of novel Ir(III) and Ru(II) glycoconjugates**

Chapter 3 details the synthesis and characterisation of novel Ir(III) and Ru(II) glycoconjugates with varied sugars and linkers designed to exploit the Warburg effect. Photophysical properties of each complex are assessed for use as Type II photosensitizers in PDT.

- **Anticancer activity and selectivity of Ir(III) glycoconjugates**

In **Chapter 4**, the biological properties of Ir(III) glycoconjugates are investigated in cancer cells. The biological activity of lead complexes with and without irradiation is measured, as well as their ability for in-cell singlet oxygen generation upon irradiation. Their GLUT1 targeting capabilities are assessed using confocal microscopy and ICP-MS to determine the cellular accumulation of complexes in the presence of a highly selective GLUT1 inhibitor.

- **Cellular distribution and oxidation states of a photoactivatable Pt(IV)-Ir(III) complex using synchrotron radiation**

Chapter 5 investigates the (photo)stability and cellular distribution of a dual mode-of-action Pt(IV)-Ir(III) photosensitizer in cryo-fixed cancer cells using synchrotron X-ray fluorescence. In addition, the oxidation state of Pt is studied to determine the extent of photoreduction from Pt(IV) to Pt(II) upon irradiation using X-ray absorption near-edge structure spectroscopy.

1.8 References

1 S. Sarkar, G. Horn, K. Moulton, A. Oza, S. Byler, S. Kokolus and M. Longacre, *Int. J. Mol. Sci.*, 2013, **14**, 21087–21113.

2 S. H. Hassanpour and M. Dehghani, *J. Cancer Res. Pract.*, 2017, **4**, 127–129.

3 G. B. Faguet, *Int. J. Cancer*, 2015, **136**, 2022–2036.

4 A. S. Ahmad, N. Ormiston-Smith and P. D. Sasieni, *Br. J. Cancer*, 2015, **112**, 943–947.

5 H. Sung, J. Ferlay, R. L. Siegel, M. Laversanne, I. Soerjomataram, A. Jemal and F. Bray, *CA. Cancer J. Clin.*, 2021, **71**, 209–249.

6 H. F. Thomas, *Cancer and the environment*, 1978, vol. 86.

7 N. Parsa, *Iran. J. Public Health*, 2012, **41**, 1–9.

8 P. Anand, A. B. Kunnumakara, C. Sundaram, K. B. Harikumar, S. T. Tharakan, O. S. Lai, B. Sung and B. B. Aggarwal, *Pharm. Res.*, 2008, **25**, 2097–2116.

9 M. R. Stratton, P. J. Campbell and P. A. Futreal, *Nature*, 2009, **458**, 719–724.

10 D. Hanahan and R. A. Weinberg, *Cell*, 2000, **100**, 57–70.

11 D. Hanahan and R. A. Weinberg, *Cell*, 2011, **144**, 646–674.

12 R. Singh, A. Letai and K. Sarosiek, *Nat. Rev. Mol. Cell Biol.*, 2019, **20**, 175–193.

13 S. Elmore, *Toxicol. Pathol.*, 2007, **35**, 495–516.

14 M. S. D'Arcy, *Cell Biol. Int.*, 2019, **43**, 582–592.

15 H. Plattner and A. Verkhratsky, *Philos. Trans. R. Soc. B Biol. Sci.*, 2016, **371**, 20150419.

16 A. Kumari, in *Sweet Biochemistry*, Elsevier, 2018, pp. 1–5.

17 L. Norton and R. DeFronzo, in *Pathobiology of Human Disease*, Elsevier, 2014, pp. 477–487.

18 C. F. Williams, in *Encyclopedia of Infection and Immunity*, Elsevier, 2022, pp. 363–376.

19 H. E. Burrell, B. Wlodarski, B. J. Foster, K. A. Buckley, G. R. Sharpe, J. M. Quayle, A. W. M. Simpson and J. A. Gallagher, *J. Biol. Chem.*, 2005, **280**, 29667–29676.

20 G. M. Cooper, in *The Cell: A Molecular Approach*, Sinauer Associates, New York, Eighth., 2019, pp. 77–106.

21 E. Alegre, M. Sammamed, S. Fernández-Landázuri, L. Zubiri and Á. González, in *Advances in Clinical Chemistry*, 2015, pp. 47–89.

22 G. Stojan and L. Christopher-Stine, in *Rheumatology*, Elsevier, 2015, pp. 1255–1263.

23 O. Warburg, *Naturwissenschaften*, 1924, **12**, 1131–1137.

24 O. Warburg, *J. Cancer Res.*, 1925, **9**, 148–163.

25 M. G. Vander Heiden, L. C. Cantley and C. B. Thompson, *Science*, 2009,

324, 1029–1033.

26 Z. E. Stine, B. J. Altman, A. L. Hsieh, A. M. Gouw and C. V. Dang, in *Pathobiology of Human Disease*, Elsevier, 2014, pp. 444–455.

27 M. Achalandabaso Boira, M. Di Martino, C. Gordillo, M. Adrados and E. Martín-Pérez, *BMC Cancer*, 2020, **20**, 1–9.

28 M. Yu, H. Yongzhi, S. Chen, X. Luo, Y. Lin, Y. Zhou, H. Jin, B. Hou, Y. Deng, L. Tu and Z. Jian, *Oncotarget*, 2017, **8**, 43356–43367.

29 S. Meziou, C. Ringuette Goulet, H. Hovington, V. Lefebvre, É. Lavallée, M. Bergeron, H. Brisson, A. Champagne, B. Neveu, D. Lacombe, J. M. Beauregard, F. A. Buteau, J. Riopel and F. Pouliot, *Prostate Cancer Prostatic Dis.*, 2020, **23**, 441–448.

30 Y. Deng, J. Zou, T. Deng and J. Liu, *Medicine*, 2018, **97**, 1–6.

31 B. Zhang, Z. Xie and B. Li, *Gene*, 2019, **689**, 76–83.

32 W. Lawrence, in *Surgery: Basic Science and Clinical Evidence: Second Edition*, 2008, pp. 1889–1900.

33 P. P. Connell and S. Hellman, *Cancer Res.*, 2009, **69**, 383–392.

34 M. Arruebo, N. Vilaboa, B. Sáez-Gutierrez, J. Lambea, A. Tres, M. Valladares and Á. González-Fernández, *Cancers*, 2011, **3**, 3279–3330.

35 P. Dobosz and T. Dzieciątkowski, *Front. Immunol.*, 2019, **10**, 2965.

36 Y. Zhang and Z. Zhang, *Cell. Mol. Immunol.*, 2020, **17**, 807–821.

37 G. Chaput and N. Sumar, *Can. Fam. Physician*, 2022, **68**, 271–276.

38 Chemotherapy, radiotherapy and surgical tumour resections in England, Public Health England, 2020.

39 M. Galanski, M. Jakupec and B. Keppler, *Curr. Med. Chem.*, 2005, **12**, 2075–2094.

40 S. Dasari and P. Bernard Tchounwou, *Eur. J. Pharmacol.*, 2014, **740**, 364–378.

41 B. Rosenberg, L. Van Camp and T. Krigas, *Nature*, 1965, **205**, 698–699.

42 B. Rosenberg, E. Renshaw, L. Vancamp, J. Hartwick and J. Drobnik, *J. Bacteriol.*, 1967, **93**, 716–721.

43 B. Rosenberg, L. Van Camp, E. B. Grimley and A. J. Thomson, *J. Biol. Chem.*, 1967, **242**, 1347–1352.

44 B. Rosenberg, L. Van Camp, J. E. Trosko and V. H. Mansour, *Nature*, 1969, **222**, 385–386.

45 L. Kelland, *Nat. Rev. Cancer*, 2007, **7**, 573–584.

46 A. M. Florea and D. Büsselberg, *Cancers*, 2011, **3**, 1351–1371.

47 A. Ibrahim, S. Hirschfeld, M. H. Cohen, D. J. Griebel, G. A. Williams and R. Pazdur, *Oncologist*, 2004, **9**, 8–12.

48 G. Hamilton and U. Olszewski, *Expert Opin. Drug Metab. Toxicol.*, 2013, **9**, 1381–1390.

49 A. Bhargava and U. N. Vaishampayan, *Expert Opin. Investig. Drugs*, 2009, **18**, 1787–1797.

50 G. Morrison, in *Clinical Methods: The History, Physical, and Laboratory Examinations*, 1990, pp. 890–894.

51 L. Ding, Y. Lian, Z. Lin, Z. Zhang and X. D. Wang, *ACS Sensors*, 2020, **5**, 3971–3978.

52 J. K. C. Lau and B. Ensing, *Phys. Chem. Chem. Phys.*, 2010, **12**, 10348–10355.

53 M. H. Shamsi and H.-B. Kraatz, *J. Inorg. Organomet. Polym. Mater.*, 2013, **23**, 4–23.

54 A. Mandic, J. Hansson, S. Linder and M. C. Shoshan, *J. Biol. Chem.*, 2003, **278**, 9100–9106.

55 J. C. Huang, D. B. Zamble, J. T. Reardon, S. J. Lippard and A. Sancar, *Proc. Natl. Acad. Sci. U. S. A.*, 1994, **91**, 10394–10398.

56 S. M. Sancho-Martínez, F. J. Piedrafita, J. B. Cannata-Andía, J. M. López-

Novoa and F. J. López-Hernández, *Toxicol. Sci.*, 2011, **122**, 73–85.

57 P. M. Bruno, Y. Liu, G. Y. Park, J. Murai, C. E. Koch, T. J. Eisen, J. R. Pritchard, Y. Pommier, S. J. Lippard and M. T. Hemann, *Nat. Med.*, 2017, **23**, 461–471.

58 J. P. C. Coverdale, PhD Thesis, University of Warwick, 2017.

59 J. Zhou, Y. Kang, L. Chen, H. Wang, J. Liu, S. Zeng and L. Yu, *Front. Pharmacol.*, 2020, **11**, 1–17.

60 D. Kilari, E. Guancial and E. S. Kim, *World J. Clin. Oncol.*, 2016, **7**, 106–113.

61 P. Abada and S. B. Howell, *Met. Based. Drugs*, 2010, **2010**, 1–9.

62 R. Fujii, M. Mutoh, K. Niwa, K. Yamada, T. Aikou, M. Nakagawa, M. Kuwano and S. Akiyama, *Japanese J. Cancer Res.*, 1994, **85**, 426–433.

63 D. W. Shen, L. M. Pouliot, M. D. Hall and M. M. Gottesman, *Pharmacol. Rev.*, 2012, **64**, 706–721.

64 B. Mansoori, A. Mohammadi, S. Davudian, S. Shirjang and B. Baradaran, *Adv. Pharm. Bull.*, 2017, **7**, 339–348.

65 D. J. Stewart, *Crit. Rev. Oncol. Hematol.*, 2007, **63**, 12–31.

66 B. Stordal, N. Pavlakis and R. Davey, *Cancer Treat. Rev.*, 2007, **33**, 347–357.

67 E. Alessio and L. Messori, *Molecules*, 2019, **24**, 1995.

68 S. Leijen, S. A. Burgers, P. Baas, D. Pluim, M. Tibben, E. Van Werkhoven, E. Alessio, G. Sava, J. H. Beijnen and J. H. M. Schellens, *Invest. New Drugs*, 2015, **33**, 201–214.

69 D. Wernitznig, K. Kiakos, G. Del Favero, N. Harrer, H. MacHat, A. Osswald, M. A. Jakupec, A. Wernitznig, W. Sommergruber and B. K. Keppler, *Metallomics*, 2019, **11**, 1044–1048.

70 C. G. Hartinger, M. A. Jakupec, S. Zorbas-Seifried, M. Groessl, A. Egger, W. Berger, H. Zorbas, P. J. Dyson and B. K. Keppler, *Chem. Biodivers.*,

2008, **5**, 2140–2155.

71 BOLD-100 in Combination With FOLFOX for the Treatment of Advanced Solid Tumours, NCT04421820, https://clinicaltrials.gov/ct2/show/NCT04421820, (accessed 8 February 2023).

72 J. L. Spratlin, G. O´Kane, R. A. Goodwin, E. McWhirter, D. Thompson, K. Halani, M. Jones, M. Snow, E. R. McAllister, A. Machado, Y. Lemmerick and J. Pankovich, *J. Clin. Oncol.*, 2022, **40**, 3031–3031.

73 K. D. Mjos and C. Orvig, *Chem. Rev.*, 2014, **114**, 4540–4563.

74 B. Cebrián-Losantos, A. A. Krokhin, I. N. Stepanenko, R. Eichinger, M. A. Jakupec, V. B. Arion and B. K. Keppler, *Inorg. Chem.*, 2007, **46**, 5023–5033.

75 G. E. Büchel, I. N. Stepanenko, M. Hejl, M. A. Jakupec, B. K. Keppler and V. B. Arion, *Inorg. Chem.*, 2011, **50**, 7690–7697.

76 S. A. Kumar, R. J. Needham, K. Abraham, H. E. Bridgewater, L. A. Garbutt, H. Xandri-Monje, R. Dallmann, S. Perrier, P. J. Sadler and F. Lévi, *Metallomics*, 2021, 13, mfaa003.

77 C. Sanchez-Cano, I. Romero-Canelón, Y. Yang, I. J. Hands-Portman, S. Bohic, P. Cloetens and P. J. Sadler, *Chem. - A Eur. J.*, 2017, **23**, 2512–2516.

78 A. Ballesta, F. Billy, J. P. C. Coverdale, J. I. Song, C. Sanchez-Cano, I. Romero-Canelón and P. J. Sadler, *Metallomics*, 2019, **11**, 1648–1656.

79 P. Zhang and H. Huang, *Dalton Trans.*, 2018, **47**, 14841–14854.

80 M. Rausch, P. J. Dyson and P. Nowak-Sliwinska, *Adv. Ther.*, 2019, **2**, 1–12.

81 A. Weiss, R. H. Berndsen, M. Dubois, C. Müller, R. Schibli, A. W. Griffioen, P. J. Dyson and P. Nowak-Sliwinska, *Chem. Sci.*, 2014, **5**, 4742–4748.

82 C. Scolaro, C. G. Hartinger, C. S. Allardyce, B. K. Keppler and P. J. Dyson, *J. Inorg. Biochem.*, 2008, **102**, 1743–1748.

83 S. Chatterjee, S. Kundu, A. Bhattacharyya, C. G. Hartinger and P. J. Dyson, *J. Biol. Inorg. Chem.*, 2008, **13**, 1149–1155.

84 K. Aratani, S. Komatsu, D. Ichikawa, T. Ohashi, M. Miyamae, W. Okajima,

T. Imamura, J. Kiuchi, K. Nishibeppu, T. Kosuga, H. Konishi, A. Shiozaki, H. Fujiwara, K. Okamoto, H. Tsuda and E. Otsuji, *Anticancer Res.*, 2017, **37**, 3129–3135.

85 G. Giordano, A. Remo, A. Porras and M. Pancione, *Cancers*, 2019, 11, 1089.

86 T. P. Zanto, K. Hennigan, M. Östberg, W. C. Clapp and A. Gazzaley, *Oncogene*, 2007, **45**, 6469–6487.

87 S. S. Chang, *Rev. Urol.*, 2004, **6 Suppl 10**, S13-8.

88 M. Eiber, W. P. Fendler, S. P. Rowe, J. Calais, M. S. Hofman, T. Maurer, S. M. Schwarzenboeck, C. Kratowchil, K. Herrmann and F. L. Giesel, *J. Nucl. Med.*, 2017, **58**, 67S-76S.

89 A. Zambrano, M. Molt, E. Uribe and M. Salas, *Int. J. Mol. Sci.*, 2019, **20**, 1–20.

90 S. Patching, *J. Diagnostic Imaging Ther.*, 2015, **2**, 30–102.

91 C. Granchi, S. Fortunato and F. Minutolo, *Medchemcomm*, 2016, **7**, 1716–1729.

92 W. Bian, Y. Wang, Z. Pan, N. Chen, X. Li, W. L. Wong, X. Liu, Y. He, K. Zhang and Y. J. Lu, *ACS Appl. Nano Mater.*, 2021, **4**, 11353–11385.

93 P. Agostinis, K. Berg, K. A. Cengel, T. H. Foster, A. W. Girotti, S. O. Gollnick, S. M. Hahn, M. R. Hamblin, A. Juzeniene, D. Kessel, M. Korbelik, J. Moan, P. Mroz, D. Nowis, J. Piette, B. C. Wilson and J. Golab, *CA. Cancer J. Clin.*, 2011, **61**, 250–281.

94 L. Finlayson, I. R. M. Barnard, L. McMillan, S. H. Ibbotson, C. T. A. Brown, E. Eadie and K. Wood, *Photochem. Photobiol.*, 2022, **98**, 974–981.

95 E. Ruggiero, S. Alonso-De Castro, A. Habtemariam and L. Salassa, *Dalton Trans.*, 2016, **45**, 13012–13020.

96 E. Jeffes, *J. Dermatolog. Treat.*, 2002, **Volume 13**, s19–s23.

97 Z. Huang, *Technol. Cancer Res. Treat.*, 2005, **4**, 283–293.

98 T. Neubert and P. Lehmann, *Ther. Clin. Risk Manag.*, 2008, **4**, 1085–1095.

99 R. Baskaran, J. Lee and S.-G. Yang, *Biomater. Res.*, 2018, **22**, 1–8.

100 G. L. Miessler, P. J. Fischer and D. A. Tarr, *Inorganic Chemistry*, Pearson, Fifth., 2014.

101 X. Jiang, J. Peng, J. Wang, X. Guo, D. Zhao and Y. Ma, *ACS Appl. Mater. Interfaces*, 2016, **8**, 3591–3600.

102 M. D. S. Baptista, J. Cadet, P. Di Mascio, A. A. Ghogare, A. Greer, M. R. Hamblin, C. Lorente, S. Cristina Nunez, M. S. Ribeiro, A. H. Thomas, M. Vignoni and T. M. Yoshimura, *Photochem. Photobiol.*, 2017, **93**, 912–919.

103 F. Bolze, S. Jenni, A. Sour and V. Heitz, *Chem. Commun.*, 2017, **53**, 12857–12877.

104 P. R. Ogilby, *Chem. Soc. Rev.*, 2010, **39**, 3181–3209.

105 F. Heinemann, J. Karges and G. Gasser, *Acc. Chem. Res.*, 2017, **50**, 2727–2736.

106 B. Muz, P. de la Puente, F. Azab and A. K. Azab, *Hypoxia*, 2015, 83.

107 G. M. F. Calixto, J. Bernegossi, L. M. De Freitas, C. R. Fontana, M. Chorilli and A. M. Grumezescu, *Molecules*, 2016, 21, 342.

108 E. Reginato, *World J. Immunol.*, 2014, **4**, 1.

109 W. Wang, K. Tabu, Y. Hagiya, Y. Sugiyama, Y. Kokubu, Y. Murota, S. I. Ogura and T. Taga, *Sci. Rep.*, 2017, **7**, 1–12.

110 D. M. Cognetti, J. M. Johnson, J. M. Curry, S. T. Kochuparambil, D. McDonald, F. Mott, M. J. Fidler, K. Stenson, N. R. Vasan, M. A. Razaq, J. Campana, P. Ha, G. Mann, K. Ishida, M. Garcia-Guzman, M. Biel and A. M. Gillenwater, *Head Neck*, 2021, **43**, 3875–3887.

111 E. F. Stranadko, *Biomed. Photonics*, 2015, **4**, 3–10.

112 S. A. McFarland, A. Mandel, R. Dumoulin-White and G. Gasser, *Curr. Opin. Chem. Biol.*, 2020, **56**, 23–27.

113 A. Sieroń, K. Sieroń-Stołtny, A. Kawczyk-Krupka, W. Latos, S. Kwiatek, D. Straszak and A. M. Bugaj, *Onco. Targets. Ther.*, 2013, **6**, 977–982.

114 C. Mari, V. Pierroz, S. Ferrari and G. Gasser, *Chem. Sci.*, 2015, **6**, 2660–2686.

115 P. I. Djurovich, D. Murphy, M. E. Thompson, B. Hernandez, R. Gao, P. L. Hunt and M. Selke, *Dalton Trans.*, 2007, 3763–3770.

116 H. Huang, S. Banerjee and P. J. Sadler, *ChemBioChem*, 2018, **19**, 1574–1589.

117 B. Kar, U. Das, N. Roy and P. Paira, *Coord. Chem. Rev.*, 2023, **474**, 214860.

118 Y. Zheng, L. He, D. Y. Zhang, C. P. Tan, L. N. Ji and Z. W. Mao, *Dalton Trans.*, 2017, **46**, 11395–11407.

119 H. Huang, S. Banerjee, K. Qiu, P. Zhang, O. Blacque, T. Malcomson, M. J. Paterson, G. J. Clarkson, M. Staniforth, V. G. Stavros, G. Gasser, H. Chao and P. J. Sadler, *Nat. Chem.*, 2019, **11**, 1041–1048.

120 M. Redrado, A. Benedi, I. Marzo, M. C. Gimeno and V. Fernández-Moreira, *Pharmaceutics*, 2021, 13, 1382.

121 C. Liu, C. Yang, L. Lu, W. Wang, W. Tan, C. H. Leung and D. L. Ma, *Chem. Commun.*, 2017, **53**, 2822–2825.

122 M. Yasukagawa, A. Shimada, S. Shiozaki, S. Tobita and T. Yoshihara, *Sci. Rep.*, 2021, **11**, 1–11.

123 Y. You, S. Cho and W. Nam, *Inorg. Chem.*, 2014, **53**, 1804–1815.

124 A. Casas, G. Di Venosa, T. Hasan and A. Batlle, *Curr. Med. Chem.*, 2011, **18**, 2486–2515.

125 B. J. Mossakowska, S. Shahmoradi Ghahe, D. Cysewski, A. Fabisiewicz, B. Tudek and J. A. Siedlecki, *Int. J. Mol. Sci.*, 2022, 23, 4117.

126 J. M. Dunn, G. D. MacKenzie, M. R. Banks, C. A. Mosse, R. Haidry, S. Green, S. Thorpe, M. Rodriguez-Justo, A. Winstanley, M. R. Novelli, S. G. Bown and L. B. Lovat, *Lasers Med. Sci.*, 2013, **28**, 707–715.

127 C. Imberti, P. Zhang, H. Huang and P. J. Sadler, *Angew. Chem.*, 2020, **132**, 61–73.

128 S. H. Ibbotson, *Front. Med.*, 2018, **5**, 1–8.

129 J. M. Ortiz Salvador, A. Pérez-Ferriols, V. Alegre de Miquel, M. Saneleuterio Temporal and J. J. Vilata Corell, *Med. Clínica (English Ed.)*, 2019, **152**, 488–492.

130 H. Shi, C. Imberti and P. J. Sadler, *Inorg. Chem. Front.*, 2019, **6**, 1623–1638.

131 H. Shi, Q. Wang, V. Venkatesh, G. Feng, L. S. Young, I. Romero-Canelón, M. Zeng and P. J. Sadler, *Dalton Trans.*, 2019, **48**, 8560–8564.

132 Z. Wang, N. Wang, S. C. Cheng, K. Xu, Z. Deng, S. Chen, Z. Xu, K. Xie, M. K. Tse, P. Shi, H. Hirao, C. C. Ko and G. Zhu, *Chem*, 2019, **5**, 3151–3165.

133 G. Canil, J. Gurruchaga-Pereda, S. Braccini, L. Marchetti, T. Funaioli, F. Marchetti, A. Pratesi, L. Salassa and C. Gabbiani, *Int. J. Mol. Sci.*, 2023, **24**, 1106.

134 H. S. Liew, C. W. Mai, M. Zulkefeli, T. Madheswaran, L. V. Kiew, N. Delsuc and M. Lee Low, *Molecules*, 2020, **25**, 1–23.

135 A. Busemann, I. Flaspohler, X. Q. Zhou, C. Schmidt, S. K. Goetzfried, V. H. S. van Rixel, I. Ott, M. A. Siegler and S. Bonnet, *J. Biol. Inorg. Chem.*, 2021, **26**, 667–674.

136 X. Xue, Y. Fu, L. He, L. Salassa, L. F. He, Y. Y. Hao, M. J. Koh, C. Soulié, R. J. Needham, A. Habtemariam, C. Garino, K. A. Lomachenko, Z. Su, Y. Qian, M. J. Paterson, Z. W. Mao, H. K. Liu and P. J. Sadler, *Inorg. Chem.*, 2021, **60**, 17450–17461.

137 ASP-1929 Photoimmunotherapy (PIT) Study in Recurrent Head/Neck Cancer for Patients Who Have Failed at Least Two Lines of Therapy, NCT03769506, https://clinicaltrials.gov/ct2/show/NCT03769506 (accessed 8 February 2023)

138 S. R. G. Fernandes, R. Fernandes, B. Sarmento, P. M. R. Pereira and J. P. C. Tomé, *Org. Biomol. Chem.*, 2019, **17**, 2579–2593.

139 X. Zhao, H. Ma, J. Chen, F. Zhang, X. Jia and J. Xue, *Eur. J. Med. Chem.*,

2019, **182**, 111625.

140 T. Wang, N. Zabarska, Y. Wu, M. Lamla, S. Fischer, K. Monczak, D. Y. W. Ng, S. Rau and T. Weil, *Chem. Commun.*, 2015, **51**, 12552–12555.

141 M. J. S. A. Silva, R. Vinck, Y. Wang, B. Saubaméa, M. Tharaud, E. Dominguez-Jurado, J. Karges, P. M. P. Gois and G. Gasser, *ChemBioChem*, 2022, **202200647**, 1–8.

142 L. Van de Sande, S. Cosyns, W. Willaert and W. Ceelen, *Drug Deliv.*, 2020, **27**, 40–53.

143 P. Zhang, H. Huang, S. Banerjee, G. Clarkson, C. Ge, C. Imberti and P. J. Sadler, *Angew. Chem.*, 2018, **1**, 2372–2376.

144 W. Peng, H. S. de Bruijn, E. Farrell, M. Sioud, V. Mashayekhi, S. Oliveira, G. M. van Dam, J. L. N. Roodenburg, M. J. H. Witjes and D. J. Robinson, *Lasers Surg. Med.*, 2018, **50**, 513–522.

145 A. Bukkuri, R. A. Gatenby and J. S. Brown, *npj Syst. Biol. Appl.*, 2022, 8:22.

146 H. Kataoka, H. Nishie, N. Hayashi, M. Tanaka, A. Nomoto, S. Yano and T. Joh, *Ann. Transl. Med.*, 2017, **5**, 183–183.

147 J.-Y. Liu, C. Wang, C.-H. Zhu, Z.-H. Zhang and J.-P. Xue, *Molecules*, 2017, **22**, 845.

148 M. Zhang, Z. Zhang, D. Blessington, H. Li, T. M. Busch, V. Madrak, J. Miles, B. Chance, J. D. Glickson and G. Zheng, *Bioconjug. Chem.*, 2003, **14**, 709–714.

149 W. H. T. Law, L. C. C. Lee, M. W. Louie, H. W. Liu, T. W. H. Ang and K. K. W. Lo, *Inorg. Chem.*, 2013, **52**, 13029–13041.

150 A. Balerna and S. Mobilio, in *Synchrotron Radiation: Basics, Methods and Applications*, eds. S. Mobilio, F. Boscherini and C. Meneghini, Springer Berlin Heidelberg, Berlin, Heidelberg, 2015, pp. 3–28.

151 G. Materlik, T. Rayment and D. I. Stuart, *Philos. Trans. R. Soc. A Math. Phys. Eng. Sci.*, **2015**, 373, 20130161.

152 E. M. Bolitho, J. P. C. Coverdale, H. E. Bridgewater, G. J. Clarkson, P. D.

Quinn, C. Sanchez-Cano and P. J. Sadler, *Angew. Chem. Int. Ed.*, 2021, **60**, 6462–6472.

153 E. M. Bolitho, C. Sanchez-Cano, H. Huang, I. Hands-Portman, M. Spink, P. D. Quinn, M. Harkiolaki and P. J. Sadler, *J. Biol. Inorg. Chem.*, 2020, **25**, 295–303.

154 E. M. Bolitho, PhD Thesis, University of Warwick, 2020.

155 R. Koba, H. Fujita, M. Nishibori, K. Saeki, K. Nagayoshi, Y. Sadakari, S. Nagai, O. Sekizawa, K. Nitta, T. Manabe, T. Ueki, T. Ishida, Y. Oda and M. Nakamura, *Int. J. Cancer*, 2020, **146**, 2498–2509.

156 J. J. Conesa, A. C. Carrasco, V. Rodríguez-Fanjul, Y. Yang, J. L. Carrascosa, P. Cloetens, E. Pereiro and A. M. Pizarro, *Angew. Chem. Int. Ed.*, 2020, **59**, 1270–1278.

157 E. M. Bolitho, H. E. Bridgewater, R. J. Needham, J. P. C. Coverdale, P. D. Quinn, C. Sanchez-Cano and P. J. Sadler, *Inorg. Chem. Front.*, 2021, **8**, 3675–3685.

158 S. Antony, J. B. Aitken, S. Vogt, B. Lai, T. Brown, L. Spiccia and H. H. Harris, *J. Biol. Inorg. Chem.*, 2013, **18**, 845–853.

159 R. Terzano, M. A. Denecke, G. Falkenberg, B. Miller, D. Paterson and K. Janssens, *Pure Appl. Chem.*, 2019, **91**, 1029–1063.

160 M. D. Hall, G. J. Foran, M. Zhang, P. J. Beale and T. W. Hambley, *J. Am. Chem. Soc.*, 2003, **125**, 7524–7525.

161 C. K. J. Chen, P. Kappen, D. Gibson and T. W. Hambley, *Dalton Trans.*, 2020, **49**, 7722–7736.

162 M. D. Hall, H. L. Daly, J. Z. Zhang, M. Zhang, R. A. Alderden, D. Pursche, G. J. Foran and T. W. Hambley, *Metallomics*, 2012, **4**, 568–575.

163 A. Levina, J. B. Aitken, Y. Y. Gwee, Z. J. Lim, M. Liu, A. M. Singharay, P. F. Wong and P. A. Lay, *Chem. - A Eur. J.*, 2013, **19**, 3609–3619.

164 A. Blazevic, A. A. Hummer, P. Heffeter, W. Berger, M. Filipits, G. Cibin, B. K. Keppler and A. Rompel, *Sci. Rep.*, 2017, **7**, 1–8.

Chapter 2

Materials, methods, and instrumentation

2 Materials, methods, and instrumentation

2.1 Materials

2.1.1 Solvents and chemical reagents

All deuterated and commercial solvents were purchased from Sigma Aldrich and used as directed by the supplier. Chemical reagents and their suppliers are shown in **Table 2.1**.

Table 2.1. Chemical reagents and suppliers.

Reagent	Supplier
Azidotrimethylsilane	Acros Organics
Hydroxylamine hydrochloride	Acros Organics
Sodium azide	Acros Organics
β-D-Glucose pentaacetate	Acros Organics
Amberlite IRA-410(Cl) ion exchange resin	Alfa Aesar
α-D-Galactose pentaacetate	Alfa Aesar
Sodium metabisulfite	BDH
2,2'-Bipyridine-4,4'-dicarboxylic acid	CarboSynth
Azido-PEG2-alcohol	CarboSynth
α-D-Mannose pentaacetate	CarboSynth
2,3,4,6-Tetra-*O*-acetyl-β-D-mannopyranosyl azide	CarboSynth
2,3,4,6-Tetra-*O*-acetyl-α-D-glucopyranosyl azide	CarboSynth
Aluminium oxide - Brockmann I neutral	Fisher
Copper(II) sulfate pentahydrate	Fisher
Dimethyl sulfoxide	Fisher

Magnesium sulfate – dried	Fisher
Selenium dioxide	Fisher
Sodium bicarbonate	Fisher
Sodium carbonate anhydrous	Fisher
Sodium sulfate anhydrous	Fisher
Trifluoroacetic acid (HPLC grade)	Fisher
Osmium trichloride hydrate	Heraeus South Africa
Iridium trichloride hydrate	Precious Metals Online
Ruthenium trichloride hydrate	Precious Metals Online
1,3-Dimethyl-1,3-diazinan-2-one (DMPU)	Sigma Aldrich
2-[2-(2-Chloroethoxy)ethoxy]ethanol	Sigma Aldrich
2-Chloroethanol	Sigma Aldrich
2-Ethynylpyridine	Sigma Aldrich
2-Phenylpyridine	Sigma Aldrich
4,4’-Dimethyl-2,2’-bipyridine	Sigma Aldrich
Acetobromo-α-D-galactose	Sigma Aldrich
Acetobromo-α-D-glucose	Sigma Aldrich
Ascorbic Acid	Sigma Aldrich
Iodomethane	Sigma Aldrich
N,N-diisopropylethylamine	Sigma Aldrich
Pd/C 10 wt.%	Sigma Aldrich
Potassium carbonate	Sigma Aldrich

Silica	Sigma Aldrich
α-D-Glucose pentaacetate	Sigma Aldrich
β-D-Galactose pentaacetate	Sigma Aldrich

2.1.2 ICP-MS/OES standards and reagents

Standards for ICP trace metal analysis (**Table 2.2**) were purchased from Inorganic Ventures and stored at 277 K. Sodium chloride for trace analysis was purchased from Sigma Aldrich. Nitric acid (72% v/v) was freshly distilled by Dr Lijiang Song (University of Warwick) and diluted with milliQ water.

Table 2.2. ICP standards and compositions.

Standard	Composition
Iridium	995±3 μg/mL, iridium chloride, 10% v/v hydrochloric acid
Ruthenium	995±4 μg/mL ruthenium chloride, 10% v/v hydrochloric acid
Platinum	1001±12 mg/L TraceCERT® platinum, 5% v/v hydrochloric acid

2.1.3 Cell lines and cell culture reagents

A549 human lung carcinoma and MRC5 human foetal fibroblasts were purchased from the European Collection of Cell Cultures (ECACC). RPMI-1640 no-phenol-red medium was purchased from Scientific Laboratory Supplies. Foetal bovine serum (heat inactivated) was purchased from Sigma Aldrich. Dulbecco's Modified Eagle Medium (DMEM), phosphate buffered saline (PBS), L-glutamine (2 mM), penicillin/streptomycin solutions and 0.25% trypsin/EDTA solutions were prepared by technicians at the School of Life Sciences, University of Warwick.

2.2 Instruments and methods

2.2.1 Nuclear magnetic resonance (NMR) spectroscopy

Samples were prepared with *ca.* 650 µL deuterated solvent in 5 mm NMR tubes. Proton and carbon spectra were recorded at 298 K on Bruker Avance III HD 300/75 MHz, Avance HD 400/101 MHz, Avance HD 500/126 MHz and Avance AV 700/176 MHz spectrometers ($^{1}H/^{13}C$ frequencies). Proton spectra were recorded with standard pulse sequences, whilst carbon spectra were recorded with the attached proton test (APT) sequence. ^{1}H chemical shifts were referenced to residual solvent peaks: $CDCl_3$ (7.26 ppm), CD_3OD (3.31 ppm), $(CD_3)_2SO$ (2.50 ppm), CD_3CN (1.94 ppm), $(CD_3)_2CO$ (2.05 ppm). TMS was used as an internal reference (0.00 ppm). Spectra recorded on 500 MHz and 700 MHz (^{1}H frequencies) instruments were obtained by Dr Rob Perry and Dr Ivan Prokes, respectively. ^{19}F NMR spectra were recorded at 298 K on an Avance HD 400 MHz (^{19}F frequency = 376 MHz) spectrometer. Data were processed in MestreNova (Mestrelab, Spain).

2.2.2 Mass spectrometry (MS)

Samples for low resolution electrospray ionisation (ESI) mass spectrometry were prepared in methanol and recorded on an Agilent 6130B single quad with a mass-to-charge range of *m/z* 50-3000. Ions were detected in positive ion mode within ranges of *m/z* 50-500, 400-1000 or 800-2000. High resolution mass spectra were obtained by Dr Lijiang Song and Ms Lynette Walsh using a Bruker UHRQ-TOF MaXis, with a positive ion scan range of *m/z* 50-3000 (spectra rate of 1 Hz). Analysis was carried out through direct infusion (2 $\mu L \cdot min^{-1}$) with a syringe pump, with sodium formate (10 mM) calibration. Source conditions: ESI (+); end plate offset: -500 V; capillary: -3000 V; nebulizer gas (N_2): 0.4 bar; dry gas (N_2): 4 $L \cdot min^{-1}$; dry temperature: 453 K; funnel RF: 200 Vpp; multiple RF: 200 Vpp; quadruple low mass: 55 m/z; collision energy: 5.0 eV; collision RF: 600 Vpp; ion cooler RF: 50-250 Vpp ramping; transfer time: 121 µs; pre-pulse storage time: 1 µs.

2.2.3 X-ray crystallography

X-ray crystallographic data were acquired by Dr Guy Clarkson (University of Warwick). A suitable crystal was selected and mounted on a glass fibre with Fomblin oil and placed on a Rigaku Oxford Diffraction Synergy-S diffractometer with a dual source equipped with a Hybrid pixel array detector. The crystal was kept at 100(2) K during data collection. Using Olex2,[1] the structure was solved by Dr Clarkson with the SHELXT[2] structure solution program using Intrinsic Phasing and refined with the SHELXL[3] refinement package using Least Squares minimisation.

2.2.4 Ultraviolet-visible (UV-vis) spectroscopy

UV-vis absorption spectra were recorded using a Varian Cary 300 Bio spectrophotometer with a PTP1 Peltier temperature control. Samples were transferred to a 600 µL quartz cuvette with 1 cm path length. Spectra were recorded over the range 800-200 nm at 1 nm intervals with a scan rate of 600 nm·min^{-1}. Data were acquired on Varian Cary Winlab UV software for Windows and processed using Microsoft Excel.

2.2.5 Photoreactor

Samples in 1 cm path length quartz cuvettes were placed in a Luzchem LZC-ICH2 photoreactor equipped with eight 420 nm lamps and set to 310 K.

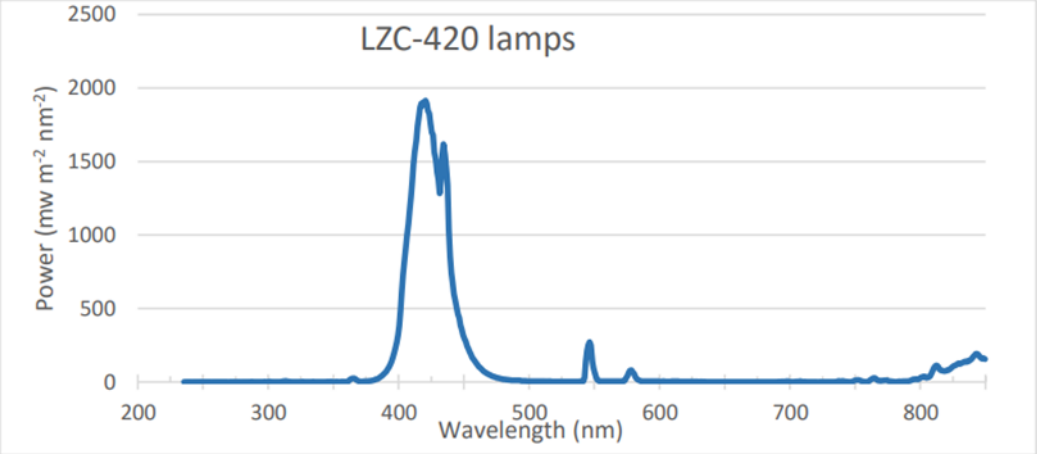

Figure 2.1. Output from LZC-420 lamps. Produced from "Technical release Luzchem Exposure Standard LES-420-16" released 8th March 2016.

2.2.6 High performance liquid chromatography (HPLC)

HPLC was performed using an Agilent 1200 system with a VWD and 100 µL loop using manual injection. The stationary phase was an Agilent ZORBAX Eclipse XDB-C18 column (250 × 4.6 mm, 5µm i.d.). HPLC grade water (solvent A) and acetonitrile (solvent B) were used as mobile phase, each with 0.1% trifluoroacetic acid as the ion-pairing agent, using a 1 $mL \cdot min^{-1}$ flow rate and linear gradient shown in **Table 2.3**.

Table 2.3. HPLC solvent gradient.

Time (min)	% B
0 - 30	10 – 80
30 – 40	80
40 – 41	80 – 10
41 – 45	10

Samples were prepared as 1 $mg \cdot mL^{-1}$ in HPLC grade acetonitrile, then diluted 1-in-10 with double-deionised water to give a 0.1 $mg \cdot mL^{-1}$ solution in 10% acetonitrile, matching the starting conditions of the mobile phase. Diluted solutions were then filtered through Minisart® SRP 4 syringe filters with 0.45 µm PTFE membrane. Sample volumes of 100 µL were injected. A detection wavelength of 254 nm was used with reference wavelengths at 360 nm and 510 nm. Chromatograms were analysed using ChemStation and peaks greater than 10 mAU were integrated. Data were processed on Microsoft Excel.

2.2.7 Liquid chromatography – mass spectrometry (LC-MS)

LC-MS was performed using an Agilent 1260 HPLC system equipped with an Agilent ZORBAX Eclipse XDB-C18 column (250 × 4.6 mm, 5µm i.d.), directly coupled with a Bruker Amazon X ESI mass spectrometer. HPLC grade water (solvent A) and acetonitrile (solvent B) were used as mobile phase, each with 0.1%

trifluoroacetic acid as the ion-pairing agent, using a 1 $mL \cdot min^{-1}$ flow rate and linear gradient shown in **Table 2.3**. Chromatograms were generated using detection at 254 nm. Mass spectra were recorded in positive ion mode with a scan range of 50-3000 m/z. Samples volumes of 20 µL were injected using an autosampler. Data were processed using Data Analysis (Bruker Daltonics).

2.2.8 Inductively coupled plasma – optical emission spectroscopy (ICP-OES)

ICP-OES was performed with the help of Dr James Coverdale on a Perkin Elmer Optima 5300 DV Optical Emission Spectrophotometer with data acquired for iridium (λ =208.882 nm, 224.268 nm, 237.277 nm), ruthenium (λ = 240.272 nm, 349.894 nm) and platinum (λ = 214.423 nm, 265.945 nm, 299.797 nm). Calibration standards were prepared from 50-700 ppb in 3.6% v/v nitric acid, and sample solutions were prepared within this range. Sodium chloride was added to the calibration standards in order to match the salinity of the cell culture media used as the sample matrix. Total dissolved solids were kept below 0.2% w/v. Data were acquired and processed using WinLab32 V3.4.1 for Windows.

2.2.9 Inductively coupled plasma – mass spectrometry (ICP-MS)

ICP-MS was performed with the help of Dr James Coverdale on an Agilent 7500 series instrument with data acquired for iridium-193, ruthenium-101 and platinum-195 in "no-gas" mode. ICP-MS TOP was used to acquire data with an erbium-166 internal standard (50 ppb). Calibration standards were prepared from 0.1-1000 ppb in 3.6% v/v nitric acid and sample solutions were prepared within this range. Total dissolved solids were kept below 0.1% w/v. Data processing was performed using Offline Data Analysis (ChemStation).

2.3 Biological studies

2.3.1 Cell maintenance - defrosting

Ampoules containing pellets of 2-3×10^6 cells were rapidly defrosted in a 310 K water bath. Cells were transferred to 15 mL falcon tubes and centrifuged at 1000 rpm for 5 min (298 K) to remove supernatant. The new pellet was then resuspended in 5 mL media and transferred to a T25 flask, then incubated at 310 K with 5% CO_2.[4]

2.3.2 Cell maintenance - passaging

A549 and MRC5 cells were grown in DMEM supplemented with 10% foetal bovine serum, 1% L-glutamine (2 mM) and 1% penicillin/streptomycin.

Cells were grown as adherent monolayers in T75 flasks (tissue-culture treated) in a 310 K incubator with 5% CO_2 until 80-90% confluence was achieved. At this point, cells were washed with 5 mL PBS, then treated with 2 mL trypsin/EDTA (0.25%) and the flask was incubated for 2-5 min. Media was added to dilute the trypsin/EDTA once cells were detached from the bottom of the flask, and a single-cell suspension was formed. An appropriate volume was then transferred into a new T75 containing fresh media and the flask placed in the incubator.[4] MRC5 cells were not used after passage 5 due to cells entering senescence.

2.4 References

1 O. V. Dolomanov, L. J. Bourhis, R. J. Gildea, J. A. K. Howard and H. Puschmann, *J. Appl. Crystallogr.*, 2009, **42**, 339–341.

2 G. M. Sheldrick, *Acta Crystallogr. Sect. A Found. Adv.*, 2015, **71**, 3–8.

3 G. M. Sheldrick, *Acta Crystallogr. Sect. C Struct. Chem.*, 2015, **71**, 3–8.

4 J. P. C. Coverdale, PhD Thesis, University of Warwick, 2018.

Chapter 3

Photoactive Ir(III) and Ru(II) glycoconjugates for PDT

3 Photoactive Ir(III) and Ru(II) glycoconjugates for PDT

This Chapter describes the synthesis and characterisation of a series of Ir(III) and Ru(II) complexes based on the commonly used $[Ir(ppy)_2(N\text{^}N)]^+$ and $[Ru(bpy)_2(N\text{^}N)]^{2+}$ scaffolds. Bidentate N^N ligands containing different sugars were designed with the purpose of enhancing cancer cell selectivity by exploiting the Warburg effect. Solution stability and photostability were observed before studying photophysical properties for further use as photosensitizers *in vitro* (Chapter 4).

3.1 Introduction

Photodynamic therapy presents an alternative approach to conventional chemotherapeutics, utilising non-toxic photosensitizers to selectively destroy cancer cells *via* catalytic ROS generation upon irradiation. Photosensitizers are typically described as Type I, which generate ROS *via* biomolecules, or Type II, where the excited state photosensitizer reacts with ground state (triplet) oxygen to generate highly reactive singlet oxygen (**Equations 3.1-3.2**).[1]

$$^1PS + h\nu \rightarrow {}^3PS^* \qquad \textbf{Equation 3.1}$$

$$^3PS^* + {}^3O_2 \rightarrow {}^1PS + {}^1O_2 \qquad \textbf{Equation 3.2}$$

Equations 3.1-3.2. Scheme for the photosensitization of oxygen. * Denotes excited state.

In biological environments, singlet oxygen has a short half-life of 1 ns to 1 µs and can lead to necrosis and apoptosis in cancer cells.[2,3] The particular subcellular location of singlet oxygen production has been found to have a significant impact on the cell death mechanism of cancer cells.[3] Many intracellular targets can be affected by singlet oxygen, which may help circumvent the issue of resistance seen regularly for traditional platinum-based chemotherapeutics.[4–7]

Porfimer sodium (Photofrin®, **Figure 3.1**) is a clinically used Type II photosensitizer comprised of a mixture of porphyrin oligomers, ranging from 2 to 8 porphyrins, that can be activated using red light (630 nm).[8,9] It was approved by the FDA for the photodynamic therapy of oesophageal cancer in 1995 and non-small cell lung cancer in 1998.[10] Extracellular singlet oxygen generated by the

clinically used photosensitizer Photofrin® has been shown to inactivate membrane-associated catalase by reacting with the histidine in the enzyme's active centre, thereby negating its antioxidant activity. Once these protective enzymes on the cell membranes are inactivated, hydrogen peroxide and peroxynitrite (constantly generated outside cancer cells) are no longer decomposed, eventually leading to the generation of secondary singlet oxygen molecules (**Equations 3.3-3.6**). These can go on to cause further inactivation of catalase enzymes, the activation of necrosis factors, or the reactivation of intercellular ROS/RNS-mediated apoptosis-inducing signalling.[4,11]

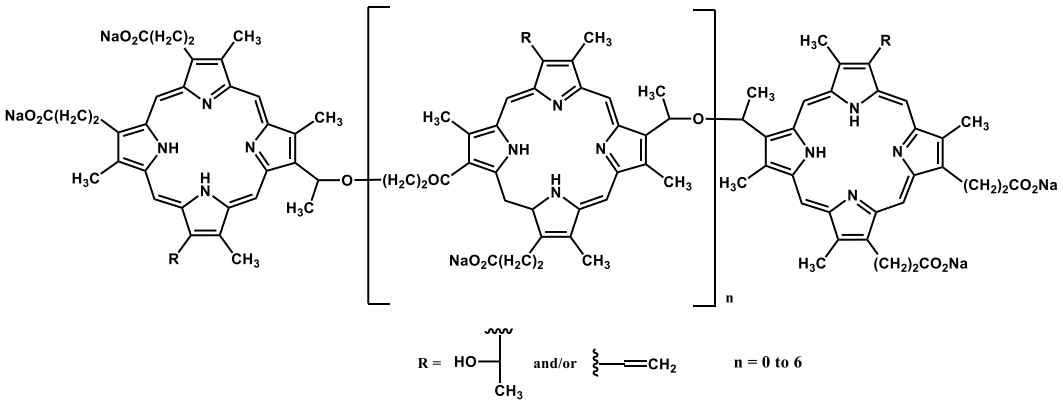

Figure 3.1. Structure of FDA-approved photosensitizer porfimer sodium (Photofrin®).

$$ONOO^- + H^+ \longrightarrow ONOOH \qquad \textbf{Equation 3.3}$$

$$ONOOH \longrightarrow {}^{\cdot}NO_2 + {}^{\cdot}OH \qquad \textbf{Equation 3.4}$$

$${}^{\cdot}OH + H_2O_2 \longrightarrow HO_2^{\cdot} + H_2O \qquad \textbf{Equation 3.5}$$

$$HO_2^{\cdot} + O_2^{\cdot -} + H^+ \longrightarrow H_2O_2 + {}^1O_2 \qquad \textbf{Equation 3.6}$$

Equations 3.3-3.6. Scheme for the generation of secondary singlet oxygen.[11]

Heavy metal complexes are being investigated for their use as photosensitizers due to their favourable properties over organic complexes, notably their high singlet oxygen quantum yields and their luminescence properties allowing for potential imaging and diagnostic capabilities ('theranostics').[12] Of particular interest are cyclometalated complexes of Ru(II), Os(II) and Ir(III) – typically very stable since

their electronic configurations are low spin d^6 – which have been synthesised and tested as photosensitizers.

Iridium(III) complexes have great promise as photosensitizers due to their tuneable photophysical and photobiological properties. They are typically highly chemically and photochemically stable, with efficient energy transfer from the excited triplet states leading to high singlet oxygen quantum yields.[13] Although Ir(III) complexes typically have shorter absorption wavelengths than Ru(II) complexes, the development of two-photon PDT (TP-PDT) could still allow longer wavelength activation with their associated deeper tissue penetration – for example, Ir(III) complexes with absorption maxima below 420 nm have been excited using near-infrared TP-PDT.[14,15] Furthermore, Ir(III) complexes are often luminescent, allowing for theranostic use in image-guided PDT,[16,17] as well as in-cell imaging without modification to get accurate depictions of organelle targeting.[18–20]

In 2016, the Ru(II) complex TLD-1433 (**Figure 3.2**) developed by McFarland *et al*. entered Phase I clinical trials for use against non-muscle invasive bladder cancer (NMIBC), becoming the first non-pyrrole-based metal photosensitizer to do so.[21] It has since progressed to Phase II clinical trials, expected to end December 2025.[22]

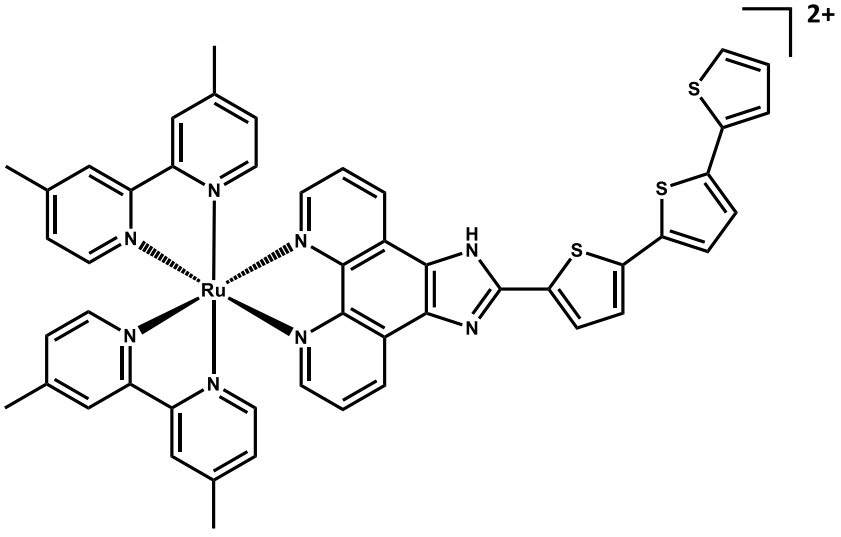

Figure 3.2. Ru complex TLD-1433 in Phase II clinical trial. Developed by McFarland et al.[23]

TLD-1433 exhibited excellent photocytotoxicity of 190 pM in SK-MEL-28 melanoma cells upon broadband visible light irradiation, with a phototoxicity index

(PI) of over 7.2×10^5. TLD-1433 is also luminescent, which may allow for its use as a theranostic complex. Interestingly, the luminescence of TLD-1433 is due to emission from the ^{3}MLCT state, whereas the photocytotoxicity is caused by two separate intraligand (IL) configurations: singlet oxygen is mostly generated *via* the ^{3}IL state, whilst the ^{3}ILCT state participates in electron-transfer reactions with oxygen and biological substrates to generate ROS, as well as reacting with other Ru(II) dyads. The potential to generate more than one reactive species for each photon absorbed has led to TLD-1433 being labelled a 'supercatalyst'.[23] Furthermore, biological activity in hypoxic conditions has been observed, attributed to the photodamage of DNA.[23] Since the ruthenium centre is chiral, TLD-1433 exists as a racemic mixture of Δ and Λ enantiomers that were not separated before use at any stage (including for clinical use).[23] Replacement of Ru in TLD-1433 with Os led to a red-shift in absorption yet lowered the photocytotoxic effect even with red light activation.[23] Osmium phenanthroline complex Os-4T, bearing a similar thienyl ring system (4 thienyls), exhibited photocytotoxicity of 17.8 pM under broadband visible light irradiation, leading to a PI of over 3.6×10^6, and had a maximum tolerated dose of over 200 $mg \cdot kg^{-1}$ in mice. Os-4T also demonstrated good photocytotoxicity in hypoxia (651 nM in 1% O_2), but with a much-reduced PI of 91. Interestingly, Os-4T is far more potent with red light activation (10 nM *vs* 2.3 μM) than TLD-1433.[24]

The overexpression of GLUT1 by cancer cells has been targeted previously by covalently attaching glucose to a variety of active complexes, however, the distance between the sugar and active complex differs. GLUT1 substrate 2-[N-(7-nitrobenz-2-oxa-1,3-diazol-4-yl)amino]-2-deoxy-D-glucose (2-NBDG) is comprised of glucosamine directly bound to a benzene-based fluorophore,[25] though further studies suggest a 9-atom linker between glucosamine and the fluorophore was optimal for GLUT1 targeting.[26] In contrast, a series of Pt complexes were conjugated to glucose *via* a short 3-atom linker, yet still exhibited GLUT1-targeting.[27] Furthermore, the relationship between GLUT1 targeting and the anomer of the sugar is unclear, with conflicting results in the literature over the preference of the α or β anomer.[28] Despite glucose being the major substrate, GLUT1 is also capable of transporting mannose and galactose.[29] This Chapter therefore details the synthesis and characterisation of a series of iridium and ruthenium glycoconjugates

with varied sugars (glucose, mannose, galactose), anomers (α and β) and linker lengths (0, 3, 6 and 9 atoms) designed to exploit the Warburg effect in cancer cells (described in **Chapter 1 Section 1.1.3**).

Iridium complexes also have the potential to be imaged in cells due to their phosphorescence, whilst ruthenium complexes typically absorb at longer wavelengths. The stability of complexes in biologically relevant media as well as the photo-stability of each complex were assessed for use in biological studies (**Chapter 4**), and singlet oxygen and emission quantum yields were determined to assess their potential for use as Type II photosensitizers in photodynamic therapy.

3.2 Experimental

^{1}H and ^{13}C NMR spectra of final complexes **1-14** are shown in **Appendix Spectra A1-A14**.

3.2.1 Synthesis of metal precursors

$[Ir(ppy)_2Cl]_2$

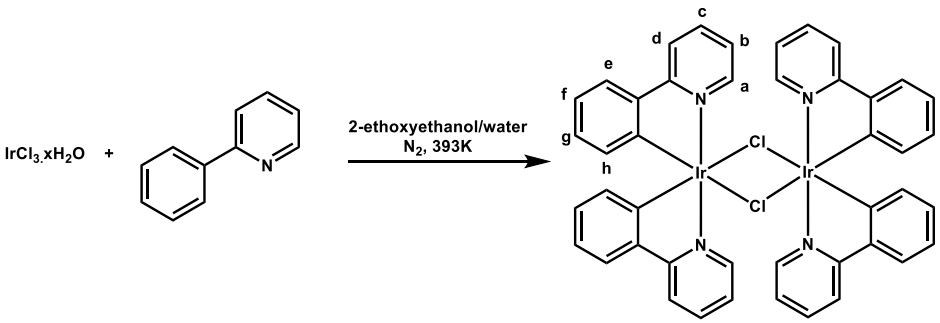

Iridium dimer $[Ir(ppy)_2Cl]_2$ was synthesised using an adapted literature procedure.[30] Iridium trichloride hydrate (1.5 g, 4.26 mmol, 1 eq) and 2-phenylpyridine (1521 µL, 10.65 mmol, 2.5 eq) were added to a 100 mL round bottom flask (RBF) and dissolved in 60 mL 3:1 2-ethoxyethanol/water solution, then refluxed under nitrogen atmosphere at 393 K for 28 h. Solution was then cooled to room temperature and left in the fridge overnight. The precipitate was filtered and washed with 50 mL water and 50 mL ether. A yellow powder was obtained. Yield = 1.8410 g (81%). ^{1}H NMR (400 MHz, $CDCl_3$) δ 9.26 (d, J = 5.6 Hz, $4H_a$), 7.89 (d, J = 8.0

Hz, 4H_d), 7.80 – 7.72 (m, 4H_c), 7.52 (t, J = 9.1 Hz, 4H_e), 6.82 – 6.72 (m, 8$H_{b/f}$), 6.58 (t, J = 7.5 Hz, 4H_g), 5.95 (d, J = 7.7 Hz, 4H_h).

$[Ru(bpy)_2Cl_2].2H_2O$

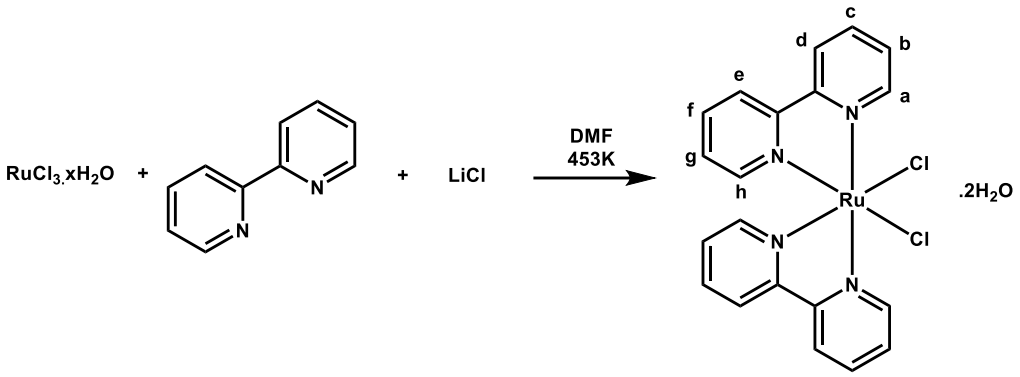

$[Ru(bpy)_2Cl_2].2H_2O$ was synthesised using an adapted literature procedure.[31] Ruthenium trichloride hydrate (1 g, 3.82 mmol, 1 eq), 2,2'-bipyridine (1.2 g, 7.69 mmol, 2.01 eq) and lithium chloride (1.1 g, 25.95 mmol, 6.8 eq) were dissolved in 10 mL DMF in a 25 mL round bottom flask and refluxed at 453 K for 24 h. The solution was allowed to cool to room temperature then poured into 20 mL acetone and the RBF was washed with 2 × 5 mL acetone. Combined acetone solutions were left in the freezer overnight, and the dark red/purple solid was filtered and washed with water and diethyl ether. Yield = 1.2854 g (65%) ^{1}H NMR (400 MHz, d_6-DMSO) δ 9.95 (d, J = 5.5 Hz, 2H_a), 8.61 (d, J = 8.1 Hz, 2H_d), 8.45 (d, J = 8.1 Hz, 2H_e), 8.06 (t, J = 7.8 Hz, 2H_c), 7.76 (t, J = 6.5 Hz, 2H_b), 7.67 (t, J = 7.8 Hz, 2H_f), 7.51 (d, J = 5.7 Hz, 2H_h), 7.09 (t, J = 6.6 Hz, 2H_g). ESI-MS m/z calc. $[M-2H_2O+Na]^+$: 507.0, found: 507.0.

3.2.2 Synthesis of sugar azides

2,3,4,6-Tetra-*O*-acetylglucopyranosyl-α-azide, 2,3,4,6-tetra-*O*-acetylmanno-pyranosyl-β-azide and 2,3,4,6-tetra-*O*-acetylglucose-β-PEG3-azide were purchased from CarboSynth. Compounds were used as received after confirming satisfactory ^{1}H NMR spectra compared to the literature for anomeric configurations.

2,3,4,6-Tetra-O-acetylglucopyranosyl-α-azide - CarboSynth

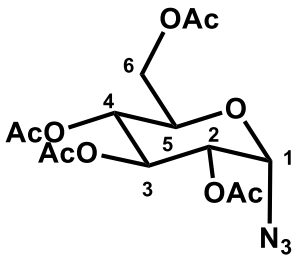

^{1}H NMR (400 MHz, $CDCl_3$) δ 5.63 (d, J = 4.3 Hz, 1H, H-1), 5.41 (t, J = 9.8 Hz, 1H, H-3), 5.09 (q, J = 9.8 Hz, 1H, H-4), 4.97 (dd, J = 10.1, 4.3 Hz, 1H, H-2), 4.29 (dd, J = 12.5, 4.6 Hz, 1H, H-6), 4.18 (dd, J = 13.4, 7.8 Hz, 2H, H-5 and H-6'), 2.12 (s, 6H, 2×OAc), 2.06 (s, 3H, OAc), 2.04 (s, 3H, OAc). ESI-MS m/z calc. $[M+Na]^+$: 396.1, found: 396.1. ^{1}H NMR in good agreement with literature values for the α configuration.[32]

2,3,4,6-Tetra-O-acetylmannopyranosyl-α-azide

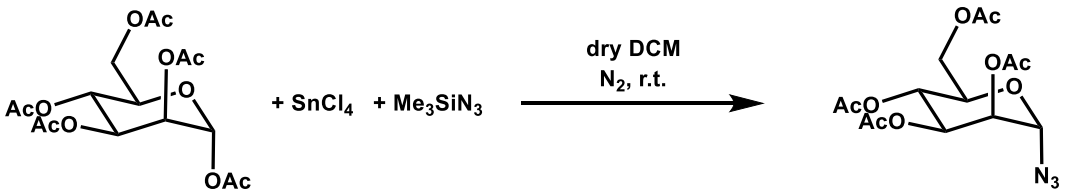

Synthesised using an adapted literature method.[33] 1,2,3,4,6-Penta-*O*-acetyl-α-mannopyranosyl (1 g, 2.6 mmol, 1 eq), azidotrimethylsilane (1433 µL, 10.8 mmol, 4.1 eq) and 1M tin(IV) chloride in DCM solution (710 µL, 0.71 mmol, 0.27 eq) were dissolved in 10 mL anhydrous DCM and stirred under nitrogen atmosphere at room temperature for 29 h. 20 mL DCM was added, then solution was washed with 10 mL saturated sodium hydrogen carbonate solution, 10 mL water and 10 mL brine. Solvent was removed by blowing nitrogen over solution overnight, leaving a colourless oil. Yield = 0.8879 g (93%). ^{1}H NMR (400 MHz, $CDCl_3$) δ 5.33 (d, J = 1.8 Hz, 1H, H-1), 5.26 – 5.22 (m, 1H, H-4), 5.20 (d, J = 3.7 Hz, 1H, H-3), 5.10 – 5.08 (m, 1H, H-2), 4.24 (dd, J = 12.4, 5.6 Hz, 1H, H-6), 4.10 (dt, J = 12.5, 4.1 Hz, 2H, H-5 and H-6'), 2.11 (s, 3H, OAc), 2.05 (s, 3H, OAc), 1.99 (s, 3H, OAc), 1.93

(s, 3H, OAc). ESI-MS m/z calc. $[M+Na]^+$: 396.1, found: 396.2. ^{1}H NMR in good agreement with literature values for the α configuration.[33]

2,3,4,6-Tetra-O-acetylgalactopyranosyl-α-azide

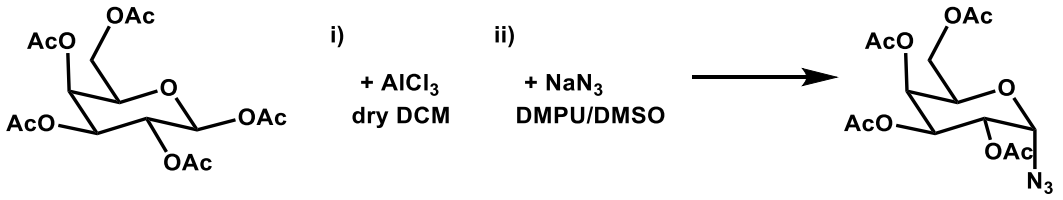

β-Galactose pentaacetate (1.45 g, 3.71 mmol, 1 eq) was dissolved in 15 mL dry DCM and stirred at room temperature. Aluminium trichloride (0.2525 g, 1.89 mmol, 0.5 eq) was added and solution was stirred at room temperature for 50 min. Reaction mixture was then poured into dry hexane then passed through celite, eluted with dry DCM and concentrated under reduced pressure without heating. The crude mixture was then dissolved in 25 mL DMPU/DMSO (3:2) and sodium azide (1.2075 g, 18.6 mmol, 5 eq) was added. Reaction mixture was stirred at room temperature for 6 h, and solution turned slightly orange-pink as sodium azide was stirred in. After 6 h, reaction mixture was poured into 200 mL water then put in the fridge until clear needles crystallised (2 weeks). Yield = 0.2850 g (21%). ^{1}H NMR (400 MHz, $CDCl_3$) δ 5.68 (d, J = 3.9 Hz, 1H, H-1), 5.48 (d, J = 2.6 Hz, 1H, H-4), 5.24 (qd, J = 10.8, 3.4 Hz, 2H, H-2 and H-3), 4.38 (t, J = 6.5 Hz, 1H, H-5), 4.20 – 4.09 (m, 2H, H-6 and H-6'), 2.17 (s, 3H, OAc), 2.13 (s, 3H, OAc), 2.08 (s, 3H, OAc), 2.01 (s, 3H, OAc). ESI-MS m/z calc. $[M+Na]^+$: 396.1, found: 396.1. ^{1}H NMR in good agreement with literature values for the α configuration.[34]

2,3,4,6-Tetra-O-acetylglucopyranosyl-β-azide

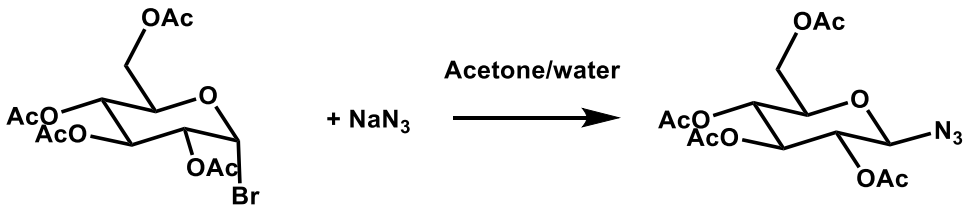

Synthesised using an adapted literature method.[35] 2,3,4,6-Tetra-*O*-acetylglucopyranosyl-α-bromide (0.791 g, 1.92 mmol, 1 eq) and sodium azide (0.500 g, 7.69 mmol, 4 eq) were dissolved in 18 mL 5:1 acetone/water and stirred overnight at room temperature. Acetone was removed by heating the solution at 323 K in an oil bath. Remaining slurry was diluted with 50 mL water then extracted with 50 mL EtOAc. Organic layer was obtained, and the aqueous layer was extracted with 2 × 50 mL EtOAc. Organic layers were combined and dried over anhydrous magnesium sulfate, then filtered and solvent evaporated under reduced pressure to leave a white solid. This was then refluxed in methanol and allowed to cool, yielding colourless needles. Yield = 0.4647 g (65%). ^{1}H NMR (400 MHz, $CDCl_3$) δ 5.24 (t, J = 9.5 Hz, 1H, H-3), 5.13 (t, J = 9.7 Hz, 1H, H-4), 4.98 (t, J = 9.2 Hz, 1H, H-2), 4.67 (d, J = 8.9 Hz, 1H, H-1), 4.30 (dd, J = 12.5, 4.8 Hz, 1H, H-6), 4.19 (dd, J = 12.5, 2.2 Hz, 1H, H-6'), 3.82 (ddd, J = 10.0, 4.8, 2.3 Hz, 1H, H-5), 2.12 (s, 3H, OAc), 2.10 (s, 3H, OAc), 2.05 (s, 3H, OAc), 2.03 (s, 3H, OAc). ESI-MS m/z calc. $[M+Na]^+$: 396.1, found: 396.2. ^{1}H NMR in good agreement with literature values for the β configuration.[32]

2,3,4,6-Tetra-O-acetylmannopyranosyl-β-azide – CarboSynth

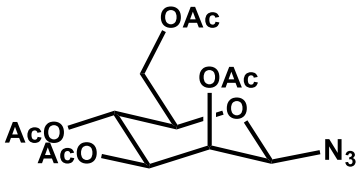

^{1}H NMR (400 MHz, $CDCl_3$) δ 5.38 (d, J = 3.1 Hz, 1H, H-2), 5.20 (t, J = 10.0 Hz, 1H, H-4), 4.98 (dd, J = 10.1, 3.2 Hz, 1H, H-3), 4.66 (s, 1H, H-1), 4.22 (dd, J = 12.4, 5.6 Hz, 1H, H-6), 4.14 (dd, J = 12.3, 2.3 Hz, 1H, H-6'), 3.73 – 3.66 (m, 1H, H-5), 2.15 (s, 3H, OAc), 2.05 (s, 3H, OAc), 1.99 (s, 3H, OAc), 1.93 (s, 3H, OAc). ESI-MS m/z calc. $[M+Na]^+$: 396.1, found: 396.1. ^{1}H NMR in good agreement with literature values for the β configuration.[36]

2,3,4,6-Tetra-O-acetylgalactopyranosyl-β-azide

Synthesised using an adapted literature method.[33] Sodium azide (0.23 g, 3.5 mmol, 1.2 eq) was added to a solution of 2,3,4,6-tetra-*O*-acetylgalactopyranosyl-α-bromide (1.2 g, 2.9 mmol, 1 eq) in 10 mL DMSO and stirred for 1 h at room temperature. Reaction mixture was diluted with 50 mL water then extracted with 100 mL EtOAc. Organic layer was dried over sodium sulfate, filtered, then solvent removed under reduced pressure to give a yellowish oil. The oil was dissolved in methanol and adsorbed onto silica, then dry loaded and purified by column chromatography (stationary phase: silica, mobile phase: 1 MeOH: 5 EtOAc: 10 Petroleum Ether 40-60 ^{o}C). Fractions were checked by mass spectrometry for product, relevant fractions being combined, and solvent removed under reduced pressure to leave an off-white oil. This was re-dissolved in ether, transferred to a 25 mL vial and dried by blowing nitrogen over the vial until a white solid was left. Yield = 0.4048 g (37%). ^{1}H NMR (400 MHz, $CDCl_3$) δ 5.45 (d, J = 3.2 Hz, 1H, H-4), 5.23 – 5.15 (m, 1H, H-2), 5.06 (dd, J = 10.4, 3.3 Hz, 1H, H-3), 4.62 (d, J = 8.7 Hz, 1H, H-1), 4.25 – 4.14 (m, 2H, H-6 and H-6'), 4.04 (t, J = 6.5 Hz, 1H, H-5), 2.19 (s, 3H, OAc), 2.12 (s, 3H, OAc), 2.09 (s, 3H, OAc), 2.01 (s, 3H, OAc). ESI-MS m/z calc. $[M+Na]^+$: 396.1, found: 396.2. ^{1}H NMR in good agreement with literature values for the β configuration.[33]

2,3,4,6-Tetra-O-acetylglucopyranosyl-β-PEG1-azide

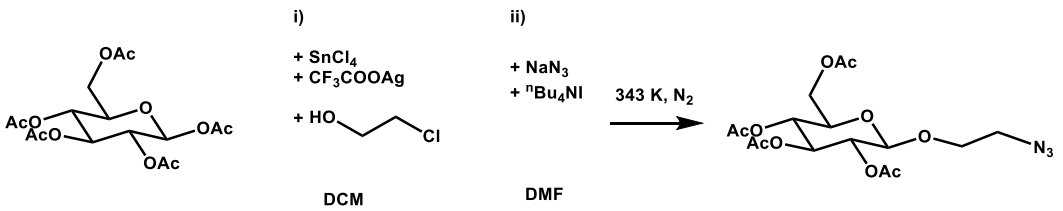

Synthesised using an adapted literature method.[37] 1M tin(IV) chloride in DCM solution (9.6 mL, 9.6 mmol, 3 eq) was added dropwise over 2 h at room temperature

to a stirred solution of 1,2,3,4,6-penta-*O*-acetyl-β-glucopyranosyl (1.25 g, 3.2 mmol, 1 eq), silver trifluoroacetate (1.05 g, 4.8 mmol, 1.5 eq) and 2-chloroethanol (325 µL, 4.8 mmol, 1.5 eq) in 30 mL anhydrous DCM and stirred for 3 h (1 h after addition of tin(IV) chloride) protected from light. Solution was then poured into 150 mL saturated $NaHCO_3$ solution and stirred vigorously for 20 min, then extracted with 3 × 40 mL DCM. The organic layers were combined and washed with saturated sodium hydrogen carbonate solution (2 × 40 mL), water (2 × 40 mL) and brine (40 mL) then dried with sodium sulfate and filtered. DCM was evaporated under reduced pressure and crude product was dissolved in 20 mL anhydrous DMF. Sodium azide (1.075 g, 16.6 mmol, 5 eq) and tetra-n-butylammonium iodide (0.1228 g, 0.325 mmol, 0.1 eq) were added and solution was stirred at 343 K under nitrogen atmosphere for 18 h. The solution was cooled to room temperature, filtered, and solid washed with EtOAc. The filtrate was diluted with EtOAc to reach 100 mL total volume, then washed with sat. $NaHCO_3$ solution (2 × 25 mL), water (2 × 25 mL) and brine (25 mL) then dried to give an off-white solid. Yield = 1.2854 g (96%). ^{1}H NMR (400 MHz, $CDCl_3$) δ 5.24 (t, J = 9.5 Hz, 1H), 5.12 (t, J = 9.7 Hz, 1H), 5.05 (dd, J = 9.4, 8.1 Hz, 1H), 4.62 (d, J = 7.9 Hz, 1H), 4.31 – 4.24 (m, 1H), 4.19 (dd, J = 12.3, 2.3 Hz, 1H), 4.10 – 4.02 (m, 1H), 3.73 (ddd, J = 13.6, 8.0, 2.8 Hz, 2H), 3.52 (ddd, J = 11.7, 8.2, 3.3 Hz, 1H), 3.35 – 3.28 (m, 1H), 2.11 (s, 3H), 2.08 (s, 3H), 2.05 (s, 3H), 2.03 (s, 3H). ESI-MS m/z calc. $[M+Na]^+$: 440.1, found: 440.1. ^{1}H NMR in good agreement with literature values.[38]

2,3,4,6-Tetra-O-acetylglucopyranosyl-β-PEG2-azide

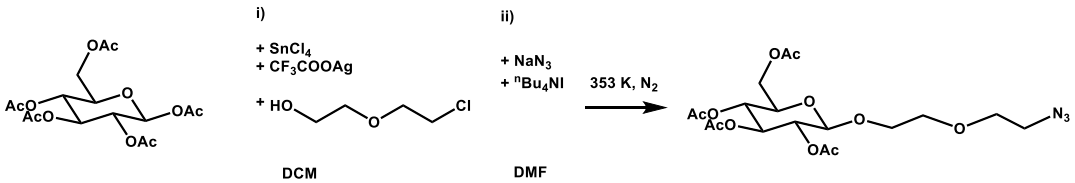

Synthesised using an adapted literature method.[37] 1M tin(IV) chloride in DCM solution (3.85 mL, 3.85 mmol, 1.5 eq) was added dropwise over 1 h at room temperature to a stirred solution of 1,2,3,4,6-penta-*O*-acetyl-β-glucopyranosyl (1 g, 2.55 mmol, 1 eq), silver trifluoroacetate (0.85 g, 3.85 mmol, 1.5 eq) and 2-(2-chloroethoxy)ethanol (406 µL, 3.85 mmol, 1.5 eq) in 30 mL anhydrous DCM and

stirred for 1.25 h (15 min after addition of tin(IV) chloride) protected from light. Solution was then poured into 200 mL saturated $NaHCO_3$ solution and stirred vigorously for 20 min, then extracted with 3 × 50 mL DCM. The organic layers were combined and washed with saturated sodium hydrogen carbonate solution (2 × 50 mL), water (2 × 50 mL) and brine (50 mL) then dried with sodium sulfate and filtered. DCM was evaporated under reduced pressure and crude product was dissolved in 25 mL anhydrous DMF. Sodium azide (0.83 g, 12.8 mmol, 5 eq) and tetra-n-butylammonium iodide (0.189 g, 0.5 mmol, 0.2 eq) were added and solution was stirred at 353 K under nitrogen atmosphere for 18 h. Solution was cooled to room temperature, filtered, and solid washed with EtOAc. Filtrate was diluted with EtOAc to reach 100 mL total volume, then washed with sat. $NaHCO_3$ solution (2 × 25 mL), water (2 × 25 mL) and brine (25 mL), then dried to give a yellowish oil. Yield = 0.8853 g (75%). ^{1}H NMR (400 MHz, $CDCl_3$) δ 5.24 (t, J = 9.5 Hz, 1H), 5.11 (t, J = 9.7 Hz, 1H), 5.06 – 4.98 (m, 1H), 4.64 (d, J = 7.9 Hz, 1H), 4.28 (dd, J = 12.3, 4.7 Hz, 1H), 4.17 (dd, J = 12.3, 2.2 Hz, 1H), 3.98 (dt, J = 11.0, 4.1 Hz, 1H), 3.84 – 3.60 (m, 6H), 3.46 – 3.35 (m, 2H), 2.11 (s, 3H), 2.08 (s, 3H), 2.05 (s, 3H), 2.03 (s, 3H). ESI-MS m/z calc. $[M+Na]^+$: 484.2, found: 484.1. ^{1}H NMR in good agreement with literature values.[39]

2,3,4,6-Tetra-O-acetylglucose-β-PEG3-azide – CarboSynth

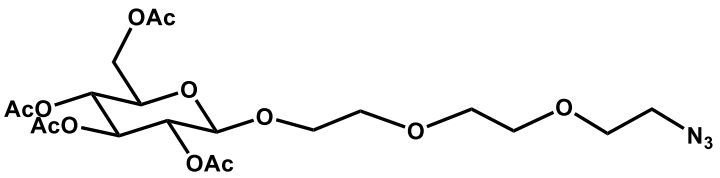

^{1}H NMR (400 MHz, $CDCl_3$) δ 5.23 (t, J = 9.5 Hz, 1H), 5.10 (t, J = 9.7 Hz, 1H), 5.01 (t, J = 8.8 Hz, 1H), 4.63 (d, J = 7.9 Hz, 1H), 4.28 (dd, J = 12.3, 4.6 Hz, 1H), 4.16 (d, J = 12.1 Hz, 1H), 4.01 – 3.92 (m, 1H), 3.82 – 3.61 (m, 10H), 3.42 (t, J = 4.8 Hz, 2H), 2.11 (s, 3H), 2.07 (s, 3H), 2.04 (s, 3H), 2.02 (s, 3H). ESI-MS m/z calc. $[M+Na]^+$: 528.2, found: 528.2. ^{1}H NMR in good agreement with literature values.[40]

3.2.3 Synthesis of ligands

General synthesis of glycoconjugate ligands

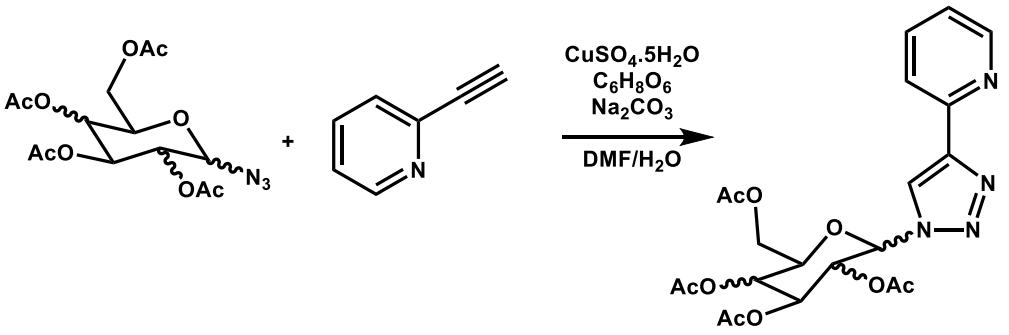

The protected sugar azide (1.05 eq), copper(II) sulfate pentahydrate (0.2 eq), ascorbic acid (1 eq) and sodium carbonate (1 eq) were dissolved in 4:1 DMF/water solution, then 2-ethynyl pyridine (1 eq) was added and solution stirred at room temperature for 24 h. Solvent was removed under reduced pressure, residue dissolved in DCM and sonicated, then washed with water, saturated $NaHCO_3$ solution and brine. Organic layer was dried over sodium sulfate, filtered and solvent removed under reduced pressure. Purified using Biotage Isolera with 10 g SNAP Si cartridge, flow rate 12 $mL \cdot min^{-1}$, mobile phase DCM/MeOH:

Column Volumes	Gradient (MeOH in DCM)
30 CV	0-10%
20 CV	10%

α-Glucose ligand

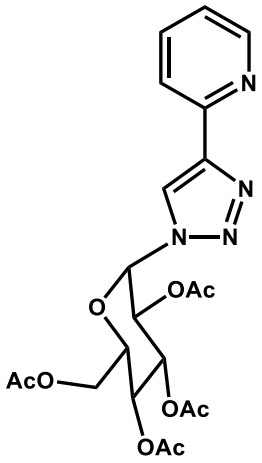

The α-glucose ligand was synthesized using the above general method using 2,3,4,6-tetra-*O*-acetylglucopyranosyl-α-azide (0.2 g, 0.536 mmol), 2-ethynylpyridine (56 µL, 0.536 mmol), copper(II) sulfate pentahydrate (0.028 g, 0.107 mmol), ascorbic acid (0.096 g, 0.536 mmol) and sodium carbonate (0.056 g, 0.536 mmol) to give a white solid. Yield = 0.100 g (39%). ^{1}H NMR (400 MHz, $CDCl_3$) δ 8.53 (s, 1H, trzH), 8.19 (s, 1H, pyrH), 8.15 (d, J = 7.5 Hz, 1H, pyrH), 7.75 (t, J = 7.2 Hz, 1H, pyrH), 7.20 (s, 1H, pyrH), 6.36 (d, J = 5.6 Hz, 1H, glu anomeric H), 6.27 (t, J = 9.5 Hz, 1H, gluH), 5.31 (dd, J = 9.3, 6.0 Hz, 1H, gluH), 5.22 (t, J = 9.7 Hz, 1H, gluH), 4.33 (d, J = 9.4 Hz, 1H, gluH), 4.21 (d, J = 12.4 Hz, 1H, gluH), 3.95 (d, J = 12.4 Hz, 1H, gluH), 2.00 (s, 6H, 2×OAc), 1.97 (s, 3H, OAc), 1.81 (s, 3H, OAc). ^{13}C NMR (101 MHz, $CDCl_3$) δ 170.52, 170.17, 169.72, 169.67, 149.58, 149.57, 148.03, 137.08, 124.28, 123.35, 120.42, 81.72, 71.21, 70.47, 69.72, 68.03, 61.30, 20.69, 20.68, 20.63, 20.37. ESI-MS m/z calc. $[M+Na]^+$: 499.1, found: 499.2.

α-Mannose ligand

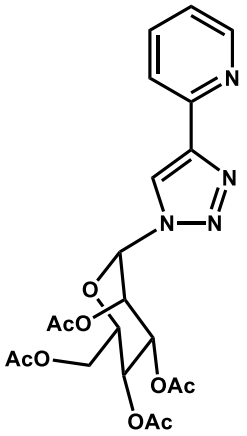

The α-mannose ligand was synthesized using the above general method using 2,3,4,6-tetra-*O*-acetylmannopyranosyl-α-azide (0.8879 g, 2.38 mmol), 2-ethynylpyridine (228.8 µL, 2.27 mmol), copper(II) sulfate pentahydrate (0.113 g, 0.453 mmol), ascorbic acid (0.399 g, 2.27 mmol) and sodium carbonate (0.240 g, 2.27 mmol) to give an off-white solid. Yield = 0.6814 g (63%). ^{1}H NMR (400 MHz, d_6-DMSO) δ 8.86 (s, 1H, trzH), 8.72 – 8.69 (m, 1H, pyrH), 8.16 (d, J = 7.9 Hz, 1H, pyrH), 8.01 (td, J = 7.8, 1.7 Hz, 1H, pyrH), 7.46 (ddd, J = 7.5, 4.9, 1.1 Hz, 1H, pyrH), 6.55 (s, 1H, man anomeric H), 5.91 (m, 2H, manH), 5.34 (t, J = 9.1 Hz, 1H, manH), 4.30 (dd, J = 12.6, 4.9 Hz, 1H, manH), 4.10 (dd, J = 12.6, 2.4 Hz, 1H, manH), 3.98 (ddd, J = 9.2, 4.6, 2.5 Hz, 1H, manH), 2.23 (s, 3H, OAc), 2.11 (s, 3H, OAc), 2.07 (s, 6H, 2×OAc). ^{13}C NMR (101 MHz, d_6-DMSO) δ 170.47, 169.96, 169.87, 169.85, 150.28, 137.88, 123.96, 120.26, 83.52, 71.78, 68.94, 68.07, 65.81, 61.90, 20.99, 20.96, 20.90, 20.84. ESI-MS m/z calc. $[M+Na]^+$: 499.1, found: 499.2.

α-Galactose ligand

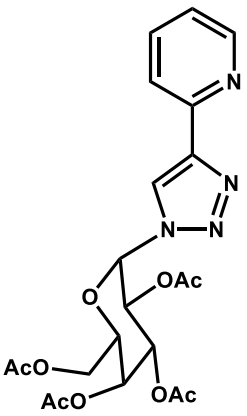

The α-galactose ligand was synthesized using the above general method using 2,3,4,6-tetra-*O*-acetylgalactopyranosyl-α-azide (0.100 g, 0.268 mmol), 2-ethynylpyridine (28 µL, 0.268 mmol), copper(II) sulfate pentahydrate (0.014 g, 0.054 mmol), ascorbic acid (0.048 g, 0.268 mmol) and sodium carbonate (0.028 g, 0.268 mmol) to give a yellowish oily solid. Yield = 0.1144 g (90%). ^{1}H NMR (400 MHz, d_6-DMSO) δ 8.87 (s, 1H, trzH), 8.63 (d, J = 4.7 Hz, 1H, pyrH), 8.09 (d, J = 7.9 Hz, 1H, pyrH), 7.95 – 7.89 (m, 1H, pyrH), 7.41 – 7.37 (m, 1H, pyrH), 6.76 (d, J = 6.0 Hz, 1H, gal anomeric H), 6.08 (dd, J = 10.9, 3.5 Hz, 1H, galH), 5.62 (d, J = 3.4 Hz, 1H, galH), 5.54 (dd, J = 10.9, 6.0 Hz, 1H, galH), 4.63 (t, J = 6.0 Hz, 1H, galH), 4.06 (d, J = 6.0 Hz, 2H, galH), 2.20 (s, 3H, OAc), 1.98 (s, 3H, OAc), 1.92 (s, 3H, OAc), 1.84 (s, 3H, OAc). ^{13}C NMR (101 MHz, d_6-DMSO) δ 170.43, 170.36, 170.02, 169.96, 150.30, 149.74, 147.13, 137.86, 123.89, 120.18, 81.87, 70.98, 68.07, 67.71, 65.95, 62.12, 36.25, 20.91, 20.86, 20.84, 20.61. ESI-MS m/z calc. $[M+Na]^+$: 499.1, found: 499.1.

β-Glucose ligand

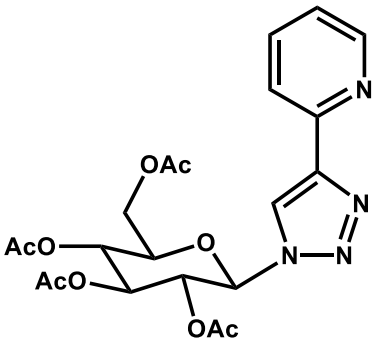

2,3,4,6-Tetra-*O*-acetylglucopyranosyl-β-azide (0.392 g g, 1.05 mmol), copper(II) sulfate pentahydrate (0.049 g, 1.0 mmol), ascorbic acid (0.176 g, 1.0 mmol) and sodium carbonate (0.106 g, 1.0 mmol) were dissolved in 20 mL 4:1 DMF/water solution, then 2-ethynylpyridine (102 µL, 1.0 mmol) was added and solution was stirred overnight. Solution was poured into 100 mL NH_4OH/EDTA-Na_2 solution (200 mL water, 13 mL NH_4OH, 5.75 g EDTA-Na_2) and stirred for an hour. A white precipitate formed and was washed with 100 mL NH_4OH/EDTA-Na_2 solution then 50 mL water and dried under vacuum to give a white solid. Yield = 0.3804 g (80%). ^{1}H NMR (400 MHz, $CDCl_3$) δ 8.63 (d, J = 4.3 Hz, 1H, pyrH), 8.42 (s, 1H, trzH),

8.17 (d, J = 7.9 Hz, 1H, pyrH), 7.80 (td, J = 7.8, 1.6 Hz, 1H, pyrH), 7.28 – 7.24 (m, 1H, pyrH), 5.95 (d, J = 8.8 Hz, 1H, glu anomeric H), 5.49 (dt, J = 18.8, 9.5 Hz, 2H, gluH), 5.29 (t, J = 9.6 Hz, 1H, gluH), 4.34 (dd, J = 12.6, 4.8 Hz, 1H, gluH), 4.18 (dd, J = 12.6, 1.8 Hz, 1H, gluH), 4.05 (ddd, J = 10.1, 4.7, 1.9 Hz, 1H, gluH), 2.11 (s, 3H, OAc), 2.10 (s, 3H, OAc), 2.06 (s, 3H, OAc), 1.92 (s, 3H, OAc). ^{13}C NMR (101 MHz, $CDCl_3$) δ 170.56, 169.75, 169.53, 169.10, 149.29, 149.39, 136.90, 135.96, 123.10, 121.02, 84.77, 75.68, 70.40, 68.33, 64.14, 63.20, 36.61, 20.89, 20.57, 20.22, 20.15. ESI-MS m/z calc. $[M+Na]^+$: 499.1, found: 499.2.

β-Mannose ligand

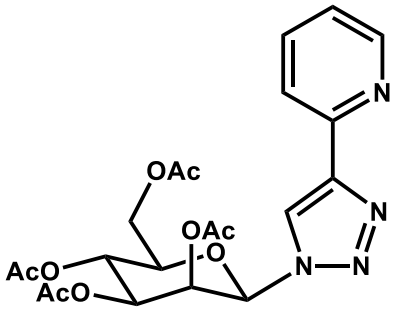

The β-mannose ligand was synthesized using the above general method using 2,3,4,6-tetra-*O*-acetylmannopyranosyl-β-azide (0.2 g, 0.536 mmol), 2-ethynylpyridine (56 µL, 0.536 mmol), copper(II) sulfate pentahydrate (0.028 g, 0.107 mmol), ascorbic acid (0.096 g, 0.536 mmol) and sodium carbonate (0.056 g, 0.536 mmol) to give a colourless oil. Yield = 0.1777 g (70%). ^{1}H NMR (400 MHz, $CDCl_3$) δ 8.61 (d, J = 4.8 Hz, pyrH), 8.45 (s, 1H, trzH), 8.20 (d, J = 7.9 Hz, 1H, pyrH), 7.81 (td, J = 7.8, 1.5 Hz, 1H, pyrH), 7.29 – 7.25 (m, 1H, pyrH), 6.22 (s, 1H, man anomeric H), 5.82 (d, J = 3.0 Hz, 1H, manH), 5.42 (t, J = 10.0 Hz, 1H, manH), 5.35 (d, J = 3.1 Hz, 1H, manH), 4.36 (dd, J = 12.5, 5.7 Hz, 1H, manH), 4.27 – 4.22 (m, 1H, manH), 4.04 – 3.98 (m, 1H, manH), 2.14 (s, 3H, OAc), 2.13 (s, 3H, OAc), 2.12 (s, 3H, OAc), 2.03 (s, 3H, OAc). ^{13}C NMR (101 MHz, $CDCl_3$) δ 170.60, 169.81, 169.55, 169.23, 149.79, 149.41, 136.98, 136.16, 123.20, 121.17, 84.88, 75.71, 70.82, 68.85, 64.88, 62.18, 36.48, 20.75, 20.67, 20.62, 20.50. ESI-MS m/z calc. $[M+Na]^+$: 499.1, found: 499.2.

β-Galactose ligand

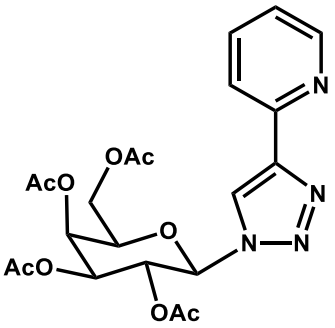

The β-galactose ligand was synthesized using the above general method using 2,3,4,6-tetra-*O*-acetylgalactopyranosyl-β-azide (0.405 g, 1.08 mmol), 2-ethynylpyridine (104 µL, 1.03 mmol), copper(II) sulfate pentahydrate (0.052 g, 0.206 mmol), ascorbic acid (0.182 g, 1.03 mmol) and sodium carbonate (0.110 g, 1.03 mmol) to give a white solid. Yield = 0.2391 g (46%). ^{1}H NMR (400 MHz, d_6-DMSO) δ 8.81 (s, 1H, trzH), 8.63 (d, J = 4.2 Hz, 1H, pyrH), 8.06 (d, J = 7.9 Hz, 1H, pyrH), 7.93 (td, J = 7.8, 1.7 Hz, 1H, pyrH), 7.40 (ddd, J = 7.4, 4.9, 0.9 Hz, 1H, pyrH), 6.34 (d, J = 9.2 Hz, 1H, gal anomeric H), 5.68 (t, J = 9.7 Hz, 1H, galH), 5.50 (dd, J = 10.1, 3.4 Hz, 1H, galH), 5.45 (d, J = 3.1 Hz, 1H, galH), 4.62 (t, J = 6.1 Hz, 1H, galH), 4.15 (dd, J = 11.6, 5.0 Hz, 1H, galH), 4.06 (dd, J = 11.6, 7.3 Hz, 1H, galH), 2.22 (s, 3H, OAc), 2.00 (s, 3H, OAc), 1.96 (s, 3H, OAc), 1.84 (s, 3H, OAc). ^{13}C NMR (101 MHz, d_6-DMSO) δ 170.57, 170.44, 169.99, 169.17, 150.20, 149.64, 148.16, 137.85, 123.93, 120.25, 84.95, 73.45, 70.85, 68.27, 67.72, 62.05, 20.95, 20.85, 20.80, 20.47. ESI-MS m/z calc. $[M+Na]^+$: 499.1, found: 499.2.

2,3,4,6-Tetra-O-acetylglucopyranosyl-β-PEG1 ligand

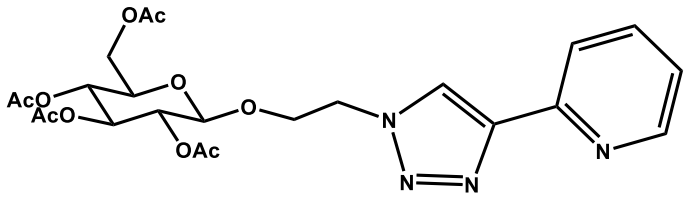

2,3,4,6-Tetra-*O*-acetylglucopyranosyl-β-PEG1 ligand was synthesized using the above general method using 2,3,4,6-tetra-*O*-acetylglucopyranosyl-β-PEG1-azide (0.2 g, 0.479 mmol), 2-ethynylpyridine (48 µL, 0.479 mmol), copper(II) sulfate

pentahydrate (0.024 g, 0.096 mmol), ascorbic acid (0.084 g, 0.479 mmol) and sodium carbonate (0.051 g, 0.479 mmol) to give a clear oil. Yield = 0.1453 g (58%). ^{1}H NMR (400 MHz, d_6-DMSO) δ 8.60 (t, J = 5.3 Hz, 1H, pyrH), 8.46 (s, 1H, trzH), 8.08 – 7.99 (m, 1H, pyrH), 7.89 (dd, J = 11.0, 4.4 Hz, 1H, pyrH), 7.35 (dt, J = 6.0, 4.4 Hz, 1H, pyrH), 5.23 (d, J = 9.6 Hz, 1H, glu anomeric H), 4.94 – 4.84 (m, 2H, gluH), 4.78 – 4.60 (m, 3H, gluH), 4.18 (dd, J = 12.5, 4.5 Hz, 2H, CH_2), 4.07 – 3.95 (m, 3H, CH_2 and gluH), 2.02 (s, 3H, OAc), 1.98 (s, 3H, OAc), 1.91 (s, 3H, OAc), 1.82 (s, 3H, OAc). ^{13}C NMR (101 MHz, d_6-DMSO) δ 170.52, 169.99, 169.73, 169.38, 150.45, 150.02, 147.59, 137.67, 123.93, 123.42, 119.78, 99.57, 72.40, 71.10, 71.06, 68.53, 67.86, 62.08, 49.90, 20.94, 20.82, 20.70, 20.51. ESI-MS m/z calc. $[M+Na]^+$: 543.2, found 543.2.

2,3,4,6-Tetra-O-acetylglucopyranosyl-β-PEG2 ligand

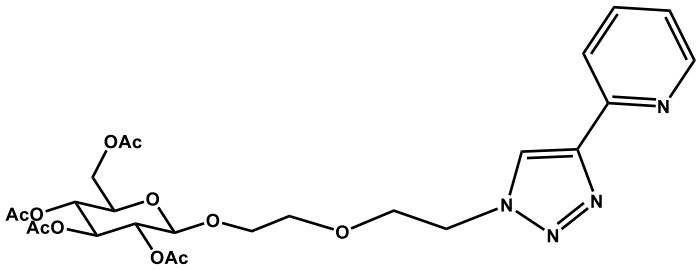

2,3,4,6-Tetra-*O*-acetylglucopyranosyl-β-PEG2 ligand was synthesized using the above general method using 2,3,4,6-tetra-*O*-acetylglucopyranosyl-β-PEG2-azide (0.2 g, 0.433 mmol), 2-ethynylpyridine (44 µL, 0.433 mmol), copper(II) sulfate pentahydrate (0.022 g, 0.087 mmol), ascorbic acid (0.076 g, 0.433 mmol) and sodium carbonate (0.046 g, 0.433 mmol) to give an off-white waxy solid. Yield = 0.2097 g (86%). ^{1}H NMR (400 MHz, d_6-DMSO) δ 8.62 (d, J = 4.6 Hz, 1H, pyrH), 8.59 (s, 1H, trzH), 8.04 (d, J = 7.9 Hz, 1H, pyrH), 7.89 (t, J = 7.1 Hz, 1H, pyrH), 7.34 (dd, J = 6.9, 5.4 Hz, 1H, pyrH), 5.29 – 5.20 (m, 1H, glu anomeric H), 4.91 (t, J = 9.7 Hz, 1H, gluH), 4.81 (d, J = 4.9 Hz, 2H, gluH), 4.60 (t, J = 5.2 Hz, 2H, gluH), 4.15 (dd, J = 12.2, 5.0 Hz, 1H, gluH), 4.04 – 3.91 (m, 2H, CH_2), 3.87 (t, J = 5.1 Hz, 2H, CH_2), 3.81 – 3.74 (m, 1H, CH), 3.68 – 3.60 (m, 1H, CH), 3.57 (t, J = 4.5 Hz, 2H, CH_2), 1.98 (s, 3H, OAc), 1.97 (s, 3H, OAc), 1.96 (s, 3H, OAc), 1.94 (s, 3H, OAc). ^{13}C NMR (101 MHz, d_6-DMSO) δ 170.53, 170.03, 169.78, 169.55, 150.45,

150.10, 147.62, 137.65, 124.12, 123.37, 119.84, 100.01, 72.60, 71.37, 71.00, 69.70, 69.05, 68.92, 68.57, 62.07, 50.01, 20.89, 20.83, 20.78, 20.74. ESI-MS m/z calc. $[M+Na]^+$: 587.2, found 587.2.

2,3,4,6-Tetra-O-acetylglucopyranosyl-β-PEG3 ligand

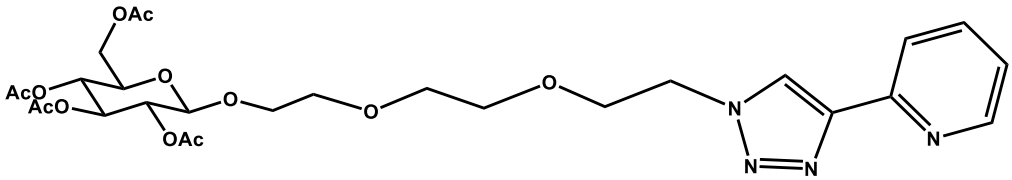

2,3,4,6-Tetra-*O*-acetylglucopyranosyl-β-PEG3 ligand was synthesized using the above general method using 2,3,4,6-tetra-*O*-acetylglucopyranosyl-β-PEG3-azide (0.150 g, 0.3 mmol), 2-ethynylpyridine (30 µL, 0.3 mmol), copper(II) sulfate pentahydrate (0.015 g, 0.06 mmol), ascorbic acid (0.052 g, 0.3 mmol) and sodium carbonate (0.031 g, 0.3 mmol) to give a clear oil. Yield = 0.093 g (51%). ^{1}H NMR (400 MHz, d_6-DMSO) δ 8.60 (d, J = 4.3 Hz, 1H, pyrH), 8.57 (s, 1H, trzH), 8.04 (d, J = 7.9 Hz, 1H, pyrH), 7.90 (t, J = 7.5 Hz, 1H, pyrH), 7.39 – 7.31 (m, 1H, pyrH), 5.24 (d, J = 9.3 Hz, 1H, glu anomeric H), 4.89 (t, J = 9.7 Hz, 1H, gluH), 4.81 – 4.71 (m, 2H, gluH), 4.61 (t, J = 5.1 Hz, 2H, gluH), 4.17 (dd, J = 12.2, 5.0 Hz, 1H, gluH), 4.06 – 3.92 (m, 2H, CH_2), 3.88 (t, J = 5.1 Hz, 2H, CH_2), 3.82 – 3.73 (m, 1H, CH), 3.64 – 3.45 (m, 7H, 3×CH_2 and CH), 2.01 (s, 3H, OAc), 1.98 (s, 3H, OAc), 1.97 (s, 3H, OAc), 1.94 (s, 3H, OAc). ^{13}C NMR (101 MHz, d_6-DMSO) δ 170.55, 170.05, 169.78, 169.57, 100.01, 72.52, 71.33, 71.01, 70.14, 70.00, 69.78, 69.11, 69.01, 68.61, 62.13, 20.93, 20.82, 20.77, 20.72. ESI-MS m/z calc. $[M+Na]^+$: 631.2, found 631.2.

Methyl ligand

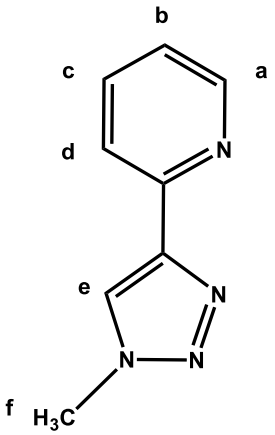

Sodium azide (0.071 g, 1.0 mmol), ascorbic acid (0.176 g, 1.0 mmol) and copper(II) sulfate pentahydrate (0.049 g, 0.2 mmol) were dissolved in 20 mL DMF and water solution (4:1 v/v). Iodomethane (125 µL, 0.284 g, 2.0 mmol) and 2-ethynylpyridine (101 µL, 0.103 g, 1.0 mmol) were then added and solution was stirred in the dark at room temperature for 24 h. The orange-red mixture was treated with 75 mL EDTA-Na_2/ammonium hydroxide solution (5.77 g EDTA-Na_2, 13 mL ammonium hydroxide (35%) in 200 mL water), then extracted with 50 mL dichloromethane. The organic layer was washed with 3 × 50 mL water and then dried over anhydrous sodium sulfate and filtered. Solvent was evaporated under reduced pressure and purified using a silica column with ethyl acetate. The solvent was then evaporated under reduced pressure to give a yellow powder. Yield = 0.052 g (33%). ^{1}H NMR (400 MHz, $CDCl_3$) δ 8.50 (d, J = 4.8 Hz, 1H, H_a), 8.11 (d, J = 7.9 Hz, 1H, H_d), 8.05 (s, 1H_e), 7.71 (td, J = 7.8, 1.7 Hz, 1H, H_c), 7.16 (ddd, J = 7.4, 4.9, 0.9 Hz, 1H_b), 4.10 (s, 3H_f). ^{13}C NMR (101 MHz, $CDCl_3$) δ 150.26, 150.05, 136.90, 136.23, 127.47, 123.43, 122.86, 36.83. ESI-MS m/z calc. $[M+Na]^+$: 183.1, found 183.1.

3.2.4 Synthesis of protected complexes

General synthesis of protected iridium complexes

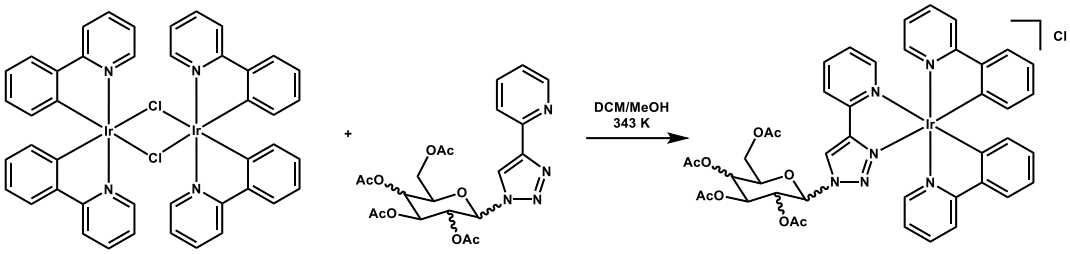

The iridium dimer (1 eq) and ligand (2.25 eq) were dissolved in 3:1 DCM/MeOH solution and refluxed at 343 K overnight. Solution was cooled to room temperature, then solvent removed under reduced pressure. Residue was purified by column chromatography (stationary phase: alumina, mobile phase: 0-5% MeOH gradient in DCM). Relevant fractions were combined and dried under reduced pressure, then residue suspended in ether, sonicated, and dried again to yield product.

[Ir(ppy)$_2$(α-Glu(OAc)$_4$)]Cl – ***1Ac***

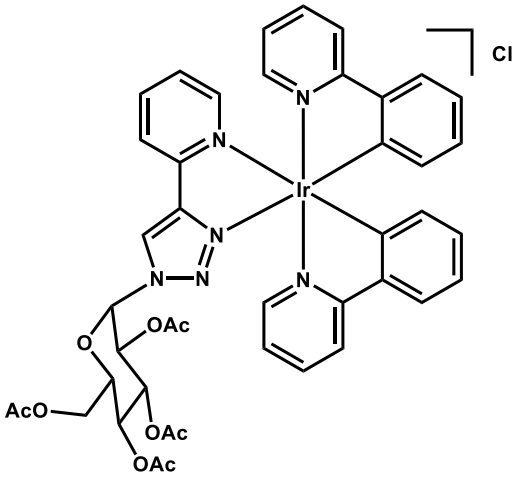

The protected iridium α-glucose complex was synthesized using α-glucose ligand (0.095 g, 0.20 mmol) and iridium dimer (0.095 g, 0.088 mmol) in 20 mL 3:1 DCM/MeOH, yielding a yellow solid. Yield = 0.1238 g (69%). ^{1}H NMR (400 MHz, MeOD) δ 9.26 (s, 1H), 9.23 (s, 1H), 8.40 – 8.30 (m, 2H), 8.19 – 8.10 (m, 6H), 7.99

– 7.94 (m, 2H), 7.94 – 7.83 (m, 8H), 7.82 – 7.75 (m, 2H), 7.73 – 7.66 (m, 2H), 7.54 – 7.44 (m, 2H), 7.18 – 7.03 (m, 6H), 7.00 – 6.92 (m, 4H), 6.90 – 6.77 (m, 2H), 6.63 (dd, J = 15.2, 5.6 Hz, 2H), 6.50 (d, J = 7.2 Hz, 1H), 6.42 (d, J = 6.8 Hz, 2H), 6.26 (d, J = 7.6 Hz, 1H), 5.63 (t, J = 9.4 Hz, 1H), 5.53 – 5.47 (m, 1H), 5.41 – 5.34 (m, 1H), 5.27 – 5.12 (m, 3H), 4.34 (d, J = 9.0 Hz, 1H), 4.24 (dd, J = 12.7, 4.0 Hz, 1H), 4.11 (dd, J = 12.7, 4.8 Hz, 2H), 3.92 (d, J = 11.0 Hz, 2H), 2.08 (s, 3H), 2.04 (s, 3H), 2.03 (s, 3H), 2.00 (s, 3H), 1.99 (s, 6H), 1.92 (s, 3H), 1.55 (s, 3H). ^{13}C NMR (101 MHz, MeOD) δ 170.95, 168.45, 167.64, 162.96, 162.49, 161.84, 157.73, 157.44, 157.39, 155.42, 150.37, 149.87, 149.08, 148.27, 145.39, 144.10, 139.64, 138.29, 131.83, 131.73, 131.52, 131.23, 130.08, 130.01, 129.69, 129.12, 126.98, 126.82, 125.02, 124.63, 124.01, 123.13, 122.98, 122.76, 122.44, 122.36, 122.15, 122.04, 121.82, 120.20, 119.55, 119.50, 119.35, 83.88, 83.85, 83.52, 75.08, 72.78, 72.25, 70.23, 68.64, 68.54, 67.36, 67.23, 67.09, 19.34, 19.26, 19.22, 19.18, 19.08, 18.96, 18.82, 18.79. HR-ESI-MS m/z calc. $[M]^+$: 977.2481, found 977.2468.

$[Ir(ppy)_2(\alpha\text{-}Man(OAc)_4)]Cl$ – ***2Ac***

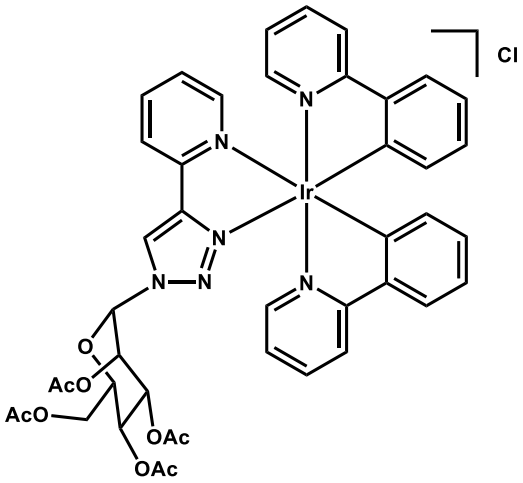

The protected iridium α-mannose complex was synthesized using α-mannose ligand (0.1759 g, 0.369 mmol) and iridium dimer (0.1765 g, 0.165 mmol) in 20 mL 3:1 DCM/MeOH, yielding a yellow solid. Yield = 0.2240 g (67%). ^{1}H NMR (400 MHz, MeOD) δ 9.23 (s, 1H), 9.18 (s, 1H), 8.25 (t, J = 7.5 Hz, 2H), 8.05 – 7.98 (m, 6H), 7.83 – 7.68 (m, 12H), 7.64 (t, J = 6.8 Hz, 2H), 7.55 (dd, J = 13.2, 5.3 Hz, 2H), 7.35 (s, 2H), 7.04 (t, J = 6.5 Hz, 2H), 6.98 – 6.91 (m, 4H), 6.87 – 6.77 (m, 4H), 6.74 –

6.66 (m, 2H), 6.33 – 6.14 (m, 4H), 5.58 (t, J = 3.6 Hz, 1H), 5.49 – 5.45 (m, 1H), 5.23 (ddd, J = 11.5, 7.2, 3.5 Hz, 2H), 5.14 – 5.06 (m, 2H), 4.41 (dd, J = 12.3, 6.2 Hz, 1H), 4.22 – 4.12 (m, 3H), 3.93 – 3.89 (m, 1H), 3.57 – 3.51 (m, 1H), 2.01 (s, 3H), 2.00 (s, 3H), 1.95 (s, 3H), 1.93 (s, 3H), 1.90 (s, 6H), 1.87 (s, 3H), 1.85 (s, 3H). ^{13}C NMR (101 MHz, MeOD) δ 171.81, 171.06, 171.05, 170.14, 169.71, 148.57, 139.67, 139.66, 138.28, 138.20, 131.64, 131.57, 130.08, 126.87, 124.59, 122.73, 122.40, 92.33, 84.73, 84.13, 83.25, 82.49, 81.73, 81.39, 79.74, 70.56, 69.17, 67.55, 60.93, 19.21, 19.13, 19.07, 19.02, 18.99, 18.93. HR-ESI-MS m/z calc. $[M]^+$: 977.2481, found 977.2476.

$[Ir(ppy)_2(\alpha\text{-}Gal(OAc)_4)]Cl$ – ***3Ac***

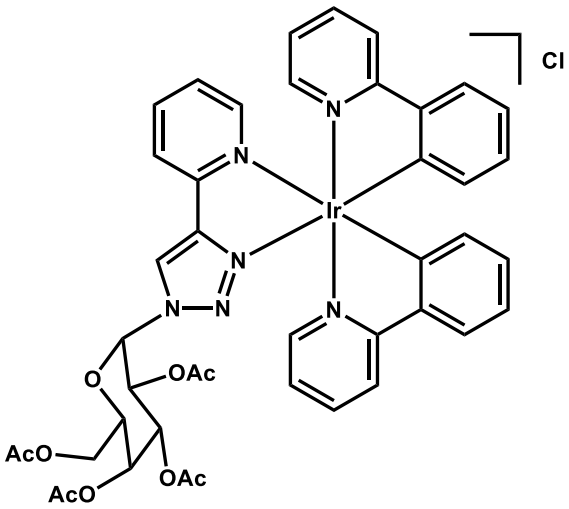

The protected iridium α-galactose complex was synthesized using α-galactose ligand (0.1039 g, 0.218 mmol) and iridium dimer (0.1039 g, 0.097 mmol) in 20 mL 3:1 DCM/MeOH, yielding a yellow solid. Yield = 0.1676 g (85%). ^{1}H NMR (400 MHz, MeOD) δ 9.26 (s, 1H), 9.23 (s, 1H), 8.40 – 8.29 (m, 2H), 8.20 – 8.07 (m, 6H), 8.00 – 7.76 (m, 12H), 7.73 – 7.66 (m, 2H), 7.53 – 7.43 (m, 2H), 7.19 – 6.80 (m, 12H), 6.70 (dd, J = 9.7, 5.8 Hz, 2H), 6.44 (dd, J = 14.0, 7.4 Hz, 2H), 6.35 (d, J = 7.0 Hz, 1H), 6.26 (d, J = 7.3 Hz, 1H), 5.66 – 5.60 (m, 1H), 5.56 – 5.47 (m, 2H), 5.43 (br s, 1H), 5.36 (br s, 1H), 5.20 (d, J = 9.8 Hz, 1H), 4.55 – 4.49 (m, 1H), 4.21 – 4.08 (m, 3H), 4.06 – 4.01 (m, 2H), 2.17 (s, 3H), 2.16 (s, 3H), 1.99 (s, 12H), 1.92 (s, 3H), 1.59 (s, 3H). ^{13}C NMR (101 MHz, MeOD) δ 179.78, 173.14, 172.11, 168.01, 166.95, 164.99, 152.76, 151.86, 151.84, 150.36, 148.61, 139.70, 138.34,

138.00, 131.74, 131.51, 129.33, 128.93, 126.84, 124.70, 124.67, 124.02, 123.19, 122.58, 122.40, 122.04, 119.88, 119.71, 119.54, 67.49, 67.12, 66.95, 66.65, 65.96, 19.87, 19.23, 19.21, 19.15, 19.03, 18.96, 18.79. HR-ESI-MS m/z calc. $[M]^+$: 977.2481, found 977.2470.

$[Ir(ppy)_2(\beta\text{-}Glu(OAc)_4)]Cl$ – ***4Ac***

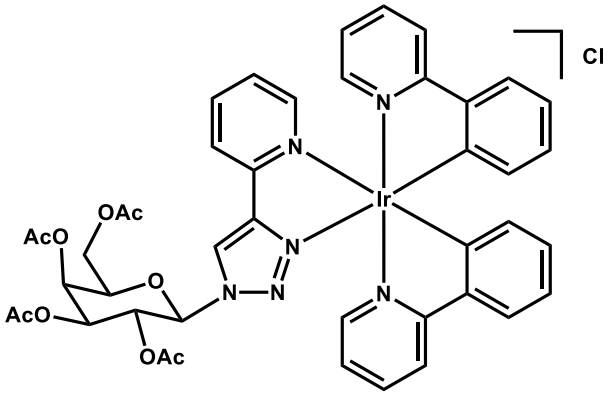

The protected iridium β-glucose complex was synthesized using β-glucose ligand (0.115 g, 0.241 mmol) and iridium dimer (0.115 g, 0.107 mmol) in 20 mL 3:1 DCM/MeOH, yielding a yellow solid. Yield = 0.1336 g (62%). ^{1}H NMR (700 MHz, MeOD) δ 9.49 (s, 1H), 9.42 (s, 1H), 8.40 (t, J = 8.4 Hz, 2H), 8.19-8.10 (m, 6H), 7.95-7.87 (m, 6H), 7.85-7.80 (m, 2H), 7.70-7.69 (m, 4H), 7.62 (d, J = 5.6 Hz, 1H), 7.49-7.43 (m, 2H), 7.18-7.07 (m, 4H), 7.04 (td, J = 7.6, 3.7 Hz, 2H), 6.96 (dd, J = 13.9, 6.9 Hz 2H), 6.93-6.87 (m, 2H), 6.83-6.76 (m, 2H), 6.33 (d, J = 7.5 Hz, 1H), 6.29 (t, J = 9.7 Hz, 1H), 6.27-6.19 (m, 3H), 6.15-6.09 (m, 1H), 5.60-5.50 (m, 2H), 5.38 (t, J = 9.2 Hz ,1H), 5.33-5.26 (m, 3H), 4.38 (ddd, J = 12.6, 9.5, 5.0 Hz, 2H), 4.32-4.27 (m, 2H), 4.27-4.21 (m, 3H), 3.33 (dt, J = 3.2, 1.6 Hz, 3H), 2.08 (s, 9H), 2.05 (s, 3H), 2.02 (s, 3H), 1.98 (s, 3H), 1.85 (s, 3H). ^{13}C NMR (101 MHz, MeOD) δ 173.31, 171.94, 170.74, 169.73, 168.34, 150.11, 149.09, 148.79, 148.72, 139.67, 138.42, 131.59, 131.52, 131.26, 131.17, 131.12, 130.11, 129.42, 129.30, 126.81, 124.64, 124.54, 124.14, 124.03, 122.93, 122.85, 122.47, 122.40, 121.96, 119.56, 119.47, 86.63, 75.04, 71.76, 71.70, 71.61, 71.26, 67.55, 61.42, 19.26, 19.21, 19.18, 19.08, 19.03, 18.99. HR-ESI-MS m/z calc. $[M]^+$: 977.2481, found 977.2475.

$[Ir(ppy)_2(\beta\text{-}Man(OAc)_4)]Cl$ – ***5Ac***

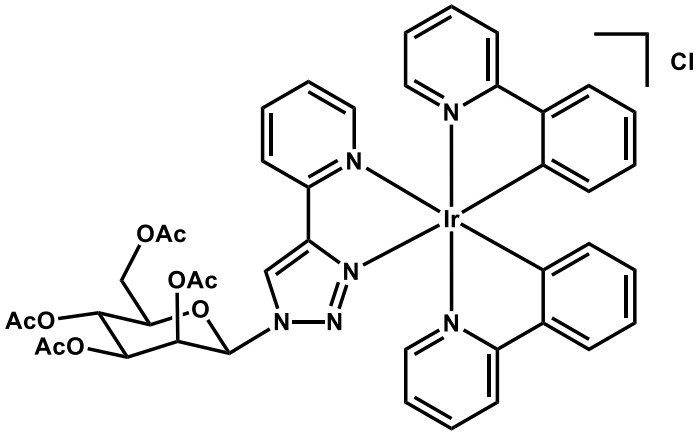

The protected iridium β-mannose complex was synthesized using β-mannose ligand (0.1777 g, 0.373 mmol) and iridium dimer (0.1777 g, 0.166 mmol) in 20 mL 3:1 DCM/MeOH, yielding a yellow solid. Yield = 0.2534 g (75%). ^{1}H NMR (400 MHz, MeOD) δ 9.33 (s, 1H), 9.27 (s, 1H), 8.40 (d, J = 7.7 Hz, 2H), 8.17 – 8.07 (m, 6H), 7.93 – 7.81 (m, 9H), 7.78 – 7.70 (m, 3H), 7.62 (dd, J = 15.4, 5.7 Hz, 2H), 7.45 (dd, J = 13.4, 6.9 Hz, 2H), 7.17 – 7.11 (m, 2H), 7.11 – 7.02 (m, 4H), 6.99 – 6.88 (m, 4H), 6.80 (dd, J = 16.4, 7.9 Hz, 2H), 6.50 (d, J = 13.7 Hz, 2H), 6.32 (d, J = 7.6 Hz, 2H), 6.24 (t, J = 7.2 Hz, 2H), 5.75 (s, 1H), 5.62 (s, 1H), 5.48 – 5.29 (m, 4H), 4.40 (ddd, J = 18.0, 13.0, 5.2 Hz, 2H), 4.32 – 4.13 (m, 4H), 2.09 (s, 3H), 2.07 (s, 12H), 2.01 (s, 3H), 1.95 (s, 3H), 1.73 (s, 3H). ^{13}C NMR (101 MHz, MeOD) δ 169.94, 169.91, 169.70, 169.68, 167.61, 167.59, 150.12, 148.53, 148.27, 145.68, 144.00, 139.71, 139.62, 138.31, 138.26, 138.22, 131.57, 131.36, 131.28, 130.07, 129.39, 129.26, 126.83, 126.69, 124.55, 124.11, 124.05, 123.14, 123.07, 122.79, 122.73, 122.45, 122.44, 121.88, 119.54, 119.50, 119.49, 119.40, 85.56, 85.35, 75.45, 75.35, 70.28, 70.06, 69.40, 68.32, 64.99, 64.85, 61.70, 19.21, 19.20, 19.13, 18.96, 18.94, 18.93, 18.82. HR-ESI-MS m/z calc. $[M]^+$: 977.2481, found 977.2472.

[Ir(ppy)$_2$(β-Gal(OAc)$_4$)]Cl – ***6Ac***

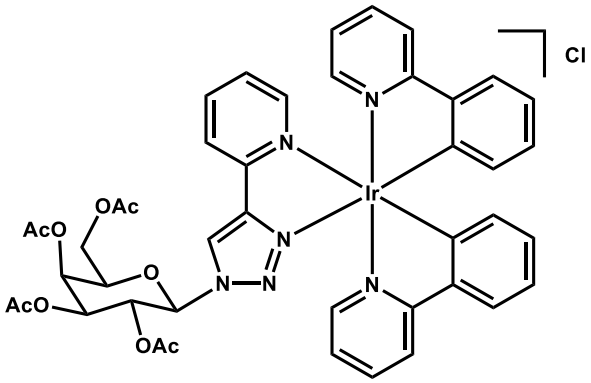

The protected iridium β-galactose complex was synthesized using β-galactose ligand (0.102 g, 0.095 mmol) and iridium dimer (0.102 g, 0.210 mmol) in 20 mL 3:1 DCM/MeOH, yielding a yellow solid. Yield = 0.071 g (37%). ^{1}H NMR (400 MHz, MeOD) δ 9.53 (s, 1H), 9.47 (s, 1H), 8.42 (d, J = 7.6 Hz, 2H), 8.17 – 8.09 (m, 6H), 7.95 – 7.71 (m, 14H), 7.48 – 7.42 (m, 2H), 7.19 – 7.02 (m, 6H), 6.94 (dt, J = 15.5, 7.0 Hz, 4H), 6.81 (dd, J = 16.2, 8.2 Hz, 2H), 6.32 (dd, J = 15.2, 7.6 Hz, 2H), 6.24 (t, J = 6.8 Hz, 2H), 6.17 (d, J = 8.8 Hz, 1H), 6.09 (t, J = 7.8 Hz, 2H), 5.48 – 5.25 (m, 5H), 4.50 (dt, J = 25.1, 6.3 Hz, 2H), 4.35 – 4.20 (m, 4H), 2.22 (s, 3H), 2.19 (s, 3H), 2.05 (s, 3H), 2.00 (s, 6H), 1.95 (s, 3H), 1.88 (s, 3H), 1.40 (s, 3H). ^{13}C NMR (101 MHz, MeOD) δ 170.59, 170.27, 170.23, 167.66, 167.60, 150.13, 150.10, 149.49, 149.31, 149.16, 148.82, 145.85, 145.81, 144.00, 139.67, 138.43, 138.29, 131.61, 131.54, 131.30, 131.10, 130.11, 129.41, 129.29, 126.82, 126.78, 124.61, 124.54, 124.19, 124.05, 123.17, 122.96, 122.88, 122.47, 122.43, 121.97, 121.90, 119.53, 119.47, 86.93, 74.22, 69.96, 69.82, 69.39, 68.91, 66.92, 66.83, 61.26, 61.15, 19.41, 19.21, 19.13, 19.07, 19.03, 19.00, 18.99, 18.95. HR-ESI-MS m/z calc. $[M]^+$: 977.2481, found 977.2473.

$[Ir(ppy)_2(PEG1\text{-}\beta\text{-}Glu(OAc)_4)]Cl$ – ***7Ac***

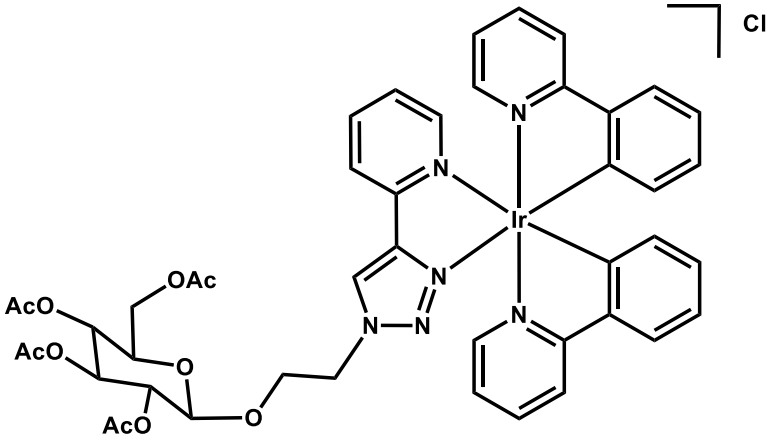

The protected iridium PEG1-β-glucose complex was synthesized using PEG1-β-glucose ligand (0.1210 g, 0.232 mmol) and iridium dimer (0.1107 g, 0.103 mmol) in 20 mL 3:1 DCM/MeOH, yielding a yellow solid. Yield = 0.1777 g (81%). ^{1}H NMR (400 MHz, MeOD) δ 9.00 (s, 1H), 8.99 (s, 1H), 8.33 (d, J = 7.9 Hz, 2H), 8.12 (s, 6H), 7.94 – 7.87 (m, 7H), 7.83 (d, J = 7.7 Hz, 2H), 7.76 (t, J = 6.6 Hz, 5H), 7.69 – 7.64 (m, 2H), 7.46 – 7.42 (m, 2H), 7.23 – 7.02 (m, 7H), 6.99 – 6.89 (m, 4H), 6.81 (t, J = 7.4 Hz, 2H), 6.33 – 6.27 (m, 4H), 5.25 (dt, J = 18.7, 9.6 Hz, 2H), 5.01 (td, J = 9.6, 5.2 Hz, 2H), 4.77 – 4.68 (m, 4H), 4.29 – 4.07 (m, 8H), 3.90 – 3.81 (m, 3H), 2.04 (s, 3H), 2.03 (s, 3H), 2.00 (s, 9H), 1.92 (s, 3H), 1.85 (s, 3H), 1.83 (s, 3H). ^{13}C NMR (101 MHz, MeOD) δ 171.47, 171.23, 170.75, 170.57, 170.11, 169.86, 150.16, 150.13, 149.57, 149.25, 149.18, 148.57, 148.55, 148.33, 147.77, 146.14, 146.08, 145.56, 144.08, 143.98, 139.57, 138.26, 138.22, 138.14, 131.62, 131.27, 130.09, 129.32, 127.52, 126.47, 124.55, 124.08, 124.03, 123.22, 123.12, 122.74, 122.54, 122.51, 122.35, 121.79, 119.47, 119.36, 100.40, 100.09, 72.53, 71.65, 71.32, 71.20, 68.34, 68.27, 66.96, 66.31, 61.60, 52.00, 51.93, 19.33, 19.32, 19.27, 19.24, 19.17, 19.13, 19.10. ESI-MS m/z calc. $[M]^+$: 1021.2743, found 1021.2733.

$[Ir(ppy)_2(PEG2\text{-}\beta\text{-}Glu(OAc)_4)]Cl$ – ***8Ac***

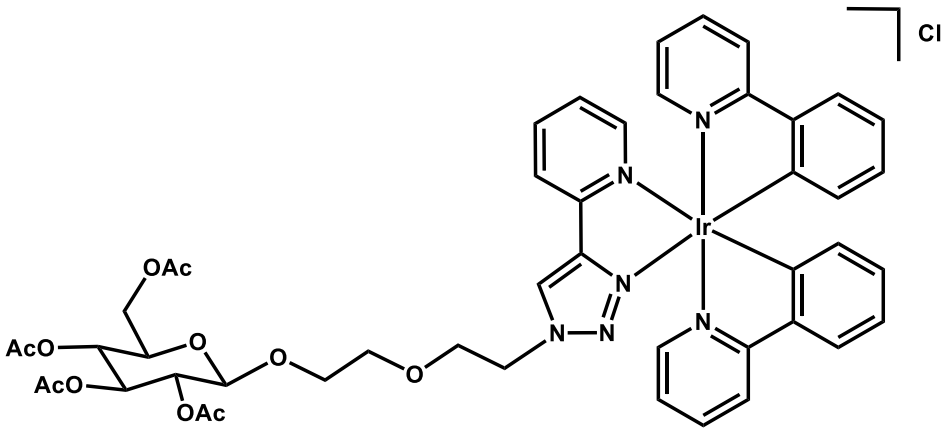

The protected iridium PEG2-β-glucose complex was synthesized using PEG2-β-glucose ligand (0.1481 g, 0.262 mmol) and iridium dimer (0.1250 g, 0.117 mmol) in 20 mL 3:1 DCM/MeOH, yielding a yellow solid. Yield = 0.2197g (86%). 1H NMR (500 MHz, d_6-DMSO + TFA) δ 9.28 (s, 2H), 8.47 – 8.41 (m, 2H), 8.26 – 8.14 (m, 6H), 7.96 – 7.86 (m, 6H), 7.81 (d, J = 8.3 Hz, 2H), 7.73 (d, J = 5.3 Hz, 2H), 7.69 – 7.61 (m, 4H), 7.57 – 7.51 (m, 2H), 7.21 – 7.10 (m, 4H), 7.04 – 6.97 (m, 2H), 6.95 – 6.86 (m, 4H), 6.83 – 6.75 (m, 2H), 6.22 – 6.13 (m, 4H), 5.31 – 5.22 (m, 2H), 4.91 (td, J = 9.6, 4.0 Hz, 2H), 4.81 – 4.71 (m, 4H), 4.66 (t, J = 4.6 Hz, 4H), 4.17 (dd, J = 12.1, 4.7 Hz, 2H), 4.06 – 3.94 (m, 4H), 3.88 – 3.80 (m, 2H), 3.80 – 3.68 (m, 4H), 3.61 – 3.53 (m, 2H), 3.53 – 3.43 (m, 4H), 1.97 (s, 6H), 1.95 (s, 6H), 1.92 (s, 6H), 1.87 (s, 3H), 1.85 (s, 3H). ^{13}C NMR (101 MHz, MeOD) δ 170.67, 170.34, 170.10, 169.92, 169.86, 168.81, 168.44, 161.53, 150.14, 149.76, 149.71, 149.28, 149.18, 148.69, 146.24, 143.99, 139.65, 139.61, 139.56, 138.19, 138.09, 131.58, 131.31, 130.06, 129.30, 126.36, 124.54, 124.03, 123.11, 122.81, 122.71, 122.55, 122.32, 121.76, 119.46, 119.32, 118.27, 100.73, 72.73, 71.47, 69.69, 69.26, 68.32, 68.11, 61.59, 51.79, 19.31, 19.29, 19.26, 19.14. ESI-MS m/z calc. $[M]^+$: 1065.3005, found 1065.2995.

[Ir(ppy)$_2$(PEG3-β-Glu(OAc)$_4$)]Cl – ***9Ac***

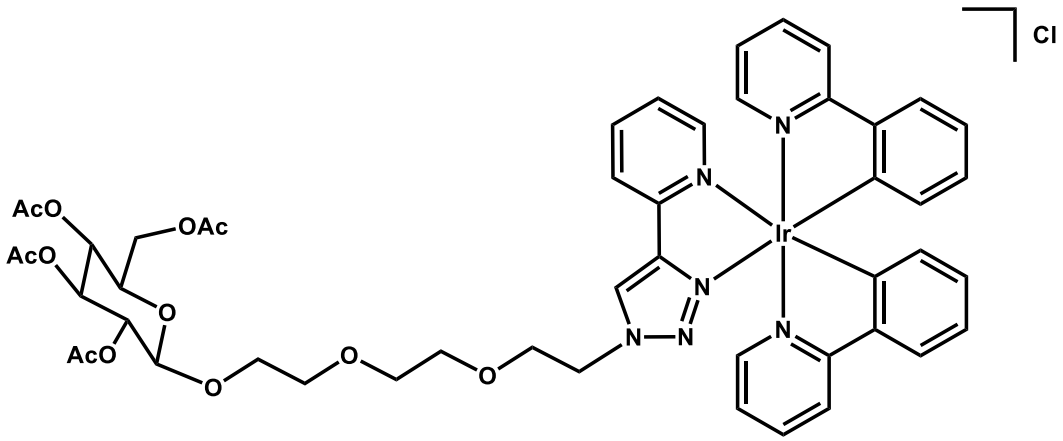

The protected iridium PEG3-β-glucose complex was synthesized using PEG3-β-glucose ligand (0.0759 g, 0.125 mmol) and iridium dimer (0.0594 g, 0.055 mmol) in 20 mL 3:1 DCM/MeOH, yielding a yellow solid. Yield = 0.0985 g (78%). ^{1}H NMR (400 MHz, d_6-DMSO + TFA) δ 9.31 (s, 2H), 8.42 (d, J = 7.5 Hz, 2H), 8.27 – 8.12 (m, 6H), 7.97 – 7.84 (m, 6H), 7.81 (d, J = 7.6 Hz, 2H), 7.73 (d, J = 5.3 Hz, 2H), 7.70 – 7.60 (m, 4H), 7.57 – 7.47 (m, 2H), 7.20 – 7.11 (m, 4H), 7.00 (t, J = 7.3 Hz, 2H), 6.97 – 6.86 (m, 4H), 6.78 (t, J = 7.5 Hz, 2H), 6.18 (dd, J = 10.7, 7.9 Hz, 4H), 5.25 (t, J = 8.8 Hz, 2H), 4.90 (dd, J = 17.1, 9.5 Hz, 2H), 4.83 – 4.73 (m, 4H), 4.73 – 4.62 (m, 4H), 4.24 – 4.11 (m, 2H), 4.03 – 3.92 (m, 4H), 3.91 – 3.72 (m, 6H), 3.62 – 3.52 (m, 2H), 3.48 – 3.34 (m, 12H), 1.96 (s, 12H), 1.91 (s, 12H). ^{13}C NMR (101 MHz, MeOD) δ 171.65, 171.54, 171.31, 170.09, 170.01, 169.89, 169.85, 139.55, 138.23, 138.11, 138.09, 131.60, 131.32, 130.05, 129.29, 126.29, 124.54, 124.03, 123.08, 122.76, 122.73, 122.71, 122.65, 122.32, 122.31, 121.74, 119.49, 119.46, 119.43, 119.35, 100.75, 100.62, 72.80, 71.53, 71.39, 71.34, 70.15, 69.91, 69.75, 69.16, 68.34, 68.20, 68.12, 51.87, 19.35, 19.31, 19.28, 19.24, 19.15. ESI-MS m/z calc. $[M]^+$: 1109.3267, found 1109.3301.

$[Ir(ppy)_2(NN\text{-}CH_3)]Cl$ - ***10***

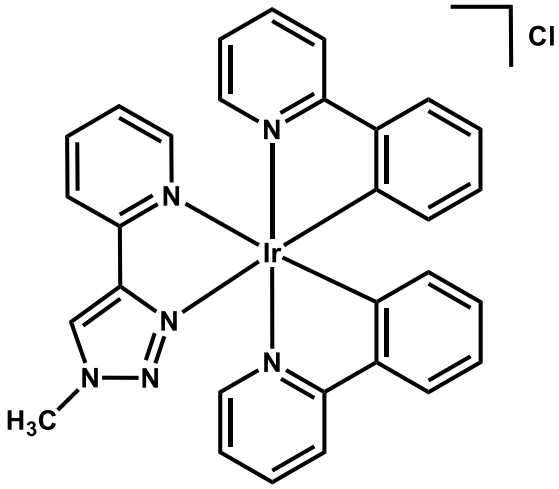

The methyl analogue was synthesised using the methyl ligand (0.045 g, 0.28 mmol) and iridium dimer (0.151 g, 0.14 mmol) in 20 mL 3:1 DCM/MeOH, yielding a yellow solid. Yield = 0.174 g (89%). ^{1}H NMR (400 MHz, d_6-DMSO) δ 9.44 (s, 1H), 8.47 (d, J = 7.9 Hz, 1H), 8.23 (ddd, J = 9.1, 8.0, 2.5 Hz, 3H), 7.98 – 7.88 (m, 3H), 7.83 (d, J = 7.5 Hz, 1H), 7.76 – 7.70 (m, 2H), 7.65 (d, J = 5.6 Hz, 1H), 7.58 – 7.52 (m, 1H), 7.19 (dd, J = 7.2, 6.0 Hz, 2H), 7.01 (t, J = 7.2 Hz, 1H), 6.91 (q, J = 7.7 Hz, 2H), 6.79 (t, J = 7.2 Hz, 1H), 6.17 (t, J = 7.0 Hz, 2H), 4.17 (s, 3H). ^{13}C NMR (101 MHz, d_6-DMSO) δ 167.14, 150.36, 150.01, 149.92, 149.59, 149.38, 148.26, 147.10, 144.51, 140.55, 139.27, 139.13, 131.90, 131.38, 130.65, 129.86, 127.39, 125.49, 125.02, 124.33, 124.21, 123.32, 122.82, 122.19, 120.39, 120.31, 39.06. HR-ESI-MS m/z calc. $[M]^+$: 661.1686, found 661.1688.

General synthesis of protected ruthenium complexes

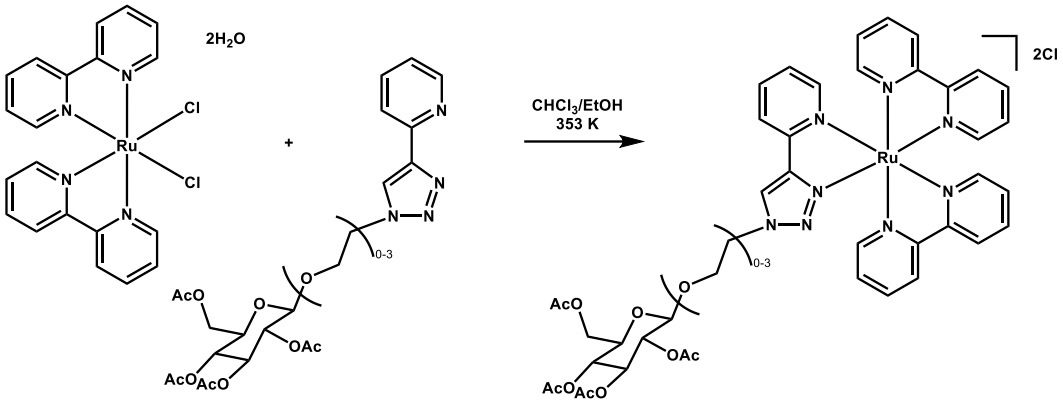

$[Ru(bpy)_2Cl_2].2H_2O$ (1 eq) and ligand (1 eq) were dissolved in 1:1 $CHCl_3$/EtOH solution and refluxed at 353 K overnight. Solution was cooled to room temperature, then solvent removed under reduced pressure. Residue was purified by column chromatography (stationary phase: alumina, mobile phase: 0-5% MeOH gradient in DCM). Relevant fractions were combined and dried under reduced pressure, then residue suspended in ether, sonicated, and dried again to yield product.

$[Ru(bpy)_2(\beta\text{-}Glu(OAc)_4)]Cl_2$ – ***11Ac***

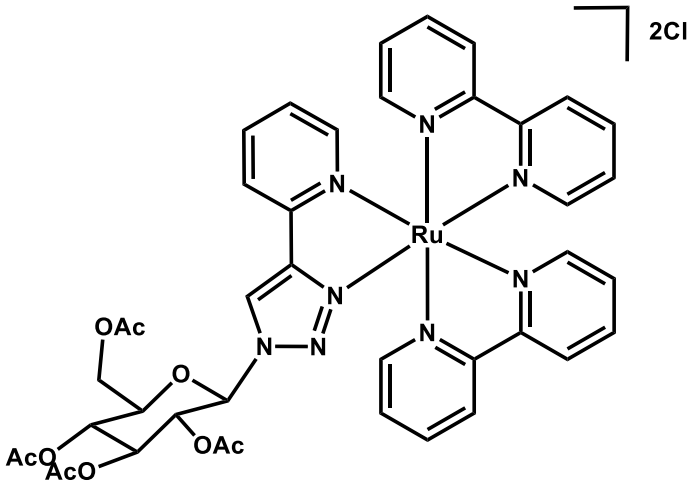

The protected ruthenium β-glucose complex was synthesized using β-glucose ligand (0.092 g, 0.192 mmol) and $[Ru(bpy)_2Cl_2].2H_2O$ (0.100 g, 0.192 mmol) in 10 mL $CHCl_3$/EtOH, yielding a red solid. Yield = 0.1345 g (73%). ^{1}H NMR (400 MHz,

MeOD) δ 9.53 (s, 1H), 9.46 (s, 1H), 8.78 – 8.66 (m, 8H), 8.39 (dd, J = 7.6, 3.5 Hz, 2H), 8.23 – 8.08 (m, 10H), 7.99 – 7.91 (m, 5H), 7.89 – 7.81 (m, 3H), 7.75 (dd, J = 12.1, 5.6 Hz, 2H), 7.62 – 7.51 (m, 6H), 7.50 – 7.41 (m, 4H), 6.21 (d, J = 8.9 Hz, 1H), 6.13 (d, J = 8.9 Hz, 1H), 5.54 – 5.47 (m, 2H), 5.37 (dt, J = 18.1, 9.2 Hz, 2H), 5.25 (t, J = 9.7 Hz, 2H), 4.39 – 4.31 (m, 2H), 4.31 – 4.18 (m, 4H), 2.07 (s, 3H), 2.05 (s, 9H), 2.01 (s, 3H), 1.98 (s, 3H), 1.76 (s, 3H), 1.54 (s, 3H). ^{13}C NMR (101 MHz, MeOD) δ 170.69, 169.82, 169.70, 169.34, 168.70, 157.57, 157.52, 157.45, 157.41, 157.36, 157.11, 157.09, 151.78, 151.68, 151.64, 151.60, 151.57, 151.46, 151.41, 151.38, 150.47, 150.40, 138.38, 138.10, 138.07, 138.04, 137.96, 137.74, 127.65, 127.58, 127.54, 127.50, 126.92, 126.81, 126.40, 126.37, 124.31, 124.28, 124.22, 124.13, 124.03, 123.77, 123.64, 123.04, 122.96, 86.33, 86.24, 74.95, 74.88, 72.00, 71.92, 71.12, 71.02, 67.42, 61.34, 61.30, 19.21, 19.19, 19.08, 19.03, 19.01, 18.99, 18.76. HR-ESI-MS m/z calc. $[M]^{2+}$: 445.0976, found 445.0975.

$[Ru(bpy)_2(PEG1\text{-}\beta\text{-}Glu(OAc)_4)]Cl_2$ – ***12Ac***

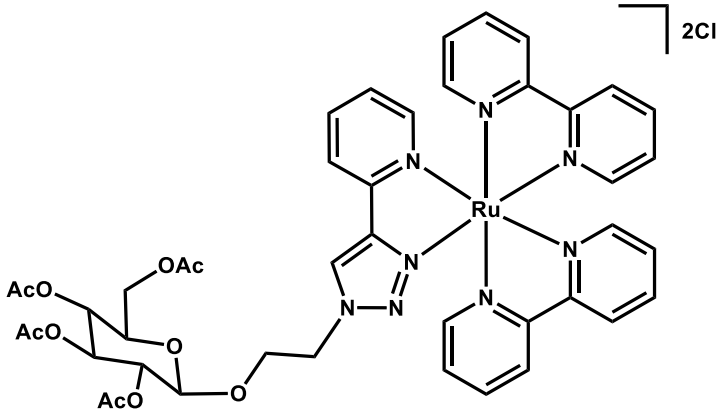

The protected ruthenium PEG1-β-glucose complex was synthesized using PEG1-β-glucose ligand (0.100 g, 0.192 mmol) and $[Ru(bpy)_2Cl_2].2H_2O$ (0.100 g, 0.192 mmol) in 10 mL $CHCl_3$/EtOH , yielding a red oily solid. Yield = 0.1164 g (60%). ^{1}H NMR (400 MHz, d_6-DMSO) δ 9.39 (s, 1H), 9.37 (s, 1H), 8.92 – 8.77 (m, 8H), 8.45 – 8.37 (m, 2H), 8.25 – 8.09 (m, 10H), 7.90 – 7.74 (m, 8H), 7.66 – 7.54 (m, 8H), 7.51 – 7.41 (m, 4H), 5.33 – 5.15 (m, 2H), 4.97 – 4.83 (m, 3H), 4.79 – 4.58 (m, 7H), 4.18 – 3.86 (m, 10H), 1.99 (s, 6H), 1.94 (s, 9H), 1.85 (s, 3H), 1.73 (s, 3H), 1.73 (s, 3H). ^{13}C NMR (126 MHz, d_6-DMSO) δ 170.30, 170.25, 169.86, 169.67,

169.35, 169.25, 157.64, 157.38, 157.37, 157.29, 157.17, 157.08, 151.80, 151.67, 150.85, 147.37, 138.64, 138.17, 137.92, 128.06, 127.33, 126.55, 124.87, 124.55, 124.21, 122.84, 99.95, 99.61, 72.33, 72.20, 71.22, 71.17, 70.98, 68.50, 67.21, 66.46, 62.04, 61.98, 52.25, 20.57, 20.47, 20.43, 20.34. HR-ESI-MS m/z calc. $[M]^{2+}$: 467.1107, found 467.1105.

$[Ru(bpy)_2(PEG2\text{-}\beta\text{-}Glu(OAc)_4)]Cl_2$ – ***13Ac***

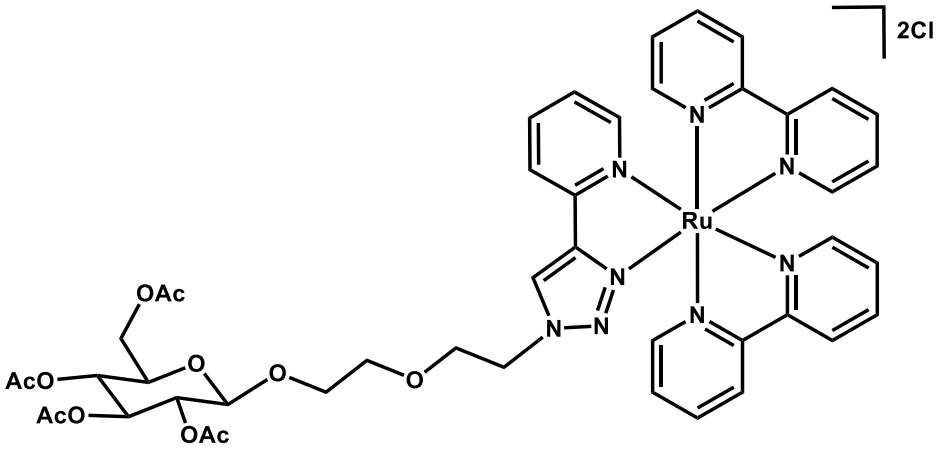

The protected ruthenium PEG1-β-glucose complex was synthesized using PEG2-β-glucose ligand (0.150 g, 0.266 mmol) and $[Ru(bpy)_2Cl_2].2H_2O$ (0.138 g, 0.266 mmol) in 10 mL $CHCl_3$/EtOH , yielding a red oily solid. Yield = 0.2103 g (75%). ^{1}H NMR (400 MHz, d_6-DMSO) δ 9.41 (s, 2H), 8.93 – 8.77 (m, 6H), 8.64 (d, J = 7.8 Hz, 1H), 8.50 (d, J = 7.6 Hz, 1H), 8.45 (d, J = 7.5 Hz, 2H), 8.23 – 8.03 (m, 10H), 7.86 (s, 4H), 7.77 (dd, J = 16.8, 5.2 Hz, 4H), 7.66 – 7.53 (m, 8H), 7.51 – 7.42 (m, 4H), 5.27 (t, J = 9.4 Hz, 2H), 4.91 (t, J = 9.2 Hz, 2H), 4.85 – 4.68 (m, 4H), 4.61 (s, 3H), 4.23 – 4.08 (m, 2H), 4.03 (d, J = 10.2 Hz, 3H), 3.87 – 3.74 (m, 2H), 3.74 – 3.64 (m, 3H), 3.62 – 3.47 (m, 3H), 3.47 – 3.35 (m, 6H), 1.99 (s, 6H), 1.98 (s, 3H), 1.97 (s, 3H), 1.94 (s, 6H), 1.90 (s, 3H), 1.88 (s, 3H). ^{13}C NMR (126 MHz, d_6-DMSO) δ 170.33, 169.94, 169.70, 169.46, 169.44, 157.66, 157.38, 157.33, 157.11, 152.11, 151.94, 151.77, 151.64, 150.91, 147.39, 138.69, 138.23, 138.00, 128.13, 127.46, 127.17, 126.58, 124.92, 124.85, 124.52, 124.25, 123.14, 123.01, 100.08, 72.42, 71.31, 71.06, 69.62, 69.03, 68.63, 68.38, 62.14, 52.14, 20.75, 20.69, 20.60, 20.53, 20.46. HR-ESI-MS m/z calc. $[M]^{2+}$: 489.1238, found 489.1244.

$[Ru(bpy)_2(PEG3\text{-}\beta\text{-}Glu(OAc)_4)]Cl_2$ – ***14Ac***

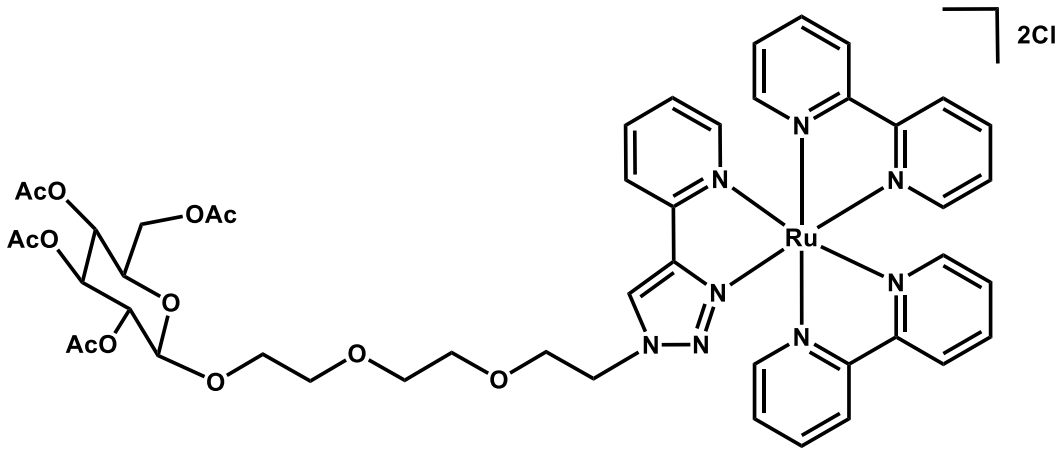

The protected ruthenium PEG3-β-glucose complex was synthesized using PEG3-β-glucose ligand (0.100 g, 0.164 mmol) and $[Ru(bpy)_2Cl_2].2H_2O$ (0.086 g, 0.164 mmol) in 10 mL $CHCl_3$/EtOH , yielding a red oily solid. Yield = 0.1101 g (61%). ^{1}H NMR (400 MHz, d_6-DMSO) δ 9.47 (s, 1H), 9.46 (s, 1H), 8.94 (d, J = 8.0 Hz, 4H), 8.87 (dd, J = 13.6, 8.2 Hz, 4H), 8.48 (d, J = 7.8 Hz, 2H), 8.29 – 8.22 (m, 6H), 8.22 – 8.15 (m, 4H), 7.92 (d, J = 4.9 Hz, 4H), 7.87 – 7.84 (m, 2H), 7.81 (d, J = 5.6 Hz, 2H), 7.68 (d, J = 5.5 Hz, 2H), 7.65 – 7.59 (m, 6H), 7.52 (dt, J = 13.3, 6.8 Hz, 4H), 5.32 (t, J = 9.4 Hz, 2H), 4.95 (td, J = 9.7, 5.7 Hz, 2H), 4.84 (dt, J = 17.5, 8.6 Hz, 4H), 4.70 – 4.63 (m, 4H), 4.28 – 4.15 (m, 2H), 4.11 – 4.02 (m, 4H), 3.90 – 3.73 (m, 6H), 3.67 – 3.60 (m, 2H), 3.54 – 3.37 (m, 12H), 2.05 (s, 9H), 2.03 (s, 3H), 2.01 (s, 3H), 2.00 (s, 9H). ^{13}C NMR (126 MHz, d_6-DMSO) δ 170.38, 170.36, 169.90, 169.67, 169.53, 169.49, 157.67, 157.38, 157.32, 157.12, 152.11, 151.94, 151.75, 151.58, 150.91, 147.36, 138.67, 138.21, 137.95, 128.10, 127.44, 126.54, 124.90, 124.82, 124.51, 124.22, 123.00, 100.10, 72.46, 71.32, 71.09, 70.06, 68.61, 68.35, 62.13, 52.19, 20.69, 20.58, 20.53, 20.47. HR-ESI-MS m/z calc. $[M]^{2+}$: 511.1369, found 511.1369.

3.2.5 Deprotection of sugars

Deprotection method 1

Following an adapted literature protocol,[41] the protected iridium complexes were dissolved in 2 mL methanol and 2 mL water in a glass microwave vessel, and 7

equivalents of triethylamine were added. The vessel was put into a CEM Discovery-SP microwave reactor with the following conditions:

- Time: 8 min
- Temperature: 71 ^{o}C
- Power: 50 W
- Pressure Cut-off: 250 psi

The solvent was then removed under reduced pressure and the crude product was purified by flash reversed-phase chromatography using a Biotage Isolera system equipped with a 10 g C18 SNAP column and water (0.1% TFA) and acetonitrile (0.1% TFA) as the mobile phase.

Column Volumes	**Acetonitrile (0.1% TFA)**
5	10%
25	10-80%
5	80%
5	80-10%

Amberlite IRA400-Cl in 1M HCl was poured into a glass column, the acid was drained, and the stationary phase was washed with 300 mL methanol. Complexes were then converted to their chloride salts by dissolving in minimal methanol and passing through an Amberlite IRA400-Cl ion exchange column with methanol as mobile phase.

[Ir(ppy)$_2$(α-Glu)]Cl – **1**

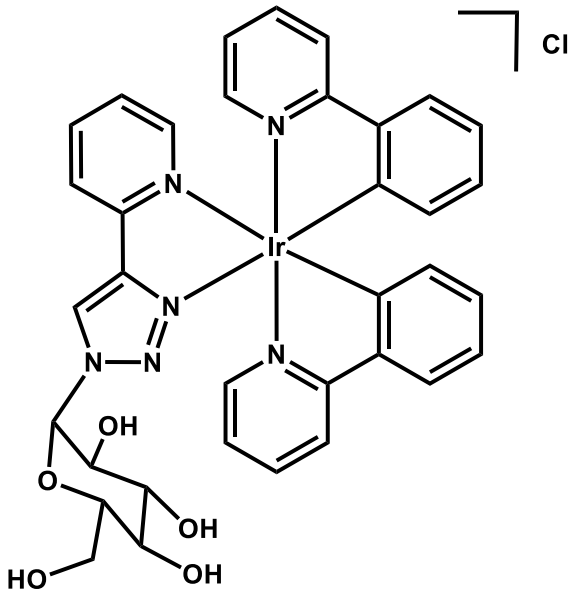

Synthesised using the protected Ir-α-glucose complex (0.050 g, 0.049 mmol) and triethylamine (48 μL, 0.346 mmol). Yield = 0.0280 g (67%). ^{1}H NMR (400 MHz, d_6-DMSO + TFA) δ 9.77 (s, 1H), 9.65 (s, 1H), 8.66 (d, J = 5.4 Hz, 2H), 8.28 – 8.17 (m, 6H), 7.99 – 7.87 (m, 6H), 7.82 (dd, J = 7.2, 3.8 Hz, 2H), 7.73 (t, J = 4.3 Hz, 2H), 7.68 – 7.62 (m, 2H), 7.59 – 7.53 (m, 3H), 7.51 (d, J = 5.4 Hz, 1H), 7.21 – 7.12 (m, 4H), 7.02 (t, J = 7.5 Hz, 2H), 6.92 (q, J = 6.9 Hz, 4H), 6.79 (t, J = 6.8 Hz, 2H), 6.37 (d, J = 5.5 Hz, 2H), 6.21 (dd, J = 7.1, 3.5 Hz, 2H), 6.15 (t, J = 7.2 Hz, 2H), 3.92 – 3.82 (m, 3H), 3.77 (t, J = 8.7 Hz, 1H), 3.59 (d, J = 11.8 Hz, 1H), 3.53 – 3.39 (m, 4H), 3.36 – 3.25 (m, 3H). ^{13}C NMR (176 MHz, d_6-DMSO) δ 167.69, 167.66, 167.25, 167.16, 150.28, 149.99, 149.46, 149.41, 149.38, 149.36, 149.33, 149.18, 148.69, 148.13, 140.50, 140.46, 139.36, 139.30, 139.16, 131.81, 131.39, 130.74, 129.91, 127.58, 125.53, 125.03, 124.42, 124.28, 124.18, 123.80, 123.75, 122.89, 122.26, 120.55, 120.34, 88.49, 88.25, 77.65, 77.25, 73.57, 72.97, 70.24, 70.14, 69.83, 69.58, 69.18, 60.67. ESI-HR-MS m/z calc. $[M]^+$: 809.2058, found 809.2060.

[Ir(ppy)$_2$(α-Man)]Cl – ***2***

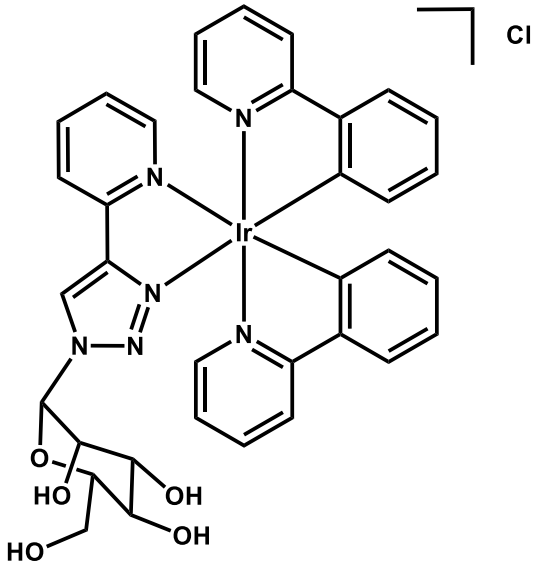

Synthesised using the protected Ir-α-mannose complex (0.050 g, 0.049 mmol) and triethylamine (48 μL, 0.346 mmol). Yield = 0.0220 g (53%). ^{1}H NMR (400 MHz, d_6-DMSO + TFA) δ 9.78 (s, 1H), 9.69 (s, 1H), 8.49 (dd, J = 12.5, 7.9 Hz, 2H), 8.27 – 8.15 (m, 6H), 7.97 – 7.85 (m, 6H), 7.82 (d, J = 7.6 Hz, 2H), 7.73 (t, J = 5.6 Hz, 2H), 7.69 (d, J = 5.8 Hz, 1H), 7.65 (t, J = 6.4 Hz, 2H), 7.59 (d, J = 5.8 Hz, 1H), 7.57 – 7.51 (m, 2H), 7.21 – 7.11 (m, 4H), 7.01 (t, J = 7.5 Hz, 2H), 6.95 – 6.86 (m, 4H), 6.79 (t, J = 7.4 Hz, 2H), 6.17 (t, J = 6.5 Hz, 4H), 5.95 (dd, J = 7.0, 2.8 Hz, 2H), 4.28 – 4.20 (m, 2H), 3.82 – 3.64 (m, 6H), 3.62 – 3.58 (m, 1H), 3.58 – 3.50 (m, 3H). ^{13}C NMR (176 MHz, d_6-DMSO) δ 167.69, 167.62, 167.16, 167.10, 150.11, 150.09, 149.99, 149.71, 149.58, 149.46, 149.42, 149.38, 149.14, 148.56, 146.89, 146.85, 144.54, 144.45, 140.58, 139.34, 139.20, 139.16, 131.89, 131.85, 131.37, 131.26, 130.70, 129.98, 129.89, 127.64, 127.59, 125.50, 125.09, 124.43, 124.35, 124.28, 124.17, 123.46, 122.90, 122.27, 120.48, 120.40, 120.36, 86.94, 86.64, 81.63, 80.97, 71.83, 71.67, 68.87, 68.49, 68.24, 67.88, 60.16, 60.07. ESI-HR-MS m/z calc. $[M]^+$: 809.2058, found 809.2064.

[Ir(ppy)$_2$(α-Gal)]Cl – ***3***

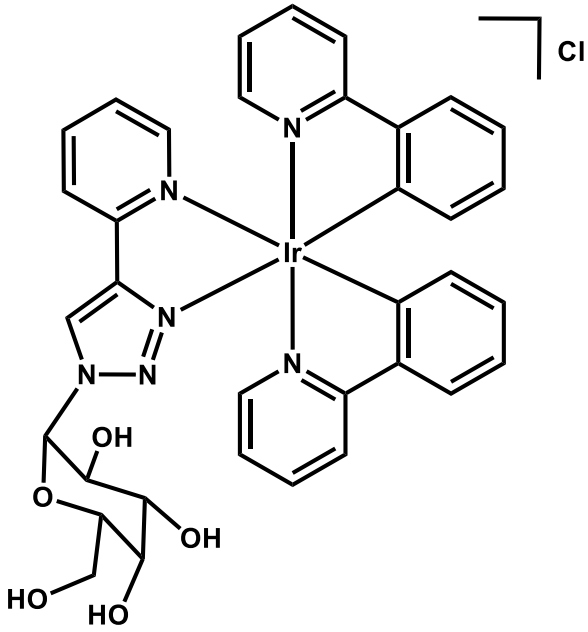

Synthesised using the protected Ir-α-galactose complex in 2 batches (2 × 0.050 g, 0.098 mmol) and triethylamine (2 × 48 μL, 0.692 mmol). Crude products were combined before purification. Yield = 0.0713 g (85%). ^{1}H NMR (400 MHz, d_6-DMSO + TFA) δ 9.70 (s, 1H), 9.57 (s, 1H), 8.58 – 8.51 (m, 2H), 8.26 – 8.16 (m, 6H), 7.97 – 7.86 (m, 6H), 7.85 – 7.80 (m, 2H), 7.76 – 7.72 (m, 2H), 7.69 – 7.63 (m, 2H), 7.60 – 7.53 (m, 3H), 7.46 (d, J = 5.6 Hz, 1H), 7.19 – 7.11 (m, 4H), 7.02 (t, J = 7.4 Hz, 2H), 6.92 (q, J = 7.8 Hz, 4H), 6.80 (t, J = 6.2 Hz, 2H), 6.40 – 6.34 (m, 2H), 6.19 (dt, J = 16.5, 8.2 Hz, 4H), 4.15 – 4.06 (m, 2H), 3.98 – 3.81 (m, 5H), 3.60 – 3.47 (m, 5H). ^{13}C NMR (176 MHz, d_6-DMSO) δ 167.68, 167.64, 167.25, 167.17, 150.30, 150.25, 150.03, 149.46, 149.44, 149.34, 149.13, 148.64, 147.99, 146.84, 144.48, 144.46, 144.43, 140.57, 140.50, 139.35, 139.28, 139.18, 139.17, 131.84, 131.79, 131.43, 131.32, 130.74, 130.69, 129.92, 129.87, 127.58, 127.54, 125.53, 125.05, 125.00, 124.41, 124.33, 124.23, 124.19, 123.62, 123.50, 122.89, 122.26, 120.52, 120.50, 120.40, 120.33, 88.22, 87.88, 77.55, 76.61, 69.77, 69.72, 68.00, 67.56, 67.54, 67.14, 60.43, 59.94. ESI-HR-MS m/z calc. $[M]^+$: 809.2058, found 809.2052.

[Ir(ppy)$_2$(β-Glu)]Cl - ***4***

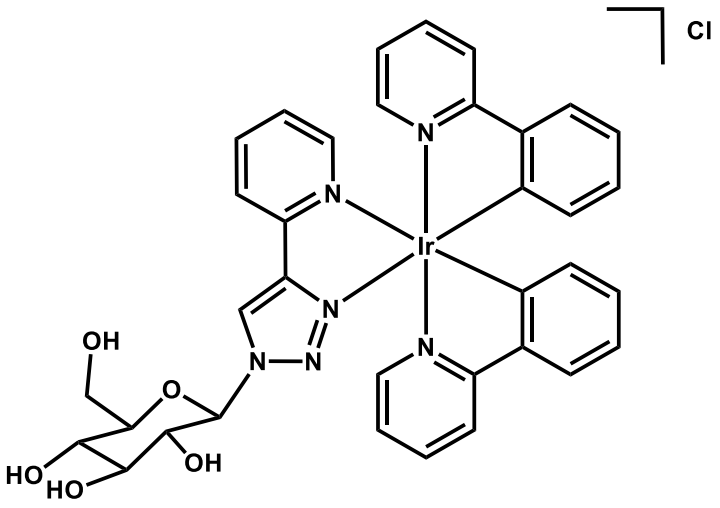

Synthesised using the protected Ir-β-glucose complex (0.120 g, 0.118 mmol) and triethylamine (115 μL, 0.83 mmol). Yield = 0.0784 g (79%). ^{1}H NMR (400 MHz, d_6-DMSO + TFA) δ 9.83 (s, 1H), 9.74 (s, 1H), 8.41 (d, J = 7.9 Hz, 2H), 8.24 – 8.20 (m, 6H), 7.96 – 7.91 (m, 4H), 7.88 (d, J = 7.6 Hz, 2H), 7.82 (d, J = 7.5 Hz, 2H), 7.75 (d, J = 5.0 Hz, 1H), 7.72 (d, J = 5.1 Hz, 1H), 7.67 (d, J = 5.8 Hz, 1H), 7.64 (d, J = 5.7 Hz, 1H), 7.62 – 7.53 (m, 4H), 7.24 – 7.12 (m, 4H), 7.01 (t, J = 7.5 Hz, 2H), 6.95 – 6.86 (m, 4H), 6.83 – 6.76 (m, 2H), 6.20 (d, J = 7.6 Hz, 2H), 6.14 (dd, J = 7.2, 2.2 Hz, 2H), 5.75 (t, J = 8.7 Hz, 2H), 3.74 – 3.57 (m, 4H), 3.57 – 3.35 (m, 6H), 3.27 (dt, J = 14.7, 9.2 Hz, 2H). ^{13}C NMR (176 MHz, d_6-DMSO) δ 167.64, 167.61, 167.15, 167.09, 150.14, 149.87, 149.68, 149.50, 149.39, 149.33, 149.25, 149.18, 148.68, 146.77, 146.75, 144.52, 144.48, 144.44, 144.41, 140.69, 140.65, 139.39, 139.23, 131.89, 131.34, 131.21, 130.73, 129.99, 129.97, 127.72, 125.53, 125.16, 125.09, 124.56, 124.31, 123.46, 123.30, 122.97, 122.90, 122.33, 122.30, 120.54, 120.49, 120.41, 89.46, 89.16, 80.77, 80.40, 76.85, 76.21, 73.73, 72.92, 69.88, 69.78, 60.92, 60.82, 45.82. ESI-HR-MS m/z calc. $[M]^+$: 809.2058, found 809.2067.

[Ir(ppy)$_2$(β-Man)]Cl – ***5***

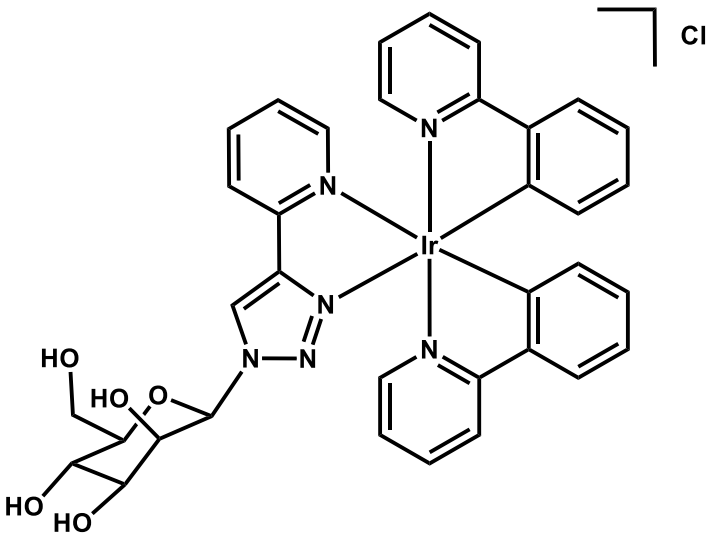

Synthesised using the protected Ir-β-mannose complex (0.050 g, 0.049 mmol) and triethylamine (48 μL, 0.346 mmol). Yield = 0.0280 g (67%). ^{1}H NMR (400 MHz, d_6-DMSO + TFA) δ 9.59 (s, 1H), 9.58 (s, 1H), 8.62 (d, J = 8.0 Hz, 2H), 8.25 – 8.14 (m, 6H), 7.96 – 7.86 (m, 6H), 7.81 (d, J = 7.7 Hz, 2H), 7.72 (d, J = 5.5 Hz, 2H), 7.69 (d, J = 5.7 Hz, 1H), 7.66 (d, J = 5.8 Hz, 2H), 7.61 (d, J = 5.6 Hz, 1H), 7.52 (t, J = 6.4 Hz, 2H), 7.25 – 7.12 (m, 4H), 7.00 (t, J = 7.3 Hz, 2H), 6.94 – 6.86 (m, 4H), 6.78 (t, J = 7.3 Hz, 2H), 6.22 – 6.13 (m, 6H), 4.01 (d, J = 2.0 Hz, 1H), 3.81 (d, J = 10.8 Hz, 1H), 3.74 (d, J = 10.6 Hz, 1H), 3.68 (d, J = 2.4 Hz, 1H), 3.61 – 3.37 (m, 8H). ^{13}C NMR (176 MHz, d_6-DMSO) δ 167.65, 167.13, 162.78, 150.28, 150.11, 149.99, 149.87, 149.52, 149.49, 149.32, 148.07, 148.03, 146.99, 146.89, 144.57, 144.51, 144.43, 140.58, 139.34, 139.22, 139.18, 131.89, 131.38, 131.24, 130.71, 129.92, 127.51, 125.52, 125.08, 125.06, 124.54, 124.45, 124.36, 124.30, 124.26, 123.50, 122.90, 122.27, 120.50, 120.47, 120.36, 120.31, 87.69, 81.06, 80.88, 72.94, 72.91, 70.56, 70.46, 66.55, 66.52, 61.50, 61.39, 40.47, 40.36, 40.24, 36.26. ESI-HR-MS m/z calc. $[M]^+$: 809.2058, found 809.2056.

[Ir(ppy)$_2$(β-Gal)]Cl – ***6***

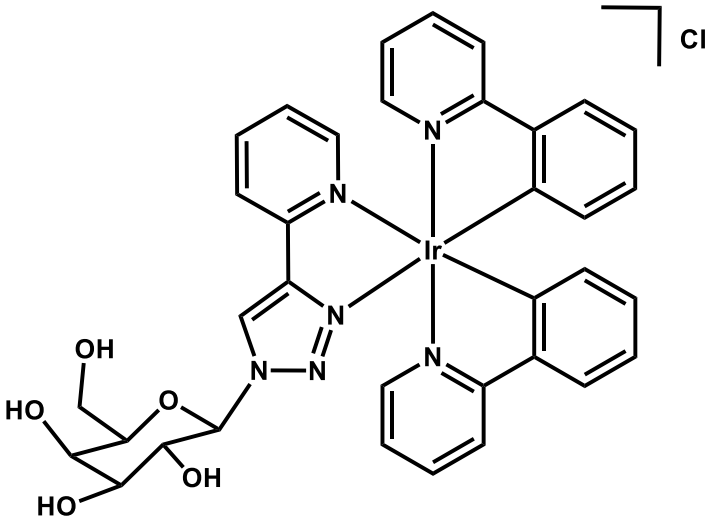

Synthesised using the protected Ir-β-galactose complex (0.050 g, 0.049 mmol) and triethylamine (48 μL, 0.346 mmol). Yield = 0.0222 g (53%). ^{1}H NMR (400 MHz, d_6-DMSO + TFA) δ 9.82 (s, 1H), 9.73 (s, 1H), 8.51 (dd, J = 18.9, 8.0 Hz, 2H), 8.26 – 8.18 (m, 6H), 7.98 – 7.91 (m, 4H), 7.89 (d, J = 7.7 Hz, 2H), 7.82 (d, J = 7.8 Hz, 2H), 7.75 (d, J = 5.5 Hz, 1H), 7.72 (d, J = 5.4 Hz, 1H), 7.68 (d, J = 5.7 Hz, 1H), 7.64 (d, J = 5.8 Hz, 1H), 7.63 – 7.59 (m, 2H), 7.59 – 7.52 (m, 2H), 7.25 – 7.11 (m, 4H), 7.01 (t, J = 7.5 Hz, 2H), 6.97 – 6.86 (m, 4H), 6.79 (dd, J = 12.5, 7.1 Hz, 2H), 6.20 (d, J = 7.4 Hz, 2H), 6.14 (d, J = 7.0 Hz, 2H), 5.68 (dd, J = 13.1, 9.1 Hz, 2H), 4.03 – 3.89 (m, 2H), 3.81 – 3.73 (m, 4H), 3.59 – 3.44 (m, 6H). ^{13}C NMR (176 MHz, d_6-DMSO) δ 167.65, 167.17, 167.09, 150.26, 150.05, 149.96, 149.69, 149.51, 149.47, 149.45, 149.41, 149.34, 149.28, 148.72, 146.78, 144.48, 140.61, 139.36, 139.22, 131.89, 131.36, 131.24, 130.72, 129.98, 127.67, 125.52, 125.20, 125.07, 124.54, 124.27, 123.48, 122.88, 122.28, 120.43, 90.15, 89.84, 79.39, 79.24, 73.72, 73.20, 70.79, 69.94, 68.60, 60.71, 60.67. ESI-HR-MS m/z calc. $[M]^+$: 809.2058, found 809.2065.

$[Ru(bpy)_2(\beta\text{-Glu})]Cl_2$ – ***11***

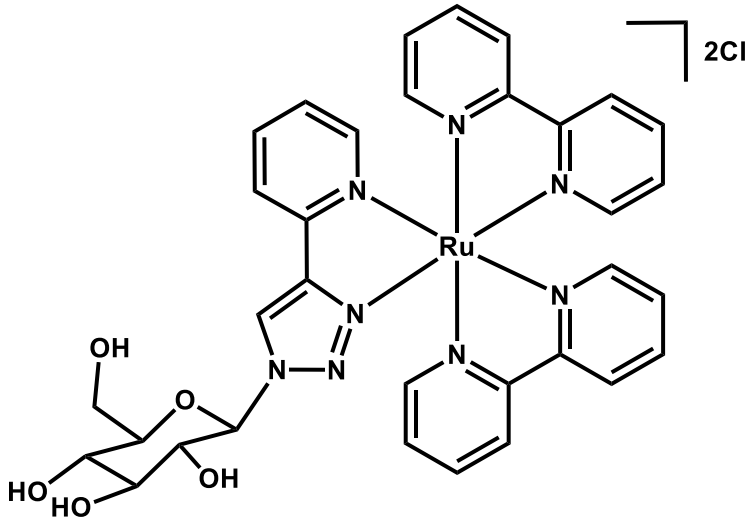

Synthesised using the protected Ru-β-glucose complex (0.0815 g, 0.071 mmol) and triethylamine (69.5 μL, 0.50 mmol). Yield = 0.0330 g (80%). ^{1}H NMR (400 MHz, d_6-DMSO + TFA) δ 9.83 (s, 1H), 9.74 (s, 1H), 8.86 – 8.71 (m, 8H), 8.36 (dd, J = 7.4, 3.0 Hz, 2H), 8.19 – 8.05 (m, 10H), 7.88 (d, J = 5.6 Hz, 1H), 7.84 (d, J = 5.3 Hz, 1H), 7.81 (d, J = 5.4 Hz, 1H), 7.78 – 7.69 (m, 5H), 7.64 (d, J = 5.3 Hz, 1H), 7.61 – 7.48 (m, 7H), 7.47 – 7.38 (m, 4H), 5.65 (t, J = 8.9 Hz, 2H), 3.72 – 3.53 (m, 4H), 3.53 – 3.33 (m, 6H), 3.24 (dt, J = 17.9, 9.0 Hz, 2H). ^{13}C NMR (176 MHz, d_6-DMSO) δ 157.59, 157.55, 157.36, 157.22, 157.18, 157.02, 152.29, 152.27, 152.05, 151.98, 151.96, 151.90, 151.85, 151.79, 151.79, 151.72, 151.66, 150.73, 150.67, 148.33, 147.89, 139.01, 139.00, 138.51, 138.50, 138.44, 138.24, 138.16, 128.52, 128.46, 128.44, 128.38, 127.77, 127.69, 126.96, 126.93, 125.05, 125.01, 124.93, 124.89, 124.81, 124.52, 123.18, 123.07, 89.44, 89.01, 80.61, 80.34, 76.65, 76.13, 73.73, 72.98, 69.79, 60.88, 34.51. ESI-HR-MS m/z calc. $[M]^{2+}$: 361.0764, found 361.0767.

Deprotection method 2

40-50 mg of protected iridium/ruthenium PEG complexes were dissolved in 10 mL methanol, then 2 mL sodium methoxide solution (0.1M in methanol) was added and solutions stirred at room temperature for 1.5 h. Complete deprotection was observed

by mass spectrometry. Samples were then neutralised with DOWEX H^+ resin, stirred for 2 minutes, then filtered and solvent removed on a rotary evaporator.

*[Ir(ppy)$_2$(PEG1-β-Glu)]Cl – **7***

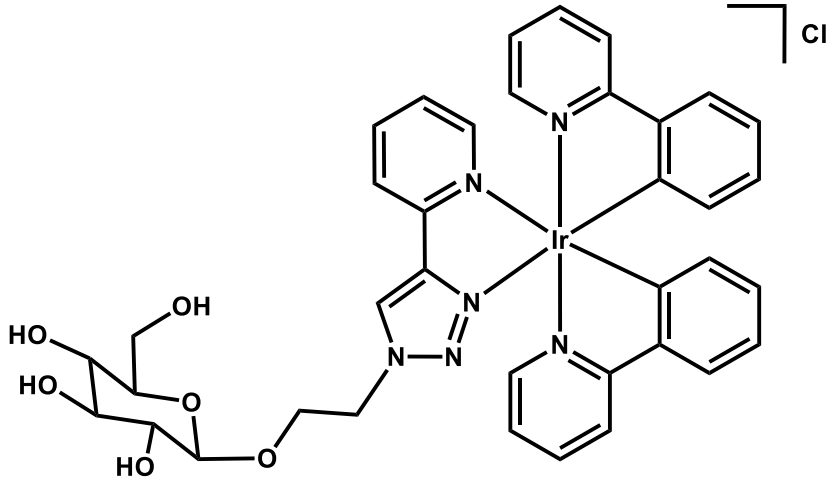

Synthesised using the protected Ir-PEG1-β-glucose complex (0.050 g, 0.047 mmol). Yield = 0.0385 g (92%). ^{1}H NMR (400 MHz, d$_6$-DMSO + TFA) δ 9.43 (s, 1H), 9.38 (s, 1H), 8.35 (d, J = 7.7 Hz, 2H), 8.20 – 8.10 (m, 6H), 7.91 – 7.80 (m, 8H), 7.77 (d, J = 7.7 Hz, 2H), 7.71 (t, J = 7.2 Hz, 3H), 7.65 (d, J = 5.5 Hz, 1H), 7.62 (d, J = 5.7 Hz, 2H), 7.51 – 7.43 (m, 2H), 7.24 – 7.06 (m, 4H), 6.98 (t, J = 7.5 Hz, 2H), 6.92 – 6.83 (m, 4H), 6.76 (t, J = 7.3 Hz, 2H), 6.17 (d, J = 7.6 Hz, 4H), 4.81 – 4.55 (m, 4H), 4.22 (d, J = 7.8 Hz, 1H), 4.19 – 4.08 (m, 2H), 4.01 – 3.92 (m, J = 8.2 Hz, 1H), 3.92 – 3.83 (m, 1H), 3.67 (dd, J = 10.3, 5.1 Hz, 1H), 3.49 – 3.38 (m, 2H), 3.21 – 2.94 (m, 8H). ^{13}C NMR (176 MHz, d$_6$-DMSO) δ 167.71, 167.69, 167.14, 167.10, 150.30, 150.26, 149.99, 149.91, 149.76, 149.64, 149.62, 149.42, 149.39, 148.28, 148.18, 147.08, 147.06, 144.51, 140.46, 139.25, 139.14, 131.90, 131.33, 130.68, 129.90, 127.41, 125.49, 125.04, 124.48, 124.45, 124.23, 123.33, 123.27, 122.85, 122.21, 120.43, 120.39, 120.32, 103.12, 103.03, 77.48, 77.43, 76.99, 73.67, 70.44, 66.84, 61.50, 52.20, 40.48. ESI-HR-MS m/z calc. $[M]^+$: 853.2320, found 853.2345.

[Ir(ppy)$_2$(PEG2-β-Glu)]Cl – ***8***

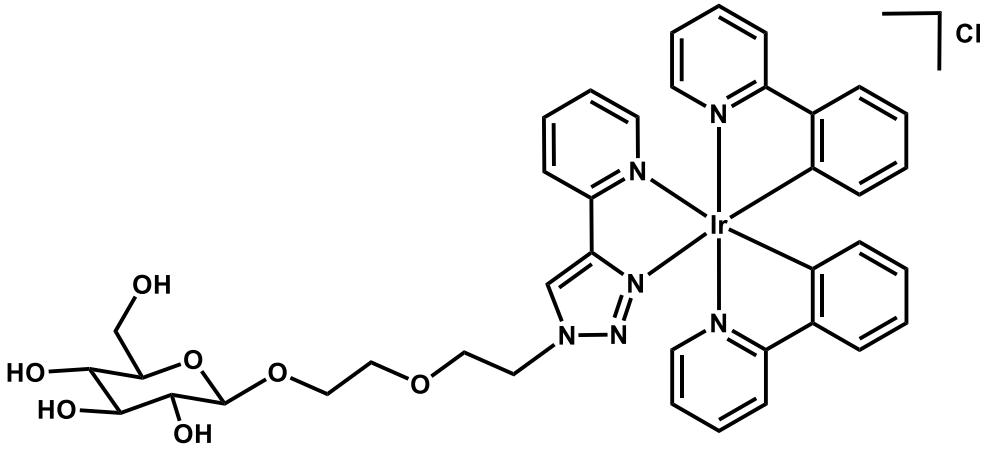

Synthesised using the protected Ir-PEG2-β-glucose complex (0.050 g, 0.045 mmol). Yield = 0.0310 g (73%). ^{1}H NMR (400 MHz, d_6-DMSO + TFA) δ 9.31 (s, 2H), 8.44 (d, J = 7.5 Hz, 2H), 8.24 – 8.12 (m, 6H), 7.95 – 7.84 (m, 6H), 7.81 (d, J = 7.6 Hz, 2H), 7.72 (d, J = 5.3 Hz, 2H), 7.69 – 7.60 (m, 4H), 7.55 – 7.47 (m, 2H), 7.23 – 7.10 (m, 4H), 7.00 (t, J = 7.4 Hz, 2H), 6.96 – 6.84 (m, 4H), 6.78 (t, J = 7.3 Hz, 2H), 6.24 – 6.12 (m, 4H), 4.71 – 4.61 (m, 4H), 4.17 (dd, J = 7.7, 2.0 Hz, 2H), 3.93 – 3.73 (m, 6H), 3.68 (d, J = 11.8 Hz, 2H), 3.59 – 3.36 (m, 8H), 3.21 – 3.02 (m, 6H), 2.97 (t, J = 8.3 Hz, 2H). ^{13}C NMR (176 MHz, d_6-DMSO) δ 167.70, 167.18, 150.33, 150.02, 149.66, 149.57, 149.52, 149.37, 148.33, 147.06, 144.53, 144.48, 140.53, 139.30, 139.16, 139.13, 131.88, 131.39, 130.69, 129.89, 127.43, 125.51, 125.03, 124.42, 124.36, 124.22, 124.19, 123.48, 123.37, 122.85, 122.22, 120.47, 120.29, 104.38, 103.39, 100.13, 77.40, 77.19, 73.94, 73.84, 73.09, 72.60, 72.44, 70.78, 70.47, 69.91, 68.31, 61.46, 60.48, 52.19, 40.48. ESI-HR-MS m/z calc. $[M]^+$: 897.2582, found 897.2604.

[Ir(ppy)$_2$(PEG3-β-Glu)]Cl – ***9***

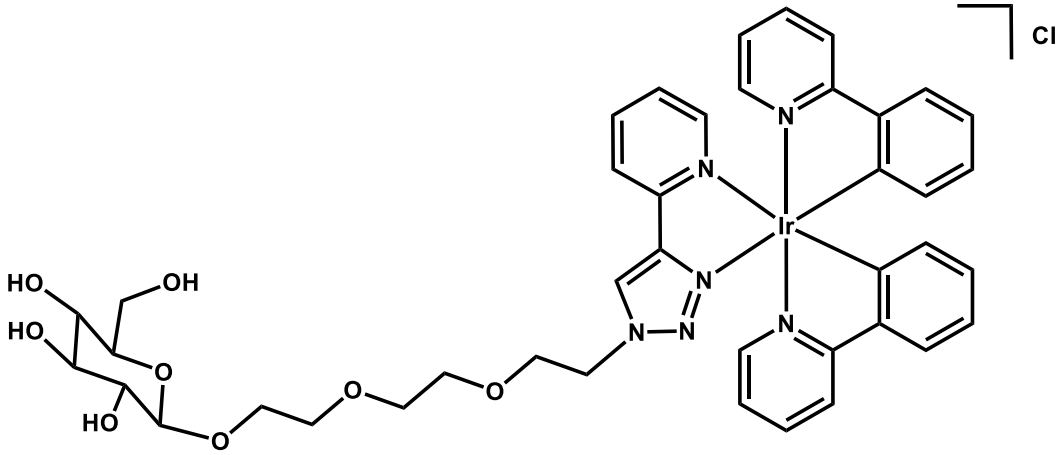

Synthesised using the protected Ir-PEG3-β-glucose complex (0.050 g, 0.044 mmol). Yield = 0.0376 g (88%). ^{1}H NMR (400 MHz, d$_6$-DMSO + TFA) δ 9.37 – 9.32 (m, 2H), 8.44 (d, J = 6.7 Hz, 2H), 8.27 – 8.15 (m, 6H), 7.97 – 7.85 (m, 6H), 7.82 (d, J = 6.9 Hz, 2H), 7.72 (d, J = 5.2 Hz, 2H), 7.67 – 7.61 (m, 4H), 7.57 – 7.50 (m, 2H), 7.21 – 7.13 (m, 4H), 7.01 (t, J = 7.2 Hz, 2H), 6.95 – 6.86 (m, 4H), 6.79 (t, J = 7.4 Hz, 2H), 6.17 (dd, J = 11.6, 7.6 Hz, 4H), 4.67 (t, J = 4.6 Hz, 4H), 4.14 (d, J = 7.7 Hz, 1H), 3.90 – 3.75 (m, 5H), 3.67 (d, J = 10.3 Hz, 2H), 3.57 – 3.31 (m, 18H), 3.10 (dt, J = 18.4, 10.5 Hz, 6H), 2.95 (t, J = 8.2 Hz, 2H). ^{13}C NMR (176 MHz, d$_6$-DMSO) δ 167.68, 167.18, 150.36, 150.02, 149.60, 149.52, 149.36, 148.27, 147.05, 144.53, 144.47, 140.58, 139.34, 139.16, 131.87, 131.41, 130.69, 129.89, 127.74, 127.44, 125.52, 125.03, 124.36, 124.21, 123.39, 122.85, 122.23, 120.48, 120.29, 103.38, 103.36, 77.38, 77.25, 73.86, 72.73, 70.49, 70.47, 70.10, 70.08, 69.92, 68.36, 68.25, 68.23, 61.50, 60.61, 52.18, 40.48, 40.36, 40.24. ESI-HR-MS m/z calc. $[M]^+$: 941.2844, found 941.2873.

$[Ru(bpy)_2(PEG1\text{-}\beta\text{-}Glu)]Cl_2$ – ***12***

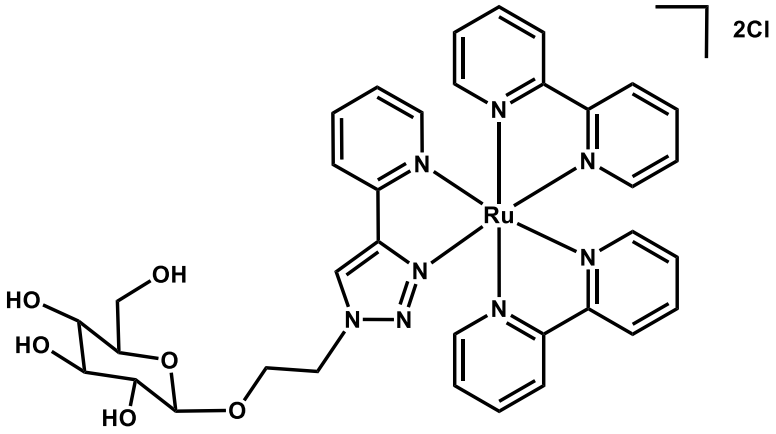

Synthesised using the protected Ru-PEG1-β-glucose complex (0.042 g, 0.042 mmol). Yield = 0.0261 g (75%). ^{1}H NMR (400 MHz, d_6-DMSO + TFA) δ 9.46 (s, 1H), 9.40 (s, 1H), 8.82 – 8.68 (m, 8H), 8.33 (d, J = 7.6 Hz, 2H), 8.16 – 8.01 (m, 10H), 7.88 – 7.71 (m, 8H), 7.62 – 7.45 (m, 8H), 7.45 – 7.31 (m, 4H), 4.69 – 4.54 (m, 4H), 4.13 (dt, J = 17.7, 9.1 Hz, 4H), 3.97 – 3.88 (m, 1H), 3.86 – 3.78 (m, 1H), 3.66 (dd, J = 10.9, 3.5 Hz, 2H), 3.47 – 3.37 (m, 2H), 3.21 – 3.03 (m, J = 24.3, 16.7, 8.4 Hz, 6H), 2.97 (dt, J = 16.5, 8.3 Hz, 2H). ^{13}C NMR (176 MHz, d_6-DMSO) δ 157.65, 157.44, 157.27, 157.02, 152.21, 151.90, 151.63, 150.99, 147.36, 147.26, 138.81, 138.33, 138.10, 128.37, 128.32, 127.63, 126.65, 125.00, 124.91, 124.88, 124.74, 124.71, 124.39, 123.11, 123.06, 103.17, 103.06, 77.44, 77.01, 73.68, 70.41, 66.80, 61.47, 52.34, 40.48. ESI-HR-MS m/z calc. $[M]^{2+}$: 383.0895, found 383.0895.

[Ru(bpy)$_2$(PEG2-β-Glu)]Cl$_2$ – ***13***

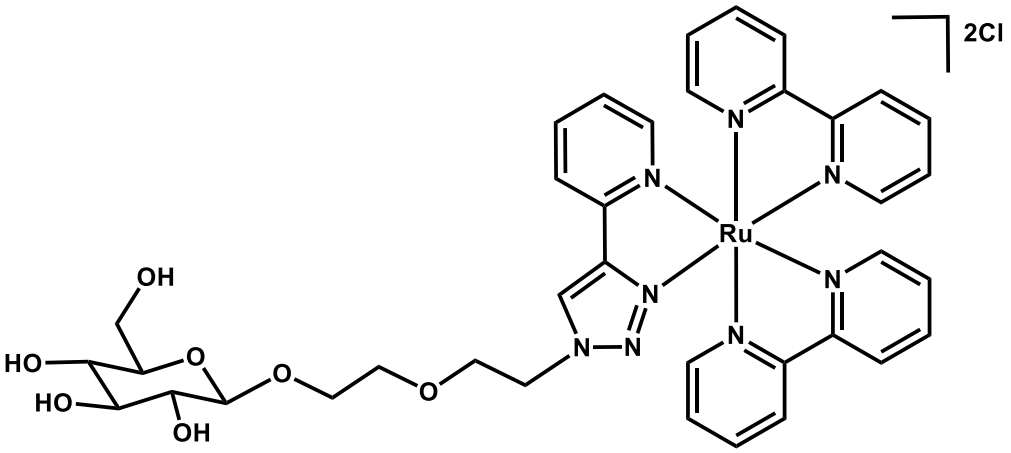

Synthesised using the protected Ru-PEG2-β-glucose complex (0.050 g, 0.048 mmol). Yield = 0.0330 g (79%). ^{1}H NMR (400 MHz, d$_6$-DMSO + TFA) δ 9.36 (s, J = 30.2 Hz, 2H), 8.92 – 8.71 (m, 8H), 8.41 (d, J = 7.3 Hz, 2H), 8.27 – 8.03 (m, 10H), 7.85 (d, J = 5.0 Hz, 4H), 7.83 – 7.77 (m, 2H), 7.74 (d, J = 5.3 Hz, 2H), 7.66 – 7.49 (m, 8H), 7.48 – 7.33 (m, 4H), 4.60 (s, 4H), 4.15 (dd, J = 7.6, 5.5 Hz, 2H), 3.88 – 3.77 (m, 2H), 3.77 – 3.61 (m, 6H), 3.50 – 3.30 (m, 8H), 3.20 – 3.02 (m, 6H), 2.95 (td, J = 8.4, 3.3 Hz, 2H). ^{13}C NMR (176 MHz, d$_6$-DMSO) δ 157.68, 157.40, 157.29, 157.09, 152.19, 152.01, 151.90, 151.84, 151.66, 150.94, 150.89, 147.38, 138.86, 138.35, 138.12, 128.32, 127.62, 126.69, 125.02, 124.95, 124.67, 124.37, 123.22, 123.14, 103.37, 97.37, 77.41, 77.22, 73.96, 72.55, 70.73, 70.43, 69.83, 68.28, 61.42, 60.43, 52.28, 40.48. ESI-HR-MS m/z calc. $[M]^{2+}$: 405.1026, found 405.1024.

[Ru(bpy)$_2$(PEG3-β-Glu)]Cl$_2$ – ***14***

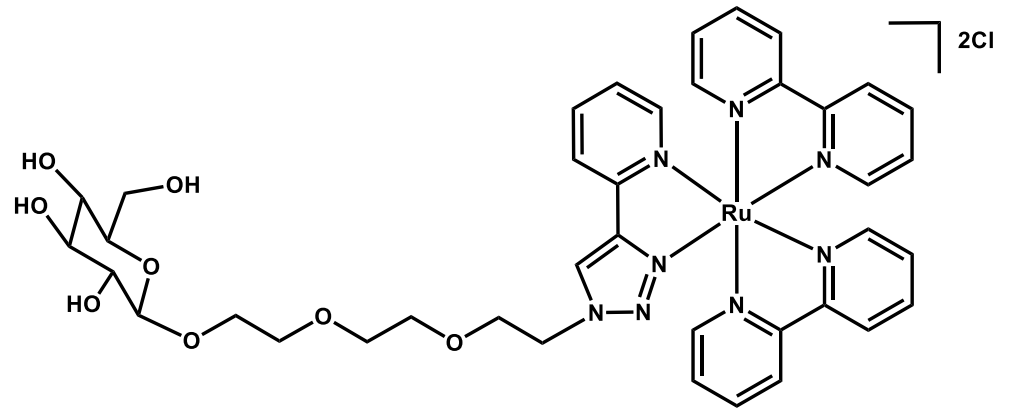

Synthesised using the protected Ru-PEG3-β-glucose complex (0.050 g, 0.046 mmol). Yield = 0.0256 g (61%). ^{1}H NMR (400 MHz, d_6-DMSO + TFA) δ 9.34 (s, 2H), 8.85 – 8.70 (m, 8H), 8.38 (d, J = 7.8 Hz, 2H), 8.18 – 8.03 (m, 10H), 7.85 (s, 4H), 7.79 (d, J = 5.3 Hz, 2H), 7.73 (d, J = 5.5 Hz, 2H), 7.60 (d, J = 5.3 Hz, 2H), 7.57 – 7.46 (m, 6H), 7.46 – 7.33 (m, 4H), 4.59 (s, 4H), 4.15 (d, J = 7.7 Hz, 2H), 3.85 – 3.76 (m, 4H), 3.74 – 3.63 (m, 4H), 3.55 – 3.27 (m, 17H), 3.20 – 3.04 (m, 5H), 2.96 (t, J = 8.4 Hz, 2H). ^{13}C NMR (176 MHz, d_6-DMSO) δ 157.69, 157.40, 157.27, 157.10, 152.19, 152.04, 151.85, 151.68, 150.89, 147.38, 147.32, 138.91, 138.38, 138.15, 128.31, 127.63, 126.70, 125.03, 124.96, 124.66, 124.36, 123.13, 103.37, 103.34, 97.37, 92.68, 77.39, 77.26, 77.22, 75.29, 73.89, 72.72, 70.45, 70.08, 70.00, 69.96, 69.89, 68.38, 68.26, 68.23, 61.64, 61.45, 60.60, 52.29, 40.48. ESI-HR-MS m/z calc. $[M]^{2+}$: 427.1157, found 427.1150.

Novel complexes that were determined to be pure by NMR and HPLC were sent for elemental analysis externally, however, results often varied even for the same batch of compound. For example, **4Ac** calcd. C: 51.01 H: 3.98 N: 8.30, results: C 34.94 / 44.95, H: 2.80 / 3.72, N: 5.67 / 7.31. Therefore, elemental analyses are not included in the characterisation of these complexes. The inconsistencies in elemental analysis were recently reviewed by Proctor *et al*.[42]

3.2.6 X-ray crystallography

Single crystals of $C_{14}H_{19}N_3O_9$ were grown from DMSO and DMPU at 277 K. X-ray crystallography was carried out by Dr Guy Clarkson (University of Warwick) as described in **Chapter 2**, **Section 2.2.3**.

3.2.7 Density functional theory (DFT)

All computations were performed by Dr. Fortuna Ponte and Prof. Emilia Sicilia (University of Calabria, Italy). DFT and time dependent DFT levels of theory were implemented in the Gaussian 16 program code.[43]

Ground singlet state optimizations were carried out in water by using the B3LYP exchange-correlation functional (XC)[44,45] and adopting the SMD continuum

solvation model as implemented in Gaussian 16 to reproduce the solvent environment (ε = 80).

The def2QZVP effective core potential[46] and the corresponding split valence basis set were used to describe the metal ions, Os, Ru and Ir. The 6-311G* standard basis set of Pople were employed for the atoms directly bound to the metal, while, for reducing the computational effort, the 6-31G** basis set was employed to describe the rest of the atoms.

Molecular orbital (MO) calculations were performed on the investigated systems and the corresponding structures were plotted.

UV−vis spectra for each complex were calculated in water as vertical electronic excitations on the ground-state structures, at the TD-DFT level adopting the B3LYP XC functional in conjunction with the same basis set used for the optimization. Such a protocol was established through the comparison of the calculated maximum absorption wavelength for the compounds under investigation and the available experimental values. Vertical excitation energies, maximum absorption wavelengths, oscillator strengths, and molecular orbital (MO) contributions for singlet excitations were reported for each investigated system.

To simplify the description of the nature of the MOs participating in the calculated transitions occurring between an excited particle and an empty hole, natural transition orbitals (NTOs) were also provided.

The spin−orbit matrix elements were calculated at the S0 optimized geometries of the investigated systems using DALTON code.[47]

The approximate one-electron spin−orbit operator with scaled nuclear charges was used for the complexes under investigation.[48]

B3LYP combined with the cc-pVDZ basis set was chosen to describe all atoms, while the SDD pseudopotential was used for metal ions.

The SOC values were obtained according to the following formula:

$$SOC_{nm} = \sqrt{\sum_i \left|\langle \psi_{S_n} | \hat{H}_{SO} | \psi_{T_{i,m}} \rangle\right|^2}; \qquad i = x, y, z \qquad \textbf{Equation 3.7}$$

where HSO is the spin–orbit Hamiltonian.

3.2.8 Solution and photo-stability

Solution stability by UV-vis

Complexes (1-2 mg) were dissolved in DMSO to form initial solutions of concentrations of *ca*. 1 mM. DMSO stocks were diluted 1-in-20 with solvent (DMSO, PBS, RPMI-1640 (no phenol red) or acetonitrile) to reduce the amount of DMSO to 5% (except in DMSO only case). Solutions were further diluted if needed to keep absorbance maxima below 1, then scanned from 800-200 nm. Samples were then incubated at 310 K for 24 h and scanned again. Baselines of solvent only were prepared identically and recorded in the same cuvette.

Photostability in acetonitrile by UV-vis

Solutions were prepared by dissolving 1-2 mg of complex in DMSO followed by 1-in-20 dilution with acetonitrile, with further dilutions performed if required to keep absorbance maxima below 1. Absorption spectra were obtained immediately after sample preparation, then solutions irradiated with 420 nm in a light oven at 310 K for 1 hour before absorption spectra were recorded again.

DMSO stability by ^{1}H NMR

6-8 mg of each complex was dissolved in 600 µL d_6-DMSO. Solutions were transferred to NMR tubes and ^{1}H NMR spectra were recorded at t = 0 h and t = 24 h on a 700 MHz spectrometer.

3.2.9 Emission spectra and luminescence quantum yields

Luminescence measurements were carried out with the help of Dr Jack Woolley at the Warwick Centre for Ultrafast Spectroscopy using the Horiba FluoroLog®-3 spectrofluorometer, and an excitation wavelength of 420 nm for all samples. A 2.5 nm slit width was applied for both excitation and emission measurements. Samples were held in a 1 cm path length quartz cuvette for luminescence and UV-vis measurements.

Luminescence quantum yields of the complexes, were obtained through **Equation 3.8** with the use of ruthenium tris bipyridine $[Ru(bpy)_3]^{2+}$ as a reference ($\Phi_{l,ref}$ = 0.018 in MeCN, 0.04 in PBS) and solutions prepared with a matching absorbance of less than 0.1.

$$\Phi_{l,sample} = \Phi_{l,ref} {}^{F_{sample}}\Big/_{F_{ref}} . {}^{f_{ref}}\Big/_{f_{sample}} . {}^{n^2_{sample}}\Big/_{n^2_{ref}} \qquad \textbf{Equation 3.8}^{49}$$

where Φ_l is the luminescence quantum yield, F is the integral photon flux and n is the refractive index at the wavelength corresponding to half the total integration of the emission spectrum.

$f = 1 - 10^{-A}$, where A is the absorbance at the excitation wavelength.

3.2.10 Luminescence lifetime measurements

Luminescence lifetime measurements were made with the help of Dr Jack Woolley at the Warwick Centre for Ultrafast Spectroscopy. The luminescence lifetimes of the complexes were measured in a 1 cm pathlength quartz cuvette, with all samples dissolved in acetonitrile to form solutions with an absorbance of 0.1 at the excitation wavelength. The time-resolved emission spectra were recorded with a Horiba Fluorolog®-3 spectrofluorometer employing a 402 nm NanoLED as the photoexcitation light source and monitoring the intensity at 500 and 620 nm. Blank traces were also collected in order to determine the instrument response associated with these measurements. The fluorescence lifetime values were extracted by fitting the time-resolved emission traces with an exponential decay convolved with a Gaussian function to account for the instrument response.

3.2.11 Singlet oxygen quantum yields

Samples were prepared in air-equilibrated acetonitrile at five concentrations with absorption at the excitation wavelength (λ = 420 nm) between 0.05-0.30, measured in a 1 cm quartz cuvette using a Cary60 UV-vis spectrophotometer. Data were visualised in Cary WinUV (v5.1.0.1016).

Singlet oxygen phosphorescence spectra were recorded on a Horiba FluoroLog®-3 spectrofluorometer fitted with a 750 nm cut-off filter and an R5509-73 liquid nitrogen cooled photomultiplier tube using an excitation wavelength of 420 nm (28 mW). Slit widths were set to 20 nm for excitation and 16 nm for the exit slit to

improve signal to noise. Data was visualised in FluorEssence v3.8 and processed in Origin 2021 and Microsoft Excel.

Peaks were fitted with a Gaussian function to determine the area of the emission peak, which was plotted against the absorption of the sample at 420 nm and a linear fit applied. Quantum yields were determined using **Equation 3.9**, where $\Phi_{\Delta,\text{ sample}}$ is the quantum yield of the sample, $\Phi_{\Delta,\text{ ref}}$ is the quantum yield of the reference ($Ru(bpy)_3Cl_2$ = 0.57), S_{sample} is the gradient of the sample linear fit, and S_{ref} is the gradient of the reference linear fit.

$$\Phi_{\Delta,sample} = \frac{S_{sample}}{S_{ref}} . \Phi_{\Delta,ref} \qquad \textbf{Equation 3.9}^{50}$$

3.3 Results

3.3.1 Synthesis and characterisation

Acetyl-protected glucose, mannose and galactose azides were purchased or successfully synthesised using literature methods for both α and β anomers, except in the case of 2,3,4,6-tetra-*O*-acetyl-α-D-galactose azide, which was synthesised *via* a novel method using a mixture of DMSO and DMPU as solvents. Azides of β-glucose with differing linker lengths were also successfully synthesised using literature methods, with 1-3 ethylene glycol units between the acetyl-protected β-glucose unit and the azide group. ^{1}H NMR spectra were in good agreement with the literature values and confirmed the anomeric configuration of each azide. Representative ^{1}H NMR spectra of the α and β anomers of 2,3,4,6-tetra-*O*-acetylglucopyranosyl azide are shown in **Figure 3.3**. The X-ray crystal structure of 2,3,4,6-tetra-*O*-acetyl-α-D-galactose azide was determined (**Section 3.3.2, Figure 3.10**).

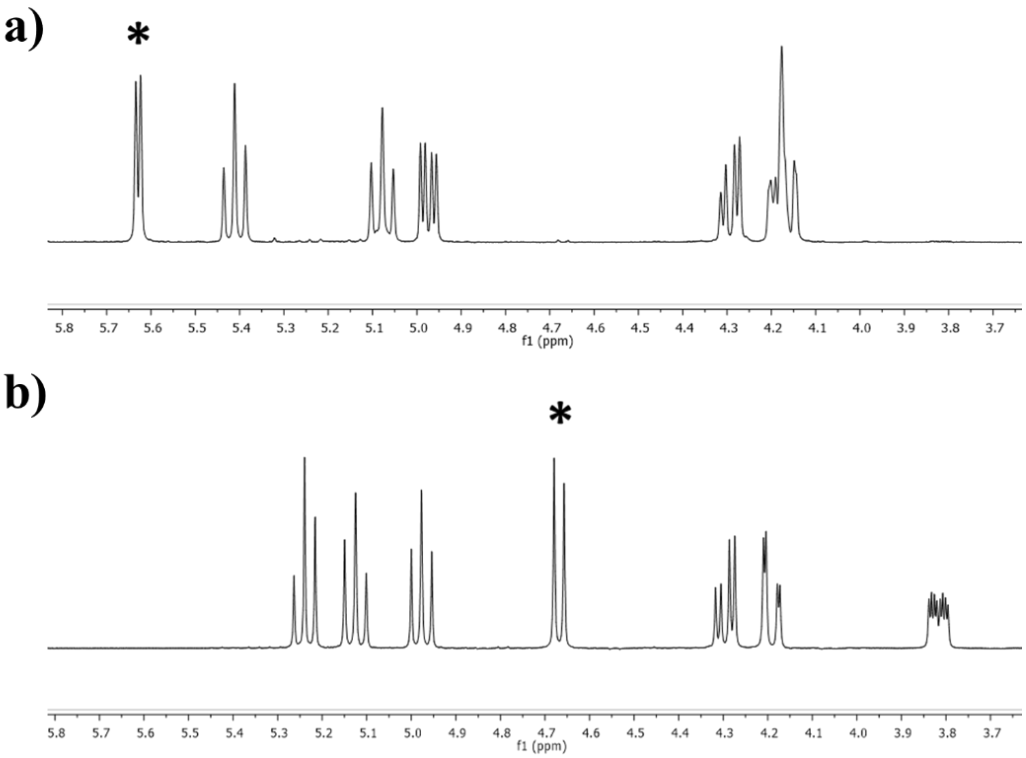

Figure 3.3. ^{1}H NMR spectra in $CDCl_3$ of a) 2,3,4,6-tetra-*O*-acetyl-α-D-glucopyranosyl azide and b) 2,3,4,6-tetra-*O*-acetyl-β-D-glucopyranosyl azide. Peaks for acetyl groups *ca*. 2.0 ppm omitted for clarity. Protons at anomeric position C1 marked with *.

Tetra-*O*-acetyl protected ligands were synthesised *via* a copper(I)-catalyzed azide-alkyne cycloaddition (**Figure 3.4a**). Refluxing these ligands with iridium dimer $[Ir(ppy_2)Cl]_2$ in methanol and dichloromethane afforded the protected iridium complexes (**Figure 3.4b**), whilst ruthenium-bipyridine analogues were synthesised by refluxing ligands with the mononuclear $[Ru(bpy)_2Cl_2]$ in chloroform and ethanol (**Figure 3.4c**).

The reaction of the acetylated complex with sodium methoxide in methanol successfully deprotected all glucose conjugates (**1Ac**, **4Ac**, **7Ac**, **8Ac**, **9Ac, Figure 3.4e**), however, the α-mannose complex showed only partial deacetylation even with long reaction times. Microwave conditions with excess triethylamine were employed to successfully remove all acetyl groups on all complexes, and purification using an automated C18 column efficiently removed triethylamine salts from the complexes (**Figure 3.4d**). A general structure of all complexes is shown in **Figure 3.5**, with each complex fully described in **Table 3.1**. The trifluoroacetic

acid in the mobile phase (used as an ion-pairing agent) led to displacement of the chloride counterions with trifluoroacetate (TFA^-). To return to the chloride salts, each complex was passed through a chloride exchange column. ^{19}F NMR spectra showed no fluorine signal, confirming the absence of TFA^-, indicating the successful replacement with chloride ions (**Figure 3.6**).

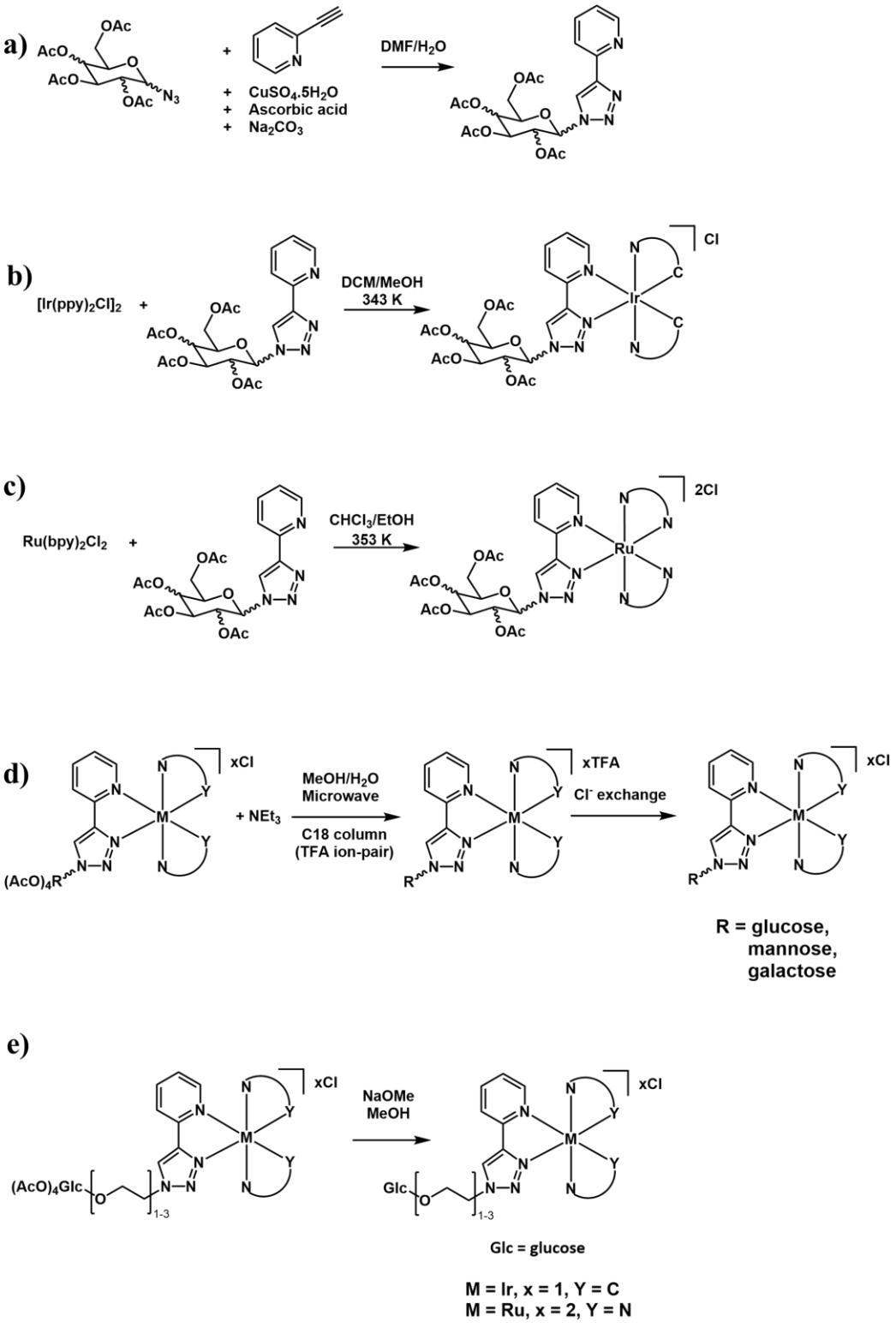

Figure 3.4. Generic synthetic procedure for glycoconjugated Ir(III) complexes **1**-**9** and Ru(II) complexes **11**-**14** from acetyl-protected sugar azides: a) Synthesis of ligands by "click" reactions; b) Synthesis of protected iridium complexes; c) Synthesis of protected ruthenium complexes; d) Deprotection using triethylamine and chloride exchange; e) Deprotection using sodium methoxide in methanol.

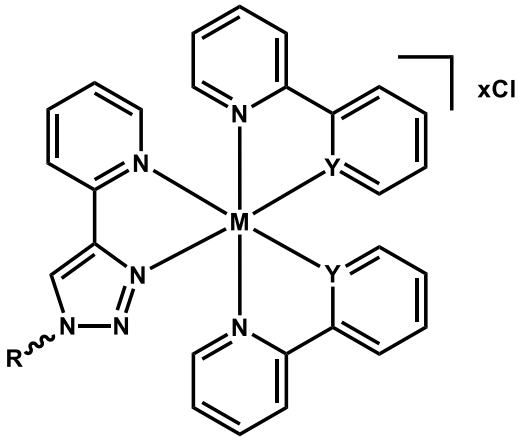

Figure 3.5. General structure of synthesised Ir and Ru glycoconjugates.

Table 3.1. Metal, charge (X), and substituent (Y) of each synthesised complex (**1-14**) and osmium complex **11-Os** (not synthesised).

Complex	Metal	X	Y	R
1	Ir	1	C	α-glucose
2				α-mannose
3				α-galactose
4				β-glucose
5				β-mannose
6				β-galactose
7				PEG1-β-glucose
8				PEG2-β-glucose
9				PEG3-β-glucose
10				CH_3
11	Ru	2	N	β-glucose
12				PEG1-β-glucose
13				PEG2-β-glucose
14				PEG3-β-glucose
11-Os*	Os	2	N	β-glucose

*Synthesis unsuccessful.

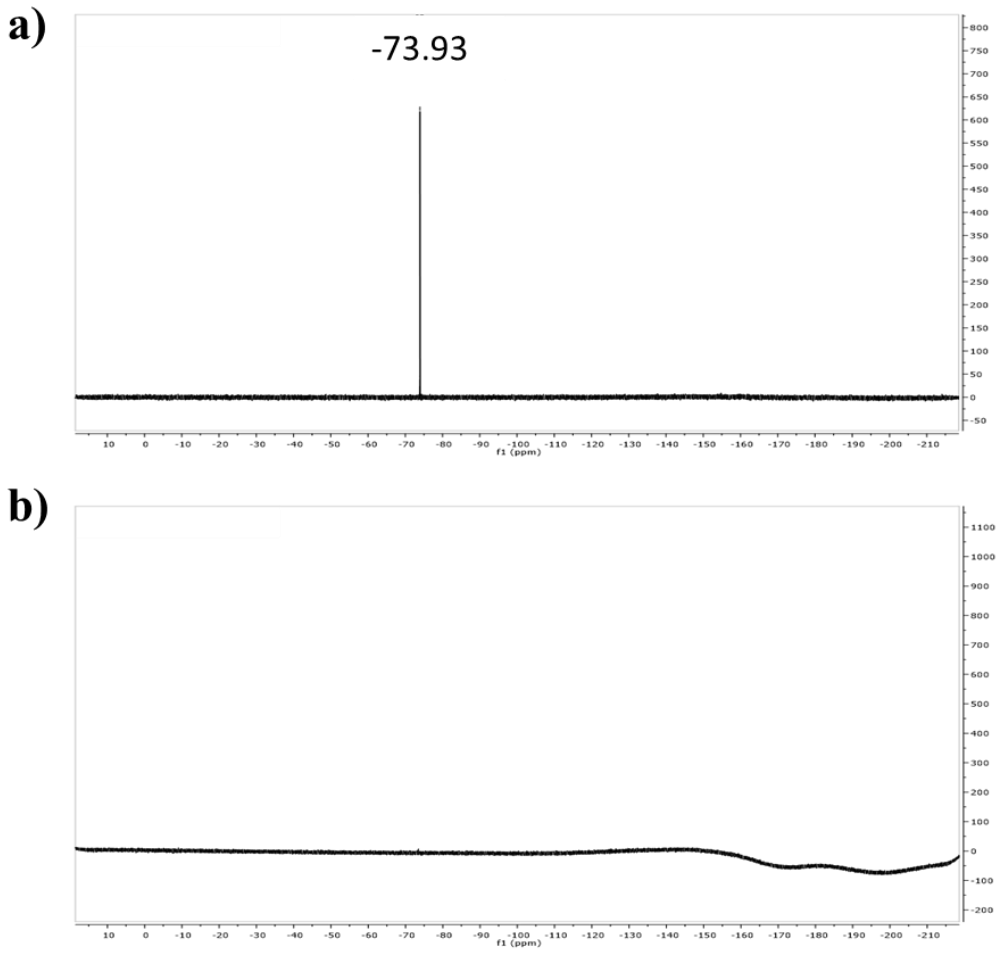

Figure 3.6. Example ^{19}F NMR spectra displaying β-mannose complex **5** a) before and b) after Cl^- exchange column.

Complexes with sugars bound directly to the triazole ring (**1**-**6** and **11**) were found to be >95% pure by HPLC, whilst the PEGylated complexes (**7**-**9** and **12**-**14**) all showed large non-product peaks (examples shown in **Figure 3.7**). LCMS confirmed these secondary peaks to be degradation products from cleavage of the glucose at the anomeric C1 position leaving an Ir/Ru-PEG-OH complex. Deprotections of pure, acetylated PEGylated glucose complexes were therefore performed using sodium methoxide in methanol to give pure products (>95%) which did not need further purification.

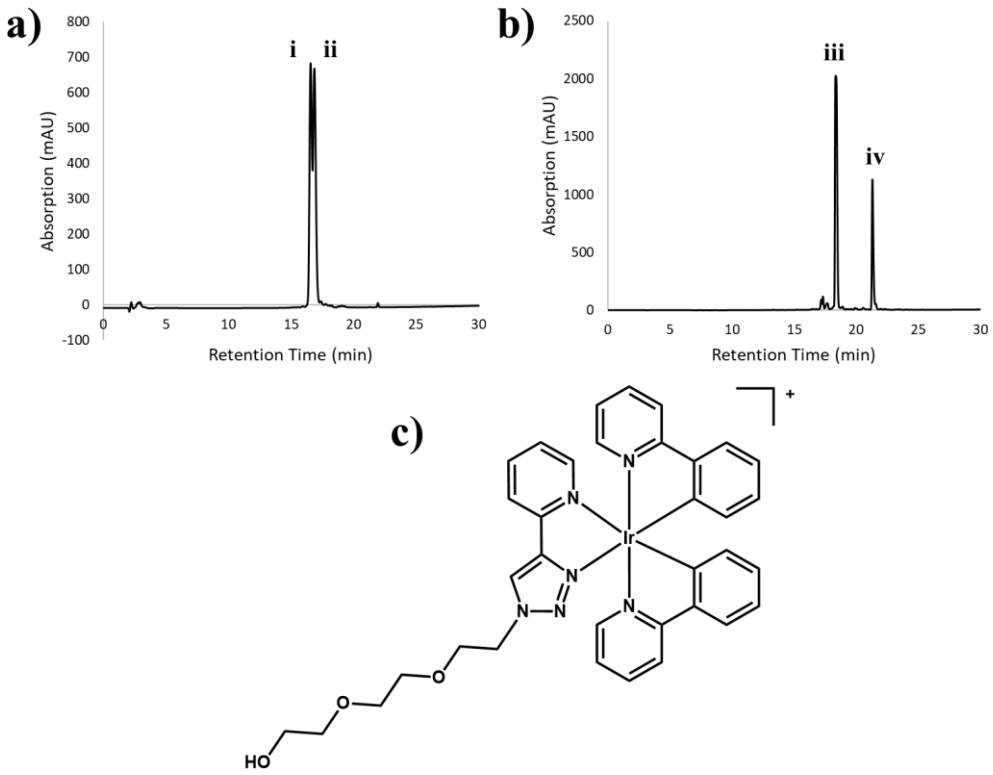

Figure 3.7. A) HPLC chromatogram of complex **4**. Peaks **i** and **ii** are the diastereomers of **4** (m/z = 809.2). B) Chromatogram of complex **9**. Peak **iii** contains both diastereomers of **9** (m/z = 941.3). Peak **iv** is the degradation product of **9**, corresponding to $[IrC_{35}H_{34}N_6O_3]^+$ which is shown in c).

Attempts to synthesise the acetylated osmium-β-glucose complex **11-Os** were unsuccessful as the harsh reaction conditions (573 K in ethylene glycol) led to loss of the glucose, observed by ESI-MS as a peak at m/z = 649.1 corresponding to $[OsC_{27}H_{21}N_8]^+$ (**Figure 3.8**). The attempted synthesis of **11-Os** from $[Os(bpy)_2Cl_2]$ is detailed in **Appendix Synthesis A1 and A2**.

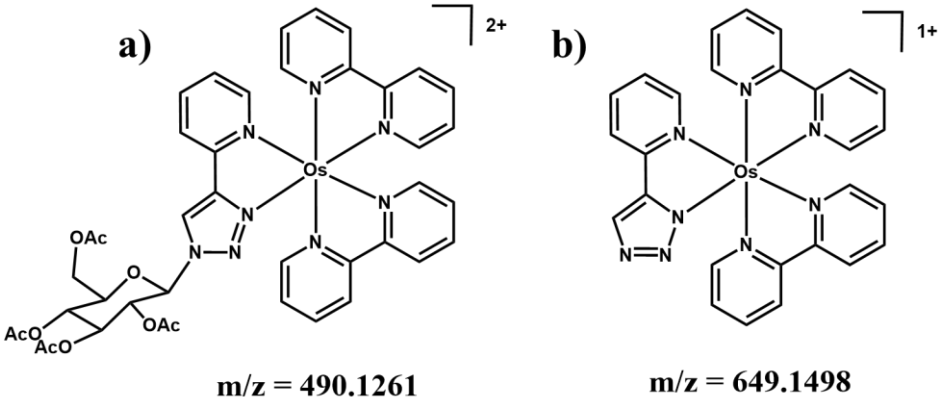

Figure 3.8. Structure of a) attempted Os glycoconjugate **11-Os** and b) potential product observed by ESI-MS.

Characterisation of the final complexes by ^{1}H NMR was performed in d_6-DMSO to avoid any residual solvent peaks overlapping with aromatic or sugar protons. Despite DMSO being dried prior to use, its hygroscopic nature led to broad water peaks in the sugar region (3-4 ppm), leading to product peaks being masked or integrals being exaggerated due to the underlying water peak. Addition of 10 µL trifluoroacetic acid immediately before obtaining the spectra led to a significant downfield shift of the water peak as well as the other exchangeable protons, resulting in a large, broad peak of the averaged signals, typically beyond 10 ppm due to their fast exchange (**Figure 3.9**).[51]

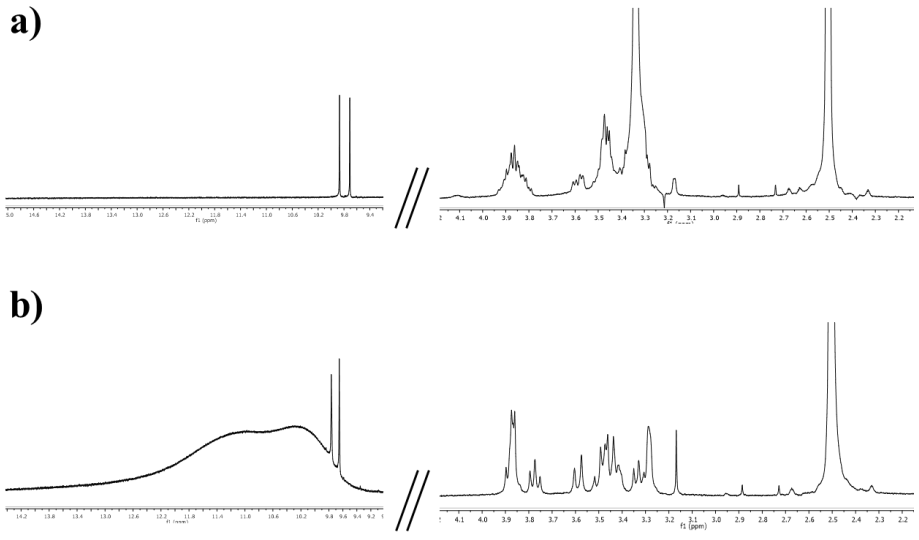

Figure 3.9. ^{1}H NMR spectra of Ir-α-glucose complex **1** in d_6-DMSO a) before and b) after addition of trifluoroacetic acid to the NMR sample.

3.3.2 X-ray crystallography

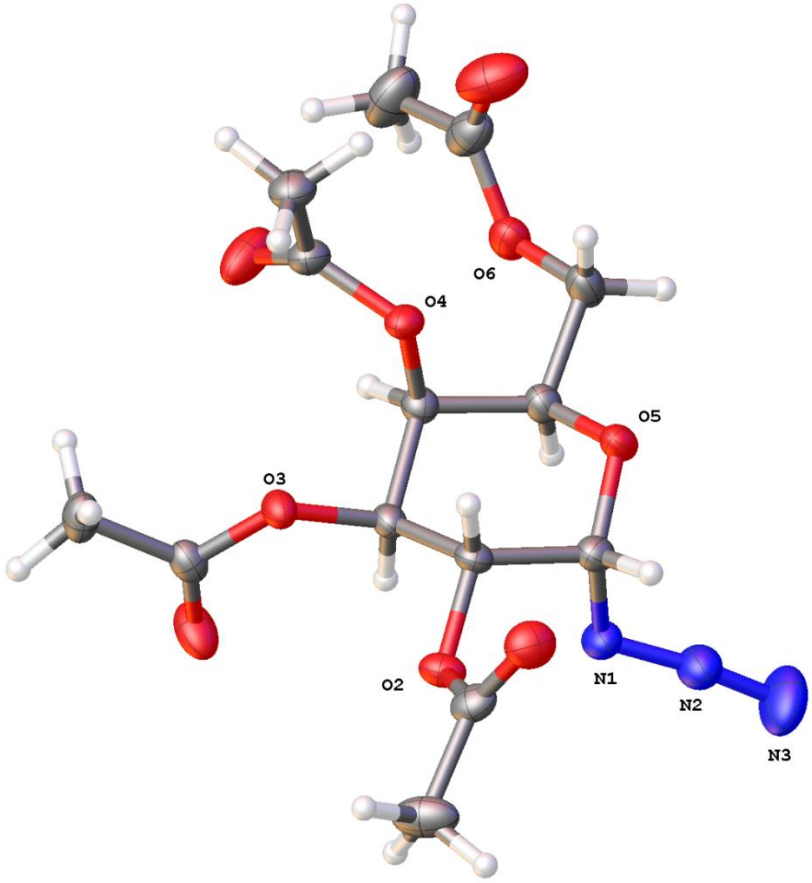

Figure 3.10. X-ray crystal structure of 2,3,4,6-tetra-*O*-acetyl-α-D-galactose azide generated using Mercury software. Thermal ellipsoids drawn at 50% probability level. Key atoms labelled and all atoms coloured by element. Cartesian atom coordinates, displacement parameters, bond lengths and bond angles in **Appendix Tables A2-A5.**

Table 3.2. X-ray crystallographic data for 2,3,4,6-tetra-*O*-acetyl-α-D-galactose azide.

	α-Gal(OAc)$_4$-N$_3$
Crystal appearance	Colourless needle
Empirical formula	$C_{14}H_{19}N_3O_9$
Formula weight	373.32
Temperature/K	100(2)
Crystal system	monoclinic
Space group	$P2_1$
a/Å	8.49673(13)
b/Å	7.39014(13)
c/Å	13.8826(2)

α/°	90
β/°	95.5481(14)
γ/°	90
Volume/Å^3	867.63(2)
Z	2
ρ_{calc}g/cm^3	1.429
μ/mm^{-1}	1.043
F(000)	392.0
Crystal size/mm^3	0.20 × 0.06 × 0.04 colourless block
Radiation	Cu Kα (λ = 1.54184)
2Θ range for data collection/°	6.396 to 160.908
Index ranges	-10 ≤ h ≤ 10, -9 ≤ k ≤ 9, -17 ≤ l ≤ 17
Reflections collected	51222
Independent reflections	3724 [R_{int}= 0.0710, R_{sigma}= 0.0225]
Data/restraints/parameters	3724/1/239
Goodness-of-fit on F^2	1.130
Final R indexes [I>=2σ (I)]	R_1 = 0.0354, wR_2 = 0.0893
Final R indexes [all data]	R_1 = 0.0367, wR_2 = 0.0904
Largest diff. peak/hole / e Å^{-3}	0.19/-0.21
Flack parameter	-0.04(9)

Colourless needle crystals suitable for X-ray diffraction were obtained from the reaction mixture (in DMSO/DMPU solution) after being incubated at 277 K for two weeks. The crystal structure of 2,3,4,6-tetra-*O*-acetyl-α-D-galactose azide has not previously been reported.

3.3.3 Density functional theory (DFT) calculations

Density functional theory (DFT) calculations were performed on the Ir-β-glucose complex **4**, Ru-β-glucose complex **11**, and structurally analogous Os-β-glucose complex **11-Os**, to explore the effects of changing the metal centre and C^N ligands. Theoretical absorption spectra for **4** and **11** are consistent with the experimental data, however, **11-Os** could not be synthesised so only a simulated spectrum was obtained (**Figure 3.11**).

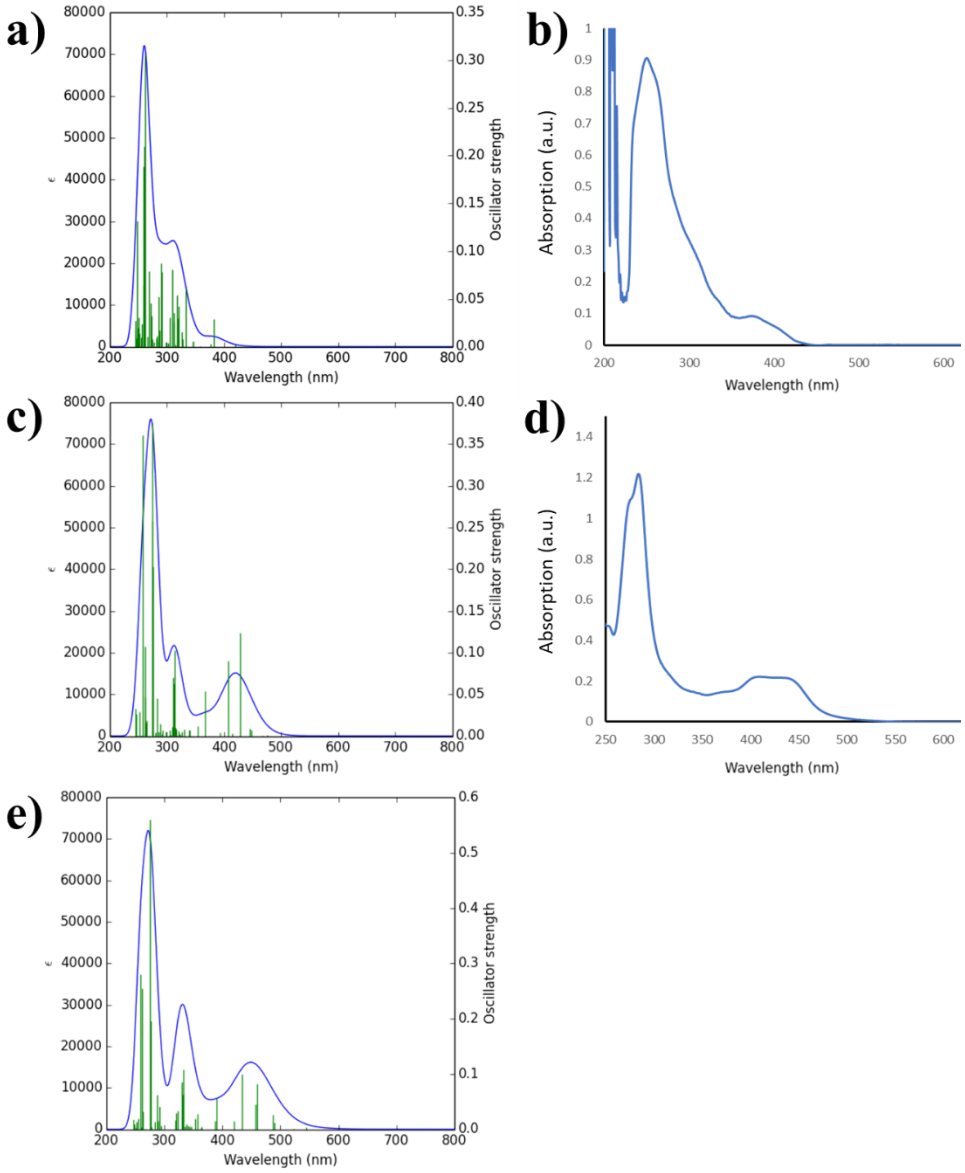

Figure 3.11. a) DFT-calculated absorption spectrum of **4** in water; b) measured absorption spectrum of **4**; c) DFT-calculated spectrum of **11** in water; d) measured absorption spectrum of **11**; e) DFT-calculated spectrum of **11-Os**.

The longest wavelength absorption peaks in the theoretical spectra increase in the order of Ir (~380 nm) < Ru (~430 nm) < Os (~450 nm). The contributions of each molecular orbital transition to these peaks are in **Appendix Tables A6-A8**.

Electron densities for the highest occupied molecular orbital (HOMO) and lowest unoccupied molecular orbital (LUMO) varied greatly on each complex (**Figure 3.12**). For the HOMO of the iridium complex **4**, 28% of electron density was calculated on the metal centre and 55% on L1 (ppy), yet for the ruthenium and osmium complexes **11** and **11-Os**, the electron density at the metal centres were 72% and 63%, respectively. Contrastingly, the LUMO of each complex was only 2-3% based on the metal centre, but the distribution across the ligands were entirely different. Ir complex **4** showed 93% on L3 (glucose ligand), whilst for **11**, 81% was on L2 (bpy) and for **11-Os** was spread across L2 and L3 (54% and 37%, respectively).

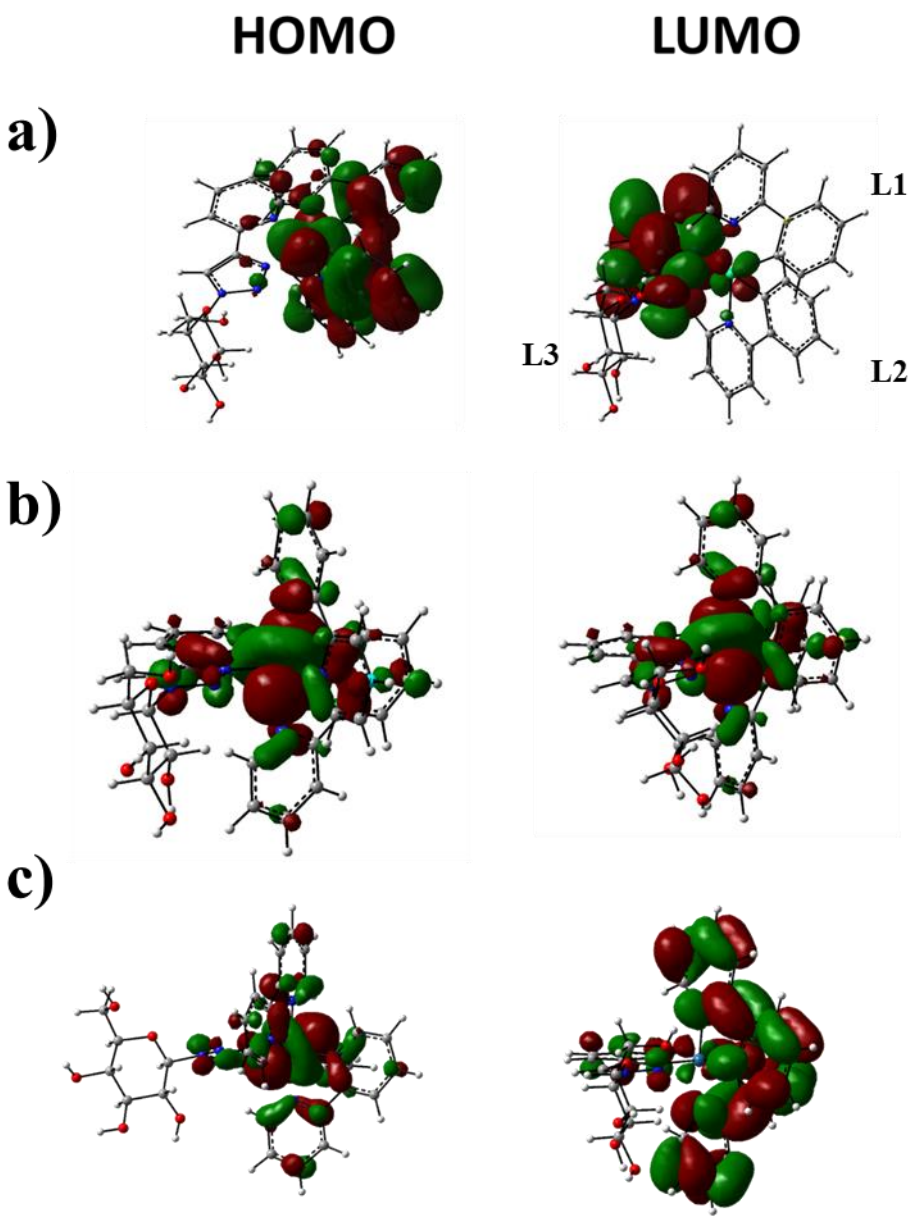

Figure 3.12. DFT-calculated electron densities for a) **4**, b) **11** and c) **11-Os**. For clarity, ligands L1, L2 and L3 are labelled in Figure 3.12a. L1 = L2 = 2-phenylpyridine (**4**) or 2,2'-bipyridine (**11**/**11-Os**); L3 = pyridyl-triazole-β-glucose ligand.

The calculated energy gaps between the ground-state and first excited singlet and triplet states increase in the order Os < Ru < Ir. However, excited states for all complexes are above the energy required to generate singlet oxygen (singlet state 0.98 eV above ground-state) (**Figure 3.13**).

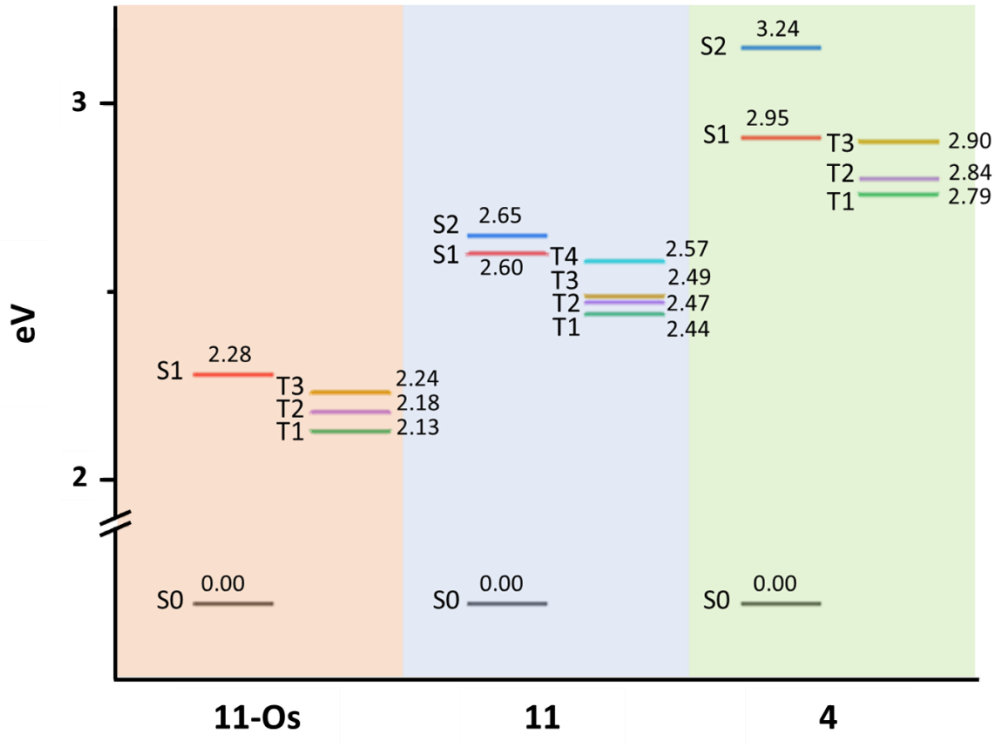

Figure 3.13. Energy gaps between ground-state and excited states of **4**, **11** and **11-Os**. Molecular oxygen = 0.98 eV.

3.3.4 Photophysical measurements – absorption and emission

The absorption spectra of all complexes were recorded in acetonitrile, PBS, and media, and emission spectra were recorded in acetonitrile and PBS (**Table 3.3**). Molar extinction coefficients were calculated for the maximum absorption wavelength ($\lambda_{max,\ abs}$) and at 425 nm (wavelength of light source for biological studies in **Chapter 4**) in each solvent after determining the accurate metal concentration of the stock solutions by ICP-OES (**Chapter 2, Section 2.2.8**).

Table 3.3. Photophysical properties of complexes **1**-**14** in acetonitrile, PBS, and cell culture medium RPMI-1640 (no phenol red).

Compound	**Solvent**	$\lambda_{max, abs}$ **(nm)**	ε_{max} **(M^{-1} cm^{-1})**	ε_{425} **(M^{-1} cm^{-1})**	$\lambda_{max, em}$[a] **(nm)**
1	MeCN	379	2343	724	479, 507
(Ir-α-glu)	PBS	377	2098	427	473, 500
	RPMI[b]	374	2225	477	n.d.
2	MeCN	378	2191	615	477, 508
(Ir-α-man)	PBS	377	1967	403	472, 499
	RPMI	375	1952	305	n.d.
3	MeCN	377	2552	770	478, 509
(Ir-α-gal)	PBS	377	2255	522	474, 501
	RPMI	377	2650	692	n.d.
4	MeCN	377	1973	485	478, 505
(Ir-β-glu)	PBS	374	2064	369	471, 499
	RPMI	373	2031	289	n.d.
5	MeCN	377	1992	311	476, 508
(Ir-β-man)	PBS	374	2171	246	471, 500
	RPMI	377	2194	347	n.d.
6	MeCN	378	2067	434	477, 506
(Ir-β-gal)	PBS	373	2349	455	472, 500
	RPMI	375	2387	441	n.d.
7	MeCN	377	1961	572	479, 505
(Ir-PEG1-	PBS	373	1975	420	473, 500
β-glu)	RPMI	374	2071	356	n.d.
8	MeCN	379	2135	557	477, 506
(Ir-PEG2-	PBS	371	2061	439	473, 502
β-glu)	RPMI	375	2329	525	n.d.
9	MeCN	378	2215	515	477, 508
(Ir-PEG3-	PBS	373	2317	510	472, 500
β-glu)	RPMI	377	2530	535	n.d.
10	MeCN	377	3096	977	475, 502

(Ir-CH_3)	PBS	373	2697	507	473, 499
	RPMI	374	2786	580	n.d.
11	MeCN	438	4425	4375	613
(Ru-β-glu)	PBS	408	4599	4483	616
	RPMI	403	5171	5006	n.d.
12	MeCN	443	4563	4413	613
(Ru-PEG1-	PBS	439	4742	4634	615
β-glu)	RPMI	411	5032	4960	n.d.
13	MeCN	443	3894	3773	609
(Ru-PEG2-	PBS	440	3903	3818	612
β-glu)	RPMI	411	4301	4211	n.d.
14	MeCN	443	4010	3913	614
(Ru-PEG3-	PBS	439	3965	3880	610
β-glu)	RPMI	411	4379	4296	n.d.

[a] λ_{ex} = 420 nm. [b] RPMI-1640 (no phenol red).

For both the Ir and Ru complexes, very little difference was observed within each series. The iridium complexes generally showed local absorption maxima at *ca*. 375 nm in all three solvents, with a major contribution (89%) from the HOMO → LUMO+1 transition at 381 nm based on DFT calculations (**Appendix Table A6**). For the ruthenium complexes, the similar local absorption maxima were much broader, ranging from *ca*. 410-450 nm in all three solvents, with a major (41%) contribution from the HOMO-1 → LUMO transition at 428 nm (**Appendix Table A7**). Iridium complexes showed relatively low absorption at 425 nm, with molar extinction coefficients between *ca.* 300-700 M^{-1} cm^{-1} across all solvents, whereas the ruthenium complexes were much higher at *ca*. 4000-5000 M^{-1} cm^{-1}.

3.3.5 Solution stability of Ir and Ru complexes

The stabilities of compounds **1-14** in deuterated DMSO were investigated by ^{1}H NMR. Spectra were recorded 24 h apart and remained unchanged, with no peaks that would indicate the formation of a DMSO adduct, suggesting good stability in DMSO (**Figure 3.14**).

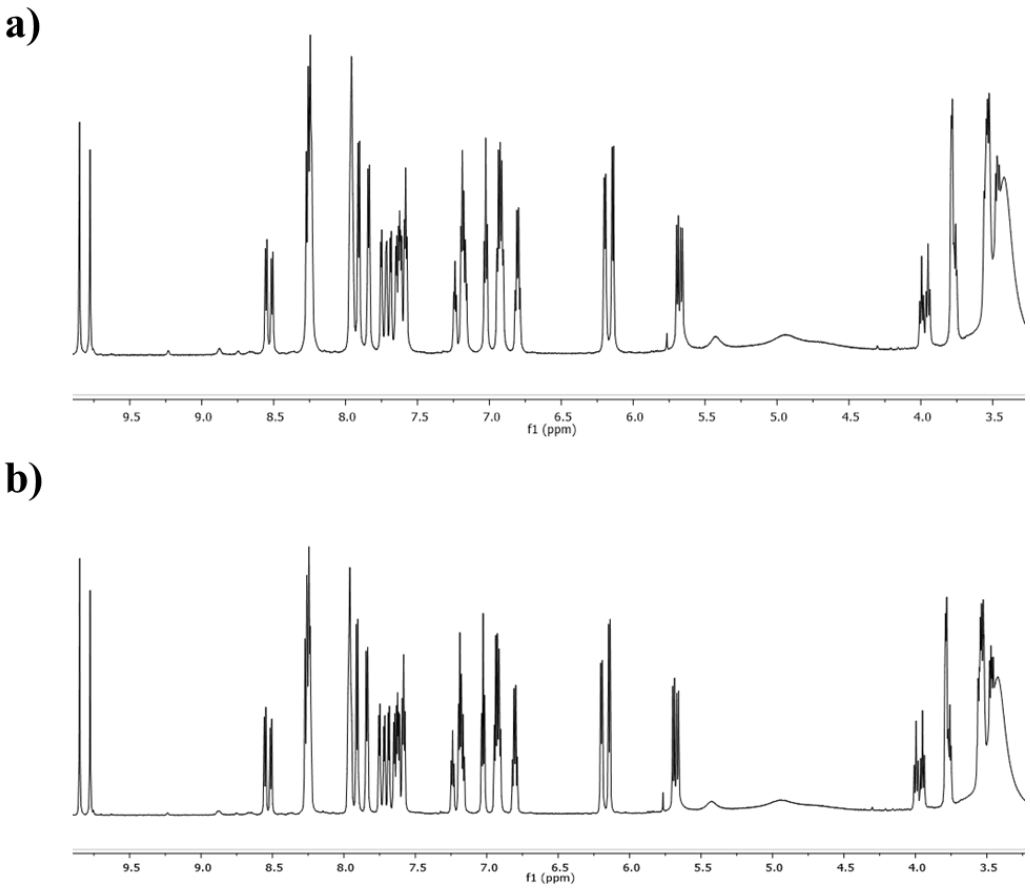

Figure 3.14. Example of DMSO stability by ^{1}H NMR: Little change in spectra of **6** in d_6-DMSO between a) t = 0 h and b) t = 24 h.

The stabilities of the synthesised complexes in DMSO, acetonitrile (MeCN), phosphate-buffered saline (PBS) and RPMI-1640 (no phenol red) cell culture media were investigated over 24 h by UV-vis spectroscopy. Minimal changes were seen between the absorption spectra recorded at 0 h and 24 h in all solvents (**Figure 3.15**).

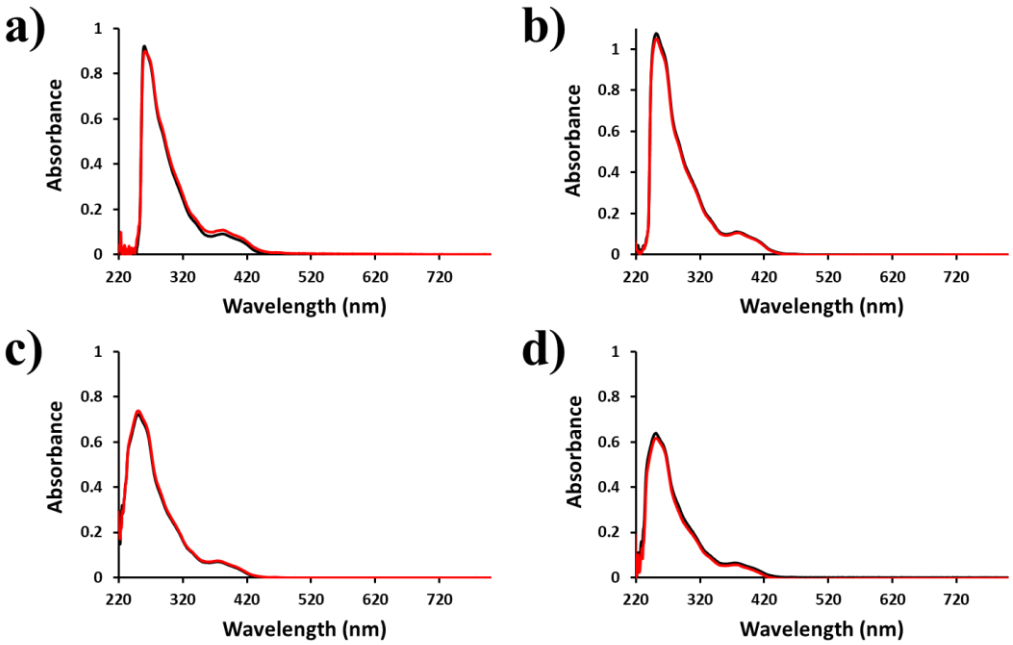

Figure 3.15. Examples of solution stability determined by UV-vis spectroscopy. Absorption spectra of complex **5** at t = 0 h (black) and t = 24 h (red) in a) DMSO; b) acetonitrile; c) PBS; d) RPMI-1640 (no phenol red).

The photo-stabilities of the complexes in acetonitrile were also investigated. Absorption spectra were obtained immediately after samples were prepared (t = 0 h) and after 1 h irradiation at 420 nm. All complexes showed minimal changes in the absorption spectra (**Figure 3.16**), indicating they are stable towards 1 h irradiation with 420 nm blue light.

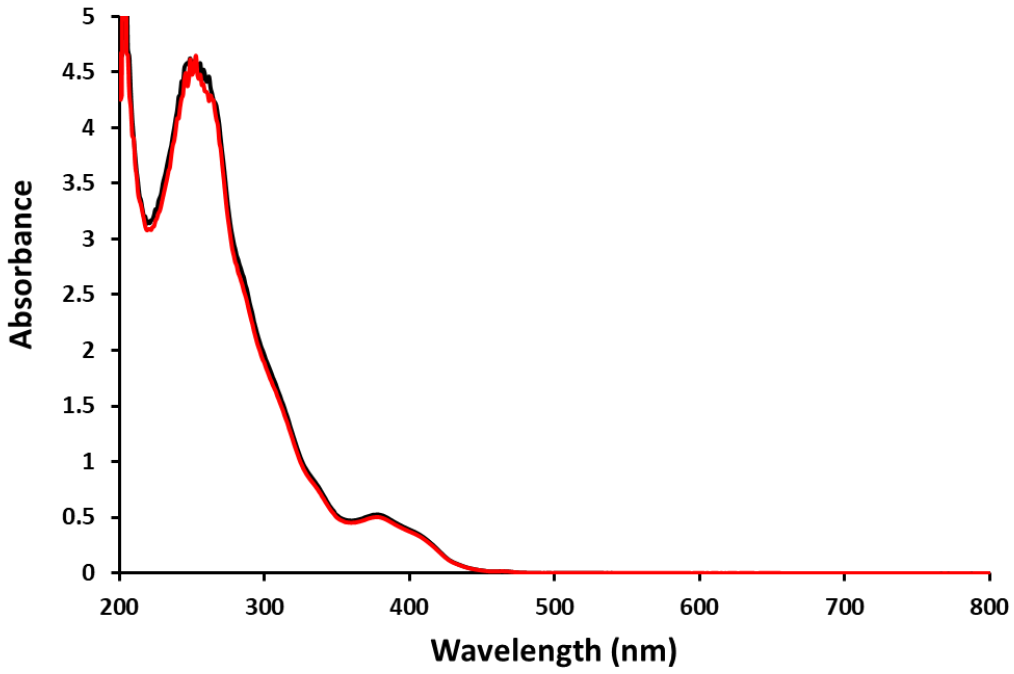

Figure 3.16. Example of photo-stability by UV-vis: Absorption spectra of **5** in acetonitrile after 0 h (black) and 1 h irradiation at 420 nm (red).

3.3.6 Photophysical properties of Ir and Ru complexes - Φ_Δ, Φ_P and excited state lifetimes

The excited state lifetimes and phosphorescence quantum yields of iridium complexes **1-10** (**Table 3.4**) and ruthenium complexes **11-14** (**Table 3.5**) were determined in acetonitrile (air-equilibrated and nitrogen-saturated) and PBS, whilst singlet oxygen quantum yields were determined in air-equilibrated acetonitrile.

Table 3.4. Excited state lifetimes, phosphorescence quantum yields (Φ_P), and singlet oxygen quantum yields (Φ_Δ) of iridium complexes **1-10** in acetonitrile and PBS.

Ir Complex	Solvent	Lifetime (ns)	Φ_P (%)	Φ_Δ
1	MeCN	56.8 ± 0.9	1.2	0.60 ± 0.02
(Ir-α-glu)	MeCN*	74.1 ± 1.2	10.8	n.d.
	PBS	373.8 ± 2.0	8.2	n.d.
2	MeCN	56.5 ± 0.9	1.3	0.62 ± 0.02
(Ir-α-man)	MeCN*	98.9 ± 1.2	15.9	n.d.

	PBS	358.8 ± 1.8	7.3	n.d.
3	MeCN	55.1 ± 0.9	1.3	0.61 ± 0.01
(Ir-α-gal)	MeCN*	102.8 ± 1.2	10.2	n.d.
	PBS	372.1 ± 1.9	7.6	n.d.
4	MeCN	60.8 ± 0.9	1.4	0.61 ± 0.03
(Ir-β-glu)	MeCN*	123.2 ± 1.2	14.2	n.d.
	PBS	434.3 ± 2.5	9.1	n.d.
5	MeCN	58.7 ± 0.9	1.3	0.66 ± 0.04
(Ir-β-man)	MeCN*	112.5 ± 1.2	10.5	n.d.
	PBS	435.8 ± 2.5	10.3	n.d.
6	MeCN	60.3 ± 0.9	1.3	0.62 ± 0.01
(Ir-β-gal)	MeCN*	97.7 ± 1.2	9.8	n.d.
	PBS	447.2 ±2.7	8.3	n.d.
7	MeCN	56.6 ± 0.9	1.1	0.58 ± 0.03
(Ir-PEG1-	MeCN*	135.2 ± 1.2	16.9	n.d.
β-glu)	PBS	443.8 ± 2.7	12.8	n.d.
8	MeCN	55.6 ± 0.9	1.3	0.56 ± 0.02
(Ir-PEG2-	MeCN*	119.2 ± 1.2	19.0	n.d.
β-glu)	PBS	434.4 ± 2.5	10.0	n.d.
9	MeCN	56.3 ± 0.9	1.3	0.58 ± 0.02
(Ir-PEG3-	MeCN*	107.5 ± 1.2	8.6	n.d.
β-glu)	PBS	428.9 ± 2.9	10.1	n.d.
10	MeCN	55.1 ± 1.0	1.0	0.63 ± 0.02
(Ir-CH_3)	MeCN*	124.4 ± 1.2	9.7	n.d.
	PBS	400.5 ± 2.7	9.0	n.d.
	MeCN	57.2 ± 1.9	1.3 ± 0.1	0.61 ± 0.03
Average	MeCN*	109.6 ± 15.7	12.6 ± 3.4	n.d.
	PBS	413.0 ± 30.3	9.3 ± 1.5	n.d.

* Nitrogen bubbled for 5 min before determination of lifetime. n.d. = not determined.

Table 3.5. Excited state lifetimes, phosphorescence quantum yields (Φ_P), and singlet oxygen quantum yields (Φ_Δ) of ruthenium complexes **11-14** in acetonitrile and PBS.

Ru Complex	Solvent	Lifetime (ns)	Φ_P (%)	Φ_Δ
11	MeCN	5.0 ± 0.9	0.05	0.01 ± 0.00
(Ru-β-glu)	MeCN*	4.9 ± 1.2	0.1	n.d.
	PBS	8.7 ± 0.9	0.1	n.d.
12	MeCN	11.8 ± 0.9	0.1	0.04 ± 0.00
(Ru-PEG1-β-glu)	MeCN*	13.5 ± 1.2	0.2	n.d.
	PBS	20.5 ± 0.9	0.1	n.d.
13	MeCN	1.5 ± 0.1	0.1	0.03 ± 0.00
(Ru-PEG2-β-glu)	MeCN*	14.4 ± 1.2	0.2	n.d.
	PBS	19.6 ± 0.9	0.2	n.d.
14	MeCN	1.5 ± 0.1	0.1	0.04 ± 0.00
(Ru-PEG3-β-glu)	MeCN*	14.2 ± 1.2	0.2	n.d.
	PBS	18.7 ± 0.9	0.2	n.d.
	MeCN	5.0 ± 4.2	0.09 ± 0.02	0.03 ± 0.01
Average	MeCN*	11.8 ± 4.0	0.18 ± 0.04	n.d.
	PBS	16.9 ± 4.8	0.15 ± 0.05	n.d.

* Nitrogen bubbled for 5 min before use. n.d. = not determined.

Excited state lifetimes of iridium complexes **1-10** in acetonitrile were over 10× greater than those of ruthenium complexes **11-14** (57.2 ± 1.9 ns *vs* 5.0 ± 4.2 ns). The lifetimes of the iridium complexes were lengthened to 109.6 ± 15.7 ns in solutions bubbled with nitrogen for 5 minutes, however, lifetimes of the ruthenium complexes remained short-lived, averaging 11.8 ± 4.0 ns.

Iridium complexes **1-10** exhibited intense two-peak emission spectra, with maxima at *ca.* 475 nm and 500 nm, compared to the broad, low intensity emission peaks observed for the ruthenium complexes **11-14** (**Figure 3.17**). Emission quantum yields for the iridium complexes were over 10× greater than those of ruthenium complexes (1.3% ± 0.1% *vs.* 0.09% ± 0.02%). Emission quantum yields increased

10-fold for iridium complexes when solutions were bubbled with nitrogen for 5 minutes (12.6% ± 3.4%), but changes for the ruthenium complexes were much less dramatic (0.18% ± 0.04%).

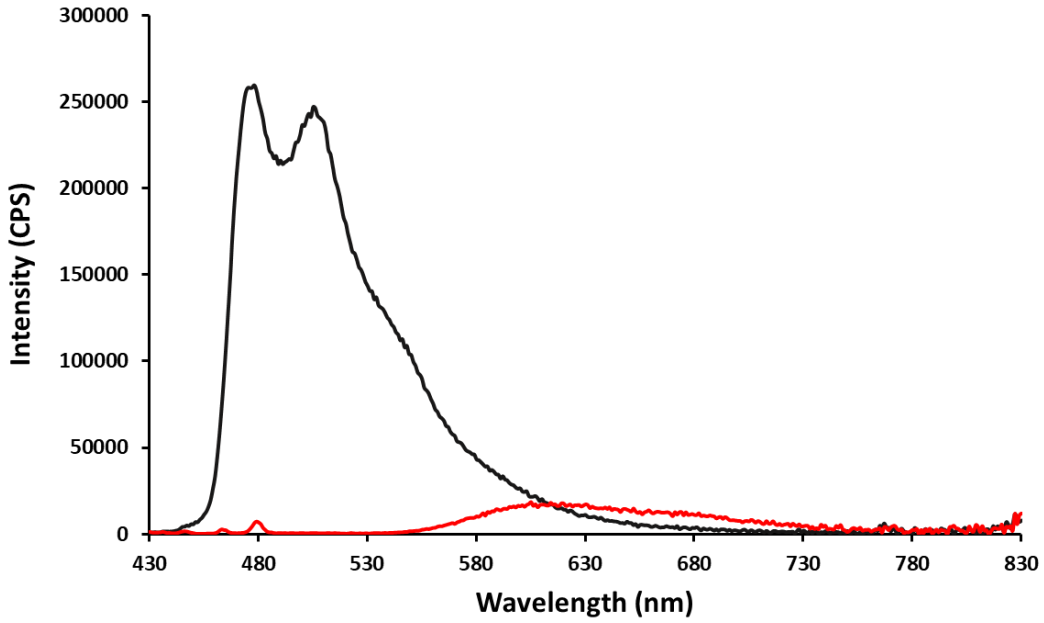

Figure 3.17. Emission spectra of Ir complex **4** (black) and Ru complex **11** (red) in acetonitrile. Abs = 0.1 at excitation wavelength (λ_{ex} = 420 nm).

Singlet oxygen quantum yields were determined by detecting the phosphorescence emitted from the excited oxygen molecules at 1270 nm. Iridium complexes **1-10** exhibited singlet oxygen quantum yields of 58-63%, however, the ruthenium complexes **11-14** showed very poor singlet oxygen quantum yields of below 5%.

3.4 Discussion

3.4.1 Synthesis and characterisation of complexes

Most sugar azides were commercially available or synthesised using adapted literature procedures.[32–40] However, 2,3,4,6-tetra-*O*-acetyl-α-galactose azide was synthesised by a novel procedure using a mixture of DMSO and DMPU as solvent instead of highly carcinogenic and mutagenic HMPA which is typically used.[52,53] This resulted in synthesis of colourless needle crystals which could be analysed by

X-ray diffraction to yield a new crystal structure. Ligands were all synthesised using the copper-catalysed azide-alkyne cycloaddition 'CuAAC' reaction, commonly referred to as 'click' reactions (**Figure 3.18**), resulting in 1,4-disubstituted 1,2,3-triazoles that could be readily bound to iridium(III) and ruthenium(II) in mild conditions.

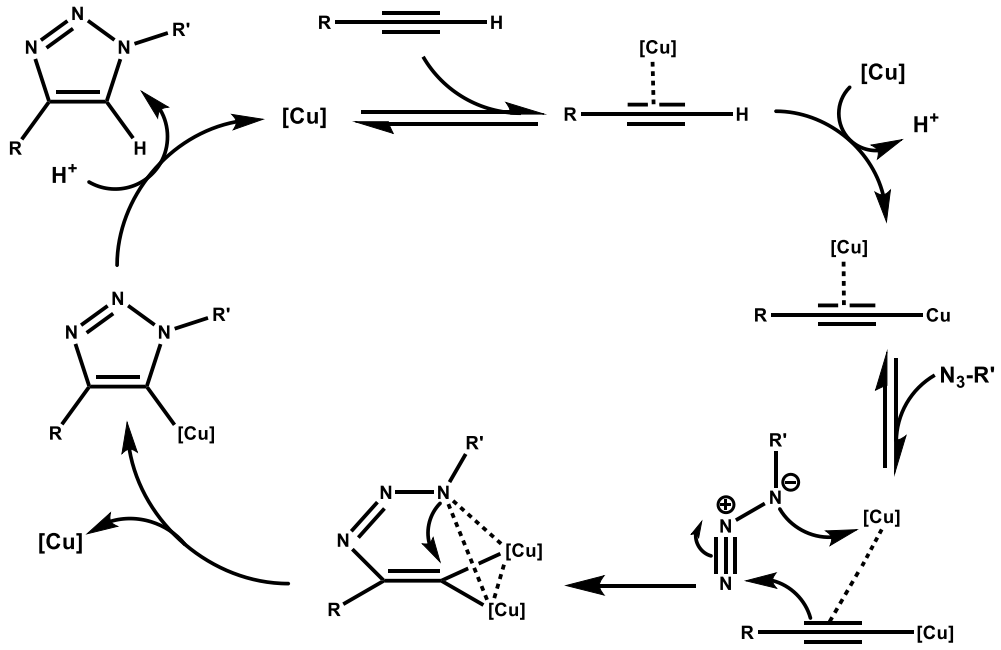

Figure 3.18. Schematic for copper-catalysed "click" reactions. Reproduced from reference.[54]

Osmium(II) analogues proved more difficult to synthesise. Literature methods similar to those used for the synthesis of the analogous Ru(II) complexes used mild conditions (reflux in ethanol) but were unsuccessful,[10] whilst harsher conditions such as microwave heating or reflux in ethylene glycol (~200 ^{o}C) were also unsuccessful.[55] In the case of refluxing, ESI-MS of the crude product showed the loss of the sugar, with the correct m/z observed for the remaining cyclometalated product (m/z = 649.1 corresponding to $[Os(bpy)_2(C_7H_5N_4)]^+$, **Section 3.3.1, Figure 3.7**).

Microwave deacetylation reactions with triethylamine were universally successful, demonstrated by the lack of any acetylated complex peaks in the mass spectra of crude products. To remove triethylamine salts, complexes were purified by column chromatography using C18 columns with a mobile phase of acetonitrile and water

containing trifluoroacetic acid as the ion-pairing agent. However, PEGylated complexes degraded when undergoing column chromatography likely due to acid-catalysed hydrolysis at the anomeric carbon.[56] This was not seen for the non-PEGylated complexes as the sugars were directly bound to the nitrogen of the triazole, which has an inaccessible lone pair due to its delocalisation in the aromatic π-system.[57] Conversely, Zemplén deacetylations using sodium methoxide in methanol successfully deprotected all acetyl groups on PEGylated complexes (**7**-**9** and **12**-**14**) without requiring further purification. However, for some non-PEGylated complexes such as α-mannose complex **2**, only a partially deacetylated product was observed using ESI-MS (m/z = 935.2 corresponding to removal of one Ac group). Partial deprotection has been previously observed in the Zemplén deacetylation of other mannose derivatives, as well as those of glucose and galactose, referred to as anomalous Zemplén reactions.[58,59] Complexes were converted back to chloride salts as TFA has been shown to inhibit cell growth.[60] Successful conversion to a chloride salt was inferred by the lack of signal at -74 ppm in the ^{19}F NMR (TFA signal is typically between -85 and -67 ppm).[61]

Full assignment of peaks to every proton in ^{1}H NMR spectra was difficult due to the presence of diastereomers, caused by there being multiple stereocentres in each complex; each carbon of the pyranose ring is chiral, as well as the metal centre. This led to double the number of proton signals which in many cases were overlapping and could therefore not be attributed to a specific proton on a specific diastereomer. In addition, samples in d_6-DMSO had to be spiked with trifluoroacetic acid to move the water peak downfield to allow integrals in the sugar region to be calculated correctly.[51] For deprotected complexes, this also caused exchangeable OH protons to be moved downfield into a large, broad peak containing all exchangeable protons. The use of NMR combined with high resolution mass spectrometry and HPLC allowed for the confident determination of the purity of each complex.

3.4.2 Density functional theory

DFT calculations were performed to evaluate whether complexes were able to generate a sufficiently high energy triplet state to react with ground-state (triplet)

oxygen to produce singlet oxygen. Calculations for the structurally similar β-glucose complexes **4** (Ir), **11** (Ru) and osmium analogue **11-Os** (not synthesised) found that changing the metal centre led to lower energy triplet T_1 excited states in the order of Ir > Ru > Os, but all were sufficiently high in energy to excite ground-state oxygen to singlet oxygen (0.98 eV).[62] A clear bathochromic (red) shift in theoretical maximum absorption wavelength was seen across the series from iridium (380 nm) to ruthenium (430 nm) to osmium (450 nm). Osmium analogues may therefore be activated with longer wavelengths of light, leading to deeper tissue penetration, which is attractive for clinical translation.[63] However, synthesis of cyclometalated Os complexes required harsher conditions than those for Ir and Ru complexes, which led to degradation of the sugar ligand. As an alternative, the absorption properties of Ir and Ru complexes can be tuned by modification of the C^N or N^N ligand, respectively, leading to complexes that absorb closer to the therapeutic window.[64,65]

3.4.3 Stability of complexes

Before being used in cell screens, complexes must be investigated for stability in a variety of different solvents. The complexes were investigated by UV-vis and ^{1}H NMR to evaluate their stability over 24 hours when incubated at 310 K in acetonitrile, DMSO, PBS, and cell culture media.

DMSO is used as a solubilising agent in biological testing when samples do not exhibit good water solubility, as it is usually non-toxic to cells at 5% v/v and below.[66,67] However, DMSO is known to react with metallodrugs such as cisplatin.[68,69] UV-vis spectra taken 24 h apart showed very little changes, demonstrating that these complexes are either highly stable in DMSO or react so quickly that the complexes have fully converted to a DMSO adduct by the time the 0 h measurement was recorded. However, ^{1}H NMR in d_6-DMSO showed identical spectra 24 h apart, with no peaks that would indicate formation of a DMSO adduct (either by replacing one of the ligands or by binding to one). This would indicate that all complexes are highly stable in DMSO.

Aqueous stability was determined in PBS due to its physiological pH (7.4) which is maintained even after the addition of complexes. Due to the low solubility of the iridium complexes in water, samples were initially dissolved in DMSO then diluted

with PBS (DMSO <5% v/v). Ruthenium complexes were more water-soluble but were also dissolved in DMSO first to be consistent. UV-vis measurements performed 24 h apart once again showed very little differences, indicating the samples do not hydrolyse. Absorption spectra in cell culture media (RPMI-1640, no phenol red) also showed little change over 24 h incubation at 310 K. PDT photosensitizers are photocatalysts for singlet oxygen generation; therefore, the complexes must be stable towards irradiation for the corresponding treatment period (1 h used in biological assays in **Chapter 4**). Photophysical measurements such as singlet oxygen quantum yields are often measured in acetonitrile,[70–75] thus stability and photo-stability of complexes were determined by UV-vis in acetonitrile. Absorption spectra showed no changes over 24 h without irradiation, as well as after 1 h irradiation, indicating acetonitrile is a suitable solvent to prepare samples in for photophysical studies. Their good overall solution and photo-stabilities demonstrate they are suitable for *in vitro* biological testing.

3.4.4 Photophysical studies

Emission spectra obtained for iridium complexes **1**-**10** all displayed vibronically structured emission spectra, demonstrated by the two emission maxima (*ca*. 475 nm and 505 nm, respectively). This is seen in other Ir(III) complexes due to relaxation from the excited triplet state to different vibrational states of the electronic ground state.[76,77] Emission bands of Ir complexes were far greater in intensity than those of the Ru complexes (250,000 *vs.* 25,000 cps), which were much broader with maxima *ca*. 610 nm. Emission quantum yields determined in air-equilibrated acetonitrile were on average over ten-fold greater for iridium complexes (1.25% ± 0.11% *vs*. 0.09% ± 0.02%, $p = 1.2 \times 10^{-11}$) with negligible phosphorescence observed for the ruthenium complexes making them ineffective as theranostic agents. Emission quantum yields of iridium complexes increased significantly (1.25% ± 0.11% to 12.56% ± 3.44%, $p = 4.0 \times 10^{-8}$) after bubbling the solutions with nitrogen, demonstrating the reactivity of the triplet state towards oxygen. This is further evidenced by the 8-fold difference in emissions between acetonitrile and PBS (1.25% ± 0.11% *vs*. 9.27% ± 1.54%, $p = 7.1 \times 10^{-8}$), which contain dissolved oxygen concentrations of 2.4 mM and 0.2 mM, respectively.[78,79] Interestingly, whilst there was a small but significant difference between ruthenium complexes in acetonitrile

before and after nitrogen-bubbling (0.09% ± 0.02% *vs*. 0.18% ± 0.04%, $p = 0.03$), the difference between air-equilibrated solutions of acetonitrile and PBS was not significant (0.09% ± 0.02% *vs*. 0.15% ± 0.05%, $p = 0.12$), suggesting the concentration of oxygen in solution has little effect on phosphorescence.

Measuring the phosphorescence signal of singlet oxygen at 1270 nm using different concentrations of photosensitizer with 420 nm irradiation resulted in an average quantum yield of 61% ± 2% for iridium complexes **1-10** in air-equilibrated acetonitrile, slightly better than the 57% known for reference complex $[Ru(bpy)_3]^{2+}$.[80] Similar results have been observed for many other cyclometalated Ir(III) complexes in acetonitrile.[81–83] This indicates efficient intersystem crossing from singlet to triplet excited states as well as efficient energy transfer from the excited triplet state to ground-state (triplet) oxygen. The singlet oxygen quantum yield dropped dramatically for ruthenium complexes **11-14**, averaging 3% ± 1% in air-equilibrated acetonitrile. Although DFT calculations predict a sufficiently high energy triplet state to generate singlet oxygen (>0.98 eV), the low singlet oxygen quantum yields are likely due to the short excited state lifetimes of around 5 ns.

For both series of complexes, the sum of the singlet oxygen and phosphorescence quantum yields do not account for 100% of the depopulation of the triplet state (Ir complexes ~ 65%, Ru complexes ~ 5%). This may be due to some electron transfer towards the sugar moiety, which would in turn lead to the short excited state lifetimes, most notably observed for the Ru series. Gasser *et al*. have reported $[Ru(bpy)_2(dipyridophenazine)]^{2+}$ complexes with singlet oxygen quantum yields as high as 90%,[84] indicating the importance of the third N^N ligand (in this case, the sugar-bearing ligand) for singlet oxygen photosensitization.

Iridium β-glucose complex **4** was also studied by collaborators Huang *et al.* as part of an investigation into the effects of modifying the C^N ligand.[85] Part of this study included determining the singlet oxygen quantum yield for complex **4** in water to be 6% using a UV-vis method based on the absorption of ABDA (a singlet oxygen scavenger) in the presence of light. This is roughly one tenth of that observed in acetonitrile, likely due to the acetonitrile having 10× more dissolved oxygen than water.[78,79] Considering the related structures of **1-10** and their similar quantum

yields in acetonitrile, it is expected that the series in water would all exhibit singlet oxygen quantum yields around 6%, though this needs experimental validation.

The complexes synthesised in this Chapter all contain a known substrate for GLUT1, which may lead to selectivity towards GLUT1-overexpressing cancer cells. The iridium complexes exhibited far better photophysical properties than the ruthenium complexes, so will be further explored in **Chapter 4** for biological activity and cancer targeting *in vitro*.

3.5 Conclusions and future work

Novel iridium(III) and ruthenium(II) glycoconjugates of glucose, mannose and galactose were prepared using facile reflux and deprotection methods with ligands synthesised using standard "click" reactions from their corresponding sugar azides. The previously unreported X-ray crystal structure of 2,3,4,6-tetra-*O*-acetyl-α-D-galactopyranosyl azide was determined. The presence of diastereomers complicated the assignment of ^{1}H NMR spectra for each complex. These complexes were stable in DMSO, PBS, cell culture media and acetonitrile, as well as photostable in acetonitrile, allowing for their use in photophysical and potentially biological studies.

Ruthenium complexes **11**-**14** were all inefficient photosensitizers, with singlet oxygen quantum yields in acetonitrile below 5% due to their excited state lifetimes being less than 15 ns, which did not increase upon saturation with nitrogen. However, iridium complexes **1**-**10** were found to have relatively high singlet oxygen quantum yields (~60%) and much longer excited state lifetimes up to 135 ns, which increased to over 400 ns when solutions in acetonitrile were saturated with nitrogen. Coupled with their phosphorescence, this makes the iridium complexes much more promising as potential phototherapeutic and diagnostic agents.

Adjusting the C^N ligands on Ir(III) complexes can dramatically change the photophysical properties of the complexes. Longer irradiation wavelengths towards the therapeutic window (600-800 nm) would make these complexes more clinically appealing, as well as potentially increasing singlet oxygen quantum yields and therefore cytotoxicity. McFarland *et al*. have demonstrated the potential of osmium

complexes as photosensitizers with longer absorption wavelengths,[24] however, here attempts to synthesise Os glycoconjugates were unsuccessful. An alternative synthetic route for potential future osmium glycoconjugates with PEG linkers is proposed below (**Figure 3.19**).

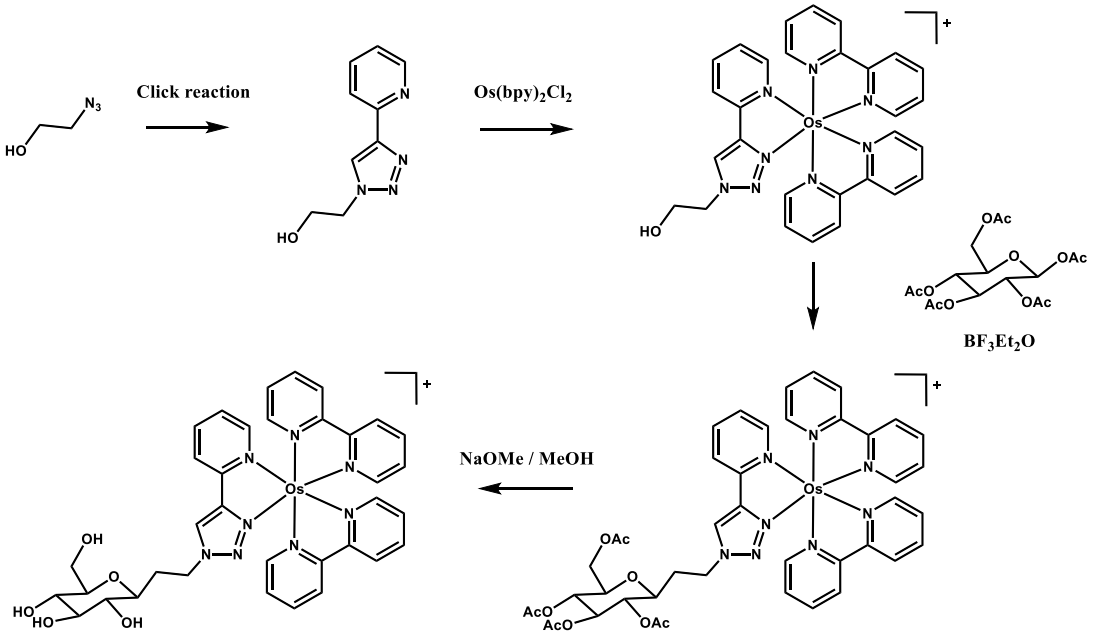

Figure 3.19. Proposed synthesis for Os-PEG-Glc complexes.

3.6 References

1 M. D. S. Baptista, J. Cadet, P. Di Mascio, A. A. Ghogare, A. Greer, M. R. Hamblin, C. Lorente, S. Cristina Nunez, M. S. Ribeiro, A. H. Thomas, M. Vignoni and T. M. Yoshimura, *Photochem. Photobiol.*, 2017, **93**, 912–919.

2 G. G. Kramarenko, S. G. Hummel, S. M. Martin and G. R. Buettner, *Photochem. Photobiol.*, 2006, **82**, 1634.

3 P. Liang, D. Kolodieznyi, Y. Creeger, B. Ballou and M. P. Bruchez, *Front. Chem.*, 2020, **8**, 1–11.

4 M. Riethmüller, N. Burger and G. Bauer, *Redox Biol.*, 2015, **6**, 157–168.

5 Z. Y. Jin, H. Fatima, Y. Zhang, Z. Shao and X. J. Chen, *Adv. Therap.*, **2022**, 5, 2100176.

6 J. Zhou, Y. Kang, L. Chen, H. Wang, J. Liu, S. Zeng and L. Yu, *Front. Pharmacol.*, 2020, **11**, 1–17.

7 H. Park, W. Park and K. Na, *Biomaterials*, 2014, **35**, 7963–7969.

8 T. Sheng, Y. Ong, T. M. Busch and T. C. Zhu, *Biomed. Opt. Express*, 2020, **11**, 4586.

9 J. Usuda, H. Kato, T. Okunaka, K. Furukawa, H. Tsutsui, K. Yamada, Y. Suga, H. Honda, Y. Nagatsuka, T. Ohira, M. Tsuboi and T. Hirano, *J. Thorac. Oncol.*, 2006, **1**, 489–493.

10 M. R. Hamblin, *Photochem. Photobiol.*, 2020, **96**, 506–516.

11 G. Bauer, *Anticancer Res.*, 2016, **36**, 5649–5663.

12 L. Ricciardi and M. La Deda, *SN Appl. Sci.*, 2021, **3**, 372.

13 H. Huang, S. Banerjee and P. J. Sadler, *ChemBioChem*, 2018, **19**, 1574–1589.

14 L. K. McKenzie, I. V. Sazanovich, E. Baggaley, M. Bonneau, V. Guerchais, J. A. G. Williams, J. A. Weinstein and H. E. Bryant, *Chem. - A Eur. J.*, 2017, **23**, 234–238.

15 X. D. Bi, R. Yang, Y. C. Zhou, D. Chen, G. K. Li, Y. X. Guo, M. F. Wang, D. Liu and F. Gao, *Inorg. Chem.*, 2020, **59**, 14920–14931.

16 H. Yang, J. Zhuang, N. Li, Y. Li, S. Zhu, J. Hao, J. Xin and N. Zhao, *Mater. Chem. Front.*, 2020, **4**, 2064–2071.

17 K. Yang, Y. Zhou, Y. Wang, S. Zhao, X. Wu, X. Peng, L. Huang, L. Jiang, M. Lan and X. Y. Yi, *Chem. - An Asian J.*, 2021, 16, 1780–1785.

18 D. L. Ma, H. J. Zhong, W. C. Fu, D. S. H. Chan, H. Y. Kwan, W. F. Fong, L. H. Chung, C. Y. Wong and C. H. Leung, *PLoS One*, 2013, **8**, 1–8.

19 K. K. W. Lo and K. Y. Zhang, *RSC Adv.*, 2012, **2**, 12069–12083.

20 K. Y. Zhang, T. Zhang, H. Wei, Q. Wu, S. Liu, Q. Zhao and W. Huang, *Chem. Sci.*, 2018, **9**, 7236–7240.

21 NCT03053635 Intravesical Photodynamic Therapy (PDT) in BCG

Refractory High-Risk Non-muscle Invasive Bladder Cancer (NMIBC) Patients, https://clinicaltrials.gov/ct2/show/NCT03053635, (accessed 8 September 2022).

22 NCT03945162 Intravesical Photodynamic Therapy (PDT) in BCG Refractory/Intolerant Non-Muscle Invasive Bladder Cancer (NMIBC) Patients, https://clinicaltrials.gov/ct2/show/NCT03945162, (accessed 8 September 2022).

23 S. Monro, K. L. Colón, H. Yin, J. Roque, P. Konda, S. Gujar, R. P. Thummel, L. Lilge, C. G. Cameron and S. A. McFarland, *Chem. Rev.*, 2019, **119**, 797–828.

24 J. A. Roque, P. C. Barrett, H. D. Cole, L. M. Lifshits, G. Shi, S. Monro, D. Von Dohlen, S. Kim, N. Russo, G. Deep, C. G. Cameron, M. E. Alberto and S. A. McFarland, *Chem. Sci.*, 2020, **11**, 9784–9806.

25 Y. Sun, M. Hu, F. Wang, H. Tan, J. Hu, X. Wang, B. Wang, J. Hu and Y. Li, *Anal. Biochem.*, 2021, **631**, 114357.

26 A. Glenister, M. I. Simone and T. W. Hambley, *PLoS One*, 2019, **14**, 1–16.

27 M. Patra, T. C. Johnstone, K. Suntharalingam and S. J. Lippard, *Angew. Chem.*, 2016, **128**, 2596–2600.

28 D. Shishmarev, C. Q. Fontenelle, I. Kuprov, B. Linclau and P. W. Kuchel, *Biophys. J.*, 2018, **115**, 1906–1919.

29 M. Mueckler and B. Thorens, *Mol. Aspects Med.*, 2013, **34**, 121–138.

30 S. Sprouse, K. A. King, P. J. Spellane and R. J. Watts, *J. Am. Chem. Soc.*, 1984, **106**, 6647–6653.

31 M. Ismael, *New J. Chem.*, 2019, **43**, 9596–9605.

32 A. Bianchi and A. Bernardi, *J. Org. Chem.*, 2006, **71**, 4565–4577.

33 V. Percec, P. Leowanawat, H. J. Sun, O. Kulikov, C. D. Nusbaum, T. M. Tran, A. Bertin, D. A. Wilson, M. Peterca, S. Zhang, N. P. Kamat, K. Vargo, D. Moock, E. D. Johnston, D. A. Hammer, D. J. Pochan, Y. Chen, Y. M. Chabre, T. C. Shiao, M. Bergeron-Brlek, S. André, R. Roy, H. J.

Gabius and P. A. Heiney, *J. Am. Chem. Soc.*, 2013, **135**, 9055–9077.

34 L. Szilágyi and Z. Györgydeák, *Carbohydr. Res.*, 1985, **143**, 21–41.

35 H. Song, PhD Thesis, University of Warwick, 2018.

36 L. Sršan and T. Ziegler, *Beilstein J. Org. Chem.*, 2020, **16**, 888–894.

37 S. Cecioni, J. P. Praly, S. E. Matthews, M. Wimmerová, A. Imberty and S. Vidal, *Chem. - A Eur. J.*, 2012, **18**, 6250–6263.

38 S. M. Paterson, J. Clark, K. A. Stubbs, T. V. Chirila and M. V. Baker, *J. Polym. Sci. Part A Polym. Chem.*, 2011, **49**, 4312–4315.

39 Q. Zhao, Y. Zou, J. Guo, S. Yu, X. Chai, H. Hu and Q. Wu, *Tetrahedron*, 2014, **70**, 7780–7787.

40 M. Li, W. Ye, K. Fu, C. zhou, Y. Shi, W. Huang, W. Chen, J. Hu, Z. Jiang and W. Zhou, *Eur. J. Med. Chem.*, 2020, **202**, 112509.

41 L. Meier, G. C. Monteiro, R. A. M. Baldissera and M. M. Sá, *J. Braz. Chem. Soc.*, 2010, **21**, 859–866.

42 S. Proctor, S. Lovera, A. Tomich and V. Lavallo, *ACS Cent. Sci.*, 2022, **8**, 874–876.

43 Gaussian 16 Revision C.01, M. J. Frisch, G. W. Trucks, H. B. Schlegel, *et al.*, Gaussian, Inc., Wallingford CT, 2016.

44 Alex D. Beck, *J. Chem. Phys.*, 1993, **98**, 5648–5656.

45 C. Lee, W. Yang and R. G. Parr, *Phys. Rev. B*, 1988, **37**, 785–789.

46 F. Weigend and R. Ahlrichs, *Phys. Chem. Chem. Phys.*, 2005, **7**, 3297–3305.

47 Dalton, a molecular electronic structure program, Release Dalton 2016. http://daltonprogram.org.

48 S. Koseki, M. W. Schmidt and M. S. Gordon, *J. Phys. Chem. A*, 1998, **102**, 10430–10435.

49 A. L. Whittock, J. M. Woolley, N. Auckloo, C. Corre and V. G. Stavros,

Molecules, 2022, 27, 2272.

50 J. Liu, A. W. Prentice, G. J. Clarkson, J. M. Woolley, V. G. Stavros, M. J. Paterson and P. J. Sadler, *Adv. Mater.*, 2023, 2210363.

51 S. A. Ross and G. Lowe, *Tetrahedron Lett.*, 2000, **41**, 3225–3227.

52 C. J. Capicciotti, J. F. Trant, M. Leclère and R. N. Ben, *Bioconjug. Chem.*, 2011, **22**, 605–616.

53 T. H. Barkae, A. M. Zeid, S. Quan, M. R. H. S. Gilani, B. Lou and G. Xu, *J. Electroanal. Chem.*, 2022, **904**, 115954.

54 B. T. Worrell, J. A. Malik and V. V. Fokin, *Science*, 2013, **340**, 457–460.

55 S. Lazic, P. Kaspler, G. Shi, S. Monro, T. Sainuddin, S. Forward, K. Kasimova, R. Hennigar, A. Mandel, S. McFarland and L. Lilge, *Photochem. Photobiol.*, 2017, **93**, 1248–1258.

56 S. Sasmal and K. Mohanty, in *Biorefining of Biomass to Biofuels*, eds. S. Kumar and R. K. Sani, Springer Nature, Cham, 2018, pp. 203–221.

57 V. Ji Ram, A. Sethi, M. Nath and R. Pratap, in *The Chemistry of Heterocycles*, Elsevier, Amsterdam, 1st edn., 2019, pp. 149–478.

58 K. Ágoston, A. Dobó, J. Rákó, J. Kerékgyártó and Z. Szurmai, *Carbohydr. Res.*, 2001, 330, 183–190.

59 Z. Szurmai, A. Lipták and G. Snatzke, *Carbohydr. Res.*, 1990, **200**, 201–208.

60 J. Cornish, K. E. Callon, C. Q. X. Lin, C. L. Xiao, T. B. Mulvey, G. J. S. Cooper and I. R. Reid, *Am. J. Physiol. - Endocrinol. Metab.*, 1999, **277**, 779–783.

61 J. Sloop, *Reports Org. Chem.*, 2013, 1.

62 S. Noimark, E. Salvadori, R. Gómez-Bombarelli, A. J. MacRobert, I. P. Parkin and C. W. M. Kay, *Phys. Chem. Chem. Phys.*, 2016, **18**, 28101–28109.

63 D. Shah, M. Eroy, J. Fakhry, A. Moffat, K. Fritz, H. D. Cole, C. G.

Cameron, S. A. McFarland and G. Obaid, *Pharmaceutics*, 2022, **14**, 2426.

64 R. Bryan Sears, L. E. Joyce and C. Turro, *Photochem. Photobiol.*, 2010, **86**, 1230–1236.

65 L. M. Quan, B. D. Stringer, M. A. Haghighatbin, J. Agugiaro, G. J. Barbante, D. J. D. Wilson, C. F. Hogan and P. J. Barnard, *Dalton Trans.*, 2019, **48**, 653–663.

66 H. Kloverpris Henrik, A. Fomsgaard, A. Handley, J. Ackland, M. Sullivan and P. Goulder, *J. Immunol. Methods*, 2010, **356**, 70–78.

67 D. Kaiser, N. M. Otto, O. McCallion, H. Hoffmann, G. Zarrinrad, M. Stein, C. Beier, I. Matz, M. Herschel, J. Hester, G. Moll, F. Issa, P. Reinke and A. Roemhild, *Front. Cell Dev. Biol.*, 2021, **9**, 1–12.

68 E. J. Anthony, E. M. Bolitho, H. E. Bridgewater, O. W. L. Carter, J. M. Donnelly, C. Imberti, E. C. Lant, F. Lermyte, R. J. Needham, M. Palau, P. J. Sadler, H. Shi, F. X. Wang, W. Y. Zhang and Z. Zhang, *Chem. Sci.*, 2020, **11**, 12888–12917.

69 S. J. Fischer, L. M. Benson, A. Fauq, S. Naylor and A. J. Windebank, *Neurotoxicology*, 2008, **29**, 444–452.

70 K. El-Naggar, H. S. Abdel-Samad, R. M. Ramadan, M. E. El-Khouly and A. A. Abdel-Shafi, *J. Photochem. Photobiol. A Chem.*, 2022, **436**, 114405.

71 A. F. Olea and F. Wilkinson, *J. Phys. Chem.*, 1995, **99**, 4518–4524.

72 S. Das and B. Pradhan, *RSC Adv.*, 2015, **5**, 73726–73731.

73 H. Sun and M. Z. Hoffman, *J. Phys. Chem.*, 1993, **97**, 11956–11959.

74 E. Baranoff, H. J. Bolink, E. C. Constable, M. Delgado, D. Häussinger, C. E. Housecroft, M. K. Nazeeruddin, M. Neuburger, E. Ortí, G. E. Schneider, D. Tordera, R. M. Walliser and J. A. Zampese, *Dalton Trans.*, 2013, **42**, 1073–1087.

75 Y. Zhou, Y. Ding, Y. Huang, L. Cai, J. Xu and X. Ma, *ACS Omega*, 2020, **5**, 3638–3645.

76 J. Guo, X. Pan, J. Li, W. Wu and J. Zhang, *Spectrochim. Acta - Part A Mol.*

Biomol. Spectrosc., 2019, **216**, 179–189.

77 J. E. Yarnell, P. De La Torre and F. N. Castellano, *Eur. J. Inorg. Chem.*, 2017, **2017**, 5238–5245.

78 Y. Zhang, D. A. Robinson, K. McKelvey, H. Ren, H. S. White and M. A. Edwards, *J. Electrochem. Soc.*, 2020, **167**, 166507.

79 C. Franco and J. Olmsted, *Talanta*, 1990, **37**, 905–909.

80 A. A. Abdel-Shafi, P. D. Beer, R. J. Mortimer and F. Wilkinson, *J. Phys. Chem. A*, 2000, **104**, 192–202.

81 N. Hasebe, Y. Deguchi, S. Murayama, T. Yoshihara, H. Horiuchi, T. Okutsu and S. Tobita, *J. Photochem. Photobiol. A Chem.*, 2016, **324**, 134–144.

82 L. P. Li and B. H. Ye, *Inorg. Chem.*, 2019, **58**, 7775–7784.

83 A. A. Abdel-Shafi, J. L. Bourdelande and S. S. Ali, *Dalton Trans.*, 2007, 2510–2516.

84 C. Mari, V. Pierroz, R. Rubbiani, M. Patra, J. Hess, B. Spingler, L. Oehninger, J. Schur, I. Ott, L. Salassa, S. Ferrari and G. Gasser, *Chem. - A Eur. J.*, 2014, **20**, 14421–14436.

85 Z. Zhu, L. Wei, Y. Lai, O. W. L. Carter, S. Banerjee, P. J. Sadler and H. Huang, *Dalton Trans.*, 2022, **51**, 10875–10879.

Chapter 4

Biochemical evaluation of Ir(III) glycoconjugates

4 Biochemical evaluation of Ir(III) glycoconjugates

In this Chapter, the cytotoxicities of a series of Ir(III) glycoconjugates and a methyl analogue synthesised in Chapter 3 are determined in A549 lung cancer cells under dark and irradiated conditions for evaluation as PDT photosensitizers. Selectivity of complexes for cancer cells is determined by confocal microscopy studies in A549 and MRC5 (non-cancerous) cells. GLUT1 targeting and relative hydrophobicity studies are performed to explain differences in cellular accumulation, whilst binding to serum proteins is investigated.

4.1 Introduction

The high metabolic and rapid proliferation rates of cancer cells increase glucose demand, and yet ATP production is carried out in an inefficient manner.[1] Even in an aerobic environment (suitable for oxidative phosphorylation) cancer cells rely on anaerobic glycolysis, despite yielding only 2 molecules of ATP per glucose molecule, instead of 36 ATP molecules generated by oxidative phosphorylation.[2] This phenomenon, known as the Warburg Effect, is a key hallmark of cancer cells.[3] Importantly, many cancer cells overexpress glucose transporter 1 (GLUT1), the major glucose transporter encoded for by the gene *SLC2A1*, in order to facilitate their higher glucose requirements.[4–7]

Expression and activity levels of GLUT1 directly influence the uptake of the clinical radiotracer 2-deoxy-2-[^{18}F]-fluoroglucose (fluorodeoxyglucose, [^{18}F]-FDG, **Figure 4.1**), a glucose analogue used in positron emission tomography/computed tomography (PET/CT) for the diagnosis, staging and restaging of cancers in patients.[8] Maximum standardised uptake value (SUV_{max}) gives a semi-quantitative measurement of [^{18}F]-FDG uptake, giving a ratio of activity in a defined region of interest compared to that of the rest of the body – an SUV_{max} greater than 2.5 is often considered a sign of malignant tissue, although this is not definitive (*i.e.* some tumours will have $SUV_{max} < 2.5$ whilst some non-malignant tissue will have $SUV_{max} > 2.5$).[9] Results from [^{18}F]-FDG PET/CT scans led to a change in treatment in 34% of lung cancer patients over two years,[10] whilst a meta-analysis of 721 small cell lung cancer patients found 15% of cases to be

restaged due to [^{18}F]-FDG PET/CT imaging.[11] Uptake of [^{18}F]-FDG was found to be GLUT1-dependent in high-risk prostate cancers, with expression of GLUT1 also linked to poor prognostic factors.[12]

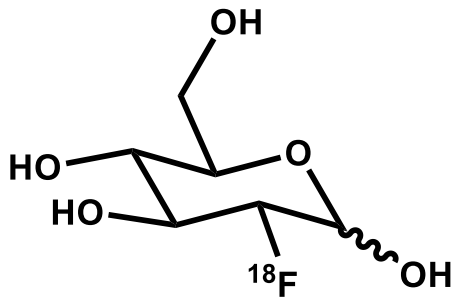

Figure 4.1. Structure of 2-deoxy-2-[^{18}F]-fluoroglucose ([^{18}F]-FDG).

A study of 30 clinical oral squamous cell carcinoma (OSCC) patients found that GLUT1 expression occurs early in the development of these cancers and increases significantly with clinical staging (1-4), suggesting GLUT1 may be useful as a prognostic biomarker in OSCC.[13] Similarly, high expression levels of GLUT1 can also be used as a biomarker for certain subtypes of breast cancer.[14] A 2018 meta-analysis by Li *et al*. including 2653 cases of lung cancer concluded that positive expression of GLUT1 leads significantly to poor prognoses and could therefore be used as a predictive biomarker in lung cancer patients.[15]

Increasing the selectivity of cancer drugs can be achieved by covalently binding active therapeutics to molecules targeted to cancer cells, exploiting many of the proteins that are overexpressed relative to non-cancerous cells (*e.g.* glucose transporter 1, epithelial growth factor receptors 1 and 2), leading to the cytotoxic compound being internalised *via* the other molecule.[16,17] Glycoconjugation to the clinically-used antineoplastic compound ifosfamide led to glufosfamide (**Figure 4.2**), a GLUT1-targeting analogue which has passed Phase I and II clinical trials in pancreatic cancer,[18] and is currently undergoing Phase III clinical trials (estimated study completion date: March 2023).[19]

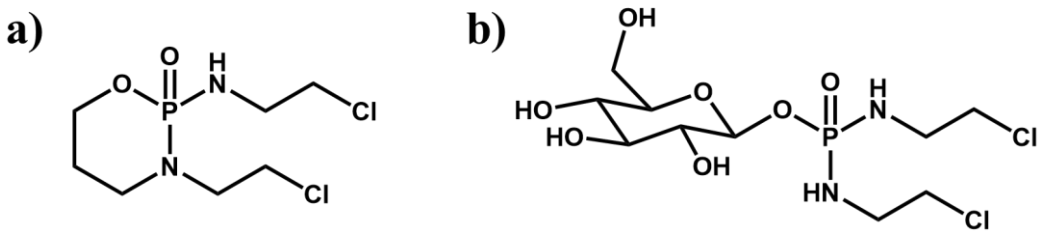

Figure 4.2. Structures of a) ifosfamide and b) glufosfamide.[18]

Several metal complexes have previously been investigated for GLUT1 targeting by covalent conjugation to glucose. Platinum complexes have been widely explored for glycoconjugation,[20–25] building on the clinical successes of cisplatin, oxaliplatin and carboplatin.[26] Lippard *et al.* demonstrated that conjugation of [(*trans*-1,2-diaminocyclohexane)(2,2-dimethyl malonato)Pt(II)] to glucose through each hydroxyl group of the sugar moiety led to differences in accumulation and antiproliferative activity across all six positional isomers (C1α, C1β, C2, C3, C4 and C6, **Figure 4.3**).[22] The preferred isomer (highest accumulation) was highly dependent on the cell line used, however, accumulation of all isomers was reduced in cells treated with 50 μM of GLUT inhibitor cytochalasin B, indicating that all six complexes were internalised *via* a glucose transporter. *In vivo* studies showed the C2 isomer delayed tumour growth as effectively as the clinically used platinum anticancer complex oxaliplatin. However, there are currently no Pt glycoconjugates in clinical trials, though their potential has been explored and recently reviewed by Patra *et al*.[27]

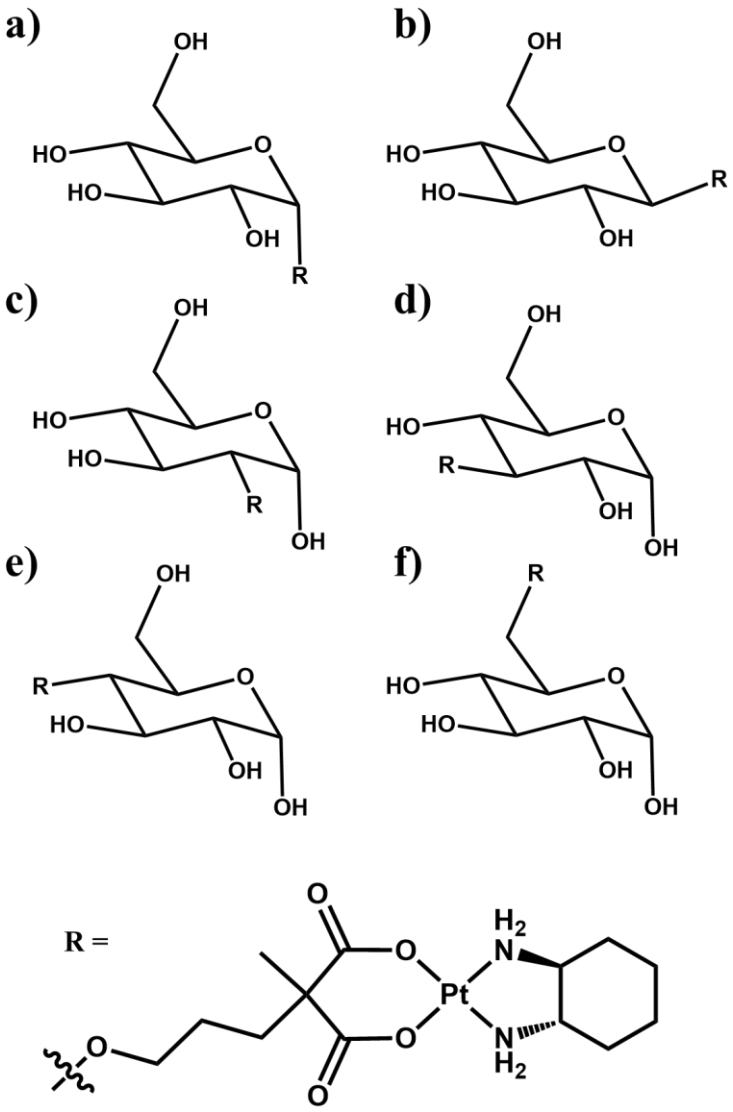

Figure 4.3. Reported platinum glycoconjugates with glucose substituted at a) C1α, b) C1β, c) C2, d) C3, e) C4, and f) C6. R = [(*trans*-1,2-diaminocyclohexane)(2,2-dimethyl malonato)Pt(II)].[22]

2-(N-(7-nitrobenz-2-oxa-1,3-diazol-4-yl)amino)-2-deoxyglucose (2-NBDG, **Figure 4.4a**) is known to be internalised *via* glucose transporters,[28] and Hambley *et al*. demonstrated that adding a 9-atom poly(ethyleneglycol) (PEG3, **Figure 4.4b**) linker led to greater glucose-dependent uptake and further penetration into multicellular spheroids.[29]

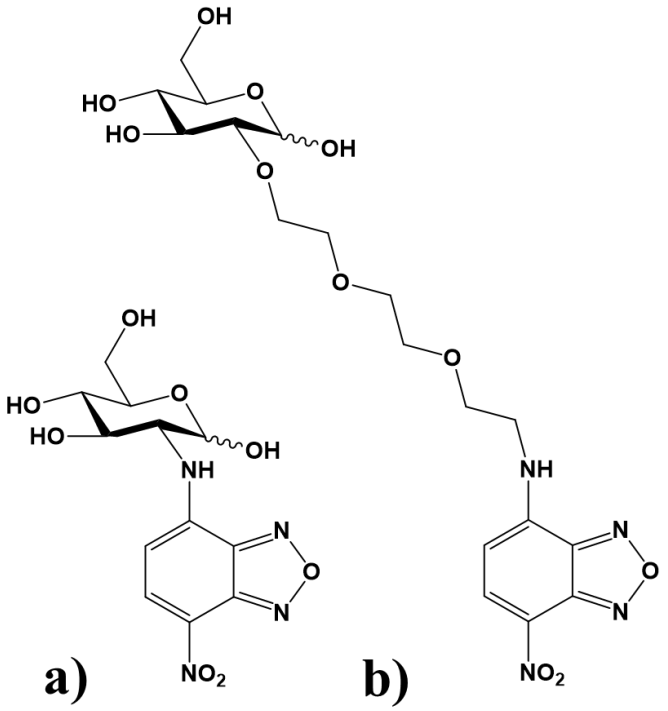

Figure 4.4. Structures of a) 2-NBDG and b) PEG3 "linker" analogue of 2-NBDG.[29]

Cyclometalated iridium(III) complexes functionalised with glucose *via* a *N*-methylamino-oxy-PEG3 linker at the C1β position were found to have greater uptakes in HeLa cells compared to galactose analogues.[30] However, comparisons were only made between the glucose complexes and the respective galactose analogues. Since these iridium(III) complexes were found to be highly luminescent and stable towards photobleaching, there was potential for use as phosphorescent glucose uptake indicators, though interestingly, there was no exploration into their suitability as photosensitizers for photodynamic therapy.

Attaching a pendant glucose has been demonstrated to be an attractive strategy for the targeting of GLUT1 by metal-based anticancer complexes. This Chapter investigates how changing the sugar (glucose, mannose, galactose) and linker lengths (PEG1, PEG2, PEG3) on iridium(III) complexes (**Chapter 3, Figure 3.5**) affects accumulation in A549 lung cancer cells which are known to overexpress GLUT1.[31–33] Importantly, non-small cell lung cancers are currently treated clinically using photodynamic therapy, highlighting the relevance of using this cell line in these studies.[34,35] Relative lipophilicity, serum protein binding and GLUT1

targeting (co-administration to cells in the presence of a highly specific GLUT1 inhibitor) were explored for the series of Ir(III) complexes, which were further evaluated to determine antiproliferative activities with and without irradiation, as well as the generation of singlet oxygen ($^1O_2$) in cells (solution $^1O_2$ determined in **Chapter 3, Section 3.3.6**). MRC5 non-cancerous lung fibroblasts were used to determine selectivity factors since MRC5 cells have low expression levels of GLUT1 and originate from the same organ (lung).[36] Ru(II) complexes **11-14** were not investigated further due to their poor singlet oxygen quantum yields, limiting their use as Type II photosensitizers. Due to limits on laboratory use and subsequent time constraints caused by COVID-19, α-anomer complexes **1-3** from **Chapter 3** were not investigated for their GLUT1 targeting, although antiproliferative activities (IC_{50}) without irradiation were determined.

4.2 Experimental

Complexes **1-10** used in this Chapter were synthesised in **Chapter 3**. GLUT1 inhibitor **BAY-876** was purchased from Sigma Aldrich. Materials and protocols for cell maintenance and media preparation are listed in **Chapter 2, Section 2.3.2**. ICP-OES and ICP-MS techniques are described in **Chapter 2, Sections 2.2.8 and 2.2.9.**

4.2.1 *In vitro* growth inhibition assay (IC_{50})

Upon reaching 80-90% confluence, A549 cells were washed with PBS (10 mL) and treated with 2 mM trypsin/EDTA (2 mL) and incubated at 310 K for 5 min. Fully prepared RPMI-1640 (no phenol red) was added to obtain a single-cell suspension, then cells counted using a haemocytometer. Cells were seeded in a 96-well black plate (clear, flat-bottomed, tissue-culture treated) at a density of 2×10^4 cells per well (150 µL) and incubated at 310 K for 48 h before use.

Stock solutions of compounds were prepared at 200 µM (5% DMSO, 95% fully prepared culture medium), then serial-diluted to achieve concentrations of 200, 100, 50, 20, 2, and 0.2 µM (for **BAY-876**, the final concentrations were 500, 100, 50, 10, 5, 1, 0.5, 0.1, 0.05, 0.01, 0.005, and 0.001 µM). In triplicate, 200 µL of each solution was added to cells. Each plate contained **$[Ru(bpy)_2(dppn)]Cl_2$** (positive photoactive control) and untreated (negative control) wells. Cells were incubated in medium containing the test compound for 1 h at 310 K. This medium was then

removed, and cells were washed using phosphate buffered saline (100 µL). RPMI-1640 (150 µL, no phenol red) was added and cells were either i) incubated in the dark for 1 h; or ii) irradiated (λ = 425 nm, 4.8 mW·cm^{-2}) for 1 h. Accounting for the surface area of each well, the total energy for each well equated to 5.74 J (**Appendix Light intensity A1**). Cells were then incubated for 24 h ("recovery time") in the dark. Aliquots of the original 200 µM stock solutions were analysed using ICP-OES to accurately determine the concentration of Ir in solution (**Section 2.2.8**).

Cell viability was determined using the Sulforhodamine B (SRB) colorimetric assay.[37] Cold trichloroacetic acid (50% v/v, 50 µL) was added to each well and the plate was refrigerated at 277 K for 1 h. The plate was then washed with water using an automated plate washer (Molecular Devices Multiwash+ microplate washer) and air-dried. To each well, 50 µL SRB dye (0.4%, in 1% acetic acid) was added and incubated for 30 min at ambient temperature. Excess dye was next removed with 1% acetic acid washing, using the automated plate washer and plates were dried. Finally, 150 µL of Tris base solution (pH 10.5, 10 mM) was added to solubilise the protein-bound dye. Plates were then left for 1 h at 298 K. Absorbance was measured using a SkanIt microplate reader (λ_{abs} = 492 nm). Cell viability was determined relative to the negative control wells. Data were processed in Microsoft Excel and plotted as normalised percentage survival *vs* Log(concentration, mM) in OriginPro 2016 and fitted with a dose-response curve. Experiments were performed in duplicate of triplicate, allowing the mean IC_{50} (half-maximal inhibitory concentration) and associated standard deviation to be calculated.

4.2.2 Cellular accumulation of iridium

A549 lung cancer cells were grown as described previously (**Chapter 2 Section 2.3.2**). Cells were seeded to achieve a density of 5 × 10^4 cells per mL. 10 mL cell suspension (5 × 10^5 cells) was then added to each P100 petri dish and incubated for 48 h.

Stock solutions of complexes (200 µM) were prepared as previously described in **Section 4.2.1**, and then diluted to achieve a final working concentration of 50 µM. The supernatant was removed from the petri dishes and 10 mL of 50 µM complex

solution was added. Samples were prepared in triplicate, in addition to untreated (culture medium only) controls. Cells were incubated with test compound for 1 h at 310 K, then the supernatant medium was removed, and cells were washed with PBS. Cells were then harvested using trypsin/EDTA and counted in a haemocytometer. Cells were transferred to 15 mL centrifuge tubes and centrifuged at 1000 rpm for 5 min at ambient temperature. The supernatant was removed, cells were resuspended in 1 mL PBS and transferred to 2 mL Eppendorf tubes, then centrifuged again at 1000 rpm for 5 min at ambient temperature. The supernatant was again removed to afford whole cell pellets, which were digested in 200 µL concentrated ultrapure nitric acid (72% *v/v*, 353 K, overnight). Finally, samples were diluted to achieve a final working acid concentration of 3.6% nitric acid, using milliQ water. Analysis for iridium (^{193}Ir) analysed using an Agilent 7900 series ICP-MS in no-gas mode. Results were normalised to cell count to enable data to be reported as femtograms of iridium per cell (fg Ir·cell^{-1}).

For experiments carried out in the presence of the GLUT1 inhibitor **BAY-876**, cells were seeded and incubated for 48 h, then pre-treated with 100 µM **BAY-876** (5 mL) for 1 h. Solutions of 100 µM complex **4**, **9** or **10** were then added to achieve final working concentrations of 50 µM Ir complex and 50 µM **BAY-876**, which were incubated for a further 1 h. After this time, cell pellets were harvested and processed as described above in **Section 4.2.2.**

4.2.3 Capacity factors

Capacity factors were determined using an Agilent 1200 Series HPLC system with a 100 µL loop and Agilent ZORBAX Eclipse XDB-C18 column (250 × 4.6 mm, 5 µm i.d.) as described previously (**Chapter 2, Section 2.2.6**) using an isocratic method (1:1 acetonitrile and water, each containing 0.1% v/v trifluoroacetic acid) at 298 K. Uracil (reference for retention times) and metal complexes were prepared at a concentration of 0.1 mg·mL^{-1} in 50% acetonitrile, 50% water and filtered through Minisart® SRP 4 syringe filters with 0.45 µm PTFE membranes. Injection volume: 100 µL. Flow rate: 1 mL·min^{-1}. All analyses were performed as experimental triplicates. Capacity factors were calculated using:

$$R_F = t_R - t_0$$

$$K = \frac{R_F}{t_0}$$

Where R_F is the retention factor, t_R is the sample retention time, t_0 is the retention time of uracil (unretained) and K is the capacity factor.

4.2.4 Human serum binding studies

5 mM stocks of **4** and **9** were prepared in DMSO and diluted 100-fold using human serum to achieve a final working concentration of 50 µM and incubated at 310 K for either 1 h or 24 h. Samples were further diluted 10-fold with 50 mM Tris solution (pH 7.4). Analysis was carried out using an Agilent 1200 HPLC system fitted with a 100 µL loop and TSK-Gel Q-STAT strong anion exchange column (7 µm, 10 cm × 4.6 mm i.d.). Injection volume: 100 µL, flow rate: 0.7 mL·min^{-1} using the linear gradient shown in **Figure 4.5**. Buffer A: 50 mM Tris (pH 7.4). Buffer B: 50 mM Tris + 1 mM ammonium acetate (pH 7.4).

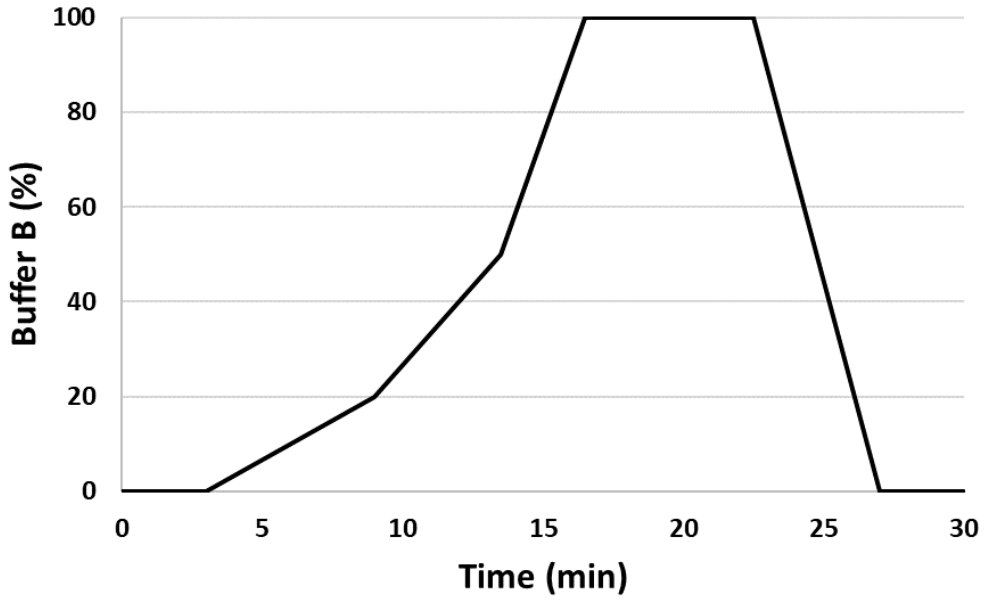

Figure 4.5. Gradient of Buffer B (%) over time. 0 min – 0%, 3 min – 0%, 9 min – 20%, 13.5 min – 50%, 16.5 min – 100%, 22.5 min – 100%, 27.5 min – 0%, 30 min – 0%.

Fractions were collected at 1 min intervals. Samples were injected four times and fractions were pooled, which were then analysed using an Agilent 7900 series ICP-MS to quantify ^{193}Ir in no-gas mode. Calibration standards were prepared in the range 0.1-1000 ppb using Buffer A. Data were acquired and processed using MassHunter 4.4 (v. C.01.04, build 544.8, patch 1) for Windows (Agilent Technologies, Inc.).

4.2.5 Confocal microscopy

A single-cell suspension of either A549 lung cancer cells or MRC5 healthy lung cells was diluted to achieve a density of 2×10^5 cells·mL^{-1}. To each quadrant of a CELLview^{TM} 35 mm petri dish was added 500 µL of the cell suspension and cells were incubated at 310 K for 24 h. After this time, the supernatant was removed and cells were treated with a 50 µM solution (500 µL in RPMI-1640) of either complex **4**, **9**, and **10** for 1 h. Cells were then washed twice with 500 µL PBS to remove Ir complex-containing solution. Cells were fixed using 2% formaldehyde solution and washed twice with 500 µL PBS. Cells were imaged with assistance from Dr Ian Hands-Portman (School of Life Sciences, University of Warwick) using a ZEISS LSM 710 confocal microscope equipped with 40× objective and a 405 nm argon excitation laser. Data were visualised using ZEN 2.3 and processed using ImageJ.

Assessment of GLUT1 targeting: this experiment was carried out with the following modification: cells were pre-treated with 250 µL of 100 µM BAY-876 solution in media for 1 h. Subsequently, 250 µL solutions of 100 µM **4**, **9** or **10** were added to give working concentrations of 50 µM inhibitor and complex. Excitation wavelength: 405 nm, detection wavelength: 489 nm. Data were processed using ImageJ with assistance from Dr Ian Hands-Portman.

Assessment of in-cell singlet oxygen generation: this experiment was carried out with the following modification: cells were treated with 50 µM Ir complex for 1 h, washed with PBS to remove Ir complex, fresh medium added, and cells were then irradiated with 425 nm blue light for 10 min. Immediately after irradiation, 5 µM

singlet oxygen sensor green (SOSG) was added and incubated for 20 min. Excitation wavelength: 514 nm, detection wavelength: 525 nm. This experiment was also carried out in the absence of Ir complex (negative control). Data were processed using ImageJ.

4.3 Results

4.3.1 Antiproliferative activity in non-irradiated A549 lung cancer cells

Antiproliferative activities (IC_{50}) of cyclometalated Ir(III) complexes **1-9** bearing sugar moieties (glucose/galactose/mannose), methyl analogue **10**, Ru(II) glycoconjugates **11-14**, and known photoactive agent **[Ru(bpy)$_2$(dppn)]Cl$_2$** (bpy = 2,2'-bipyridine, dppn = benzo[i]- dipyrido[3,2-a:20,30-c] phenazine, **Figure 4.6**),[38] were initially determined towards A549 epithelial lung cancer cells without irradiation ("Dark IC_{50}") to evaluate potency without irradiation. Cells were exposed to complexes across the concentration range 200-0.2 μM for 1 h, then washed with PBS to remove supernatant complex. Cells were then incubated in fresh medium in the dark for 1 h, followed by a 24 h recovery period. Concentrations were corrected by ICP-OES analysis of Ir or Ru. All complexes demonstrated no toxicity in the dark (IC_{50} > 100 μM), irrespective of the metal centre (Ru(II) or Ir(III)), sugar group (glucose, mannose, galactose, or no sugar group), or linker length (PEG1, PEG2, PEG3).

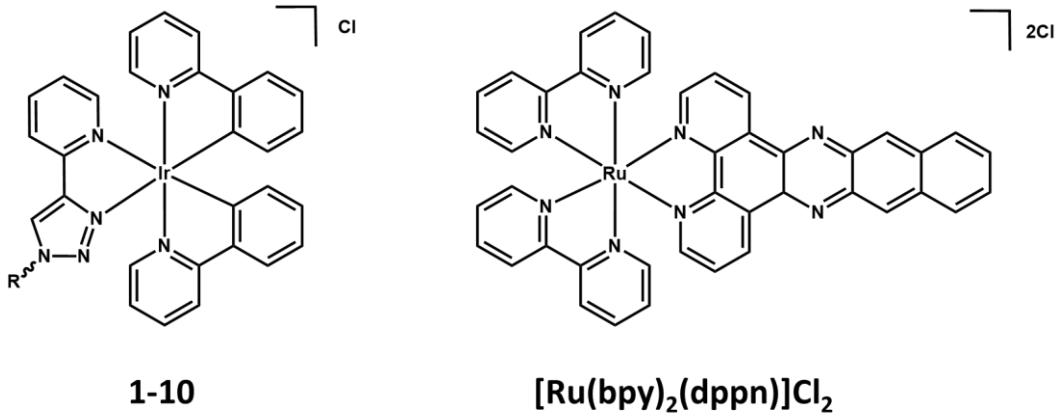

Figure 4.6. General structure of Ir(III) complexes **1-10** and **[Ru(bpy)$_2$(dppn)]Cl$_2$** synthesised by Turro et al.[38]

Table 4.1. Antiproliferative activity (IC_{50}) of complexes **1-10** and **$[Ru(bpy)_2(dppn)]Cl_2$** in the dark (no irradiation). Determined by SRB colorimetric assay with 1 h incubation, 1 h no irradiation, and 24 h recovery.

Complex		Dark IC_{50} (μM)
1	Ir-α-glucose	>100
2	Ir-α-mannose	>100
3	Ir-α-galactose	>100
4	Ir-β-glucose	>100
5	Ir-β-mannose	>100
6	Ir-β-galactose	>100
7	Ir-PEG1-β-glucose	>100
8	Ir-PEG2-β-glucose	>100
9	Ir-PEG3-β-glucose	>100
10	Ir-Methyl	>100
$[Ru(bpy)_2(dppn)]Cl_2$		>100

4.3.2 Cellular accumulation of iridium complexes in A549 lung cancer cells

To determine the effects of changing the sugar and linker lengths on cellular accumulation, iridium β-glycoconjugates **4-9** and methyl analogue **10** were studied in A549 cells with no light exposure at equimolar, non-toxic concentrations (50 μM) for 1 h. Intracellular iridium content in cells treated with glycoconjugates **4-9** varied, but all treated cells contained significant amounts of iridium compared to untreated controls (**Table 4.2**). For cells treated with glycoconjugates **4-9**, the least Ir was observed in cells treated with β-galactose complex **6** (1.6 ± 0.3 fg·cell^{-1}), whilst the most was observed in cells treated with PEG3-β-glucose complex **9** (3.4 ± 0.3 fg·cell^{-1}). A549 cells treated with methyl complex **10** contained over 20× more Ir than any glycoconjugate (74.9 ± 2.8 fg·cell^{-1}). No significant differences were observed between cells treated with non-linker complexes **4** (β-glucose), **5** (β-mannose) and **6** (β-galactose), however, intracellular iridium of cells treated with PEG3-β-glucose complex **9** was significantly greater than all three non-linker

complexes. Intracellular iridium content of A549 cells treated with complexes **4-10** are shown in **Table 4.2** and **Figures 4.7 and 4.8**.

Table 4.2. Intracellular iridium in A549 cells treated with 50 μM **4-10** for 1 h. Negative controls were treated with cell growth medium only. Statistical significance between complex and negative control: * $p < 0.05$, ** $p < 0.01$, *** $p < 0.001$.

Complex	**R**	**Intracellular Ir (fg·cell^{-1})**
4	β-Glucose	2.2 ± 0.3 **
5	β-Mannose	2.2 ± 0.2 *
6	β-Galactose	1.6 ± 0.3 *
7	PEG1-β-Glucose	2.1 ± 0.2 ***
8	PEG2-β-Glucose	2.8 ± 0.2 ***
9	PEG3-β-Glucose	3.4 ± 0.2 *
10	Methyl	74.9 ± 2.8 ***
Negative Control	n/a	0.28 ± 0.07

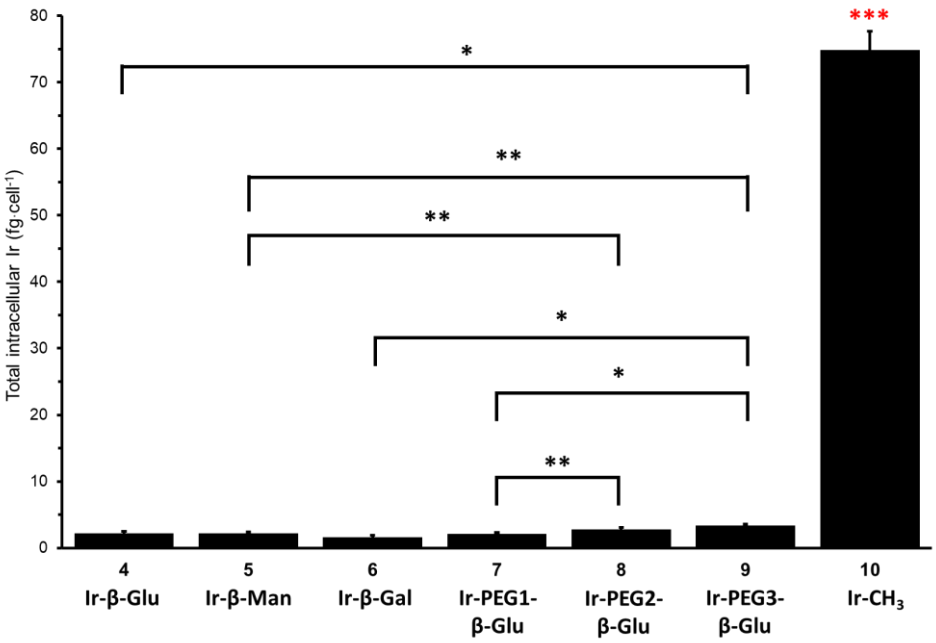

Figure 4.7. Intracellular iridium (fg·cell^{-1}) in A549 lung cancer cells treated with Ir complexes **4-10** (50 μM). Statistical significance between complexes: * $p < 0.05$, ** $p < 0.01$. *** $p < 0.001$ between complex **10** and each of **4-9**.

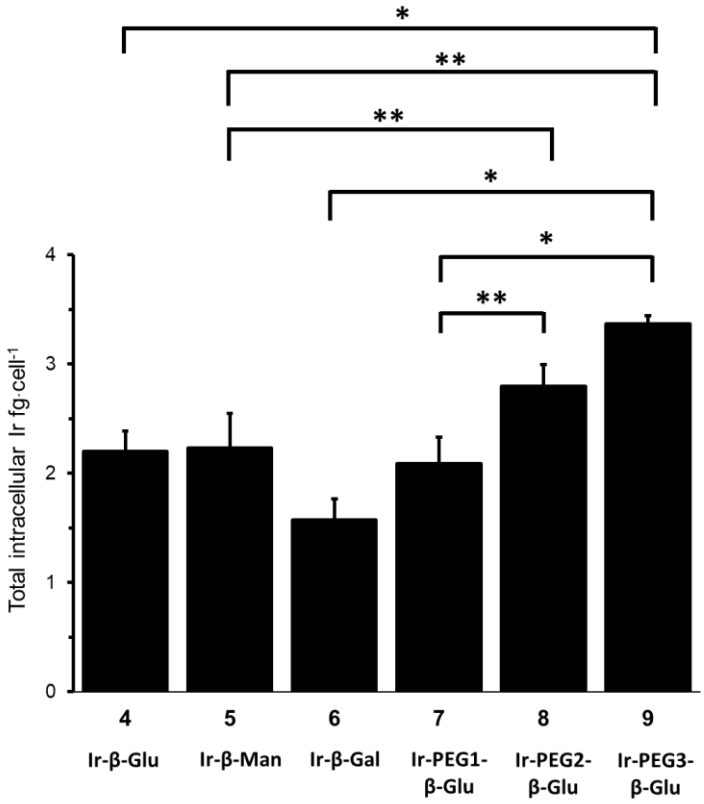

Figure 4.8. Intracellular iridium (fg·cell^{-1}) in A549 lung cancer cells treated with glycoconjugates **4-9** (50 μM), rescaled from **Figure 4.7**. Statistical significance between complexes: * $p < 0.05$, ** $p < 0.01$.

4.3.3 Antiproliferative activity in irradiated A549 lung cancer cells

After investigating the uptake of complexes **4** (β-glucose), **9** (PEG3-β-glucose) and **10** (methyl), photocytotoxicity assays were performed to determine whether cellular accumulation affected antiproliferative activities upon exposure to 425 nm irradiation. Cells were treated with 200-0.2 μM solutions of complexes **4**, **9**, **10** or **[Ru(bpy)$_2$(dppn)]Cl$_2$** (**Figure 4.6**, positive control, known photoactive agent) for 1 h then washed twice with PBS to remove Ir complex in the supernatant medium. Fresh medium was added, then plates were irradiated with 425 nm blue light for 1 h, then incubated for a 24 h recovery period.

All tested complexes were non-toxic in the dark (>100 μM, **Section 4.3.1**), but were significantly more active upon 425 nm irradiation, with phototoxicity indexes varying greatly between complexes (**Table 4.3**). Methyl complex **10** was the most potent of the Ir complexes (0.85 ± 0.01 μM), almost 2× more active than PEG3-β-glucose complex **9** (1.64 ± 0.15 μM) and 16× more active than β-glucose complex **4** (13.60 ± 1.71 μM). The activity of photoactive complex **[Ru(bpy)$_2$(dppn)]Cl$_2$** under these assay conditions was determined as 0.60 ± 0.01 μM.

Table 4.3. Dark and irradiated IC_{50} (μM), phototoxicity index and cellular accumulation (fg·cell^{-1}) of **4**, **9** and **10** in A549 lung cancer cells. IC_{50} values were determined using the SRB assay with 1 h incubation, 1 h dark/irradiation (λ = 425 nm, 4.8 mW·cm^{-2}) and 24 h recovery. Cellular accumulation in A549 cells incubated for 1 h with 50 μM solution of complex **4**, **9** or **10**. Statistical significance between Irradiated IC_{50} and Dark IC_{50}: * $p < 0.05$, ** $p < 0.01$, *** $p < 0.001$.

Complex		Irradiated IC_{50} (μM)	Dark IC_{50} (μM)	Phototoxicity Index	Intracellular Ir (fg·cell^{-1})
4	β-glucose	13.60 ± 1.71 **	> 100	> 7	2.2 ± 0.3
9	PEG3-β-glucose	1.64 ± 0.15 ***	> 100	> 60	3.4 ± 0.2

10	Methyl	0.85 ± 0.01 ***	> 100	> 117	74.9 ± 2.8
	$[Ru(bpy)_2(dppn)]Cl_2$	0.60 ± 0.01 ***	> 100	>166	n.d.

Phototoxicity index (PI) = (Dark IC_{50}) / (Irradiated IC_{50}), n.d. = not determined.

4.3.4 In-cell photosensitized singlet oxygen generation

To investigate whether the Ir complexes act as Type II photosensitizers *in vitro*, the generation of singlet oxygen ($^1O_2$) by complexes **4**, **9** and **10** in irradiated (λ = 425 nm, 4.8 $mW \cdot cm^{-2}$) A549 cells was determined by confocal microscopy using Singlet Oxygen Sensor Green (SOSG). SOSG initially emits weak blue fluorescence (λ_{ex} = 372/393 nm, λ_{em} = 395/415 nm) which changes to strong green fluorescence (λ_{ex} = 504 nm, λ_{em} = 525-536 nm) after reacting with singlet oxygen.

Cells only treated with SOSG and light showed limited green fluorescence (**Figure 4.9a**). However, green fluorescence was clearly elevated in cells incubated with 50 µM of iridium complex **4**, **9** or **10** relative to the iridium-free irradiated cells (**Figure 4.9b-d**).

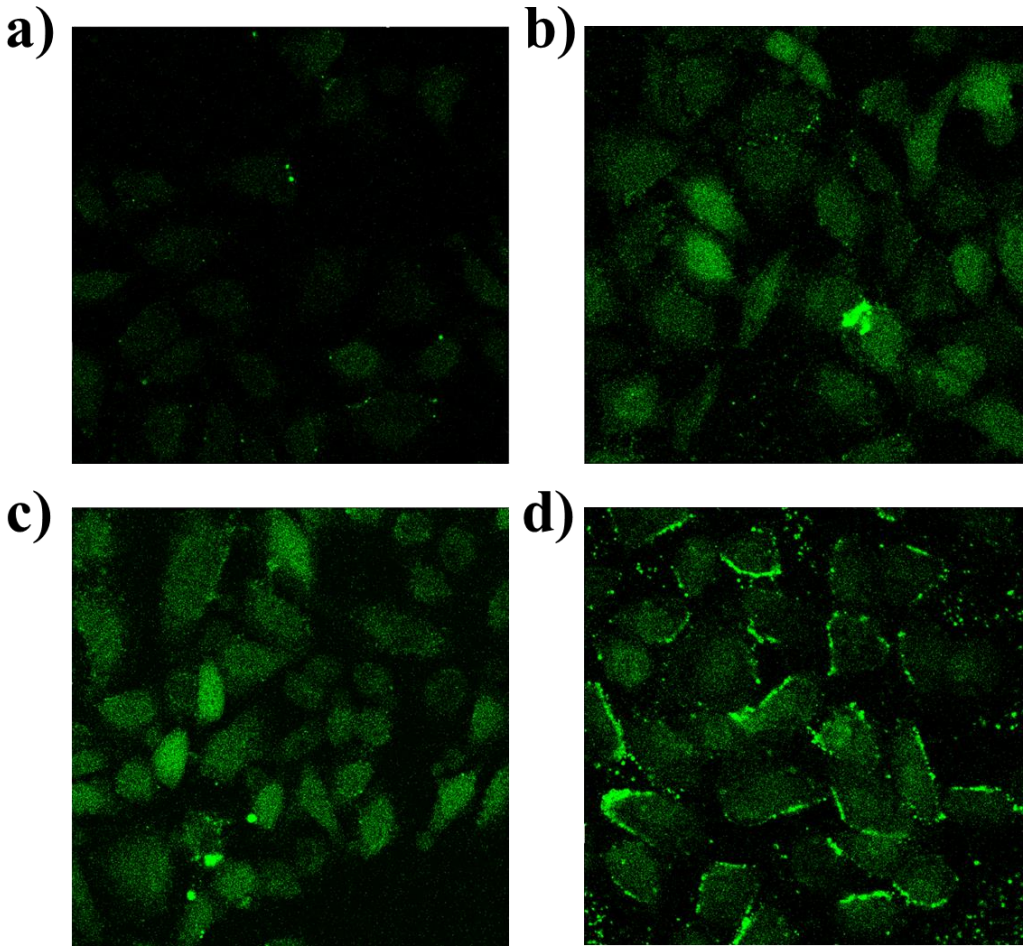

Figure 4.9. Confocal microscopy images of A549 cells after 10 min irradiation (λ = 425 nm) and addition of SOSG. Cells were treated for 1 h with a) media-only, b) 50 μM complex **4**, c) 50 μM complex **9**, and d) 50 μM complex **10**. Cells were incubated in SOSG (200 μM) for 20 min after irradiation. Images acquired using ZEISS LSM 710 with 40× objective. Excitation wavelength: 504 nm, detection wavelength: 525 nm. Data processed using ImageJ.

4.3.5 Influence of GLUT1 on uptake of iridium complexes

Initially, the IC_{50} of GLUT1 inhibitor **BAY-876** in A549 cells was investigated using the SRB assay to ensure a non-toxic dose was co-administered with the Ir complex of interest (**Section 4.2.1**). **BAY-876** was found to be non-toxic to A549 cells in the concentration range investigated (IC_{50} > 250 μM) and so it was decided to co-administer cells with complexes **4**, **9** and **10** in the presence of 100 μM **BAY-876** (pre-treatment for 1 h) before adding 100 μM media solutions of each complex to achieve final working concentrations of 50 μM for both **BAY-876** and complex. In addition, the toxicity of complexes **4**, **9** and **10** was investigated in non-cancerous

MRC5 lung cells to determine a non-toxic dose for confocal microscopy studies. All three iridium complexes exhibited low toxicity (IC_{50} > 100 μM) in MRC5 cells.

Intracellular iridium by ICP-MS

Intracellular iridium content was determined by ICP-MS as described in **Section 4.2.2**. Representative sub-series **4** (β-glucose, no linker), **9** (PEG3-β-glucose) and **10** (methyl, no sugar) were selected for co-administration with GLUT1 inhibitor **BAY-876**. The average iridium content in cells treated with PEG3-β-glucose complex **9** reduced by *ca*. 13 % after treatment with **BAY-876** (3.4 ± 0.2 fg·cell^{-1} *vs.* 2.97 ± 0.03 fg·cell^{-1}, p = 0.22, **Table 4.4**), however, due to the large standard deviation in Ir accumulation of samples in the absence of inhibitor, this reduction in intracellular Ir was not statistically significant. Similarly, cells treated with non-linker complex **4** showed no statistical difference in intracellular iridium content (2.2 ± 0.3 fg·cell^{-1} *vs.* 2.3 ± 0.1 fg·cell^{-1}, p = 0.67). Interestingly, treatment with **BAY-876** led to a 3.5-fold increase in the accumulation of methyl complex **10** (74.9 ± 2.8 fg·cell^{-1} *vs.* 255.5 ± 11.3 fg·cell^{-1}, p = 0.023).

Table 4.4. Intracellular iridium accumulation (fg·cell^{-1}) in A549 cells treated with **4**, **9** and **10** (50 μM) with and without GLUT1 inhibitor **BAY-876**. Pre-incubation period of 1 h in 100 μM **BAY-876**, followed by addition of Ir complex (100 μM) for 1 h, resulting in 50 μM working concentration. Iridium content determined by ICP-MS after nitric acid digestion (**Chapter 2, Section 2.2.9**). * p < 0.05.

	Complex	**Intracellular iridium (fg·cell^{-1})**		***p* values**
		- BAY-876	**+ BAY-876**	
4	Ir-β-Glucose	2.2 ± 0.3	2.3 ± 0.1	0.67
9	Ir-PEG3-β-Glucose	3.4 ± 0.2	2.97 ± 0.03	0.22
10	Ir-Methyl	74.9 ± 2.8	255.5 ± 11.3	0.023 *

Negative Control	n/a	0.28 ± 0.07	0.21 ± 0.02	0.38

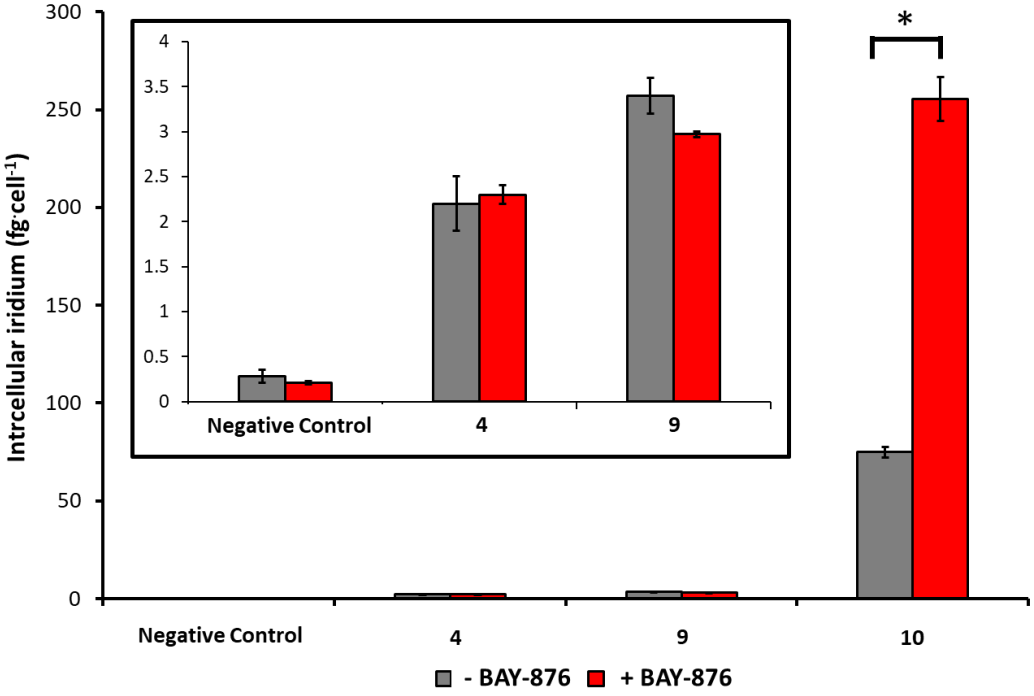

Figure 4.10. Intracellular iridium (fg·cell^{-1}) in A549 cells treated with 50 μM **4**, **9**, and **10** with (red) and without (grey) co-treatment with GLUT1 inhibitor **BAY-876**. Inset: data for negative control, **4** and **9** rescaled. * $p < 0.05$. Intracellular iridium in cells treated with complexes **4**, **9**, and **10** were all significantly greater than in the negative control cells ($p < 0.05$).

In-cell phosphorescence of complexes by confocal microscopy

The in-cell phosphorescence of **4**, **9** and **10** was determined in A549 cells in the presence or absence of GLUT1 inhibitor **BAY-876** (50 μM) as well as in MRC5 cells. Cells were treated with 50 μM solutions of each complex. Excitation laser power was optimised for each complex to avoid saturating the detectors, therefore, data for one complex across all three cell lines are comparable, whilst different complexes cannot be directly compared by this method. Mean in-cell pixel intensity was calculated using ImageJ (**Table 4.5**).

No autofluorescence was observed in cells without treatment of Ir complexes (**Figure 4.11**). The mean pixel intensity of cells treated with non-linker β-glucose complex **4** (**Figure 4.12**) was not significantly different between A549 cells without and with **BAY-876** ($3.1 \pm 1.4 \times 10^6$ *vs.* $2.3 \pm 1.4 \times 10^6$, $p = 0.094$), but was significantly lower in MRC5 cells ($0.7 \pm 0.5 \times 10^6$, $p = 1 \times 10^{-8}$). However, A549 cells treated with PEG3-β-glucose complex **9** alone (**Figure 4.13**) displayed significantly brighter phosphorescence than those co-treated with **BAY-876** ($1.1 \pm 0.4 \times 10^6$ *vs.* $0.6 \pm 0.2 \times 10^6$, $p = 0.00103$) and MRC5 cells ($0.4 \pm 0.4 \times 10^6$, $p = 1.9 \times 10^{-5}$). In contrast, phosphorescence in A549 cells co-treated with methyl complex **10** (**Figure 4.14**) and **BAY-876** ($8.1 \pm 5.6 \times 10^6$) was significantly brighter than both A549 cells ($1.6 \pm 0.8 \times 10^6$, $p = 0.0001$) and MRC5 cells ($1.3 \pm 0.7 \times 10^6$, $p = 6.4 \times 10^{-5}$) treated with **10** alone.

Table 4.5. Mean in-cell pixel intensity determined by confocal microscopy for cells treated with 50 μM solutions of **4**, **9** and **10** in A549 cells with/without **BAY-876** and MRC5 cells. Data acquired using ZEISS LSM 710 with 40× objective. Excitation wavelength: 405 nm. Detection wavelength: 489 nm. Excitation power optimised for each complex. Calculated using ImageJ. Statistical significance compared with A549 (no inhibitor): * $p < 0.05$, ** $p < 0.01$, *** $p < 0.001$.

	Mean In-Cell Pixel Brightness ($\times 10^6$)		
Complex	**A549**	**A549 + BAY-876**	**MRC5**
4	3.1 ± 1.4	2.3 ± 1.4	0.7 ± 0.5 ***
9	1.1 ± 0.4	0.6 ± 0.2 **	0.4 ± 0.4 ***
10	1.6 ± 0.8	8.1 ± 5.6 ***	1.3 ± 0.7

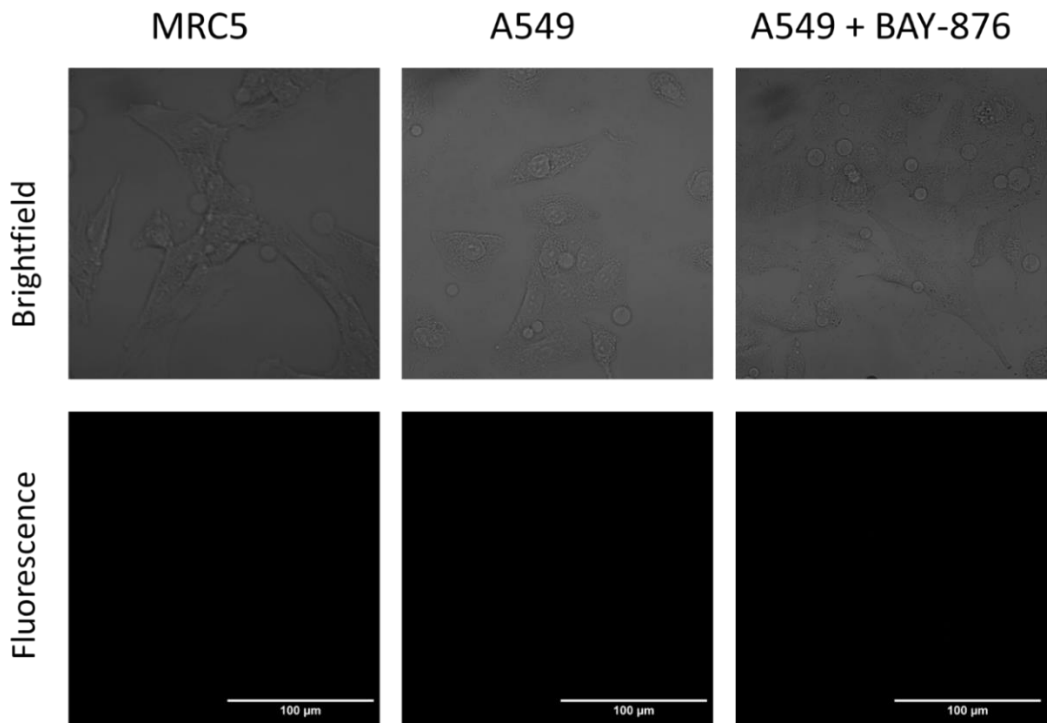

Figure 4.11. MRC5 and A549 cells with/without **BAY-876**. Cells incubated for 1 h in media only. Images acquired using ZEISS LSM 710 with 40× objective. Excitation wavelength: 405 nm. Detection wavelength: 489 nm.

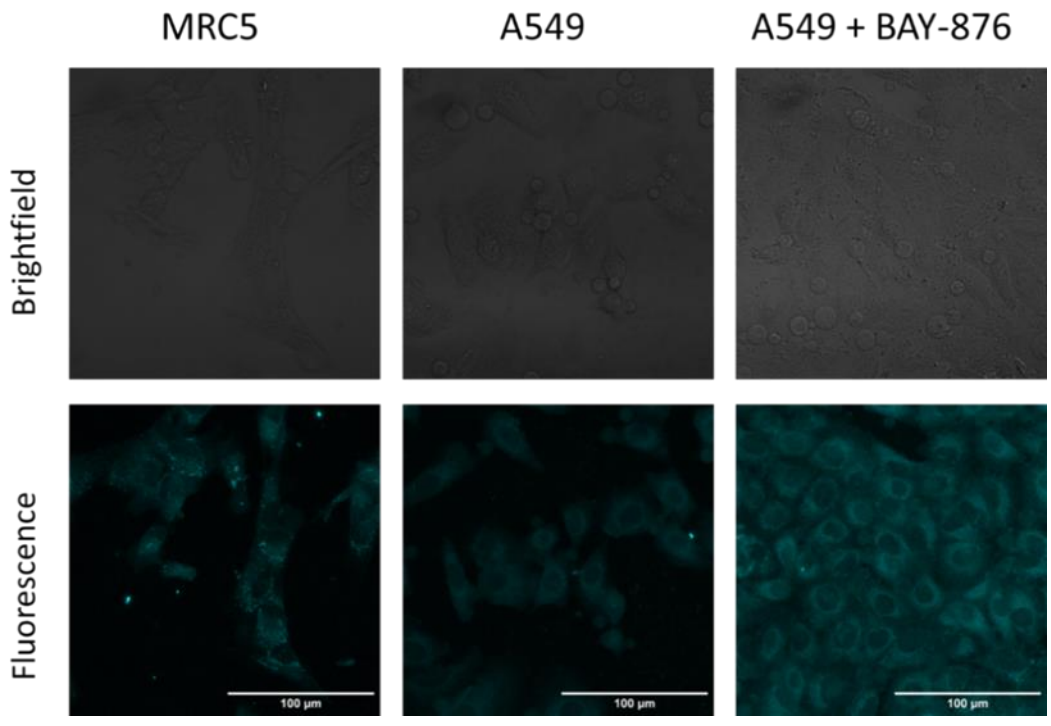

Figure 4.12. MRC5 and A549 cells with/without **BAY-876**. Cells incubated for 1 h in 50 µM complex **4**. Images acquired using ZEISS LSM 710 with 40× objective. Excitation wavelength: 405 nm. Detection wavelength: 489 nm.

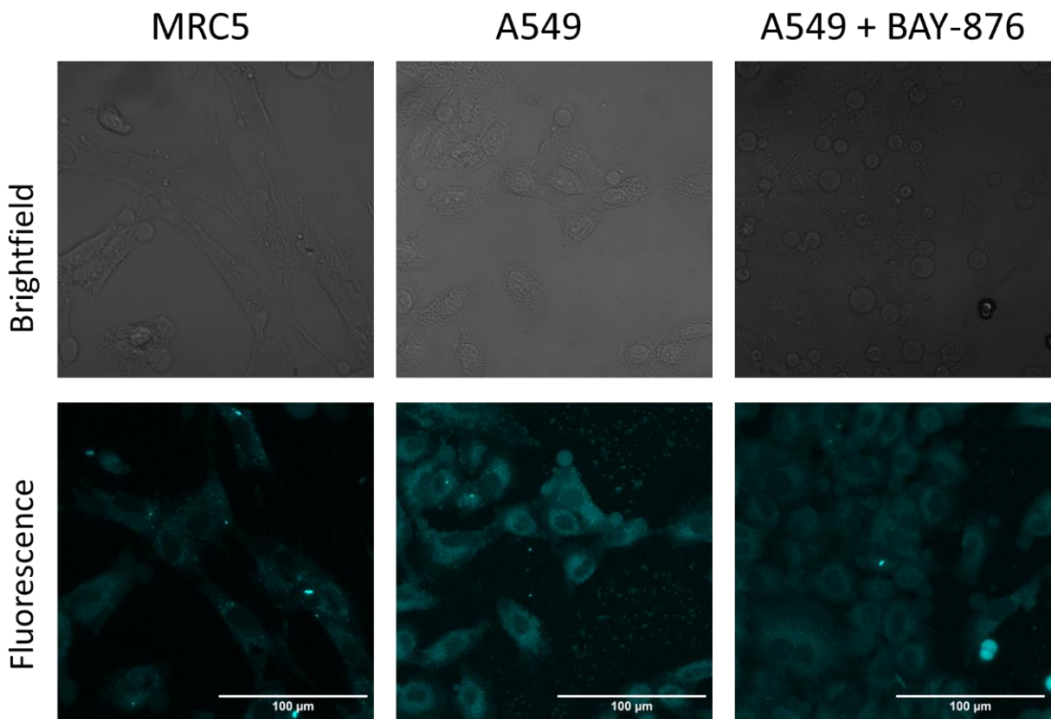

Figure 4.13. MRC5 and A549 cells with/without **BAY-876**. Cells incubated for 1 h in 50 µM complex **9**. Images acquired using ZEISS LSM 710 with 40× objective. Excitation wavelength: 405 nm. Detection wavelength: 489 nm.

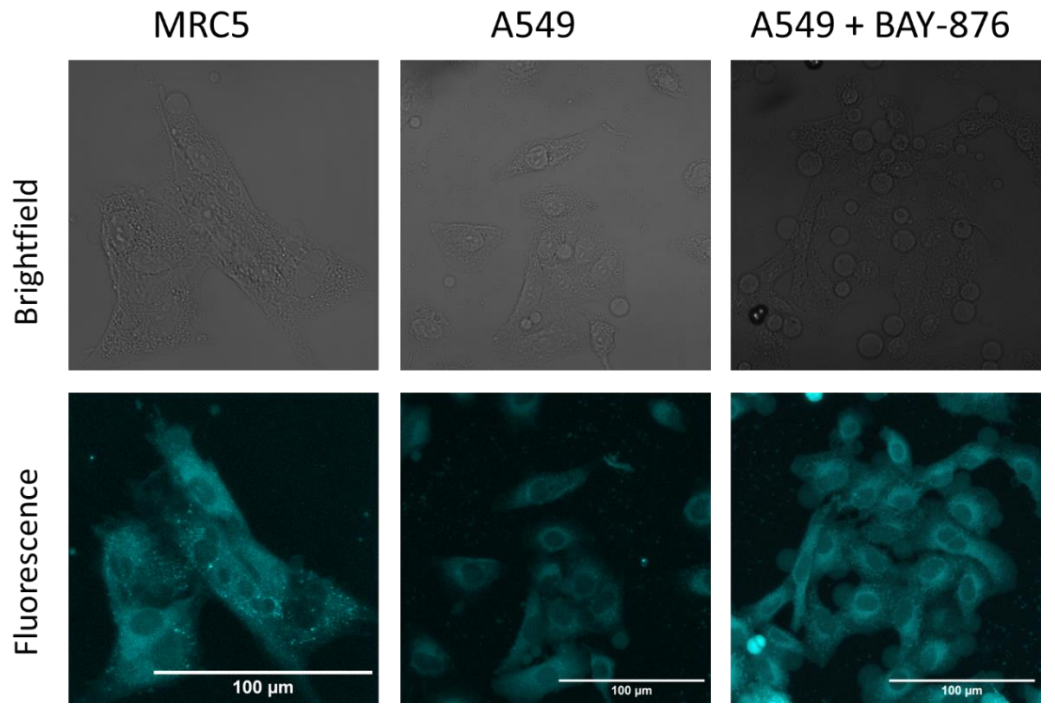

Figure 4.14. MRC5 and A549 cells with/without **BAY-876**. Cells incubated for 1 h in 50 µM complex **10**. Images acquired using ZEISS LSM 710 with 40× objective. Excitation wavelength: 405 nm. Detection wavelength: 489 nm.

4.3.6 Capacity factors and relative hydrophobicity

To determine whether the difference in uptake of complexes was caused by differences in lipophilicity, capacity factors of glycoconjugates **4-9** and methyl complex **10** were investigated using reverse-phase HPLC with an isocratic acetonitrile (50%) and water (50%) mobile phase and uracil as a reference sample for retention times (**Section 4.2.3**). Ir(III) glycoconjugates **4-9** were retained for 3.6-3.9 min on the column, whilst methyl complex **10** was retained for 9.1 min, leading to capacity factors of *ca.* 0.6 and 2.7, respectively (**Table 4.6**). Thus, methyl complex **10** is far more lipophilic than glycoconjugates **4-9**.

Table 4.6. Capacity factors of iridium glycoconjugates **4**-**9** and methyl complex **10** determined by reverse-phase HPLC using a C18 column. Mobile phase: 50% acetonitrile, 50% water. Uracil used as retention time reference.

Compound		Retention time (t_R) / min	Capacity factor (K)
	Uracil	2.358 ± 0.005	N/A
4	β-glucose	3.731 ± 0.002	0.582 ± 0.002
5	β-mannose	3.889 ± 0.005	0.650 ± 0.003
6	β-galactose	3.706 ± 0.003	0.572 ± 0.003
7	PEG1-β-glucose	3.694 ± 0.074	0.567 ± 0.031
8	PEG2-β-glucose	3.734 ± 0.003	0.584 ± 0.003
9	PEG3-β-glucose	3.728 ± 0.010	0.581 ± 0.005
10	Methyl	9.063 ± 0.012	2.844 ± 0.008

4.3.7 Human serum binding studies

To determine whether the difference in uptake of iridium glycoconjugates was in part due to differences in serum protein binding, β-glucose complex **4** and PEG3-β-glucose complex **9** were incubated at 310 K in human serum for either 1 h or 24

h and analysed by anion-exchange chromatography (AEX) and ICP-MS (offline LC-ICP-MS).

ICP-MS monitoring ^{193}Ir determined iridium recovery of 102.5% and 99.3% for serum incubated in 50 μM solutions of **4** for 1 h and 24 h, respectively (**Figure 4.15a/b**). For serum incubated in 50 μM solutions of **9**, recovery was 103.0% and 100.5% for 1 h and 24 h incubations, respectively (**Figure 4.15c/d**). Retention times (t_R) of single protein standards of human serum albumin and holo-transferrin were also determined (albumin: t_R = 10-13 min, transferrin: t_R = 6-9 min).

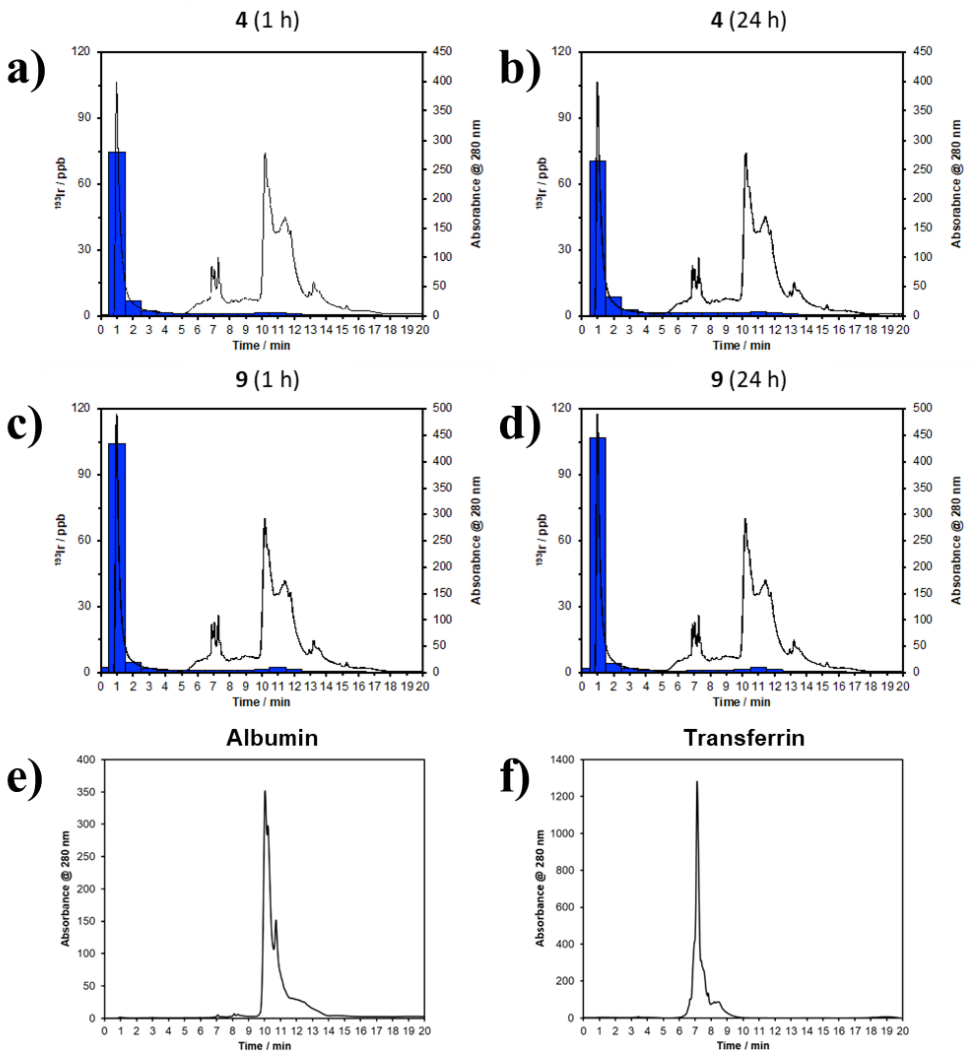

Figure 4.15. Offline LC-ICP-MS chromatograms (λ_{abs} = 280 nm) of human serum incubated with a) 50 μM complex **4** (1 h), b) 50 μM complex **4** (24 h), c) 50 μM complex **9** (1 h), and d) 50 μM complex **9** (24 h). Chromatograms for single protein standards of e) albumin and f) transferrin were obtained to identify serum proteins by retention time. Separation was achieved using a TSK-Gel Q-STAT strong anion exchange column (7 μm, 10 cm × 4.6 mm i.d.) with a flow rate of 0.7 mL·min^{-1} and an injection volume of 100 μL. Buffer A: 50 mM Tris base, pH 7.4. Buffer B: 50 mM Tris base + 1 M ammonium acetate, pH 7.4. Overlaid blue bars depict ^{193}Ir content in fractions collected at 1 min intervals and processed offline using ICP-MS.

In serum incubated with **4** for 1 h, 84.0% of the total Ir was detected in the flow-through fractions (t_R = 0-2 min), whilst 4.2% was found in serum fractions with t_R = 6-9 min, and a further 4.8% bound to fractions with t_R = 10-13 min. After 24 h, the flow-through fractions contained 88.2% of total Ir, whilst the iridium content in the latter fractions increased to 5.4% and 5.9%, respectively. In serum incubated with **9**, 80.5% of total Ir was detected in flow-through fractions, with only 2.9% of total Ir found in fractions with t_R = 6-9 min and 4.6% found in the fractions with t_R = 10-13 min. Very little change was observed after 24 h, with 2.6% and 4.7% in each group of fractions, respectively, although the Ir content of flow-through fractions increased to 88.7%. Retention times of major protein fractions and their corresponding Ir content are shown in **Table 4.7.**

Table 4.7. Iridium content determined by ICP-MS (^{193}Ir) in fractions of human serum treated with 50 μM solutions of complex **4** or **9** after HPLC. Separation was achieved using a TSK-Gel Q-STAT strong anion exchange column (7 μm, 10 cm × 4.6 mm i.d.) with a flow rate of 0.7 mL·min^{-1} and an injection volume of 100 μL. Buffer A: 50 mM Tris base, pH 7.4. Buffer B: 50 mM Tris base + 1 M ammonium acetate, pH 7.4.

Complex	**Retention Time (min)**	**Iridium Content (% of total recovered)**	
		1 h	**24 h**
4 Ir-β-Glucose	0-2	84.0	88.2
	6-9	4.2	2.9
	10-13	4.8	4.6
	0-2	80.5	88.7

9 Ir-PEG3-β-Glucose	6-9	5.4	2.6
	10-13	5.9	4.7

4.4 Discussion

4.4.1 Anticancer activity and cellular accumulation of Ir(III) complexes

The antiproliferative activity (IC_{50}) of Ir complexes **1-10** was initially determined in A549 lung cancer cells without exposure to irradiation to determine a non-toxic dose for cellular accumulation studies. In accordance with literature protocols (as used by the Sadler, McFarland and Turro groups) for photoactivated complexes, cells were incubated for 1 h in cell culture medium solutions of complexes **1-10**.[39–43] Cells were then washed twice to remove any complex in the supernatant, thereby avoiding any toxicity caused by extracellular singlet oxygen generation that could be generated upon irradiation (*vide infra*). Complexes were then incubated for 1 h in the dark, followed by a 24 h recovery period. Glycoconjugates **1-9** and methyl complex **10** were all found to have low toxicity without irradiation (IC_{50} > 100 μM).

Uptake studies were performed in A549 lung cancer cells at equimolar concentrations to keep the concentration of the sugars equal, allowing the determination of any effects caused by changes to the sugar group. Incubation periods of 1 h were used to determine the amount of iridium in the cells at the point irradiation takes place (irradiated IC_{50} data in **Section 4.3.3**). Due to the low toxicity of complexes, cells were incubated in 50 μM solutions of complexes. Intracellular iridium was determined by ICP-MS after 1 h incubation with β-glycoconjugates **4-9**, with methyl complex **10** used as a non-glycosylated reference to determine the effects of glycoconjugation on cellular uptake. No significant differences in intracellular Ir content were observed between complexes **4** (β-glucose, 2.2 ± 0.3 fg·cell^{-1}), **5** (β-mannose, 2.2 ± 0.2 fg·cell^{-1}), and **6** (β-galactose, 1.6 ± 0.3 fg·cell^{-1}), which do not contain a linker between the sugar and triazole. Cells treated with PEG1-β-glucose complex **7** contained less Ir than those treated with PEG2-β-

glucose complex **8** and PEG3-β-glucose complex **9** (2.1 ± 0.2, 2.8 ± 0.2, 3.4 ± 0.2 fg·cell^{-1}, respectively). Strong correlation between linker length and intracellular iridium was observed (R^2 = 0.85, **Figure 4.16**), demonstrating that the length of the PEG linker plays an important role in the uptake of these glycoconjugates, potentially by improving the recognition of the glucose group by GLUT1.[29] Interestingly, cells treated with methyl complex **10** contained over 20× more Ir (74.9 ± 2.8 fg·cell^{-1}) than those treated with **4**-**9**. Increased cellular accumulation can also be influenced by lipophilicity,[44–46] as well as coordination (covalently or electrostatically) to biomolecules, which has been shown to both increase (*e.g.* antibody-drug conjugates)[47,48] and hinder (NAMI-A binding to albumin and transferrin)[49,50] transport across cellular membranes.

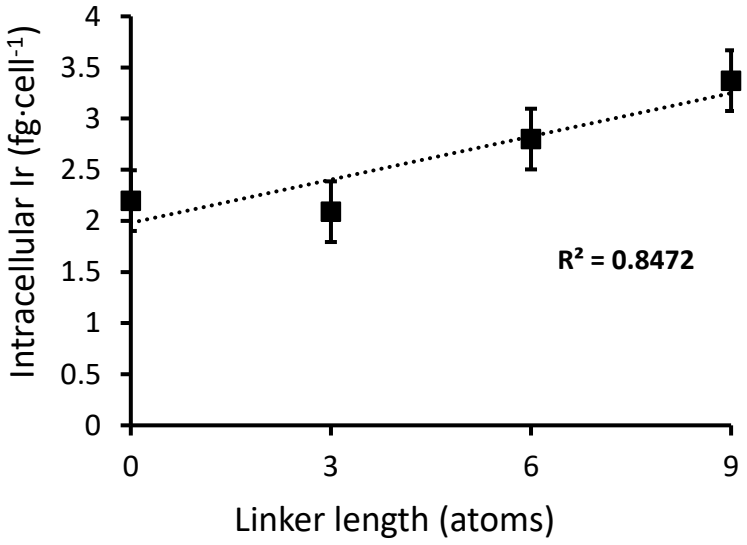

Figure 4.16. Correlation between intracellular iridium and linker length between glucose and triazole ring for A549 cells treated with 50 μM **4**, **7**, **8** and **9** (linker lengths of 0, 3, 6 and 9 atoms, respectively).

The sub-series of complexes **4** (no linker), **9** (PEG3 linker) and **10** (methyl) were selected for further investigation to investigate the effects of cellular accumulation on photocytotoxicity in A549 lung cancer cells. **[Ru(bpy)$_2$(dppn)]Cl$_2$** was also tested in order to compare the photocytotoxicities of the Ir complexes to a known metal-based photoactive agent. A549 cells were incubated with complexes for 1 h, washed with PBS, then irradiated for 1 h with 425 nm blue light, followed by a 24 h recovery period. A 425 nm LED array built in-house (**Appendix LED array A1**)

was used to irradiate the cells since DFT calculations of Ir complex **4** determined the HOMO → LUMO transition into the excited singlet state (S_1) could be induced at 428 nm (**Appendix Table A6**). This can then undergo intersystem crossing to an excited triplet state (T_1), from which singlet oxygen generation and phosphorescence can occur.

Antiproliferative activity upon irradiation ("Irradiated IC_{50}") was significantly increased for complex **4, 9** and **10**, with phototoxicity indexes of 7, 60 and 117, respectively. As expected, the activity of known photoactive agent **[Ru(bpy)$_2$(dppn)]Cl$_2$** increased dramatically upon irradiation, with a phototoxicity index of 166. Whilst the activity of Ir complex **4** was moderate upon irradiation (13.6 ± 1.7 μM), complexes **9**, **10** and **[Ru(bpy)$_2$dppn]Cl$_2$** all exhibited excellent photocytotoxicity (< 2 μM). Upon irradiation, complexes **9** and **10** were more active than the literature values for clinically used anticancer drug cisplatin (not irradiated; A549 IC_{50} = 21 μM), despite the far shorter drug incubation times (1 h *vs.* 24 h).[51] The photocytotoxicity of Ir complexes **4**, **9** and **10** correlated with intracellular Ir content, with both increasing in the order of **4** < **9** < **10**. ICP-MS does not determine whether a complex remains intact as it only detects for the metal centre, however, since Ir(III) complexes are typically stable in cells,[52–54] it is likely that the photocytotoxicity of the Ir complexes is due to the cellular uptake of intact complexes. Longer incubation times have been reported to increase the uptake of complexes in cells; therefore, increasing the incubation times may result in greater activity upon irradiation, although further work would be required to determine whether this would also lead to toxicity in the dark, as has been seen for other Ir(III) photosensitizers.[55]

Confocal microscopy of A549 cells treated with singlet oxygen sensor green (SOSG) was used for mechanistic studies to determine whether photosensitized singlet oxygen is generated in cells. SOSG was chosen as a probe for singlet oxygen as it is highly selective for singlet oxygen, with no response to superoxide or hydroxyl radicals, therefore useful in proving whether complexes are Type II photosensitizers. SOSG exhibits weak blue fluorescence ($\lambda_{ex/em}$ = 372/395 nm and 393/416 nm) until it reacts with singlet oxygen to form the endoperoxide product SOSG-EP, which exhibits intense green fluorescence ($\lambda_{ex/em}$ = 504/525 nm). Cells

were treated with 50 μM solutions of **4**, **9** or **10**, as well as an iridium-free control, irradiated (λ = 425 nm) for 10 min, washed, then 5 μM solutions of SOSG were added. Irradiation was limited to 10 min to maintain a high proportion of viable cells.

Cells without iridium complexes had very little green fluorescence upon irradiation, indicating little singlet oxygen was generated, whereas those treated with Ir complexes **4**, **9** and **10** all exhibited far more intense green fluorescence (**Figure 4.9**), proving that the Ir complexes are effective as Type II photosensitizers. SOSG has been reported to generate singlet oxygen upon irradiation with UV (355 nm) and visible (532 nm) light,[56,57] so it is likely the cause of the singlet oxygen generated in cells without Ir complexes. The green fluorescence signal in cells treated with glycoconjugates **4** and **9** was observed across the whole cell cytoplasm, with no particular bright spots that would imply localised photosensitizers. Conversely, membranes of cells treated with methyl complex **10** were notably brighter than the cytoplasms, potentially indicating that **10** is membrane-bound. SOSG has previously been shown to have unequal penetration between cells,[56] which is reflected in the difference in fluorescence intensities in cells treated with the same complex (*i.e.* cells treated with complex **4**).

The activities of complexes **4**, **9** and **10** were further investigated in non-cancerous MRC5 lung cells to determine whether complexes could potentially harm healthy tissue surrounding cancer cells. In PDT, the use of directed light leads to high spatial control of the treatment, thereby lessening the exposure of healthy cells to irradiation.[58,59] Thus, MRC5 cells were treated with complexes **4**, **9**, **10** and **[Ru(bpy)$_2$(dppn)]Cl$_2$** using the dark protocol. All four complexes exhibited the same low toxicity as was seen in cancer cells without irradiation (IC_{50} > 100 μM). Similar results have been observed for Pt(IV) photoactivated chemotherapeutic (PACT) agents, as well as Ir(III) and Ru(II) cyclometalated complexes using similar conditions.

4.4.2 Influence of GLUT1, lipophilicity and protein binding on cellular accumulation of Ir(III) complexes

Glycoconjugates **4** and **9** were designed to target GLUT1 in order to exploit the Warburg Effect; cancer cells overexpress GLUT1 to meet the increased glucose demands caused by inefficient production of ATP *via* glycolysis rather than oxidative phosphorylation.[2] To determine whether Ir glycoconjugates **4** and **9** target GLUT1, cellular accumulation experiments were performed in A549 lung cancer cells (GLUT1-overexpressed)[31–33] in the presence of a highly selective GLUT1 inhibitor, **BAY-876**.[60,61] In addition, non-cancerous MRC5 lung cells were used to explore whether complexes were selective for the cancerous cells, as MRC5 cells do not overexpress GLUT1.[36] Methyl complex **10** was used as a non-glycosylated control, with uptake not expected to be dependent on GLUT1.

Confocal microscopy and ICP-MS were used as complementary techniques to study the influence of GLUT1 on the cellular accumulation of iridium complexes. Confocal microscopy has the advantage of indicating whether complexes that enter cells are intact, since the excitation and emission wavelengths of complexes are known and can change drastically upon degradation of the complex (as seen for Pt(IV) PACT complexes).[62] On the other hand, ICP-MS does not give any indication of any degradation as the plasma atomises and ionises the samples,[63] but can accurately determine the intracellular metal content at levels as low as parts per quadrillion (ppq).[64]

Although the concentrations of Ir in stock solutions of the complexes were determined by ICP-OES so as to achieve a similar Ir concentration in each test, differences in phosphorescence quantum yields (**Chapter 3, Section 3.3.6**) could lead to differences in pixel intensity that are not related to concentration due to quenching effects. In addition, the excitation laser power and gain were optimised for each complex in order to obtain the optimum signal across the three cell conditions (A549 cells with/without **BAY-876** and MRC5 cells). Therefore, results between different complexes cannot be directly compared with this technique in this instance. The phosphorescence quantum yields for each complex were assumed to be constant between different cell lines, allowing for comparisons in phosphorescence intensities.

ICP-MS studies were used to quantify the difference in accumulation caused by the GLUT1 inhibitor **BAY-876**. Iridium content in cells treated with β-glucose complex **4** did not change in the presence of **BAY-876** (2.2 ± 0.3 fg·cell^{-1} *vs.* 2.3 ± 0.1 fg·cell^{-1}), indicating GLUT1 is not involved in the uptake of complex **4**. A 13% reduction in Ir was seen in cells treated with PEG3-β-glucose complex **9** (3.4 ± 0.2 fg·cell^{-1} *vs.* 2.97 ± 0.03 fg·cell^{-1}). Although not statistically significant ($p = 0.2$), it may suggest that complex **9** is at least partially internalised by GLUT1. Ir content in cells treated with methyl complex **10** increased dramatically when incubated with **BAY-876** (74.9 ± 2.8 fg·cell^{-1} *vs.* 255.5 ± 11.3 fg·cell^{-1})**,** confirming the methyl complex **10** does not target the GLUT1 receptor, and suggests the inhibitor has interesting effects of potential pharmacological use on the uptake of other complexes.

Confocal microscopy studies were conducted using cells treated identically to the ICP-MS studies, with cells incubated with 50 μM solutions of complexes after pre-treatment with the inhibitor. No statistical difference was seen between the mean in-cell pixel intensity of A549 cells treated with β-glucose complex **4** in the presence and absence of **BAY-876** ($3.1 \pm 1.4 \times 10^6$ *vs.* $2.3 \pm 1.4 \times 10^6$, $p = 0.094$), which supports ICP-MS results indicating no involvement of GLUT1 in the uptake of complex **4**. However, the phosphorescence intensity in MRC5 cells was significantly reduced ($0.7 \pm 0.5 \times 10^6$, $p = 1 \times 10^{-8}$), indicating that **4** is selective for cancer cells, although whether this is GLUT1-dependent requires further research. In cells treated with PEG3-β-glucose complex **9**, the phosphorescence intensity was significantly higher in A549 cells without **BAY-876** ($1.1 \pm 0.4 \times 10^6$) than in both A549 cells with **BAY-876** ($0.6 \pm 0.2 \times 10^6$, $p = 0.001$) and MRC5 cells ($0.4 \pm 0.4 \times 10^6$, $p = 1.9 \times 10^{-5}$), which indicates **9** is selective for cancer cells due to GLUT1-targeting. The phosphorescence intensity of A549 cells (no **BAY-876**) treated with methyl complex **10** did not differ significantly ($p = 0.09$) from that of MRC5 cells, indicating the methyl complex is not selective for cancer cells. However, phosphorescence in A549 cells treated with **BAY-876** and complex **10** was significantly higher than both A549 and MRC5 cells ($p < 0.001$). This may indicate either i) GLUT1 inhibitor **BAY-876** has off-target effects that alter the cellular uptake of complex **10**, or ii) **10** reacts with **BAY-876** to form a GLUT1-targeted adduct. However, further studies are required to determine whether any

such adducts are formed with complex **10**. In addition, the consistency between the phosphorescence measurements and ICP-MS results, as well as earlier results confirming singlet oxygen generation, indicate that these complexes remain intact inside the cells.

Cellular accumulation of metal complexes has previously been demonstrated to be highly dependent on the hydrophobicity of the complexes.[45] More lipophilic complexes often have increased accumulation in cells; however, complexes must be hydrophilic enough to remain soluble in the bloodstream. Retention times of β-glycoconjugates **4-9** and methyl complex **10** in reverse-phase HPLC were used to calculate capacity factors (*K*) – a relative measure of the hydrophobicity of complexes – in order to determine the effects of changing the triazole substituent on hydrophobicity and uptake.[45,65] Changing the sugar (glucose/mannose/ galactose) had little effect on the relative hydrophobicity of complexes **4-6**, with all non-linker glycoconjugates being retained on the column for *ca.* 3.7 min ($K \approx 0.6$). This was expected as the sugars are structurally similar, with 4 OH groups available for hydrogen bonding to water (mobile phase). The ethylene glycol linker units did not affect the retention times, with complexes **7-9** also being retained on the column for *ca.* 3.7 min. Since changing the sugar and linker length did not result in a change in hydrophobicity, no correlation was found between the difference in cellular accumulation of the glycoconjugated complexes **4-9** and their hydrophobicity ($R^2 = 0.0009$, **Figure 4.17 inset**), which further supports complex **9** being GLUT1-targeting. In contrast, methyl complex **10** was drastically more hydrophobic, with a retention time of 9.1 min ($K = 2.8$). This was expected as adding aliphatic groups to complexes has previously been shown to increase hydrophobicity,[44,45] which results in the dramatic increase in intracellular iridium for cells treated with **10** (**Figure 4.17**). Since no difference was seen in the uptake of **4** by cells treated with **BAY-876** by both confocal microscopy and ICP-MS, yet uptake into MRC5 cells was significantly lower, further research is needed to clarify the uptake mechanism for **4**. Future experiments may benefit from increasing incubation times with **BAY-876** as this may lead to more drastic inhibition of glucose uptake, therefore clarifying whether complex **4** is GLUT1-targeting or not.

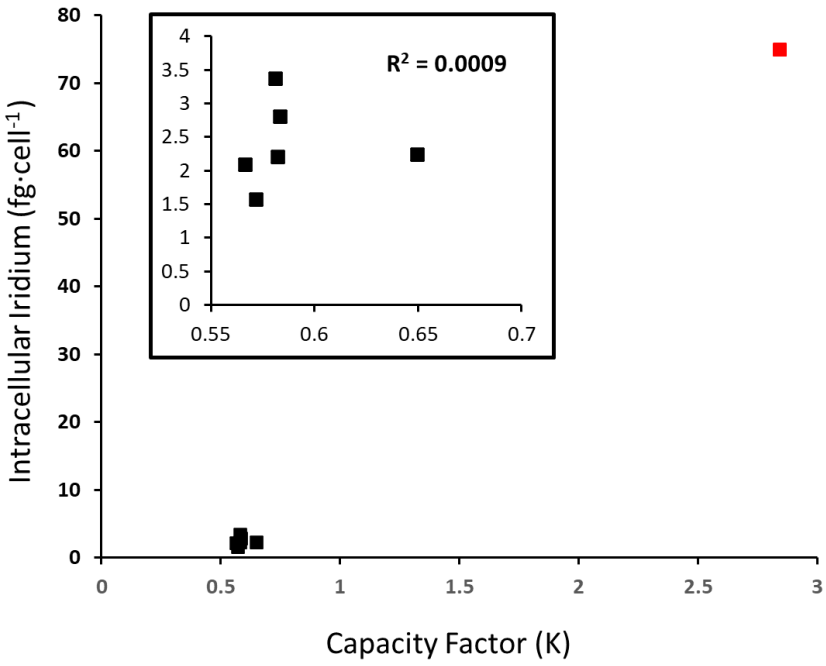

Figure 4.17. Correlation of intracellular iridium content of A549 cells treated for 1 h with complexes **4**-**10** with corresponding capacity factors. ■ – Glycoconjugates **4**-**9**. ■ – Methyl complex **10**. Inset: complexes **4**-**9** rescaled; R^2= 0.0009.

Ir glycoconjugates **4** and **9** were selective for cancer cells, yet differed in their GLUT1-targeting, which may be explained by differences in binding to serum proteins (*e.g.* albumin, transferrin). Cancer cells are known to internalise albumin preferentially, which can lead to selectivity of albumin-bound complexes towards cancer cells over non-cancerous cells.[66] In addition, many cancer cells overexpress the transferrin receptor TfR1, which may also increase the selectivity of transferrin-bound complexes.[67,68] Metal complexes are known to bind to serum proteins, which can lead to successful transportation (cisplatin – albumin) or inactivation (NAMI-A – albumin/transferrin).[49,50] Notably, albumin is known to covalently bind irreversibly up to 98% of clinical platinum anticancer agent cisplatin,[69] although both bound and unbound cisplatin are thought to contribute to anticancer activity.[49] In addition, protein binding is known to affect the clearance of drugs, with strong protein binding linked to reduced hepatic and renal clearance,[70] leading to increased drug elimination half-lives.[71] For the clinical photosensitizer Photofrin®, the long biological half-life of 410 hours leads to skin accumulation and photosensitivity for weeks.[72,73]

Liquid chromatography (LC) followed by ICP-MS (LC-ICP-MS) is a powerful tool for the determination of elemental speciation in many fields, ranging from biological to environmental applications.[74] In metal binding studies, size-exclusion chromatography-ICP-MS (SEC-ICP-MS) has previously been used to study interactions between Zn and serum proteins,[75] whilst anion exchange chromatography-ICP-MS (AEX-ICP-MS) has been used to determine extractable copper in serum.[76] AEX uses a positively charged stationary phase to separate serum proteins based on their charge, with negatively charged proteins retained longer on the column. For a protein to be negatively charged, the isoelectric point (pI) must be lower than the pH used (physiological pH = 7.4). Most proteins are found in the pI range 4-7,[77] including albumin (pI = 5.0) and transferrin (pI = 5.7),[78,79] making AEX a suitable choice for the separation of proteins at physiological pH. Proteins with a pI around 7.4 will likely be neutral at physiological pH and therefore will not be retained by the column.

Human serum was incubated with complex **4** or **9** for 1 h in order to investigate the extent of protein binding during biological assays (IC_{50} experiments: 1 h incubation). Serum was also incubated with solutions of complex **4** or **9** for 24 h to probe potential effects on elimination *in vivo*. Excellent recovery of Ir was observed by ICP-MS in all tested conditions (99.3-103.0%). Single protein standards of human serum albumin (t_R = 10-13 min) and human holo-transferrin (t_R = 6-9 min) were used to identify the two abundant metalloproteins in serum chromatograms.

The majority of Ir was recovered in the initial fractions of each analysis (flow-through), indicating the complexes have a low affinity to serum proteins, or bind to proteins that are not retained by the AEX column (*i.e.* proteins that do not possess a net anionic charge at pH 7.4). In total, 9% of **4** is bound to albumin and transferrin after 1 h, which increased to 11.3% after 24 h. Conversely, only 7.5% of **9** was bound to these proteins after 1 h, which remained similar at 24 h (7.3%). Whilst more of complex **4** is bound to albumin and transferrin than complex **9**, it is unlikely the difference is significant enough to explain the differences in cellular accumulation observed by confocal microscopy. However, the similar amount of Ir in the flow-through fractions of serum treated with **4** and **9** after 24 h incubation

(*ca.* 88%) may indicate similar, relatively short biological half-lives *in vivo* due to the high proportion of free complex available for metabolism in the liver/kidneys.

4.5 Conclusions

Glycoconjugates **1**-**9** and methyl analogue **10** exhibited low toxicity towards A549 lung cancer cells in the absence of irradiation (IC_{50} > 100 μM). Intracellular Ir accumulation experiments showed no dependence on the specific sugar when no linker was involved (glucose/mannose/galactose), however, increasing the length of the linker between glucose and the triazole of the iridium complex led to an increased amount of intracellular iridium. In contrast, the intracellular accumulation of Ir in cells treated with methyl complex **10** was almost 20-fold greater.

Photocytotoxicity experiments revealed significantly enhanced potency in A549 cells upon blue light irradiation, with irradiated IC_{50} values below 20 μM (**4**: 13.60 ± 1.71 μM, PI > 7; **9**: 1.64 ± 0.15 μM, PI > 60; **10**: 0.85 ± 0.01 μM, PI > 117). However, these complexes were not as potent as control ruthenium complex **[Ru(bpy)$_2$(dppn)]Cl$_2$** (Irradiated IC_{50} = 0.60 ± 0.01 μM, PI > 166). The activities of **4**, **9** and **10** increased with increasing intracellular iridium content. Photocytotoxicity was attributed to singlet oxygen generation, observed by confocal microscopy as green fluorescence due to the reaction of singlet oxygen and SOSG. Dark cytotoxicity experiments performed in MRC5 cells found complexes **4**, **9**, **10** and **[Ru(bpy)$_2$(dppn)]Cl$_2$** to all be non-toxic up to 100 μM.

ICP-MS experiments of A549 cells treated with GLUT1 inhibitor **BAY-876** did not lead to any change in the intracellular accumulation of **4**, suggesting complex **4** is not internalised *via* GLUT1. Although found to be insignificant at a 95% confidence level, a 13% reduction in the average iridium content was observed in cells treated with PEG3 complex **9** and inhibitor, which could be indicative of GLUT1 targeting. Interestingly, there was a significant increase in intracellular iridium in cells treated with **10** and the GLUT1 inhibitor, indicating either that the inhibitor reacts with the methyl complex to form a GLUT1-targeting complex, or leads to other interesting effects on cellular uptake pathways. Further uptake studies using confocal microscopy showed a significant decrease in the intracellular phosphorescence of

complex **9** after treatment with the inhibitor, implying a GLUT1-dependent uptake mechanism. In contrast, no statistical difference was observed in cells treated with **4**, suggesting GLUT1 is not involved in the uptake of **4**. Furthermore, the intracellular phosphorescence of non-cancerous MRC5 cells treated with complexes **4** and **9** were significantly lower than those of A549 cells, indicating both are selective for cancer cells. The selectivity of **9** is likely due to the lower expression of GLUT1 in MRC5 compared to A549 cells, however, the reasons for the selectivity of **4** are unclear since no GLUT1 targeting was seen in GLUT1 inhibition studies.

Glycoconjugates **1**-**9** were found to be equally hydrophilic ($K \approx 0.6$), regardless of sugar, anomer, or PEG linker lengths, demonstrating that lipophilicity is unaffected by these substituents. Lipophilicity is therefore unlikely to contribute to the differences in uptake of glycoconjugates **1**-**9**, however, methyl complex **10** is far more lipophilic ($K = 2.8$), which may contribute to its 10-fold greater accumulation in A549 cells.[80]

Metal drugs are known to bind to serum proteins, which can lead to successful transportation into tumours (cisplatin – albumin) or inactivation of the complex (NAMI-A – albumin/transferrin).[49,50] AEX-ICP-MS of human serum incubated with complexes **4** and **9** revealed slight differences of total iridium bound to albumin or transferrin, although it is unlikely to play a significant part in the differences in uptake. Serum incubated for 24 h with either complex had 88% of total Ir in the flow-through fractions, so it is likely that the majority of the Ir complexes remain unbound, therefore making them available for metabolism by the liver/kidneys, though future *in vivo* experiments are necessary to prove this.

Overall, Ir glycoconjugates **4** and **9** exhibited differences in uptake most likely due to **9** being GLUT1 targeting, whilst **4** was not. Complex **9** could therefore act as a template for future GLUT1-targeting Ir(III) complexes with modified C^N ligands, with the potential for cancer cell selectivity and relatively short biological half-lives. Accumulation of methyl complex **10** in cancer cells was significantly higher than both glycoconjugates, attributed to greater lipophilicity, though no selectivity was observed between cancerous and non-cancerous cells.

4.6 Future work

Time-dependent cellular accumulation. ICP-MS studies of intracellular metal content at different time points can determine the optimal incubation period for complexes *in vitro*.[81] Using the optimal incubation period may therefore lead to increased photoactivity, allowing for reduced dosages. However, further non-photoactive studies will be required to determine whether any cytotoxicity is observed in the dark.

3D cell culture. Cell spheroids facilitate the determination of whether singlet oxygen can still be produced in a more tumour-like 3D environment,[82] since tumours are known to possess hypoxic regions.[83]

Ligand structural modification. Huang *et al*. have demonstrated that tuning the C^N ligands (*e.g.* from 2-phenylpyridine to 1-isophenylquinoline) can lead to a large red shift in absorption of Ir glycoconjugates, leading to activity with longer wavelength irradiation such as green light, which has greater tissue penetration than the blue light used in these studies.[42] This may result in greater photocytotoxicity in 3D cell spheroids, though this is dependent on singlet oxygen generation.

Intracellular speciation. To determine whether Ir complexes remain coordinated and do not undergo ligand exchange reactions within the intracellular environment, the glucose moiety could be labelled with a heavy halogen such as Br to allow for direct imaging using synchrotron X-ray fluorescence (XRF) to determine co-localisation of Ir and Br, which has been previously reported with Os(II) complexes bearing brominated azopyridine ligands.[80] Conversely, Br labelling and cell fractionation with ICP-MS could be used to determine the content of Ir and Br in different cellular components.[80] A potential route for the synthesis of a Br-labelled Ir glycoconjugate based on literature methods is shown in **Figure 4.18**.[84,85]

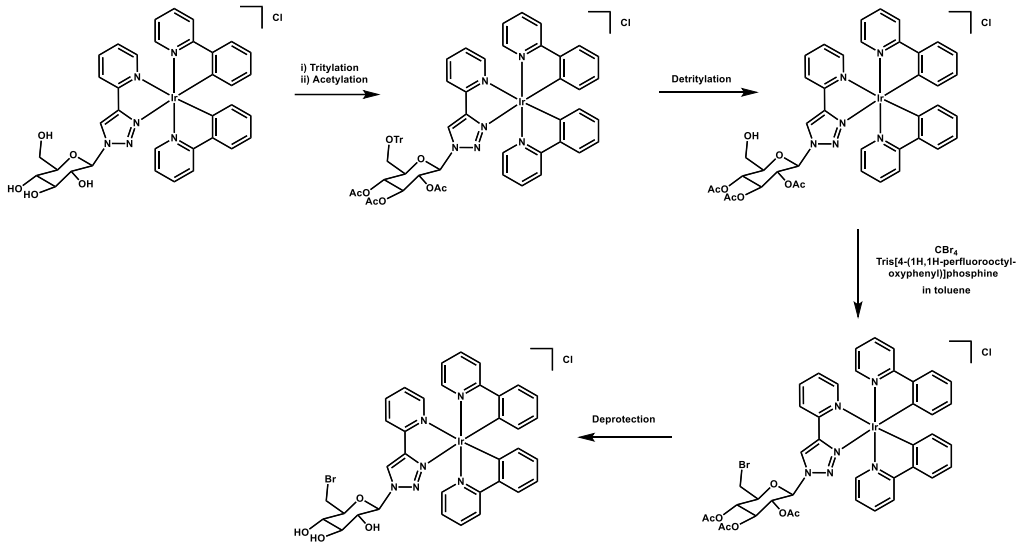

Figure 4.18. Proposed synthesis of Br-labelled Ir glycoconjugate based on literature procedures for synchrotron X-ray fluorescence or cell fractionation studies.

4.7 References

1 M. Jang, S. S. Kim and J. Lee, *Exp. Mol. Med.*, 2013, **45**, 1–8.

2 M. G. Vander Heiden, L. C. Cantley and C. B. Thompson, *Science*, 2009, **324**, 1029–1033.

3 L. Schwartz, C. Supuran and K. Alfarouk, *Anticancer. Agents Med. Chem.*, 2017, **17**, 164–170.

4 A. Zambrano, M. Molt, E. Uribe and M. Salas, *Int. J. Mol. Sci.*, 2019, **20**, 1–20.

5 T. Yamamoto, Y. Seino, H. Fukumoto, G. Koh, H. Yano, N. Inagaki, Y. Yamada, K. Inoue, T. Manabe and H. Imura, *Biochem. Biophys. Res. Commun.*, 1990, **170**, 223–230.

6 G. Cantuaria, A. Fagotti, G. Ferrandina, A. Magalhaes, M. Nadji, R. Angioli, M. Penalver, S. Mancuso and G. Scambia, *Cancer*, 2001, **92**, 1144–1150.

7 M. Yu, H. Yongzhi, S. Chen, X. Luo, Y. Lin, Y. Zhou, H. Jin, B. Hou, Y. Deng, L. Tu and Z. Jian, *Oncotarget*, 2017, **8**, 43356–43367.

8 S. Patching, *J. Diagnostic Imaging Ther.*, 2015, **2**, 30–102.

9 K. Mah and C. B. Caldwell, in *PET-CT in Radiotherapy Treatment Planning*, Elsevier, 2008, pp. 52–89.

10 E. Budak, G. Çok and A. Akgün, *Mol. Imaging Radionucl. Ther.*, 2018, **27**, 73–80.

11 F. Martucci, M. Pascale, M. C. Valli, G. A. Pesce, P. Froesch, L. Giovanella, A. Richetti and G. Treglia, *Front. Med.*, 2020, **6**, 1–9.

12 S. Meziou, C. Ringuette Goulet, H. Hovington, V. Lefebvre, É. Lavallée, M. Bergeron, H. Brisson, A. Champagne, B. Neveu, D. Lacombe, J. M. Beauregard, F. A. Buteau, J. Riopel and F. Pouliot, *Prostate Cancer Prostatic Dis.*, 2020, **23**, 441–448.

13 J. M. Harshani, S. Yeluri and V. R. Guttikonda, *J. Oral Maxillofac. Pathol.*, 2014, **18**, 372–378.

14 K. Zeng, G. Ju, H. Wang and J. Huang, *Transl. Cancer Res.*, 2020, **9**, 2363–2377.

15 B. Zhang, Z. Xie and B. Li, *Gene*, 2019, **689**, 76–83.

16 O. Levy, W. N. Brennen, E. Han, D. M. Rosen, J. Musabeyezu, H. Safaee, S. Ranganath, J. Ngai, M. Heinelt, Y. Milton, H. Wang, S. H. Bhagchandani, N. Joshi, N. Bhowmick, S. R. Denmeade, J. T. Isaacs and J. M. Karp, *Biomaterials*, 2016, **91**, 140–150.

17 S. Benson, F. de Moliner, A. Fernandez, E. Kuru, N. L. Asiimwe, J. S. Lee, L. Hamilton, D. Sieger, I. R. Bravo, A. M. Elliot, Y. Feng and M. Vendrell, *Nat. Commun.*, 2021, **12**, 1–12.

18 M. I. Molejon, G. Weiz, J. D. Breccia and M. I. Vaccaro, *World J. Clin. Oncol.*, 2020, **11**, 110–120.

19 NCT01954992 - Glufosfamide Versus 5-FU in Second Line Metastatic Pancreatic Cancer, https://clinicaltrials.gov/ct2/show/NCT01954992,

(accessed 16 January 2022).

20 A. Annunziata, A. Amoresano, M. E. Cucciolito, R. Esposito, G. Ferraro, I. Iacobucci, P. Imbimbo, R. Lucignano, M. Melchiorre, M. Monti, C. Scognamiglio, A. Tuzi, D. M. Monti, A. Merlino and F. Ruffo, *Inorg. Chem.*, 2020, **59**, 4002–4014.

21 J. Ma, Q. Wang, Z. Huang, X. Yang, Q. Nie, W. Hao, P. G. Wang and X. Wang, *J. Med. Chem.*, 2017, **60**, 5736–5748.

22 M. Patra, S. G. Awuah and S. J. Lippard, *J. Am. Chem. Soc.*, 2016, **138**, 12541–12551.

23 J. Ma, H. Liu, Z. Xi, J. Hou, Y. Li, J. Niu, T. Liu, S. Bi, X. Wang, C. Wang, J. Wang, S. Xie and P. G. Wang, *Front. Chem.*, 2018, 6, 386.

24 M. Patra, T. C. Johnstone, K. Suntharalingam and S. J. Lippard, *Angew. Chem.*, 2016, **128**, 2596–2600.

25 X. Gao, S. Liu, Y. Shi, Z. Huang, Y. Mi, Q. Mi, J. Yang and Q. Gao, *Eur. J. Med. Chem.*, 2017, **125**, 372–384.

26 S. Alassadi, M. J. Pisani and N. J. Wheate, *Dalton Trans.*, 2022, **51**, 10835–10846.

27 S. P. Vaidya and M. Patra, *Curr. Opin. Chem. Biol.*, 2023, **72**, 102236.

28 Y. Sun, M. Hu, F. Wang, H. Tan, J. Hu, X. Wang, B. Wang, J. Hu and Y. Li, *Anal. Biochem.*, 2021, **631**, 114357.

29 A. Glenister, M. I. Simone and T. W. Hambley, *PLoS One*, 2019, **14**, 1–16.

30 W. H. T. Law, L. C. C. Lee, M. W. Louie, H. W. Liu, T. W. H. Ang and K. K. W. Lo, *Inorg. Chem.*, 2013, **52**, 13029–13041.

31 S. Zhang, X. Wang, R. Zhang, Y. Cui, H. Zhang, W. Song, X. Hou, S. Fu, Q. Gao and S. Liu, *Anal. Chim. Acta*, 2021, **1167**, 338593.

32 R. Zhang, L. Song, B. Jiang, L. Wang, N. Wu, S. Guo and D. Shi,

Bioorganic Med. Chem. Lett., 2017, **27**, 2488–2492.

33 H. Zhao, J. Sun, J. Shao, Z. Zou, X. Qiu, E. Wang and G. Wu, *J. Cancer*, 2019, **10**, 4989–4997.

34 G. Shafirstein, A. Battoo, K. Harris, H. Baumann, S. O. Gollnick, J. Lindenmann and C. E. Nwogu, *Ann. Am. Thorac. Soc.*, 2016, **13**, 265–275.

35 K. Wang, B. Yu and J. L. Pathak, *J. Cancer*, 2021, **12**, 1154–1160.

36 D. Barbaro, L. Di Bari, V. Gandin, C. Evangelisti, G. Vitulli, E. Schiavi, C. Marzano, A. M. Ferretti and P. Salvadori, *PLoS One*, 2015, 10(4), e0123159.

37 V. Vichai and K. Kirtikara, *Nat. Protoc.*, 2006, **1**, 1112–1116.

38 Y. Sun, L. E. Joyce, N. M. Dickson and C. Turro, *Chem. Commun.*, 2010, **46**, 2426–2428.

39 A. P. Lanquist, S. Gupta, K. F. Al-Afyouni, M. Al-Afyouni, J. J. Kodanko and C. Turro, *Chem. Sci.*, 2021, **12**, 12056–12067.

40 R. Lincoln, L. Kohler, S. Monro, H. Yin, M. Stephenson, R. Zong, A. Chouai, C. Dorsey, R. Hennigar, R. P. Thummel and S. A. McFarland, *J. Am. Chem. Soc.*, 2013, **135**, 17161–17175.

41 M. Stephenson, C. Reichardt, M. Pinto, M. Wa, T. Sainuddin, G. Shi, H. Yin, S. Monro, E. Sampson, B. Dietzek and S. A. Mcfarland, *J. Phys. Chem. A*, 2014, 10507–10521.

42 Z. Zhu, L. Wei, Y. Lai, O. W. L. Carter, S. Banerjee, P. J. Sadler and H. Huang, *Dalton Trans.*, 2022, **51**, 10875–10879.

43 H. Shi, J. Kasparkova, C. Soulié, G. J. Clarkson, C. Imberti, O. Novakova, M. J. Paterson, V. Brabec and P. J. Sadler, *Chem. - A Eur. J.*, 2021, **27**, 10711–10716.

44 P. O. Asekunowo, R. A. Haque and M. R. Razali, *Rev. Inorg. Chem.*, 2017, **37**, 29–50.

45 R. J. Needham, H. E. Bridgewater, I. Romero-Canelón, A. Habtemariam, G. J. Clarkson and P. J. Sadler, *J. Inorg. Biochem.*, 2020, **210**, 111154.

46 B. J. Bennion, N. A. Be, M. W. McNerney, V. Lao, E. M. Carlson, C. A. Valdez, M. A. Malfatti, H. A. Enright, T. H. Nguyen, F. C. Lightstone and T. S. Carpenter, *J. Phys. Chem. B*, 2017, **121**, 5228–5237.

47 B. Teicher, *Curr. Cancer Drug Targets*, 2009, **9**, 982–1004.

48 Y. Chen, G. Liu, L. Guo, H. Wang, Y. Fu and Y. Luo, *Int. J. Cancer*, 2015, **136**, 182–194.

49 A. I. Ivanov, J. Christodoulou, J. A. Parkinson, K. J. Barnham, A. Tucker, J. Woodrow and P. J. Sadler, *J. Biol. Chem.*, 1998, **273**, 14721–14730.

50 A. Bergamo, L. Messori, F. Piccioli, M. Cocchietto and G. Sava, *Invest. New Drugs*, 2003, **21**, 401–411.

51 W. J. Liu, P. Y. Pan, Y. Sun, J. B. Wang, H. Zhou, X. Xie, Z. Y. Duan, H. Y. Dong, W. N. Chen, L. De Zhang and C. Wang, *Front. Oncol.*, 2022, **11**, 1–17.

52 C. Huang, C. Liang, T. Sadhukhan, S. Banerjee, Z. Fan, T. Li, Z. Zhu, P. Zhang, K. Raghavachari and H. Huang, *Angew. Chem. Int. Ed.*, 2021, **60**, 9474–9479.

53 C. Liu, C. Yang, L. Lu, W. Wang, W. Tan, C. H. Leung and D. L. Ma, *Chem. Commun.*, 2017, **53**, 2822–2825.

54 N. Roy, U. Sen, S. Ray Chaudhuri, V. Muthukumar, P. Moharana, P. Paira, B. Bose, A. Gauthaman and A. Moorthy, *Dalton Trans.*, 2021, **50**, 2268–2283.

55 W. W. Qin, Z. Y. Pan, D. H. Cai, Y. Li and L. He, *Dalton Trans.*, 2020, **49**, 3562–3569.

56 A. Prasad, M. Sedlářová and P. Pospíšil, *Sci. Rep.*, 2018, **8**, 1–13.

57 X. Ragàs, A. Jiménez-Banzo, D. Sánchez-García, X. Batllori and S. Nonell,

Chem. Commun., 2009, 2920–2922.

58 S. C. Hester, M. Kuriakose, C. D. Nguyen and S. Mallidi, *Photochem. Photobiol.*, 2020, **96**, 260–279.

59 J. P. Celli, B. Q. Spring, I. Rizvi, C. L. Evans, K. S. Samkoe, S. Verma, B. W. Pogue and T. Hasan, *Chem. Rev.*, 2010, **110**, 2795–2838.

60 Q. Wu, W. Ba-alawi, G. Deblois, J. Cruickshank, S. Duan, E. Lima-Fernandes, J. Haight, S. A. M. Tonekaboni, A. M. Fortier, H. Kuasne, *et al.*, *Nat. Commun.*, 2020, 11, 4205.

61 H. Yang, M. Z. H. Zhang, H. W. Sun, Y. T. Chai, X. Li, Q. Jiang and J. Hou, *Front. Oncol.*, 2021, **11**, 1–15.

62 H. Shi, C. Imberti and P. J. Sadler, *Inorg. Chem. Front.*, 2019, **6**, 1623–1638.

63 S. C. Wilschefski and M. R. Baxter, *Clin. Biochem. Rev.*, 2019, **40**, 115–133.

64 A. A. Ammann, *J. Mass Spectrom.*, 2007, **42**, 419–427.

65 M. H. M. Klose, S. Theiner, H. P. Varbanov, D. Hoefer, V. Pichler, M. Galanski, S. M. Meier-Menches and B. K. Keppler, *Inorganics*, 2018, 6, 130.

66 E. N. Hoogenboezem and C. L. Duvall, *Adv. Drug Deliv. Rev.*, 2018, **130**, 73–89.

67 P. V. Candelaria, L. S. Leoh, M. L. Penichet and T. R. Daniels-Wells, *Front. Immunol.*, 2021, **12**, 1–21.

68 T. R. Daniels, E. Bernabeu, J. A. Rodríguez, S. Patel, M. Kozman, D. A. Chiappetta, E. Holler, J. Y. Ljubimova, G. Helguera and M. L. Penichet, *Biochim. Biophys. Acta - Gen. Subj.*, 2012, **1820**, 291–317.

69 R. Kato, T. Sato, A. Iwamoto, T. Yamazaki, S. Nakashiro, S. Yoshikai, A. Fujimoto, H. Imano, Y. Ijiri, Y. Mino, M. Chikuma, K. Tanaka and T.

Hayashi, *Biopharm. Drug Dispos.*, 2019, **40**, 242–249.

70 P. K. Deb, O. Al-Attraqchi, M. R. Prasad and R. K. Tekade, *Protein and Tissue Binding: Implication on Pharmacokinetic Parameters. Implication on Pharmacokinetic Parameters.*, Elsevier Inc., 2018.

71 F. Keller, M. Maiga, H. H. Neumayer, H. Lode and A. Distler, *Eur. J. Drug Metab. Pharmacokinet.*, 1984, **9**, 275–282.

72 S. P. Pereira, L. Ayaru, R. Ackroyd, D. Mitton, G. Fullarton, M. Zammit, Z. Grzebieniak, H. Messmann, M.-A. Ortner, L. Gao, M. M. Trinh and J. Spénard, *Aliment. Pharmacol. Ther.*, 2010, **32**, 821–827.

73 G. Bozzini, P. Colin, N. Betrouni, P. Nevoux, A. Ouzzane, P. Puech, A. Villers and S. Mordon, *Photodiagnosis Photodyn. Ther.*, 2012, **9**, 261–273.

74 M. Montes-Bayón, K. DeNicola and J. A. Caruso, *J. Chromatogr. A*, 2003, **1000**, 457–476.

75 J. P. C. Coverdale, J. P. Barnett, A. H. Adamu, E. J. Griffiths, A. J. Stewart and C. A. Blindauer, *Metallomics*, 2019, **11**, 1805–1819.

76 C. D. Quarles, M. MacKe, B. Michalke, H. Zischka, U. Karst, P. Sullivan and M. P. Field, *Metallomics*, 2020, **12**, 1348–1355.

77 P. Novák and V. Havlíček, in *Proteomic Profiling and Analytical Chemistry: The Crossroads: Second Edition*, 2016, pp. 52–62.

78 H. Wiig, O. Kolmannskog, O. Tenstad and J. L. Bert, *J. Physiol.*, 2003, **550**, 505–514.

79 O. Vesterberg and U. Breig, *J. Immunol. Methods*, 1981, **46**, 53–62.

80 E. M. Bolitho, H. E. Bridgewater, R. J. Needham, J. P. C. Coverdale, P. D. Quinn, C. Sanchez-Cano and P. J. Sadler, *Inorg. Chem. Front.*, 2021, **8**, 3675–3685.

81 A. Ballesta, F. Billy, J. P. C. Coverdale, J. I. Song, C. Sanchez-Cano, I. Romero-Canelón and P. J. Sadler, *Metallomics*, 2019, **11**, 1648–1656.

82 A. S. Nunes, A. S. Barros, E. C. Costa, A. F. Moreira and I. J. Correia, *Biotechnol. Bioeng.*, 2019, **116**, 206–226.

83 M. Zanoni, F. Piccinini, C. Arienti, A. Zamagni, S. Santi, R. Polico, A. Bevilacqua and A. Tesei, *Sci. Rep.*, 2016, **6**, 1–11.

84 T. Takeda, Y. Sugiura, C. Hamada, R. Fujii, K. Suzuki, Y. Ogihara and S. Shibata, *Chem. Pharm. Bull.*, 1981, **29**, 3196–3201.

85 L. Desmaris, N. Percina, L. Cottier and D. Sinou, *Tetrahedron Lett.*, 2003, **44**, 7589–7591.

Chapter 5

Synchrotron X-ray analysis of cancer cells treated with Pt-Ir photosensitizer

5 Synchrotron X-ray analysis of cancer cells treated with Pt-Ir photosensitizer

This Chapter describes research on a novel Pt-Ir conjugate as a potential theranostic anticancer agent. The project was initiated in 2018 by Dr Huaiyi Huang and Dr Huayun Shi in our laboratory. They carried out the initial synthesis and characterisation, and Dr Shi studied its activity in cancer cells, including photocytotoxicity. PhD student Elizabeth Bolitho carried out the initial X-ray absorption and fluorescence studies of the complex in cancer cells at Diamond Light Source (2019). This was followed (2021-22) by the author's studies described here including the repeat synthesis and characterisation of the complex, and further synchrotron X-ray studies (assisted by Dr Cinzia Imberti).

First, I summarise the previous studies on this conjugate since they are unpublished (except as PhD theses by Dr H. Shi and Dr E. Bolitho).[1,2] Overall progress on this project has been greatly hindered by Covid-19 restrictions from 2020-22 on access to both chemistry and biology laboratories at University of Warwick as well as the facilities at Diamond Light Source.

5.1 Introduction

Selective activation of otherwise inert prodrugs using light is the fundamental process behind three modern modes of potential cancer treatments: photodynamic therapy (PDT), photothermal therapy (PTT) and photoactivated chemotherapy (PACT). Whilst PTT mostly utilises gold nanoparticles, PDT and PACT have a wide array of chemical structures available to them, both organic and organometallic in nature. One of the main advantages of PDT is the catalytic process of generating radicals/singlet oxygen to kill cells.[3] However, this is often highly dependent on oxygen and can therefore be limited in hypoxic environments.[4–6] Although PACT is non-catalytic, since the pathway to generate radicals and toxic species is *via* photodecomposition, there is no dependence on oxygen – a distinct advantage in hypoxic environments.[7–10]

Platinum has been used extensively in the clinic since the introduction of Pt(II) complex cisplatin, but side effects and resistance are well-documented across a

range of Pt(II) complexes due to their similar modes of action.[11–15] A series of Pt(IV) complexes that released azide radicals upon irradiation were reported in 1978,[16] and further compounds with high dark stability and photodecomposition have been reported since. Farrer *et al*. reported the synthesis of *trans, trans, trans*-$[Pt^{IV}(N_3)_2(OH)_2(pyridine)_2]$ (FM190, complex **15**) in 2010 by hydrogen peroxide oxidation of a stable *trans*-bipyridyl Pt(II) complex, which was shown to be phototoxic in cells upon irradiation with wavelengths from 360-500 nm.[17] This compound has since formed the basis of numerous other Pt(IV) complexes, including being conjugated to a peptide to form a potent, integrin-targeted PACT agent.[18]

More recently, complex **15** was conjugated to **Ir-NH$_2$** (complex **16**), an Ir(III) PDT agent, to develop dual-mode-of-action PDT-PACT agent **17** (Pt-Ir, **Figure 5.1**).[1] By combining a PDT and PACT agent, the limitations of oxygen-dependence could be reduced in hypoxic regions whilst still benefiting from photocatalytic singlet oxygen generation in more oxygenated environments. Complex **17** was shown to have good dark stability over 2 h in aqueous solution when monitored by UV-vis spectroscopy, and the absorption intensity at 298 nm decreased upon blue light irradiation as azide radicals were released. The major photodecomposition products observed by LC-MS were $[2\{Pt^{II}(N_3)_2(py)(OH_2)\}+Na]^+$, $[Pt^{II}(CH_3CN)(HCOO)(py)_2]^+$, $[Pt^{II}(CH_3CN)(N_3)(py)_2]^+$ and $[Ir^{III}(ppy)_2(CH_3\text{-}bpy\text{-}CH_2NHCO(CH_2)_2COOH)]^+$, showing that the complex can lose both azidyl radicals and pyridine ligands as well as lead to separate Pt(II) and Ir(III) species.

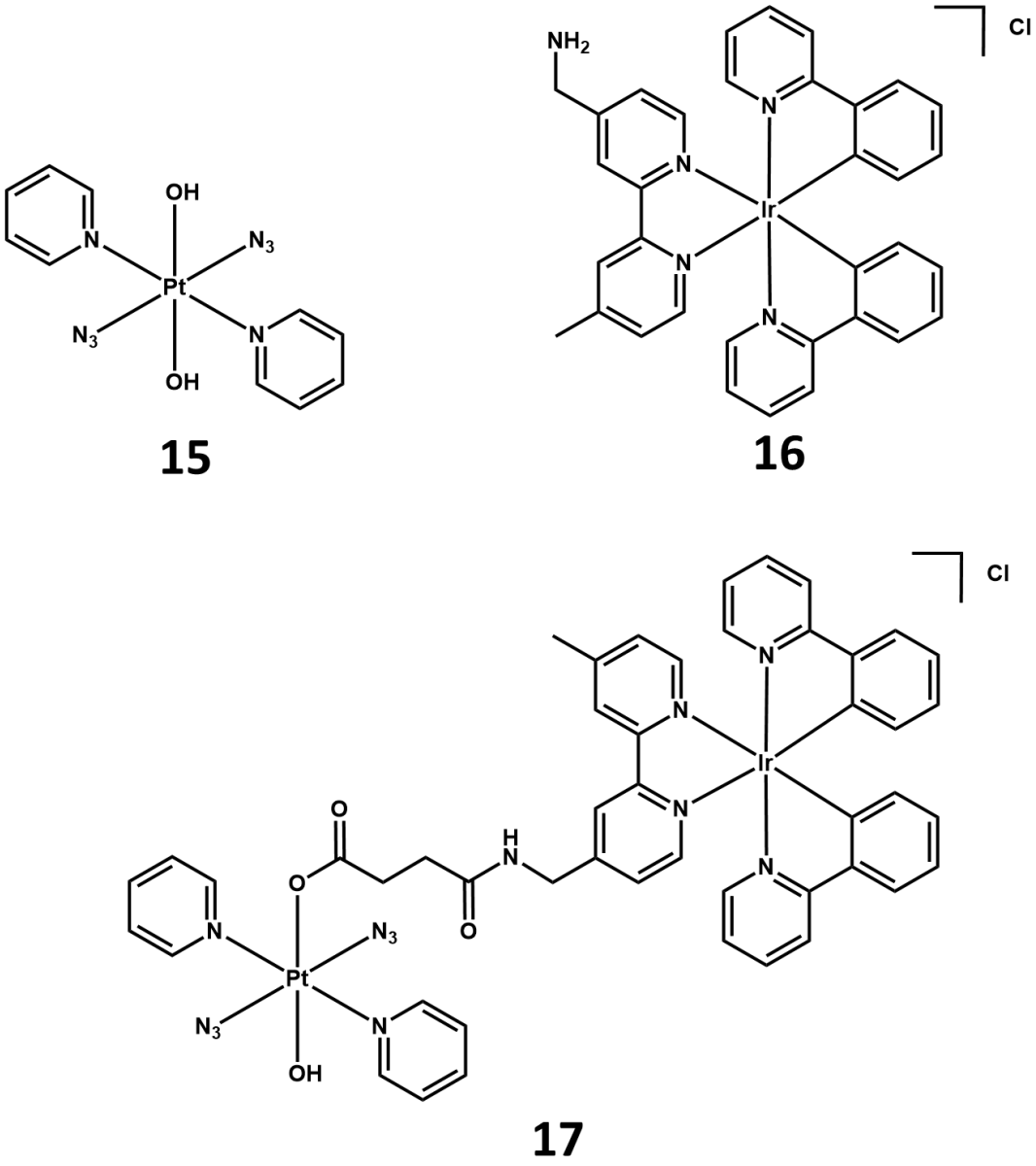

Figure 5.1. Structures of complexes **15** (FM190), **16** (Ir-NH_2) and **17** (Pt-Ir).

EPR spectroscopy showed that the novel Pt-Ir complex **17** retained the ability to release azide radicals upon 463 nm irradiation that is seen for Pt complex **15**, as well as the ability to generate singlet oxygen like Ir complex **16**. The intensity of the singlet oxygen infrared phosphorescence was similar for both iridium-containing species (**16** and **17**), whilst very little signal was observed for Pt complex **15**.

Based on these studies, complex **17** was likely to be effective as both a PDT and PACT photosensitizer. It was screened in A2780 ovarian carcinoma, A549 lung

carcinoma, PC3 prostate adenocarcinoma cells, as well as MRC5 lung fibroblasts (non-cancerous primary cells), to determine its toxicity in the dark and after 1 h irradiation with 465 nm (blue) light. For comparison, similar experiments were also performed with complexes **15** and **16**, as well as clinically used cisplatin (**Table 5.1**).

Table 5.1. IC_{50} values (μM) and phototoxicity indexes (PI) of **15** (FM190), **16** (Ir-NH_2), **17** (Pt-Ir) and cisplatin in A2780, PC3 and A549 cancer cells. Cells were treated with 1 h drug incubation, 1 h irradiation at 465 nm (or dark), and 24 h recovery. Cell viability determined by SRB assay. Reproduced from reference.[1]

Cell line		**IC_{50} (μM)**			
		15 (FM190)	**16** (Ir-NH_2)	**17** (Pt-Ir)	**Cisplatin**
A2780	Dark	>100	>100	>100	>100
	465 nm	7.1 ± 0.4	10.8 ± 0.4	1.3 ± 0.1	>100
	PI*	>14.0	> 9.2	>76.9	-
PC3	Dark	>100	>100	>100	>100
	465 nm	55.6 ± 0.9	>100	9.7 ± 2.3	>100
	PI	> 1.7	-	>10.3	-
A549	Dark	>100	>100	>100	>100
	465 nm	51.9 ± 2.5	20.2 ± 2.3	3.5 ± 0.1	>100
	PI	> 1.9	> 4.9	>28.5	-
MRC5	Dark	>100	>100	>100	>100

*PI = phototoxicity index (IC_{50} dark / IC_{50} light)

All three tested compounds were non-toxic (IC_{50} >100 μM) in A2780, PC3, A549 and MRC5 cell lines without irradiation, but activity upon irradiation varied greatly. For example, irradiation of PC3 cells treated with Ir complex **16** resulted in no change in cell viability, yet irradiation led to a 9-fold increase in toxicity towards A2780 cells when treated with **16**. Most importantly, Pt-Ir complex **17** was more potent upon irradiation than both parent compounds (**15** and **16**) in all tested cell lines.

The accumulation of platinum in the A2780 (ovarian), A549 (lung) and PC3 (prostate) cancer cells was determined by ICP-MS after 1 h treatment with 10 μM solutions of **15** and **17**. For all three cell lines, accumulation of intracellular platinum was 2-3× higher for Pt-Ir than FM190. This was linked to Pt-Ir being more lipophilic than FM190. Since both uptake and toxicity are higher for Pt-Ir than the parent Pt compound, it is likely that toxicity is related to how much complex gets into the cells.

Table 5.2. Platinum accumulation (fg·cell^{-1}) in A2780 (ovarian), A549 (lung) and PC3 (prostate) cancer cells after 1 h incubation with 10 μM Pt complex **15** and Pt-Ir complex **17** (no irradiation). Reproduced from reference.[1]

	Platinum accumulation (fg·cell^{-1})		
Complex	**A2780**	**A549**	**PC3**
15 (Pt)	1.19 ± 0.04	1.0 ± 0.2	1.5 ± 0.3
17 (Pt-Ir)	3.53 ± 0.03	2.8 ± 0.1	3.8 ± 0.6

Since complex **17** is luminescent in solution, confocal microscopy could be used to determine intracellular distribution in A549 cells. Cells were pre-incubated with SYTO™ 17, LysoTracker™ Deep Red and MitoTracker™ Red to stain nuclei, lysosomes and mitochondria, respectively, then incubated with a 10 μM solution of **17** for 1 h. Cells were then either kept dark or irradiated at 465 nm for 1h. For dark-treated cells, **17** luminescence was mostly detected in the mitochondria with no damage to nuclei. However, upon irradiation, the nuclear membranes were damaged and chromosomes were released (**Figure 5.2**), which was not observed under similar conditions with Ir complex **16**. This indicates the damage is caused by the photoproducts from the platinum moiety: azidyl radicals, and toxic, DNA-binding Pt(II) species. When interpreting the localisation of **17**, it is important to recognise that the emission spectra of **17** (Pt-Ir) and **16** (Ir) are identical in PBS, with emission maxima around 600 nm, indicating that the luminescence of **17** is mostly (if not entirely) attributable to the luminescence of the iridium moiety.[19] This means it is possible that the luminescence observed could be due to a cleaved, iridium-only compound, especially in the irradiated samples.

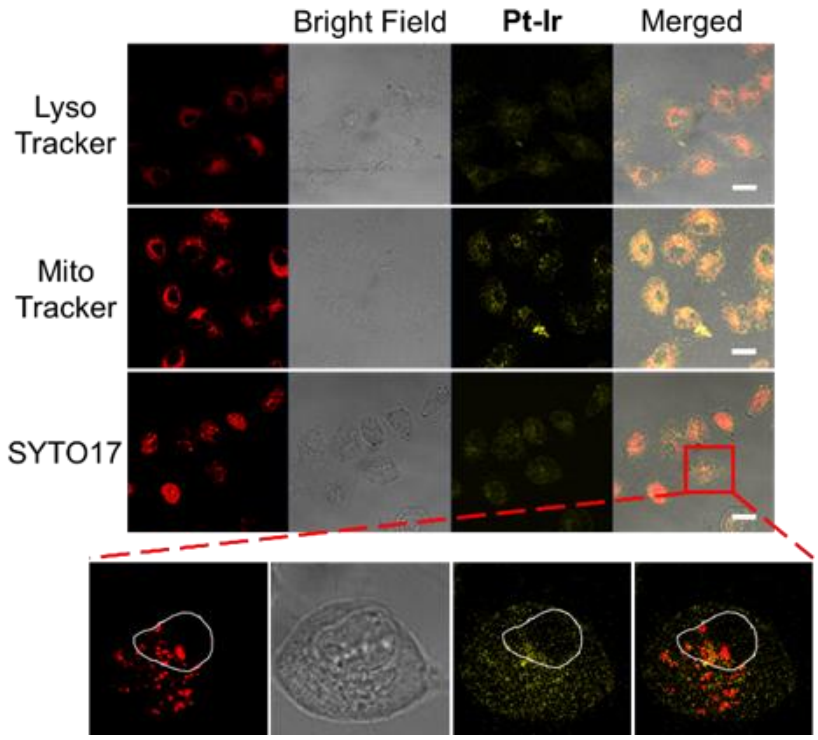

Figure 5.2. Confocal microscopy fluorescence images of A549 cells treated with **17** (10 μM, $\lambda_{ex}/\lambda_{em}$ = 405/460-560 nm) after 1 h incubation and 1 h irradiation (465 nm, 4.8 mW·cm^{-2}), then stained with SYTO^{TM} 17 (2.5 μM, $\lambda_{ex}/\lambda_{em}$ = 633/637-753 nm), LysoTracker^{TM} Deep Red (0.5 μM, $\lambda_{ex}/\lambda_{em}$ = 633/637-753 nm), and MitoTracker^{TM} Red (0.5 μM, $\lambda_{ex}/\lambda_{em}$ = 561/567-620 nm) to stain nuclei, lysosomes and mitochondria, respectively. Scale bar: 20 μm. Reproduced from reference (unpublished).[19]

A549 cells incubated with each complex and ROS scavenger DCFH-DA showed ROS were generated only upon irradiation of treated cells, as dark and untreated cells showed no signal. The signal intensities for cells treated with Ir-containing complexes **16** and **17** were both stronger than for **15**, indicating the ROS were singlet oxygen produced by the iridium moiety. Singlet Oxygen Sensor Green (SOSG) confirmed the production of singlet oxygen by **17** (see **Figure 5.3b**).

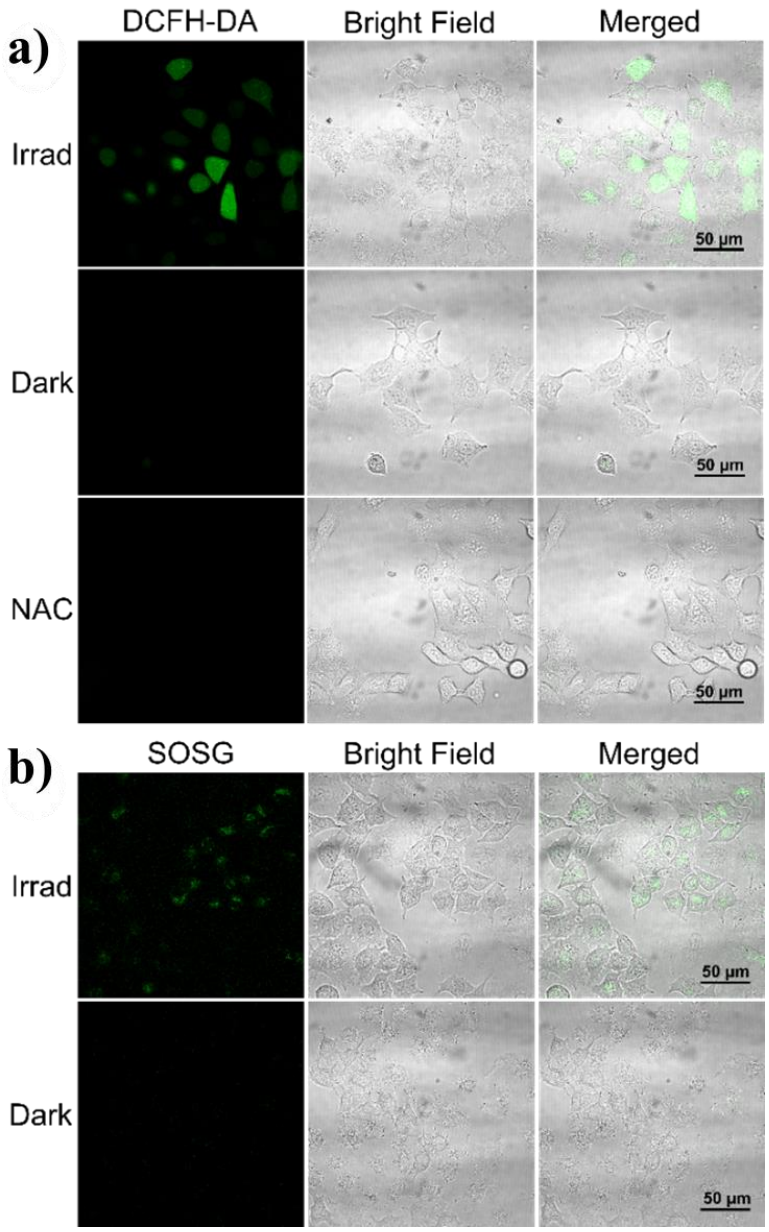

Figure 5.3. Fluorescence and brightfield images of A549 cells incubated for 1 h with a 10 µM solution of **17** then irradiated for 1 h (465 nm, 4.8 mW·cm^{-2}), stained with a) DCFH-DA (20 µM, $\lambda_{ex}/\lambda_{em}$ = 488/502-532 nm), and b) SOSG (1 µM, $\lambda_{ex}/\lambda_{em}$ = 488/517-559 nm). Scale bar: 50 µm. Reproduced from reference (unpublished).[19]

Based on these findings, hard X-ray synchrotron studies were performed on cryo-fixed and freeze-dried A549 lung cancer cells treated with a 500 µM solution of complex **17** in the dark. XRF maps displaying Pt and Ir, as well as endogenous elements Zn, S, P, and K, allowed for the determination of co-localisation between elements. Cells treated with 500 µM complex **17** exhibited signs of damage such as increased cell roundness, often observed in cell death pathways.[19,20]

Cell nuclei are identifiable by high concentrations of intracellular Zn.[21] Co-localisation of Pt and Zn was much higher than that of Ir and Zn ($r = 0.65 \pm 0.05$ and $r = 0.33 \pm 0.12$, respectively), indicating Pt is more localised in the nucleus. Moderate co-localisation of Pt and Ir was observed ($r = 0.51 \pm 0.10$), implying that some intact intracellular **17** is present. However, quantification of intracellular metal content revealed 4.13-4.63× more Pt than Ir in treated cells. This indicates that most of the **17** is cleaved since the separate Ir and Pt species localise in different areas. Further work is needed to confirm whether this cleavage occurs extracellularly or intracellularly.

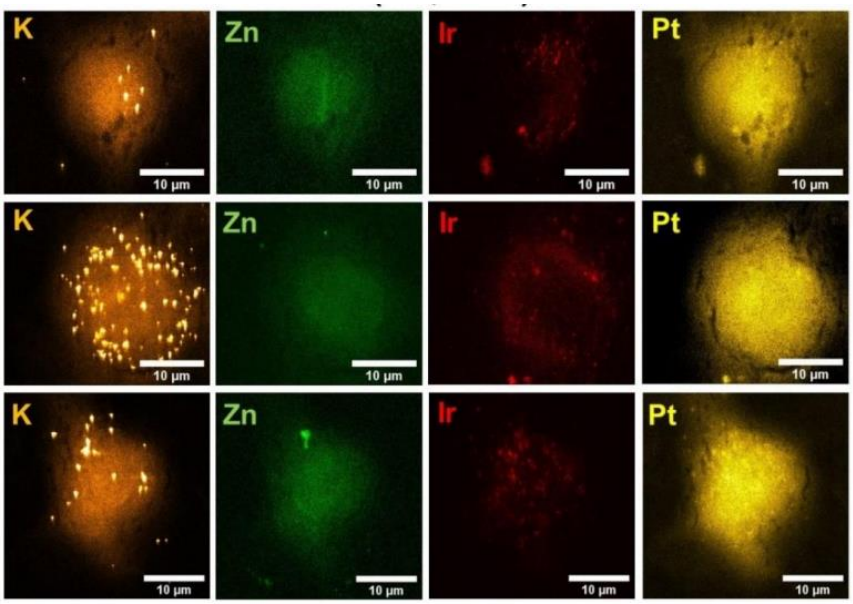

Figure 5.4. XRF elemental maps of cryo-fixed and freeze-dried A549 cells on silicon nitride membranes treated with 500 µM **17** for 2 h. Incident energy: 12.5 keV, 100 nm steps, 0.1 s exposure, 50×75 nm beam size. Data analysed using PyMCA and images generated using ImageJ. K (■), Zn (■), Ir (■) and Pt (■). Reproduced from reference.[2]

In this Chapter, A549 lung cancer cells treated with biologically relevant concentrations (3-5× IC_{50}) of **17** under dark and irradiated conditions were fixed on silicon nitride membranes (200 – 500 nm thickness), dehydrated, and examined by synchrotron X-ray Fluorescence (XRF), X-ray Absorption Near-Edge Structure (XANES) spectroscopy and Differential Phase Contrast (DPC) at Diamond Light Source, Harwell Campus, Didcot, UK. This Chapter details the analysis of synchrotron X-ray data for A549 lung cancer cells treated with lower, biologically

relevant concentrations of complex **17** to avoid the damage previously seen at 500 μM. Analysis of irradiated samples was performed in addition to dark and untreated control samples, and Pt oxidation states in dark cells were determined using XANES.

5.2 Experimental

5.2.1 Synthesis

The reagent and solvent suppliers are listed in **Chapter 2 Section 2.1**.

4-Methyl-2,2'-bipyridine-4'-carboxaldehyde

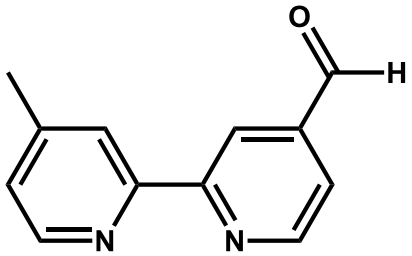

A 20 mL solution of selenium dioxide (4.42 g, 37.05 mmol, 1.45 eq) in 1,4-dioxane (4% H_2O) was added to a 200 mL solution of 4,4'-dimethyl-2,2'-bipyridine (5.25 g, 28.5 mmol. 1 eq) in 1,4-dioxane and gently refluxed at 403 K for 20 h. The mixture was then filtered through Celite while hot, and the Celite was washed with 50 mL ethanol. The ethanol was then combined with the filtrate and solvents removed under reduced pressure. The remaining residue was suspended in 50 mL saturated sodium bicarbonate solution and extracted with 5 × 50 mL DCM. Organic phases were combined, dried with magnesium sulfate, filtered, then solvent removed under reduced pressure. Residue was dissolved in 100 mL 0.3 M aqueous sodium metabisulfite solution and stirred for 30 min. The solid was filtered off then resuspended in 50 mL 0.3 M sodium metabisulfite solution, stirred for 30 min and filtered. Filtrates were combined and washed with 2 × 25 mL ethyl acetate. Sodium bicarbonate (18 g) was added slowly to the sodium metabisulfite solution and product was extracted with 20 × 40 mL DCM. Organic phases were combined, dried with magnesium sulfate, filtered, and dried under reduced pressure to give final product. Yield = 0.9773 g (17%). ^{1}H NMR (400 MHz, $CDCl_3$) δ 10.12 (s, 1H, CHO), 8.83 (d, J = 4.9 Hz, 1H, pyr H), 8.77 (s, 1H, pyr H), 8.51 (d, J = 4.9 Hz, 1H, pyr H), 8.22 (s, 1H, pyr H), 7.66 (dd, J = 4.9, 1.5 Hz, 1H, pyr H), 7.13 (d, J = 4.2

Hz, 1H, pyr H), 2.40 (s, 3H, CH_3). ESI-MS: $[M+Na]^+$ (m/z) calc., 221.1; found, 221.2.

4-Methyl-2,2'-bipyridine-4'-carbaldehyde oxime

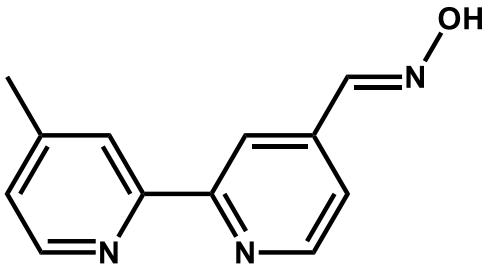

4-Methyl-2,2'-bipyridine-4'-carboxaldehyde (0.9773 g, 4.93 mmol, 1 eq) was dissolved in 15 mL methanol. Hydroxylamine hydrochloride (1.0278 g, 14.8 mmol, 3 eq) and potassium carbonate (2.7257 g, 19.7 mmol, 4 eq) were dissolved in water. Solutions were combined and refluxed at 353 K for 1 h, then allowed to cool to room temperature and poured into 100 mL ice cold water to form a precipitate. This was filtered, washed with 10 mL cold water, then dried overnight in a vacuum desiccator. Yield = 0.8650 g (82%). ^{1}H NMR (400 MHz, $CDCl_3$) δ 11.33 (s, 1H, NOH), 8.68 (s, 1H, CHN), 8.64 (d, J = 5.0 Hz, 1H, pyr H), 8.47 (d, J = 5.1 Hz, 1H, pyr H), 8.13 (s, 2H, 2× pyr H), 7.34 (dd, J = 5.0, 1.1 Hz, 1H, pyr H), 7.13 (d, J = 4.7 Hz, 1H, pyr H), 2.39 (s, 3H, CH_3). ESI-MS: $[M+Na]^+$ (m/z) calc., 236.1; found, 236.1.

4-Methyl-2,2'-bipyridine-4'-methanamine

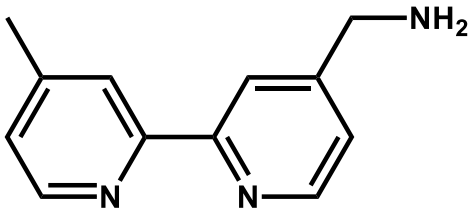

4-Methyl-2,2'-bipyridine-4'-carbaldehyde oxime (1 g, mmol, 4.69 mmol, 1 eq) was placed in a glass reaction vessel and dissolved in 70 mL methanol. Pd/C catalyst (10 wt.%, 150 mg) and a stirrer bar were added, and the vessel placed in a hydrogenator at 15 bar for 20 h. The solution was then passed through celite,

washed with methanol and dried under reduced pressure to give an off-white solid. Yield = 0.3136 g (34%). ^{1}H NMR (400 MHz, $CDCl_3$) δ 8.54 (d, J = 4.7 Hz, 1H, pyr H), 8.45 (d, J = 4.7 Hz, 1H, pyr H), 8.26 (s, 1H, pyr H), 8.16 (s, 1H, pyr H), 7.21 (d, J = 3.8 Hz, 1H, pyr H), 7.06 (d, J = 4.4 Hz, 1H, pyr H), 3.90 (s, 2H, CH_2), 2.36 (s, 3H, CH_3), NH_2 not visible due to exchange with solvent. ESI-MS: $[M+Na]^+$ (m/z) calc., 222.1; found, 222.1.

$[Ir(ppy)_2(NH_2CH_2\text{-}bpy\text{-}CH_3)]Cl$, (Ir-$NH_2$) – ***16***

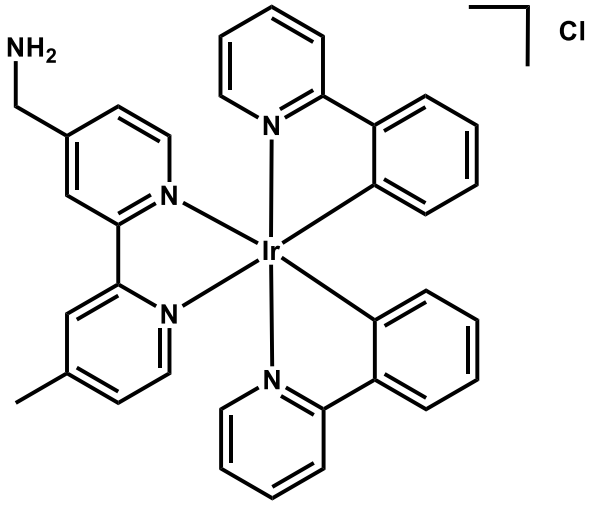

4-Methyl-2,2'-bipyridine-4'-methanamine (0.092 g. 0.46 mmol, 3 eq) and iridium dimer $[Ir(ppy)_2Cl]_2$ (0.165 g, 0.15 mmol, 1 eq) were dissolved in 30 mL DCM/methanol (2:1 v/v) and refluxed at 333 K for 21 h. The mixture was cooled to room temperature then solvents removed under reduced pressure to leave a yellow oil, which was purified using the Biotage method described in **Chapter 3, Section 3.2.5**. Solvent was removed, then product was redissolved in methanol and passed through an Amberlite IRA-410(Cl) ion exchange column to remove the trifluoroacetate. Yield = 0.120 g (54%). ^{1}H NMR ($CDCl_3$, 500 MHz): 9.41 (br, s, 2H, NH_2), 9.05 (s, 1H, bpy H), 8.52 (s, 1H. bpy H), 7.93-7.89 (m, 3H), 7.79-7.74 (m, 3H), 7.69 (d, J = 7.2 Hz, 2H), 7.56 (d, J = 5.5 Hz, 1H), 7.48 (d, J = 5.2 Hz, 2H), 7.20 (d, J = 5.4 Hz, 1H), 7.05 (t, J = 6.9 Hz, 3H), 6.98 (t, J = 6.7 Hz, 1H), 6.95-6.91 (m, 2H), 6.31 (t, J = 8.0 Hz, 2 H), 4.43 (s, 2H, CH_2), 2.57 (s, 3H, CH_3). ESI-HR-MS: $[M]^+$ (m/z) calc., 700.2047; found, 700.2033.

All syntheses from this point were performed by Dr Huayun Shi in the dark with minimal light exposure.

Caution! Heavy metal azides can be shock-sensitive and should be handled with care, although no problems were encountered in this synthesis.

Trans, trans, trans - $[Pt^{IV}(py)_2(N_3)_2(OH)(OCOCH_2CH_2CO_2NC_4H_4O_2)]$ - ***Pt-NHS***

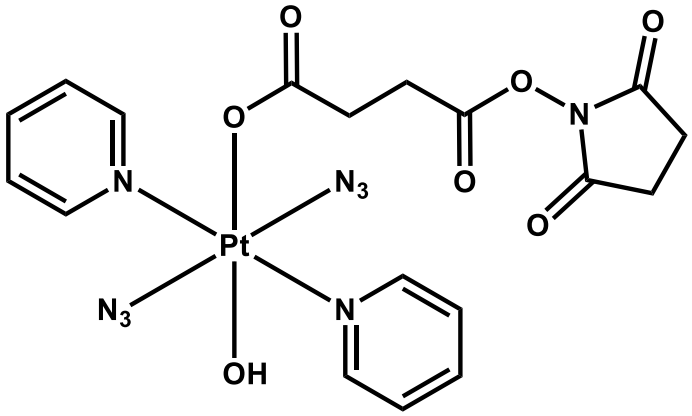

Pt-NHS was synthesised according to the literature procedure.[22]

Trans, trans, trans - $[Pt^{IV}(py)_2(N_3)_2(OH)(OCOCH_2CH_2CONHCH_2$-bpy-$CH_3)Ir^{III}(ppy)_2]Cl$, (Pt-Ir) - ***17***

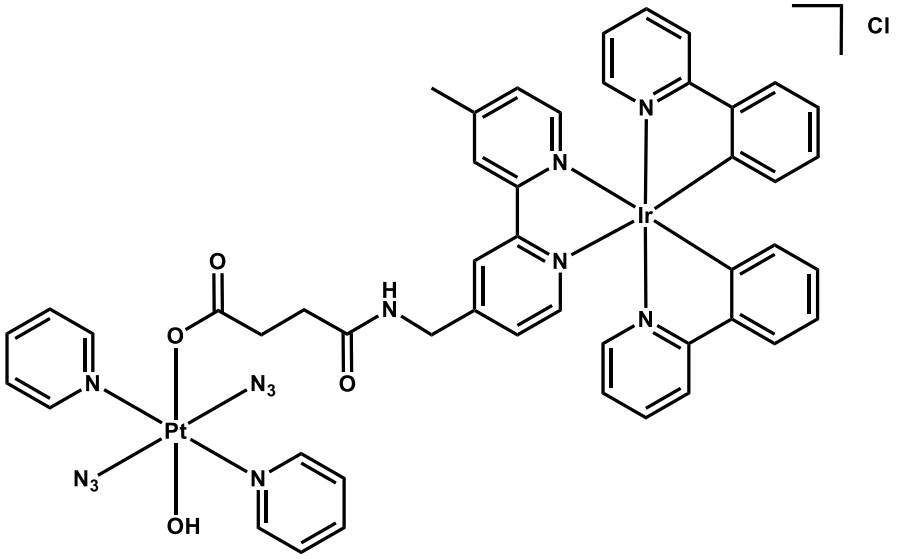

Freshly prepared **Pt-NHS** (10.4 mg, 15.5 µmol, 1.03 eq) and Ir-NH_2 complex **16** (11.0 mg, 15.0 µmol, 1.0 eq) were dissolved in 2 mL DMF with DIPEA (20 µL, 114.8 µmol, 7.65 eq) and stirred under nitrogen at 298 K overnight. Solvent was removed under reduced pressure and the crude product purified by column chromatography on alumina using a mobile phase of 6% methanol in dichloromethane. ^{1}H NMR ($CDCl_3$, 600 MHz): 9.66 (t, J = 6.3 Hz, 1H, C(O)NH), 9.46 (s, 1H, H bpy), 9.08 (s, 1H, H bpy), 8.96 (d with Pt satellite, J = 5.8 Hz, 4H, Hα py), 8.02 (t, J = 7.6 Hz, 2H, Hγ py), 7.91 (t, J = 8.6 Hz, 2H, H ppy), 7.78-7.72 (m, 8H, Hβ py and H ppy), 7.68 (d, J = 7.8 Hz, 2H, H ppy), 7.51 (d, J = 5.8 Hz, 1H, H bpy), 7.45 (d, J = 5.8 Hz, 1H, H bpy), 7.37 (d, J = 5.6 Hz, 1H, H bpy), 7.15 (d, J = 5.6 Hz, 1H, H bpy), 7.03 (t, J = 7.9 Hz, 2H, H ppy), 7.01 (d, J = 7.0 Hz, 2H, H ppy), 6.96 (t, J = 6.6 Hz, 1H, H ppy), 6.91 (t, J = 7.4 Hz, 2H, H ppy), 6.29 (dd, J = 13.6, 7.6 Hz, 2H, H ppy), 4.69 (d, J = 6.2 Hz, 2H, CH2), 2.84 (t, J = 7.5 Hz, 2H, CH_2), 2.70 (t, J = 7.8 Hz, 2H, CH_2), 2.61 (s, 3H, CH_3). ^{13}C NMR ($CDCl_3$, 150 MHz): 176.12, 173.69, 167.97, 167.84, 155.95, 155.83, 153.69, 152.08, 150.79, 150.51, 149.64, 149.54, 149.23, 148.67, 148.31, 143.51, 143.43, 141.06, 137.97, 137.87, 131.74, 131.70, 130.79, 130.69, 128.52, 127.01, 126.90, 126.26, 124.94, 124.79, 124.70, 123.23, 123.10, 122.56, 122.44, 119.64, 119.44, 41.90, 32.45, 32.23, 21.61. ^{195}Pt NMR ($CDCl_3$, 129 MHz): 961.07. ESI-HR-MS: $[M]^+$ (m/z) Calc., 1253.2833; Found, 1253.2838.

5.2.2 Synchrotron sample preparation

Pt-Ir complex **17** was dissolved in DMSO and analysed by ICP-MS (**Chapter 2, Section 2.2.9**) by Dr Huayun Shi to determine a concentration of 3276 µM. This was diluted with RPMI-1640 (no phenol red) to give solutions **A** and **B** with concentrations of 17.5 µM ($5\times IC_{50}$) and 10.5 µM ($3\times IC_{50}$), respectively, with DMSO kept below 1% v/v.

A549 lung cancer cells were grown in T75 flasks with DMEM containing 10% FCS, penicillin/streptomycin and L-glutamine (**Chapter 2, Section 2.3.2**). When cells had reached 80-90% confluence, medium was removed and cells were washed with PBS, and then detached from the surface with 2 mL trypsin/EDTA solution. A single-cell suspension was formed with fresh media and cells were counted in a

haemocytometer. The cell suspension was then diluted to a 50,000 cell·mL^{-1} suspension.

In sterile 6-well plates, silicon nitride grids were sterilised by adding 2 mL ethanol to the well for 5 minutes, followed by 2 mL 70% ethanol solution for 5 minutes. After removal of the 70% ethanol, grids were left to air dry. Two drops of poly-L-lysine were added directly to the membrane and left for 20 minutes. Membranes were washed with 2 mL PBS, then left to air dry. Once dry, 2 × 50 µL of the 50,000 cell·mL^{-1} suspension was added directly to each membrane and plates were left in an incubator at 310 K with 5% CO_2 for 2 hours, then 2 mL of the same cell suspension was added to each well and plates were incubated for 24 hours.

From this point on, all sample preparation was performed under minimal light due to the photosensitive nature of the complex. Medium was removed from the wells, then 2 mL of solution **A** or **B** (or media for negative controls) was added and incubated in the dark for 1 h. For "Dark" samples, grids were left in the incubator for another hour in the dark, whilst "Light" samples were removed from the incubator and placed under a 465 nm 96-LED array for 1 h (4.8 mW·cm^{-2}, 17.28 J·cm^{-2}). Supernatants were then removed, and grids were washed twice with 2 mL HBSS, then left in 2 mL HBSS and plates wrapped in foil and immediately taken for plunge-freezing.

Cryo-vials were placed into a box and filled with liquid nitrogen. Grids were dipped in 3 mL sterile water for 3 seconds, blotted with filter paper then frozen in liquid ethane using a manual plunge-freezer. They were then quickly transferred into liquid nitrogen and then into a cryo-vial. Once all samples were in cryo-vials, excess nitrogen was removed and vials were covered with parafilm with a hole pierced. Vials were then placed in a freeze-dryer for 24-48 h.

5.2.3 Synchrotron XRF, XANES and DPC – I14, Diamond Light Source

Experiments were performed remotely with the assistance of Dr Cinzia Imberti using NoMachine software, whilst Dr Paul Quinn, Dr Miguel Gomez Gonzalez and Dr Julia Parker assisted on site at I14.

Silicon nitride membranes were loaded into sample holders and analysed on the beamline at 298 K. XRF maps were constructed using raster scanning with 12 keV incident energy, xy step size = 100 nm, 0.1 s exposure. The focused X-ray beam size for this experiment was 70×70 nm^2. The sample was raster scanned (continuous scanning) through the X-ray focus, and the fluorescent X-rays collected by a four-element silicon drift detector (Rayspec) located in backscatter geometry, with a solid collection angle of 0.8 sr. AXO standards of known elemental composition were used to estimate photon flux. A Merlin Quad (Quantum Detectors, UK) photon counting detector is available in transmission geometry at I14 beamline for differential phase contrast (DPC) imaging (effective pixel <55 μm),[23] which was placed 1.85 metres distant from the sample with a He-filled flight tube in between closing the air gap. The intensity on the detector at this distance can be contained in a single quadrant and is typically cropped to 128×128 pixels around the nominal beam centre. The masking of the beam is automated to account for small adjustments of the KB mirrors or movement of the Merlin detector. The phase integration step requires both continuity and differentiability of the phase gradient, which is retrieved by applying a series of fast Fourier Transform and discrete cosine transforms mathematical calculations.

XANES spectra were acquired using an energy range across the Pt L_3-edge (11.57 keV, range: 11.46-11.75 keV). Spectra were recorded over areas previously mapped by XRF. Reference pellets of cisplatin [$\mathbf{Pt^{II}}Cl_2(NH_3)_2$], potassium tetrachloroplatinate [$K_2\mathbf{Pt^{II}}Cl_4$] and FM190 [*trans, trans, trans*-$\mathbf{Pt^{IV}}(OH)_2(N_3)_2(py)_2$] (complex **15**), were prepared at the beamline by mixing with cellulose and applying 1.5 T force with a manual hydraulic pellet press (Specac, UK).

5.2.4 Synchrotron data processing and analysis

All data processing was performed by Dr Miguel Gomez Gonzalez at beamline I14. XRF data were fitted and analysed using PyMCA software to perform a pixel-by-pixel data subtraction and to batch fit the fluorescence peaks, providing a RGB image for each element present in the sample.[24] Fitted data were viewed in ImageJ to determine the distribution of platinum, iridium, and endogenous elements, and

for the colocalization of elements. Known standards (AXO Dresden GmbH, Germany) were used to calibrate the fitting and quantify data. Maximum cell thickness was assumed as 6 μm.[25] Multiple XRF spectra of the regions of interest were obtained along the Pt L_3-edge (11.564 keV). An active drift compensation method was used to maintain alignment between successive scans over the course of the XANES spectromicroscopy.[26] Furthermore, the XANES maps were stacked, aligned, and normalised using the I_0 intensity *via* an in-house python-based script. Principle Component Analysis was performed on the XANES spectra, followed by cluster analysis using MANTiS spectromicroscopy software.[27]

The individual XANES spectra extracted from each cluster were analysed in Athena XAS Data Analysis Software.[28] The background was subtracted applying a linear fit through the Pt pre-edge region and the autobk routine in Athena for the spline fit through the full XAS region.

Linear combination fits (LCF) were performed on Pt XANES data using solid pellets with varying ratios of Pt(II):Pt(IV) complexes following the method developed by Hambley *et al*.[29]

5.3 Results

5.3.1 Synthesis of Pt-Ir (17)

Synthesis of the amine ligand starting from 4,4'-dimethyl-2,2'-bipyridine was performed using methods adapted from literature.[30] Whilst overall yields differed, ^{1}H NMR spectra were in good agreement with those reported. Complex **16** (Ir-NH_2) was previously synthesised in the Sadler group by Dr Huaiyi Huang, but at the time of writing, this work is not yet published. Due to the photodecomposition of the platinum species, all platinum-containing reactions were performed in the dark. The structure of complex **17** was confirmed by ^{1}H, ^{13}C and ^{195}Pt NMR in addition to high-resolution mass spectrometry.

5.3.2 Synchrotron studies at I14, Diamond Light Source

Although irradiated and dark samples were prepared for both 3× and 5×IC_{50}, time constraints and damaged grids led to a full dataset (*i.e.*, XRF maps, DPC images

and XANES spectra for light and dark) of only the $5\times IC_{50}$ samples and untreated controls (no XANES). Further XANES data was also acquired for $3\times IC_{50}$ light samples (**Appendix Table A9**).

Co-localisation and quantification

Entire cells were not imaged due to the time taken to obtain XRF elemental maps in each condition, so properties such as cell roundness and area were not calculated. However, large sections of each cell were imaged, including the majority of the nucleus and cytoplasm. XRF maps of endogenous elements produced information on the condition of the cells. DPC images were collected simultaneously with the XRF maps, which could also be used to observe the morphology of the cells (**Appendix Figures A1-A13**). Platinum and iridium content was calculated by extrapolation using the copper K-edge signal from an AXO standard (RG01-200-S5460-02, www.axo-dresden.de) with a known copper content (2.4 ± 0.2 ng·mm^{-2}). Data were batch-fitted quantitatively using PyMCA, using a fundamental-parameters algorithm, which outputs the data as a mass fraction.[31–33] The mass fraction of the element divided by the product of the mass fraction of Cu in the AXO standard and its known concentration, equalled to the Pt/Ir concentration in ng·mm^{-2}, which was subsequently converted to molar units (mol·mm^{-2}).

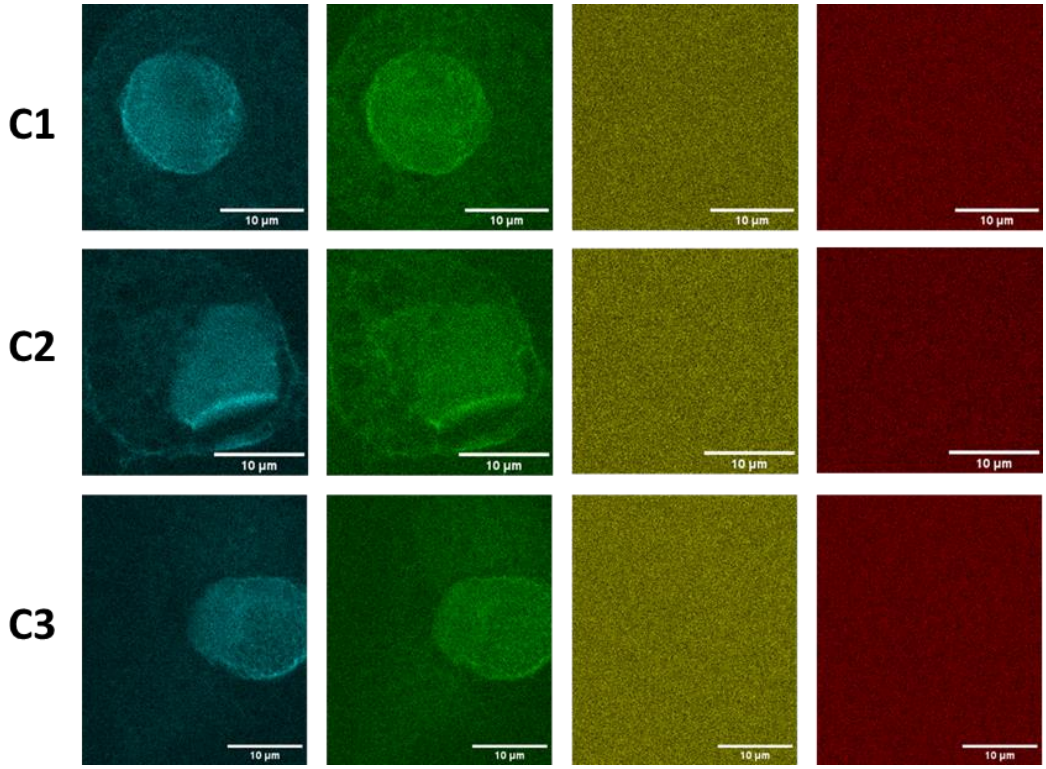

Figure 5.5. XRF maps for Zn, P, Pt and Ir of cryo-fixed and freeze-dried A549 lung cancer cells (**C1-C3**) on silicon nitride grids incubated in cell culture media only (no Pt-Ir complex **17**). Incident energy: 12 keV, 100 nm steps, 0.1 s exposure, 70×70 nm^2 beam size. Data analysed using PyMCA and images generated using ImageJ. Zn (■), P (■), Pt (■) Ir (■).

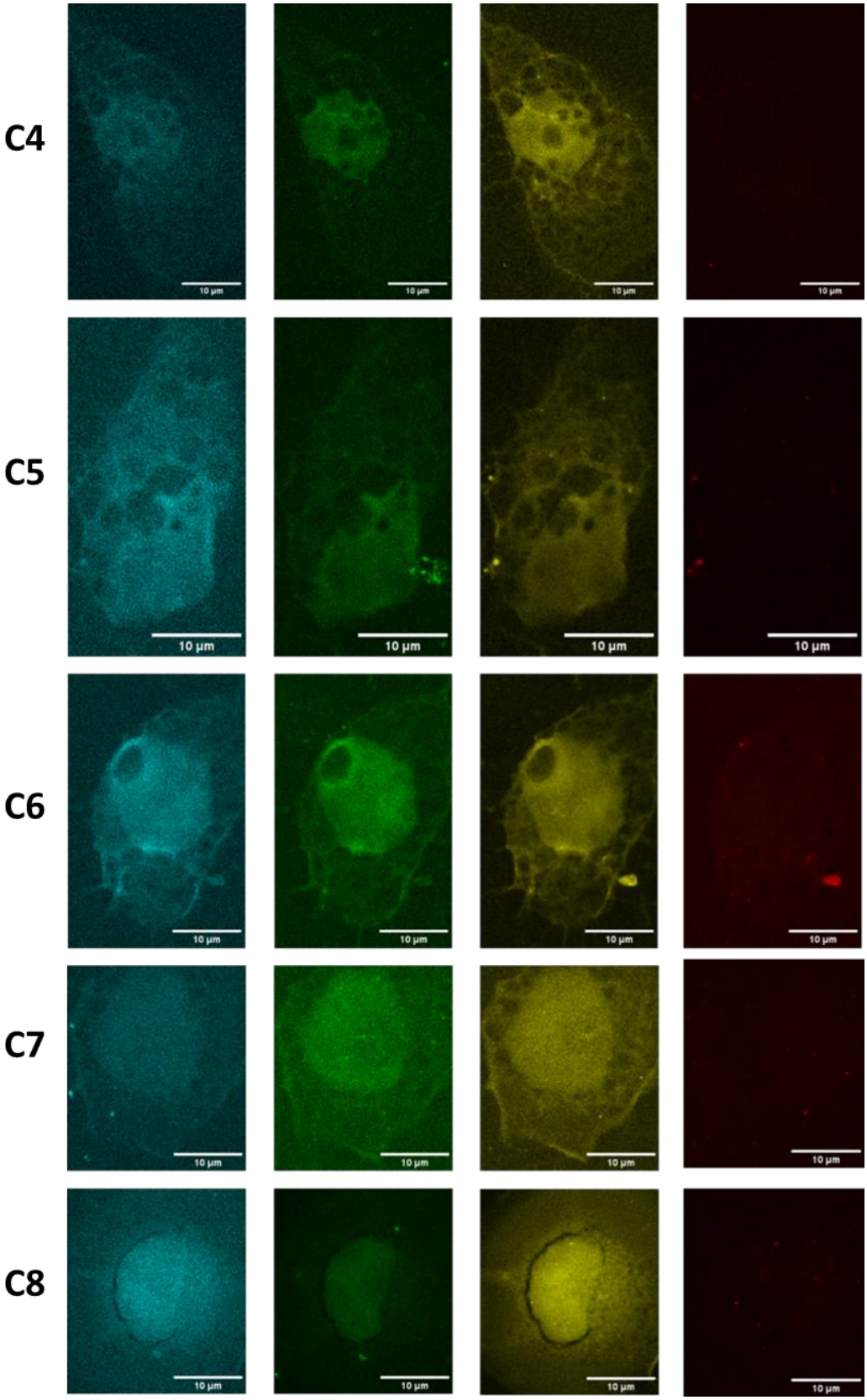

Figure 5.6. XRF maps for Zn, P, Pt and Ir of cryo-fixed and freeze-dried A549 lung cancer cells (**C4**-**C8**) on silicon nitride membranes incubated with Pt-Ir complex **17** ($5\times IC_{50}$) for 1 h, then exposed to blue light irradiation for 1 h (λ = 465 nm, 4.8 $mW\cdot cm^{-2}$). Incident energy: 12 keV, 100 nm steps, 0.1 s exposure, 70×70 nm^2 beam size. Data analysed using PyMCA and images generated using ImageJ. Zn (■), P (■), Pt (■) Ir (■).

Untreated A549 cells **C1**-**C3** (**Figure 5.5**) have clearly resolved nuclei indicated by the highly concentrated Zn and P regions, whilst cytoplasmic Zn and P are both relatively low. As expected, no X-ray fluorescence was observed for Pt or Ir (signals in **Figure 5.5** are noise). Nuclei of cells **C1** and **C3** are both much rounder than the nucleus of **C2**, which also exhibits holes in the cytoplasm. Conversely, **C1** and **C3** both seemed to have a far more intact cytoplasm. Background levels of Pt and Ir were calculated to be 5.345 ± 1.252 pmol·mm^{-2} and 1.592 ± 1.329 pmol·mm^{-2}, respectively (**Table 5.3**).

Table 5.3. Background levels of Pt and Ir in cryo-fixed and freeze-dried A549 lung cancer cells with no exposure to complex **17**.

Cell	Pt (pmol·mm^{-2})	Ir (pmol·mm^{-2})
C1	3.910 ± 0.003	3.394 ± 0.003
C2	5.165 ± 0.004	1.155 ± 0.001
C3	6.962 ± 0.006	0.228 ± 0.000
Average	5.345 ± 1.252	1.592 ± 1.329

A549 cells treated with a 5×IC_{50} (17.5 μM) solution of **17** and irradiated for 1 h with blue light (**C4**-**C8**, **Figure 5.6**) have damaged cytoplasms, whilst cells **C4**-**C6** also exhibit damaged nuclei. Pt is distributed throughout the cells, leading to XRF maps similar to those of K and Zn. Conversely, the signal of Ir throughout cells is less intense, with small hotspots observed around the cytoplasm. The quantity of Pt in these cells was significantly higher than Ir (p = 0.05, **Table 5.4, Figure 5.7**). The mean Pt content was *ca.* 1 nmol·mm^{-2}, whilst the mean Ir content was *ca*. 22 pmol·mm^{-2}. Co-localisation between Pt, Ir and Zn was determined by calculating Pearson's R values (r) and Spearman's Rank Correlation values (r_s) using ImageJ (**Table 5.5**). High Pt/Zn co-localisation (r = 0.53 ± 0.13, r_s = 0.46 ± 0.13) indicates a high proportion of Pt accumulates in the cell nucleus, whilst low Ir/Zn co-localisation indicates Ir in the nucleus is sparse (r = 0.08 ± 0.05, r_s = 0.08 ± 0.05). Little co-localisation was seen between Pt and Ir (r = 0.15 ± 0.10, r_s = 0.11 ± 0.08).

Table 5.4. Metal content in cryo-fixed and freeze-dried A549 cells treated with Pt-Ir complex **17** ($5\times IC_{50}$) for 1 h followed by 1 h blue light irradiation (λ = 465 nm, 4.8 mW·cm^{-2}).

Cell[a]	Pt (nmol·mm^{-2})	Ir (pmol·mm^{-2})	Pt/Ir ratio
C4	0.557 ± 0.000	11.689 ± 0.010	48
C5	0.791 ± 0.001	15.603 ± 0.013	51
C6	1.800 ± 0.002	43.601 ± 0.036	41
C7	0.635 ± 0.001	17.076 ± 0.014	37
Average	0.946 ± 0.500	21.992 ± 12.630	44 ± 6

[a] **C8** not included due to anomalous data (Pt/Ir ratio = 5832).

Table 5.5. Pearson's R Values and Spearman's Rank Correlation Values for the co-localisation of Pt, Ir and Zn in cryo-fixed and freeze-dried A549 cells treated with Pt-Ir complex **17** ($5\times IC_{50}$) for 1 h followed by 1 h irradiation with blue light (λ = 465 nm, 4.8 mW·cm^{-2}).

Cell	Pearson's R value (r)			Spearman's Rank Correlation value (r_s)		
	Pt/Zn	Ir/Zn	Pt/Ir	Pt/Zn	Ir/Zn	Pt/Ir
C4	0.36	0.03	0.00	0.24	0.02	-0.01
C5	0.49	0.04	0.21	0.48	0.06	0.12
C6	0.71	0.14	0.27	0.60	0.15	0.21
C7	0.43	0.04	0.05	0.43	0.05	0.04
C8	0.66	0.14	0.21	0.56	0.14	0.19
Average	0.53 ± 0.13	0.08 ± 0.05	0.15 ± 0.10	0.46 ± 0.13	0.08 ± 0.05	0.11 ± 0.08

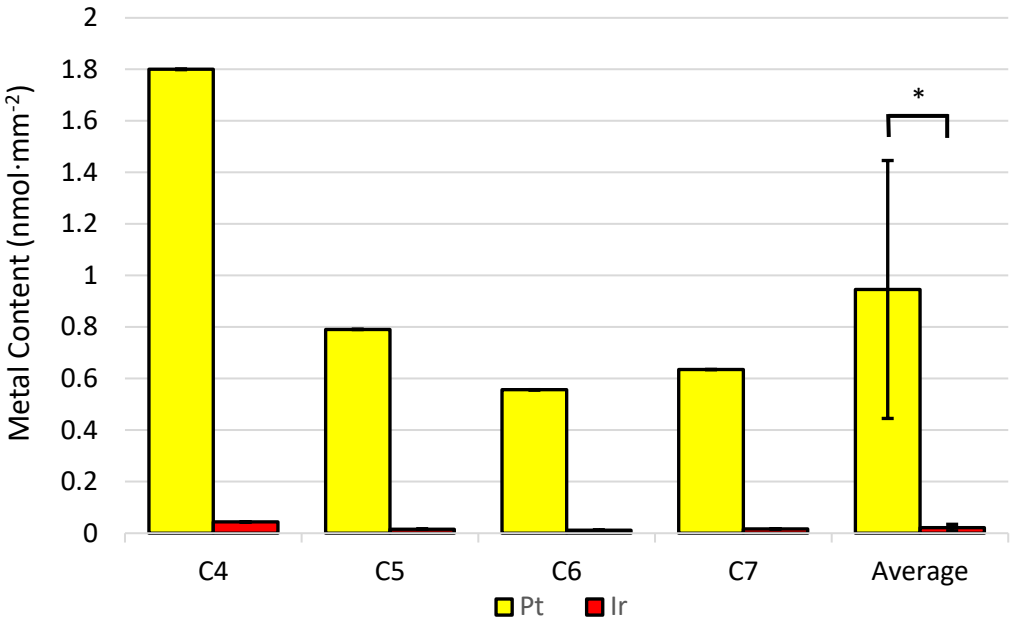

Figure 5.7. Quantity of Pt and Ir in A549 cells treated with 5×IC_{50} Pt-Ir complex **17** followed by 1 h blue light irradiation (λ = 465 nm, 4.8 mW·cm^{-2}). * $p < 0.05$.

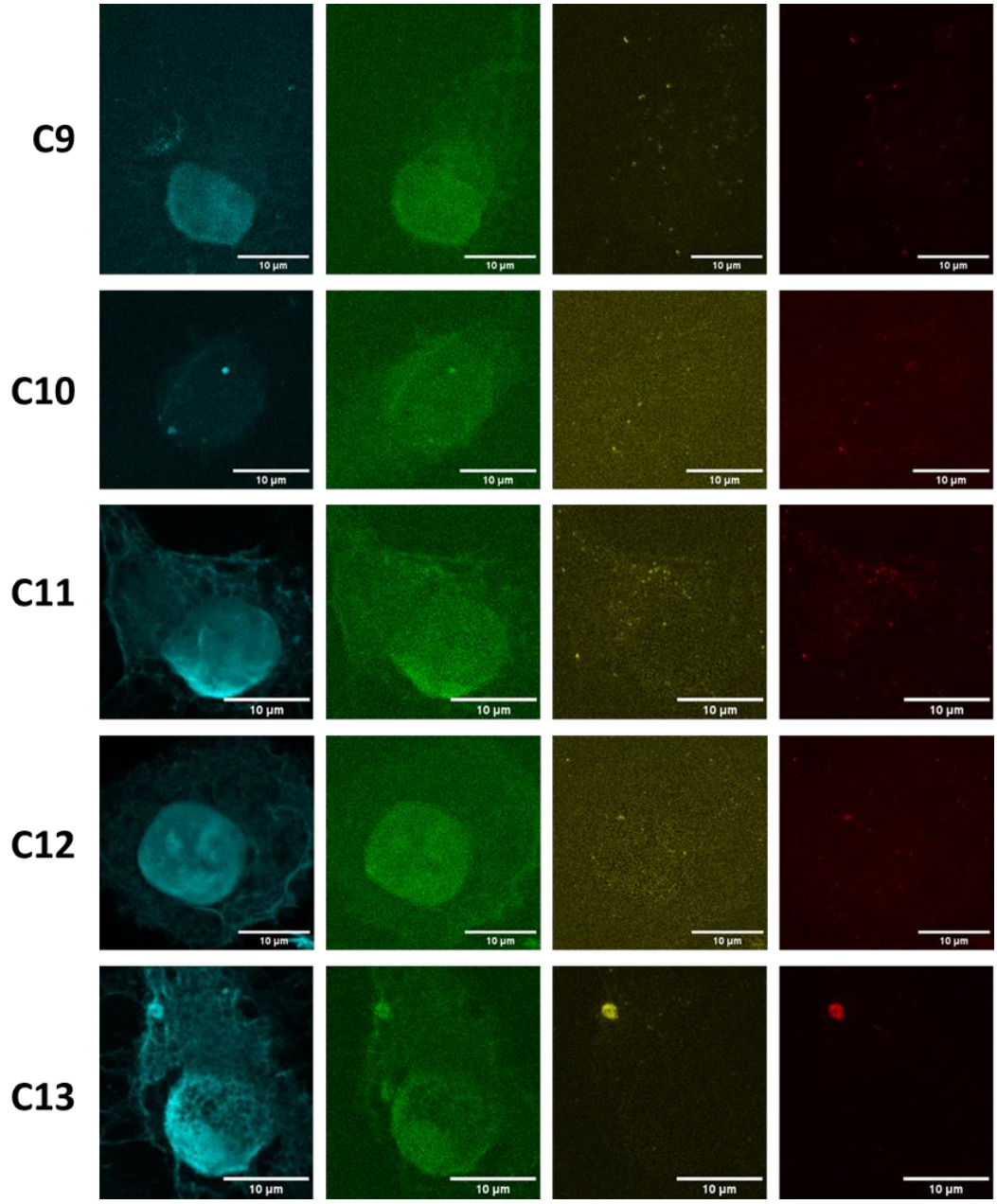

Figure 5.8. XRF maps of cryo-fixed and freeze-dried A549 lung cancer cells (**C9-C13**) on silicon nitride membranes incubated with Pt-Ir complex **17** ($5\times IC_{50}$) for 2 h (no irradiation). Incident energy: 12 keV, 100 nm steps, 0.1 s exposure, 70×70 nm^2 beam size. Data analysed using PyMCA and images generated using ImageJ. Zn (■), P (■), Pt (■) Ir (■).

A549 cells treated with a $5\times IC_{50}$ solution of **17** for 2 h in the dark (with no blue light irradiation, **C9-C13**, **Figure 5.8**) generally have intact nuclei and cell membranes, although damage is noticeable in **C13**. The XRF signal for Pt is distributed throughout the cell, however, the signals are mostly low intensity except for small hotspots and the clear aggregation of Pt seen in **C13** (coinciding with a bright spot of Ir, P and Zn). Hotspots of Ir are also present within each cell. Co-

localisation between Pt, Ir and Zn in dark cells was determined by calculating Pearson's R values (r) and Spearman's Rank Correlation values (r_s) using ImageJ (**Table 5.6**). Co-localisation between Pt and Zn was low (r = 0.09 ± 0.04, r_s = 0.09 ± 0.06), as were co-localisations of Ir and Zn (r = 0.14 ± 0.09, r_s = 0.17 ± 0.13) and Pt and Ir (r = 0.13 ± 0.10, r_s = 0.01 ± 0.04). Metal content in the dark treated cells was very low (**Table 5.7**), with the average amount of Ir (67.808 ± 18.808 pmol·mm^{-2}) around twice that of Pt (35.894 ± 32.009 pmol·mm^{-2}), although this was not statistically significant at the 95% confidence level (p = 0.20).

Table 5.6. Pearson's R Values and Spearman's Rank Correlation Values for the co-localisation of Pt, Ir and Zn in cryo-fixed and freeze-dried A549 cells treated with Pt-Ir complex **17** (5×IC_{50}) for 2 h in the dark (no irradiation).

Cell	**Pearson's R value**			**Spearman's Rank Correlation value**		
	Pt/Zn	**Ir/Zn**	**Pt/Ir**	**Pt/Zn**	**Ir/Zn**	**Pt/Ir**
C9	0.06	0.04	0.22	0.05	0.05	0.02
C10	0.03	0.05	0.01	0.02	0.04	-0.03
C11	0.14	0.18	0.24	0.17	0.30	0.07
C12	0.11	0.27	0.04	0.10	0.28	-0.02
C13	n.d.	n.d.	n.d.	n.d.	n.d.	n.d.
Average	0.09 ± 0.04	0.14 ± 0.09	0.13 ± 0.10	0.09 ± 0.06	0.17 ± 0.13	0.01 ± 0.04

n.d. = not determined. Coefficients for **C13** not calculated due to clear damage to the cell.

Table 5.7. Metal content in cryo-fixed and freeze-dried A549 cells treated with Pt-Ir complex **17** ($5\times IC_{50}$) for 2 h in the dark (no irradiation).

Cell	Pt (pmol·mm^{-2})	Ir (pmol·mm^{-2})	Pt/Ir ratio
C9	6.795 ± 0.006	84.095 ± 0.070	0.1
C10	6.865 ± 0.006	45.188 ± 0.038	0.2
C11	45.989 ± 0.038	88.553 ± 0.074	0.5
C12	83.926 ± 0.070	53.395 ± 0.045	1.6
C13	n.d.	n.d.	n.d.
Average	35.894 ± 32.009	67.808 ± 18.808	0.6 ± 0.6

n.d. = not determined. Coefficients for **C13** not calculated due to clear damage to the cell.

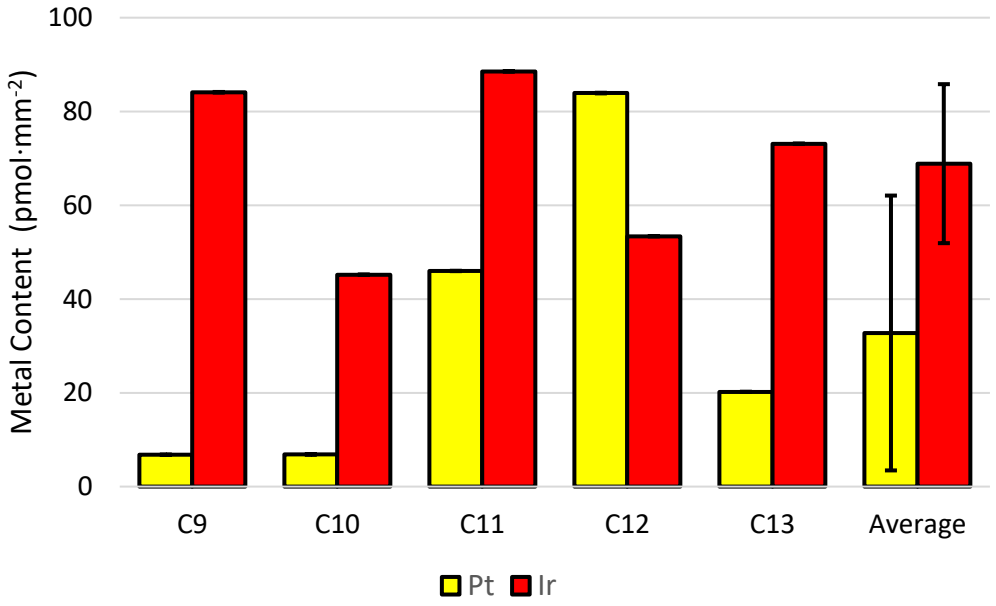

Figure 5.9. Quantity of Pt and Ir in A549 cells treated with $5\times IC_{50}$ Pt-Ir complex **17** in the dark for 2 h (no irradiation).

Platinum oxidation state in cells

Data obtained for irradiated cells incubated with a $5\times IC_{50}$ solution of **17** were analysed in comparison to solid pellets containing mixtures of Pt(II) and Pt(IV)

complexes (**Section 5.2.3**). Pt(II) accounted for 59.9 ± 5.9% of the total platinum signal in irradiated cells treated with 5×IC_{50} **17** (**Table 5.8**).

Table 5.8. Percentage of Pt(II) observed by LCF in samples treated with 5×IC_{50} **17** followed by 1 h blue light irradiation (λ = 465 nm, 4.8 mW·cm^{-2}).

Sample	Pt(II) %
C4	54.0
C5	65.7
Average	59.9 ± 5.9

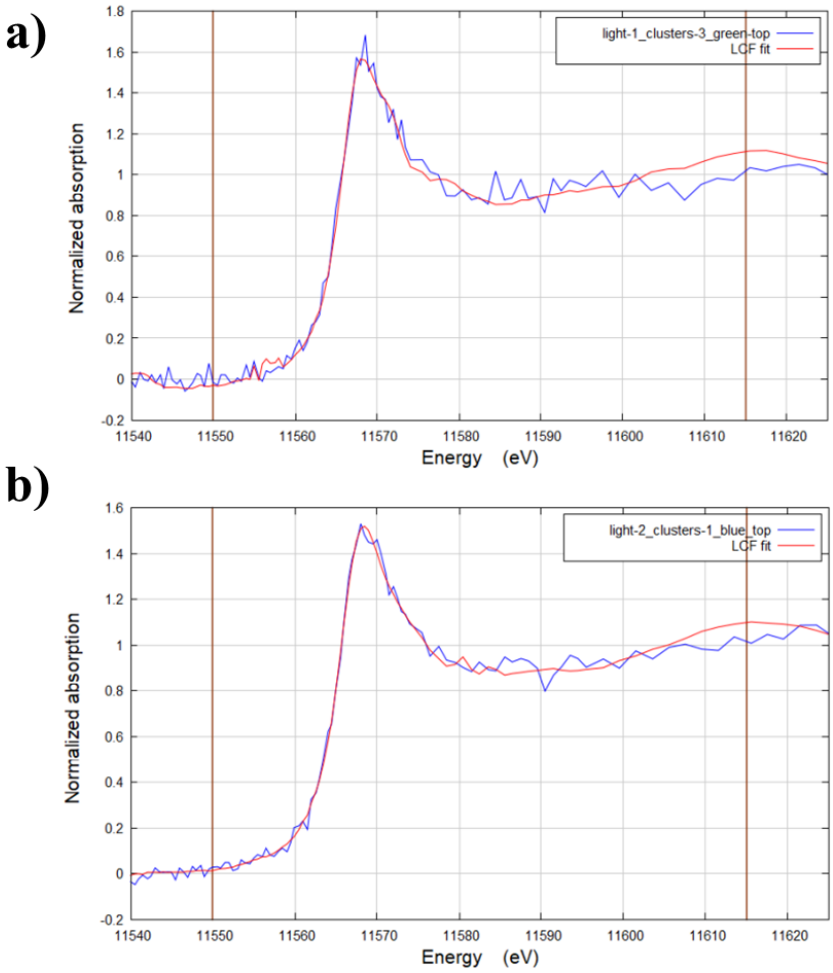

Figure 5.10. X-ray absorption spectra (blue line) and Linear Combination Fitting (red line) obtained from irradiated treated cells a) **C4** and b) **C5**.

Principal Component Analysis and cluster analysis were performed on data collected for dark cells treated with **17** (**C11** and **C13**), however, linear combination fitting (LCF) was not possible as the spectra were too noisy (**Figure 5.11**), meaning average Pt oxidation state could not be determined.

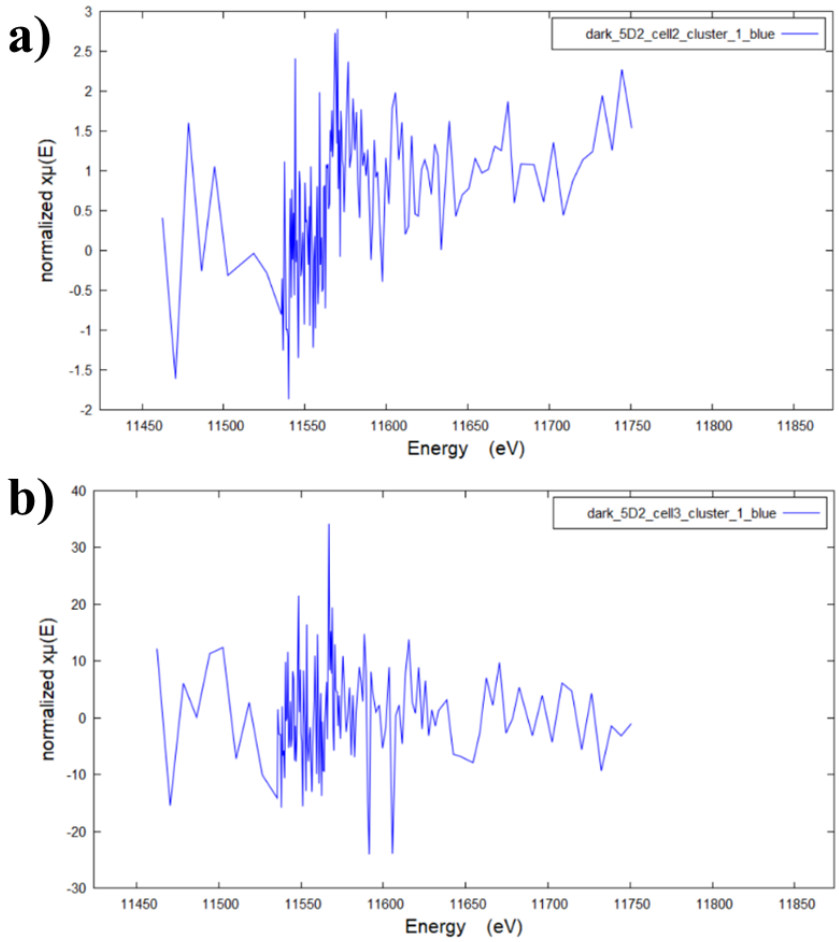

Figure 5.11. X-ray absorption spectra obtained from dark treated cells a) **C11** and b) **C13**. LCF was not possible due to the noise.

5.4 Discussion

Co-localisation and quantification of elements

Endogenous elements are conserved in cells grown on silicon nitride membranes that have undergone cryo-fixation and dehydration.[34] Cell nuclei contain between 30-40% of intracellular Zn despite typically accounting for only *ca*. 8% of the total cell volume.[35,36] However, nuclei in A549 lung cancer cells account for *ca*. 28% of the total cell volume.[37] Nuclei in A549 cells can therefore be observed by their distinct size and higher density of Zn in XRF maps. A549 cells without treatment

with **17** showed no X-ray fluorescence attributable to Pt or Ir, with spectra resembling only noise. Both the cytoplasm and nucleus of **C2** appear to be damaged, demonstrated by the holes in the cytoplasm as well as the less round nucleus when compared to **C1** and **C3**. Since the cells were not exposed to complex or irradiation, it is likely this damage was caused by plunge-freezing and/or freeze-drying process. DPC and phase gradient normalised images (**Appendix Figures A1-A13**) also show damage to **C2** as well as the morphologies of the cells. Background levels of Pt and Ir were calculated to be 5.3 ± 1.3 pmol·mm^{-2} and 1.6 ± 1.3 pmol·mm^{-2}, respectively (**Table 5.4**).

The XRF maps of Ir were very low intensity in cells treated with a 5×IC_{50} solution of **17** and irradiated with blue light, although small hotspots around the cytoplasm could indicate localisation in organelles. Very little Ir was observed in the nucleus, demonstrated by the low Ir/Zn co-localisation (r = 0.08 ± 0.05). Pt was dispersed well throughout the cell, with XRF maps similar to those of Zn and P. Co-localisation of Pt and Zn was high (r = 0.53 ± 0.13), suggesting the Pt moiety is nucleus-targeting. Blue light irradiation of **17** leads to photoreduction *via* the release of azidyl radicals and carboxylate-bearing axial ligands, generating Pt(II) complexes which bind to DNA.[1] Loss of the axial ligands causes the separation of the Pt and Ir species, hence their different distributions throughout the cells and little colocalization (r = 0.15 ± 0.10). Cells **C4-C6** have notably damaged nuclei, with holes seen in the Zn and Pt maps potentially caused by azidyl radicals, supported by the nuclear damage observed by confocal microscopy.[1] Further damage was seen in the cytoplasms of cells **C4-C8**, potentially due to cytoplasmic azidyl radicals or singlet oxygen produced by the photocatalytic Ir moiety released upon photoreduction of **17**. Interestingly, Pt was 37-51× more abundant than Ir across cells **C4-C8**, with the average Pt content significantly greater than Ir at the 95% confidence level (Pt: 946 ± 500 pmol·mm^{-2}, Ir: 21.992 ± 12.630 pmol·mm^{-2}, p = 0.05). This could be due to efflux of the Ir fragment whilst the Pt moiety binds to the DNA in the nucleus. Furthermore, since irradiation occurs with Pt-Ir complex **17** in the solution surrounding the cells, it is likely that extracellular Pt(II) species are generated upon irradiation, which may be internalised similarly to other known Pt(II) complexes (*e.g.*, cisplatin), potentially increasing the amount of intracellular Pt. In contrast, extracellular cleavage of the Pt-Ir complex **17** caused by enzymes

such as cathepsin K, a lysosomal cysteine protease known to be overexpressed in A549 cells which can be secreted into the extracellular matrix, could lead to differences in uptake between the Pt and Ir moieties based on their likely differing lipophilicities.[38] Whilst the amount of Pt was significantly higher in irradiated cells treated with **17** than the background detected in untreated cells (p = 0.05), the difference in Ir content was not found to be significant (p = 0.09), highlighting how little Ir remained in the cells.

A549 cells incubated in the dark with a 5×IC_{50} solution of **17** for 2 hours (no irradiation) were generally less damaged than the irradiated samples, with cytoplasms and nuclei exhibiting far less holes. The notable exception was cell **C13**, which had clear holes throughout the whole cell likely caused by the cryo-fixation and dehydration processes. XRF maps of Pt presented with lower intensity than those of the irradiated samples, with much more noise present in XRF maps of **C10**, **C11** and **C12**. This is due to significantly less Pt being present in the dark cells (32.756 ± 29.310 pmol·mm^{-2}, p = 0.05). Interestingly, the Pt content in irradiated cells is 29× greater than in the dark cells. Since cells are irradiated with **17** still in the surrounding cell growth medium, the extracellular generation of azidyl radicals could lead to cell membrane damage, increasing cell permeability which allows greater accumulation of the photoproducts as seen by cryo-X-ray tomography for similar Pt(IV) agent FM190 (complex **15**) in PC3 prostate cancer cells.[39] These cells had 3× more intracellular Pt after irradiation than dark cells, a much smaller increase than observed for **17**, although a 20-fold increase in intracellular Pt upon irradiation was observed in bladder cancer cells treated with similar Pt(IV) PACT agents.[39,40] Using different cell lines can drastically alter the accumulation of the same complex, as seen for cells treated with osmium complex [Os(*p*-cymene)(TsDPEN)] – intracellular Os in PC3 cells was *ca*. 2× that observed in A549 cells (32 ± 2 fg·cell^{-1} and 18 ± 2 fg·cell^{-1}, respectively).[41]

XRF maps of Ir were much clearer than in the irradiated samples, corresponding with a significant increase in intracellular Ir (dark: 68.870 ± 16.956 pmol·mm^{-2}, irradiated: 21.992 ± 12.630 pmol·mm^{-2}, p = 0.004). The difference in intracellular Pt and Ir content in dark cells was not statistically significant (p = 0.07), which would correlate with more intact **17** entering into the cells. Both Pt and Ir maps showed localised hotspots in the same regions (**Figure 5.8**), potentially suggesting

the intact Pt-Ir complex **17** accumulates in organelles. This is supported by confocal microscopy data which showed mitochondria-targeting that previously could not be confidently attributed to the full complex since **17** and Ir parent complex **16** have almost identical emission spectra.[1] However, co-localisation of Pt and Ir (r = 0.23 ± 0.23) was not statistically different from irradiated samples (r = 0.15 ± 0.10, p = 0.80). It is possible that co-localisation of Pt and Ir in dark cells is lower than the true value due to their significantly lower Pt content leading to more noise in the XRF maps. Synchrotron studies on beamline I14 using A549 cells treated for 2 h in the dark with a 500 μM solution of **17** found co-localisation between Pt and Ir to be significantly higher than the current experiment (r = 0.51 ± 0.10 *vs*. r = 0.15 ± 0.10, p = 0.006), indicating far more intact **17** enters the cells in the dark, which would be expected since no photodecomposition should have occurred.[2]

Oxidation state of platinum in cells

The oxidation state of Pt in cells was probed by XANES mapping in order to determine the degree of photoreduction achieved in cells upon blue light irradiation. X-ray absorption spectra were obtained for 4 cells treated with a 5×IC_{50} solution of **17**: two irradiated cells (**C4** and **C5**) and two dark cells (**C11** and **C13**). Pt(II) was found to be the dominant Pt species in cells **C4** and **C5**, accounting for approximately 60% of the total Pt signal (**Table 5.8**). Combined with the high co-localisation of Pt and Zn (r = 0.53 ± 0.13), this supports the hypothesis irradiation leads to Pt(II) photoproducts which are nucleus-targeting. Further XANES studies examining the Pt in the nucleus and cytoplasm separately may be beneficial, as this might show a far higher percentage of Pt(II) in the nucleus compared to in the cytoplasm, essentially confirming the presence of Pt(II)-DNA adducts in cells. Unfortunately, X-ray absorption spectra obtained for dark cells **C11** and **C13** were too noisy to perform Linear Combination Fitting (**Figure 5.11**), meaning no data on the average oxidation state could be obtained. This is most likely due to the very low concentration of Pt seen in these cells, which does not significantly differ from the untreated control cells (32.8 ± 29.3 pmol·mm^{-2} *vs.* 5.3 ± 1.3 pmol·mm^{-2}, p = 0.13). XANES experiments performed on PC3 cells treated with Pt(IV) parent complex **15** (FM190) found Pt(II) accounted for 20-25% of the total Pt signal in

dark cells (2 h treatment as used for Pt-Ir), with Pt(IV) accounting for the remaining 75-80%. This indicates that Pt(IV) complexes are not extensively reduced in cells without blue light irradiation. Repeat experiments using a higher concentration of **17** could provide better insights into the oxidation state of Pt in cells not exposed to irradiation. In addition, experiments using A549 cells treated with **15** may provide information on whether **17** is more or less prone to reduction in cells without irradiation compared to its parent Pt complex **15**.

5.5 Conclusions and future work

Synchrotron XRF and XANES at the I14 beamline were used to examine A549 lung cancer cells treated with a biologically relevant concentration ($5\times IC_{50}$ = 17.5 μM) of platinum-iridium PDT-PACT agent **17** in both dark and irradiated conditions. Maps of endogenous elements allowed for the identification of the nucleus in each cell and the determination of any morphological changes between cells. Pt and Ir maps were used to determine the stability, photostability and intracellular distribution of **17**, as well as allowing for the calculation of Pt and Ir in each sample using the copper K-edge signal of an AXO standard as a reference. Three control cells (not incubated with **17**) were studied, with damage to one likely caused by the processes of cryo-fixation (plunge-freezing in liquid ethane) and dehydration (freeze-drying). The remaining two cells were more intact, with clear nuclei identified as Zn-dense regions.

A549 cells treated with **17** under irradiated conditions showed damaged cytoplasms and nuclei caused by the generation of singlet oxygen and azidyl radicals upon irradiation. Intracellular Pt levels were significantly higher than Ir (*ca*. 44×), with Ir levels not being significantly different from controls, proving the Pt-Ir complex **17** is not intact after irradiation. Approximately 60% of the Pt was observed as Pt(II). High co-localisation between Pt and Zn indicates nuclear targeting of the Pt species. A combination of the efficient efflux of the Ir species in addition to the formation of Pt(II)-DNA adducts preventing the Pt from being removed from the cell could explain the high disparity between intracellular levels of Pt and Ir.

Cells treated under dark conditions were generally less damaged than irradiated cells. Small hotspots of Pt and Ir may indicate targeting of cytoplasmic organelles

(*e.g.* mitochondria and lysosomes) as suggested by confocal microscopy in dark samples.[1] Intracellular Ir was significantly higher (*ca.* 3×) than in irradiated cells, however, 29× more Pt was observed in irradiated cells. This could be due to the production of extracellular azidyl radicals and singlet oxygen damaging cell membranes and enhancing cell permeability, or greater accumulation of Pt(II) species generated in the extracellular matrix upon irradiation, in addition to the Pt-DNA adducts formed leading to less efflux of Pt. Levels of intracellular Pt and Ir were not significantly different under dark conditions. The oxidation state of Pt in cells treated under dark conditions could not be determined due to the low concentration of Pt leading to noisy XANES spectra, though previous studies on structurally similar Pt PACT agents were around 80% Pt(IV) without irradiation.[39]

Low sample quality can significantly impact the quality of the data, as cell damage may not be categorically assigned to the treatment rather than the sample preparation. It may be beneficial to prepare more samples when undertaking future experiments, as damaged silicon nitride membranes, ice on the samples, and damaged cells reduce the number of usable samples at the beamline. This would increase the reliability of the data with more conclusive outcomes. Poor signal intensities caused by low levels of intracellular Pt and Ir led to difficulties in processing data, most notably the noisy XANES spectra of cells treated under dark conditions. In future, higher concentrations that remain biologically relevant could be screened by rapid access synchrotron studies to determine an optimal concentration for XRF and XANES mapping, allowing more complete datasets to be obtained on subsequent visits.

Furthermore, co-treatment of the parent Ir(III) and Pt(IV) complexes has not yet been performed. Cell viability assays using combinations of these complexes under dark and irradiated conditions should be considered in order to determine whether the conjugation is required to enhance the photoactivity of the Ir(III) and Pt(IV) complexes.

5.6 References

1 H. Shi, PhD Thesis, University of Warwick, 2019.

2 E. M. Bolitho, PhD Thesis, University of Warwick, 2020.

3 E. Meggers, *Chem. Commun.*, 2015, **51**, 3290–3301.

4 C. J. Gomer and N. J. Razum, *Photochem. Photobiol.*, 1984, **40**, 435–439.

5 H. S. Jung, J. Han, H. Shi, S. Koo, H. Singh, H.-J. Kim, J. L. Sessler, J. Y. Lee, J.-H. Kim and J. S. Kim, *J. Am. Chem. Soc.*, 2017, **139**, 7595–7602.

6 J. An, S. Tang, G. Hong, W. Chen, M. Chen, J. Song, Z. Li, X. Peng, F. Song and W. H. Zheng, *Nat. Commun.*, 2022, **13**, 1–10.

7 Y. Chen, H. Xiang, S. Zhuang, Y. Shen, Y. Chen and J. Zhang, *Adv. Mater.*, 2021, **33**, 2100129.

8 A. Busemann, I. Flaspohler, X. Q. Zhou, C. Schmidt, S. K. Goetzfried, V. H. S. van Rixel, I. Ott, M. A. Siegler and S. Bonnet, *J. Biol. Inorg. Chem.*, 2021, **26**, 667–674.

9 A. Li, C. Turro and J. J. Kodanko, *Chem. Commun.*, 2018, **54**, 1280–1290.

10 J. Roque, D. Havrylyuk, P. C. Barrett, T. Sainuddin, J. McCain, K. Colón, W. T. Sparks, E. Bradner, S. Monro, D. Heidary, C. G. Cameron, E. C. Glazer and S. A. McFarland, *Photochem. Photobiol.*, 2020, **96**, 327–339.

11 M. M. K. Shahzad, G. Lopez-Berestein and A. K. Sood, *Drug Resist. Updat.*, 2009, **12**, 148–152.

12 G. Giaccone, *Drugs*, 2000, **59**, 9–17.

13 J. H. Burchenal, K. Kalaher, K. Dew, L. Lokys and G. Gale, *Biochimie*, 1978, **60**, 961–965.

14 L. Galluzzi, L. Senovilla, I. Vitale, J. Michels, I. Martins, O. Kepp, M. Castedo and G. Kroemer, *Oncogene*, 2012, **31**, 1869–1883.

15 R. Oun, Y. E. Moussa and N. J. Wheate, *Dalton Trans.*, 2018, **47**, 6645–6653.

16 A. Vogler, A. Kern and J. Hüttermann, *Angew. Chem. Int. Ed. English*, 1978, **17**, 524–525.

17 N. J. Farrer, J. A. Woods, L. Salassa, Y. Zhao, K. S. Robinson, G. Clarkson, F. S. Mackay and P. J. Sadler, *Angew. Chem. Int. Ed.*, 2010, **49**, 8905–8908.

18 H. Shi, Q. Wang, V. Venkatesh, G. Feng, L. S. Young, I. Romero-Canelón, M. Zeng and P. J. Sadler, *Dalton Trans.*, 2019, **48**, 8560–8564.

19 H. Shi, E. Bolitho, O. Carter, C. Huang, C. Imberti, B. K. Allam, M. Staniforth, S. Banerjee, M. Wills, V. G. Stavros, H. Huang and P. J. Sadler, *Unpublished Manuscript.*

20 J. C. Goldstein, R. M. Kluck and D. R. Green, *Ann. N. Y. Acad. Sci.*, 2006, **926**, 132–141.

21 C. Sanchez-Cano, I. Romero-Canelón, Y. Yang, I. J. Hands-Portman, S. Bohic, P. Cloetens and P. J. Sadler, *Chem. - A Eur. J.*, 2017, **23**, 2512–2516.

22 Y. Min, J. Li, F. Liu, E. K. L. Yeow and B. Xing, *Angew. Chem. Int. Ed.*, 2014, **53**, 1012–1016.

23 P. D. Quinn, F. Cacho-Nerin, M. A. Gomez-Gonzalez, J. E. Parker, T. Poon and J. M. Walker, *J. Synchrotron Radiat.*, 2023, **30**, 200–207.

24 V. A. Solé, E. Papillon, M. Cotte, P. Walter and J. Susini, *Spectrochim. Acta - Part B At. Spectrosc.*, 2007, **62**, 63–68.

25 J. L. Gregg, K. M. McGuire, D. C. Focht and M. A. Model, *Pflugers Arch. Eur. J. Physiol.*, 2010, **460**, 1097–1104.

26 P. D. Quinn, M. Gomez-Gonzalez, F. Cacho-Nerin and J. E. Parker, *J. Synchrotron Radiat.*, 2021, **28**, 1528–1534.

27 M. Lerotic, R. Mak, S. Wirick, F. Meirer and C. Jacobsen, *J. Synchrotron Radiat.*, 2014, **21**, 1206–1212.

28 B. Ravel and M. Newville, *J. Synchrotron Radiat.*, 2005, **12**, 537–541.

29 M. D. Hall, G. J. Foran, M. Zhang, P. J. Beale and T. W. Hambley, *J. Am. Chem. Soc.*, 2003, **125**, 7524–7525.

30 C. Busche, P. Comba, A. Mayboroda and H. Wadepohl, *Eur. J. Inorg. Chem.*, 2010, 1295–1302.

31 A. P. Morrell, J. F. W. Mosselmans, K. Geraki, K. Ignatyev, H. Castillo-Michel, P. Monksfield, A. T. Warfield, M. Febbraio, H. M. Roberts, O. Addison and R. A. Martin, *J. Synchrotron Radiat.*, 2018, **25**, 1719–1726.

32 R. M. Rousseau, *Rigaku J.*, 1998, **15**, 13–28.

33 V. Thomsen, *Spectroscopy*, 2007, **22**, 46–50.

34 C. Bissardon, S. Reymond, M. Salomé, L. André, S. Bayat, P. Cloetens and S. Bohic, *J. Vis. Exp.*, 2019, 154, e60461.

35 H. Tapiero and K. D. Tew, *Biomed. Pharmacother.*, 2003, **57**, 399–411.

36 H. Cantwell and P. Nurse, *Curr. Genet.*, 2019, **65**, 1281–1285.

37 R. De Jiang, H. Shen and Y. J. Piao, *Rom. J. Morphol. Embryol.*, 2010, **51**, 663–667.

38 H. Yang, J. Heyer, H. Zhao, S. Liang, R. Guo and L. Zhong,

Molecules, **2020**, 25, 4136.

39 E. M. Bolitho, C. Sanchez-Cano, H. Shi, P. D. Quinn, M. Harkiolaki, C. Imberti and P. J. Sadler, *J. Am. Chem. Soc.*, 2021, **143**, 20224–20240.

40 A. F. Westendorf, L. Zerzankova, L. Salassa, P. J. Sadler, V. Brabec and P. J. Bednarski, *J. Inorg. Biochem.*, 2011, **105**, 652–662.

41 J. P. C. Coverdale, PhD Thesis, University of Warwick, 2017.

Chapter 6

Conclusions and future work

6 Conclusions and future work

6.1 Conclusions

The high spatial resolution of phototherapies such as PDT and PACT facilitates a more targeted approach to anticancer medicine than standard chemotherapeutics. Selectively activating prodrugs only within the tumour environment reduces the chance of side effects, improving the patient's quality of life. For PDT photosensitizers, the generation of ROS is catalytic, allowing for minimised dosages which further reduce off-target effects. Selectivity can also be achieved by the introduction of targeting vectors able to direct the phototherapeutic agent to specific receptors overexpressed in cancer cells. One such receptor is the major glucose transporter GLUT1. Cancer cells favour inefficient glycolysis over oxidative phosphorylation to rapidly produce energy (Warburg effect), leading to the overexpression of GLUT1. Targeting GLUT1 has previously been achieved with glycoconjugation to metal complexes, including a range of Pt complexes with carboplatin-like leaving groups developed by Lippard *et al*.[1,2]

This work aimed to combine the selective irradiation in photodynamic therapy with the use of targeting vectors to develop more highly targeted compounds. In **Chapter 3,** a series of cyclometalated Ir(III) and Ru(II) complexes with pendant monosaccharides was synthesised and characterised by NMR, HR-MS and HPLC. Synthesis of the iridium dimer and sugar azides were performed using standard literature methods, whilst glycoconjugated ligands were synthesised using facile CuAAC click reactions. A methylated Ir(III) complex was also synthesised as a non-glycosylated control for later biological studies. Complexes were not sensitive to air, and were stable in acetonitrile, PBS and cell culture medium at 310 K over 24 h. Complexes were also stable towards 425 nm irradiation for 1 h and therefore suitable for further irradiated studies.

Excited state lifetimes in acetonitrile increased for all iridium complexes when air-equilibrated solutions were saturated with nitrogen (57 ns to 110 ns), with a further dramatic increase observed in PBS (413 ns), all indicating reactions of the excited state with oxygen. In contrast, ruthenium complexes exhibited only slight increases in excited state lifetimes upon nitrogen saturation or in PBS (from 5 ns to 12 ns and 17 ns, respectively), indicating very little interaction with oxygen. Studies in

acetonitrile revealed good singlet oxygen quantum yields ($\Delta_\Phi \approx 60\%$) for all iridium complexes, whilst ruthenium complexes were not as effective ($\Delta_\Phi < 5\%$). In addition, Ir(III) complexes exhibited phosphorescence with peaks around 475 nm and 500 nm, whilst a broad, low intensity peak was observed around 610 nm for the Ru(II) complexes. Phosphorescence quantum yields were an order of magnitude greater for Ir(III) complexes compared to the Ru(II) complexes ($\Delta_P \approx 1\%$ *vs.* 0.1%), which again increased more dramatically for Ir complexes in the absence of oxygen. Overall, the Ir(III) complexes were better candidates for biological studies due to both their phosphorescence (allowing in-cell tracking) and singlet oxygen generation (Type II photosensitization).

The biological properties and cancer targeting capabilities of the Ir(III) series were explored in **Chapter 4**. Ir(III) glycoconjugates and the methyl analogue were non-toxic towards A549 lung cancer cells ($IC_{50} > 100$ μM). Accumulation in cells did not vary between complexes directly conjugated to β-glucose (**4**), β-mannose (**5**), and β-galactose (**6**). Since glucose is the primary substrate of GLUT1, the lack of trend between different sugars indicates these complexes do not target GLUT1. This may be due to the nitrogen atom instead of oxygen atom in the C1 position. GLUT1 binds to the oxygen atoms of the hydroxyl groups at C1, C3, and C4 through hydrogen bonding.[11] However, the accumulation of complexes increased with increasing linker length between glucose and the triazole ligand, with PEG3 complex **9** accumulating in cells more than any other glycoconjugate. Hydrogen bonding is still possible for complexes **7-9** due to the PEG linker containing an oxygen at the C1 position, whilst the longer chain may allow for better recognition of the glucose moiety due to decreased steric hindrance. Interestingly, accumulation of methyl complex **10** was over 20× greater than that of **9**. Glucose complexes **4** and **9** were selected as lead complexes to further investigate the effects of adding the PEG3 linker, whilst methyl complex **10** was selected due to its significantly higher cellular accumulation and its lack of glucose moiety.

Complexes **9** and **10** exhibited good photocytotoxicity towards A549 lung cancer cells, similar to known photoactive Ru(II) complex **[Ru(bpy)$_2$(dppn)]Cl$_2$**, whilst **4** exhibited moderate photocytotoxicity. These results correlated with the accumulation of each complex (*i.e.*, higher accumulation led to greater potency). Treatment with SOSG showed each complex generated singlet oxygen in cells,

confirming their status as Type II photosensitizers. Accumulation studies of complexes **4**, **9** and **10** in A549 cells co-treated with a highly selective GLUT1 inhibitor confirmed β-glucose complex **4** and methyl complex **10** do not enter cells *via* GLUT1, whereas PEG3-β-glucose complex **9** is most likely internalised by GLUT1 to some extent. Interestingly, accumulation of **10** increased 3-fold in the presence of the inhibitor.

The capacity factor of each glycoconjugated complex (**1-9**) determined by HPLC was similar regardless of sugar choice or linker length ($K \approx 0.57$), however, methyl complex **10** was found to be far more lipophilic ($K = 2.8$), likely responsible for the dramatically higher cellular accumulation. Confocal microscopy studies demonstrated both **4** and **9** were selective for cancerous cells over non-cancerous cells, despite differences in GLUT1 targeting. Complexes **4** and **9** incubated in human serum bound albumin and transferrin to a similar extent, with little change from 1 h and 24 h incubation. The high percentage of Ir detected in flow-through fractions after 24 h incubation (*ca.* 88%) indicates the vast majority of both complexes remains unbound, which may lead to a shorter biological half-life *in vivo*.

In addition to the development and biological evaluation of novel Ir(III) glycoconjugates as photosensitizers, this thesis also explored the use of synchrotron techniques to investigate the in-cell (photo)stability and localisation of a bimetallic complex designed to act as both a PDT and PACT agent. In **Chapter 5**, A549 cells were treated with a Pt(IV)-Ir(III) complex in either dark or irradiated conditions, then cryo-fixed and dehydrated to be examined at the I14 beamline at Diamond Light Source. Using X-ray fluorescence, cells treated with the complex and irradiation were found to contain 44× more Pt than Ir, proving that the complex does not remain intact after irradiation. Pt co-localised strongly with Zn, indicative of nuclear targeting, where DNA-adducts may prevent the efflux of the Pt species, leading to the disparity in intracellular Pt and Ir. In dark conditions, levels of Pt and Ir were not significantly different, with small hotspots of both metals implying accumulation in organelles such as mitochondria and lysosomes. XANES spectra of Pt in irradiated cells found 60% of Pt as Pt(II), but spectra in dark cells were too noisy to analyse due to the significantly lower Pt content. However, XANES analysis of a structurally similar Pt(IV) PACT agent (based on parent complex

FM190, **15**) in dark PC3 cells exhibited only 20-25% Pt(II),[3] indicating the relatively good in-cell stability of Pt(IV) complexes.

6.2 Future work

This thesis demonstrated the capacity for iridium photosensitizers to be targeted towards cancer cells, however, further research is needed to determine whether such complexes could be translated to clinical use.

6.2.1 Improving physical and photophysical properties

Metal tris chelates are formed as Δ and Λ enantiomers, though are often employed as a racemic mixture. This is most notable in the case of Ru(II) complex TLD-1433, administered to patients as a racemic mixture in clinical trials.[4] Since the Ir(III) complexes described in this thesis are conjugated to the chiral glucose molecule, the glycoconjugated complexes are formed as diastereomers, which are resolvable by NMR and leads to the doubling (and overlapping) of signals. Separation of diastereomers would therefore lead to clearer NMR spectra, and the specific rotation of each diastereomer could be determined.

The complexes designed in this thesis are activated by blue light (λ = 425 nm). However, increasing the activation wavelength towards the therapeutic window (600-800 nm) is important to expand the scope of these agents for clinical translation beyond superficial lesions. This may be achieved in two ways:

1. Modifications to the C^N ligand (in this case 2-phenylpyridine) can have a drastic effect on the absorption properties of iridium photosensitizers. Co-workers Huang *et al*. developed a series of coumarin-based Ir(III) glycoconjugates based on complex **4** with absorption maxima in the region of 500 nm.[5] Further modifications may lead to red-light activatable Ir(III) glycoconjugates.
2. Lilge *et al.* developed a series of cyclometalated Os(II) complexes that generate singlet oxygen upon irradiation with red light (λ = 635 nm), some of which retained photoactivity in hypoxia.[6] Glycoconjugation to cyclometalated Os(II) complexes may therefore lead to targeted Os(II) photosensitizers that can be activated by visible light in the therapeutic window. A potential synthetic method is described in Chapter 3.

Alternatively, longer wavelength activation can be achieved using two-photon PDT, where two photons of a lower energy are absorbed simultaneously to generate the excited state *via* a virtual state. The two-photon cross-section of a complex determines the likelihood of two-photon absorption. Several iridium(III) complexes using the $[Ir(ppy)_2(N\text{^}N)]^+$ scaffold have been designed with high two-photon cross sections in the therapeutic window, capable of live cell imaging and generating singlet oxygen for photodynamic therapy.[7–9] Determining the two-photon cross-sections of the complexes synthesised in Chapter 3 can therefore be used to evaluate their potential use in two-photon photodynamic therapy.

6.2.2 Further biological studies of glycoconjugated iridium(III) photosensitizers

D-Glucose is the major biological substrate of GLUT1. However, literature regarding the preferred glucose anomer is conflicting, with results ranging from 3× faster influx of β-glucose to 1.7× faster influx of α-glucose, or even no differences observed between them.[10] Since GLUT1 hydrogen bonds to the oxygen atom at C1,[11] an α-glucose analogue of **9** could be synthesised to determine the preferred anomer for the internalisation of these Ir(III) glycoconjugates.

ICP-MS studies have been used to determine the cellular accumulation of osmium half-sandwich complexes in cancer cells treated with different incubation periods.[12] Determining the incubation period necessary to achieve peak cellular accumulation of the complexes studied in this thesis may lead to greater photoactivity. Since GLUT1 is overexpressed in a wide variety of cancers, studying the uptake and (photo)cytotoxicity of the lead complexes, especially PEG3-β-glucose complex **9**, in other cell lines could determine an optimal cancer type for GLUT1 targeting.

Ideally, a photosensitizer will undergo both Type I and Type II processes in order to possess activity in hypoxic environments which are commonly found inside tumours.[4] Iridium(III) complexes based on the $[Ir(ppy)_2(N\text{^}N)]^+$ scaffold have been reported to oxidize biomolecules under oxygen-free conditions using Type I processes, leading to excellent photoactivity in tumour spheroids despite the use of weakly penetrating 405 nm light.[13] Therefore, it is important to study whether

radicals and ROS other than singlet oxygen are generated by the Ir(III) glycoconjugates in order to assess their potential in hypoxic environments.

Multicellular tumour spheroids (MCTS) are 3D cancer models that can be used before *in vivo* studies, allowing cells to mimic more biologically relevant environments.[14] The 3D nature of MCTS can lead to hypoxic cores,[15] which can be used to evaluate the effectiveness of photosensitizers in areas with lower oxygen concentrations. Moreover, uptake experiments in MCTS can determine the penetration of the complex, whilst using different sized MCTS can determine the achievable depth of activation for a specific wavelength.

The FDA requires diastereomers of chiral complexes to be fully resolved and biologically tested separately, as the differences in chirality can lead to differences in binding to chiral biomolecules.[23] TLD-1433, currently in Phase II clinical trials as a racemic mixture, has only recently been resolved into its enantiomers,[24] although to the best of my knowledge, no biological studies on each enantiomer have yet been published. As such, the lead glycoconjugated complex will need to be separated into its diastereomers in large enough quantities to undertake full biological evaluation of each complex.

6.2.3 Subcellular location of Pt-Ir complex (17)

Chapter 5 details the in-cell stability and localisation of Pt-Ir using synchrotron XRF, however, the specific subcellular compartments containing Pt-Ir have not been fully elucidated. Previous studies using confocal microscopy on cells treated with Pt-Ir without irradiation determined the complex to localise in mitochondria, however, the phosphorescence of the complex could potentially be entirely attributed to the Ir moiety. If this is the case, previous confocal microscopy experiments cannot determine whether both the Ir and Pt moieties localise in the same organelles. The following methods may be more useful to determine the intracellular localisation of the full Pt-Ir complex more conclusively:

1. Cellular fractionation followed by ICP-MS can ascertain the amount of Ir and Pt in different cellular compartments. However, cell fractionation kits typically separate cells into three fractions: cytoplasmic, membrane/organelles, and nuclear/cytoskeletal. This may provide more insight into the general

distribution of Pt and Ir in cells treated under both dark and irradiated conditions, however, specific subcellular locations may not be possible.

2. Confocal microscopy of luminescent compounds can be used to determine their intracellular localisation by co-treating with specific organelle stains (*e.g.* membrane, mitochondria, lysosome, nucleus). Whilst this has already been performed for **17**, the luminescence is likely to be based on the iridium moiety. Using a fluorescent ligand on the Pt species could allow for in cell detection of the Ir and Pt moieties separately, however, the novel, fluorescently labelled complex may lead to significant changes in the lipophilicity of the complex, leading to a difference in subcellular localisation compared to the original unlabelled complex. On the other hand, Farrer *et al*. previously demonstrated the ability of the azido ligand in FM190, parent complex of Pt-Ir, to undergo copper-free click reactions with several alkynes.[25] Therefore, it may be possible to visualise the Pt moiety using in cell click chemistry with an alkyne-based fluorophores such as AlexaFluor®-647. Additionally, the emission of this fluorophore does not overlap with the Ir complex, so each species should be resolved. However, in cell imaging in irradiated samples will be significantly hindered as azide radicals are released upon activation.

Zebrafish (*Danio rerio*) embryos have become a useful model for studying the toxicity of drugs *in vivo*.[16] Approximately 70% of human genes have orthologues in zebrafish,[17] and since embryos are transparent, phosphorescent molecules (such as the Ir(III) complexes in this thesis)[18,19] and dyes for ROS detection can be visualised in live animal models.[20,21] In addition, the use of zebrafish embryos allows for high-throughput screening at low cost, with less ethical concerns than other vertebrate models since zebrafish embryos experiments can be performed before the development of stress and pain responses (*ca.* 5 days post fertilization).[22] With this in mind, testing Pt-Ir complex **17** in zebrafish is an attractive option for future studies to determine toxicity and ROS generation *in vivo*.

6.3 References

1 M. Patra, S. G. Awuah and S. J. Lippard, *J. Am. Chem. Soc.*, 2016, **138**, 12541–12551.

2 M. Patra, T. C. Johnstone, K. Suntharalingam and S. J. Lippard, *Angew. Chem. Int. Ed.*, 2016, **55**, 2550–2554.

3 E. M. Bolitho, C. Sanchez-Cano, H. Shi, P. D. Quinn, M. Harkiolaki, C. Imberti and P. J. Sadler, *J. Am. Chem. Soc.*, 2021, **143**, 20224–20240.

4 S. Monro, K. L. Colón, H. Yin, J. Roque, P. Konda, S. Gujar, R. P. Thummel, L. Lilge, C. G. Cameron and S. A. McFarland, *Chem. Rev.*, 2019, **119**, 797–828.

5 Z. Zhu, L. Wei, Y. Lai, O. W. L. Carter, S. Banerjee, P. J. Sadler and H. Huang, *Dalton Trans.*, 2022, **51**, 10875–10879.

6 S. Lazic, P. Kaspler, G. Shi, S. Monro, T. Sainuddin, S. Forward, K. Kasimova, R. Hennigar, A. Mandel, S. McFarland and L. Lilge, *Photochem. Photobiol.*, 2017, **93**, 1248–1258.

7 X. D. Bi, R. Yang, Y. C. Zhou, D. Chen, G. K. Li, Y. X. Guo, M. F. Wang, D. Liu and F. Gao, *Inorg. Chem.*, 2020, **59**, 14920–14931.

8 C. Jin, J. Liu, Y. Chen, L. Zeng, R. Guan, C. Ouyang, L. Ji and H. Chao, *Chem. - A Eur. J.*, 2015, **21**, 12000–12010.

9 X. Tian, Y. Zhu, M. Zhang, L. Luo, J. Wu, H. Zhou, L. Guan, G. Battaglia and Y. Tian, *Chem. Commun.*, 2017, **53**, 3303–3306.

10 D. Shishmarev, C. Q. Fontenelle, I. Kuprov, B. Linclau and P. W. Kuchel, *Biophys. J.*, 2018, **115**, 1906–1919.

11 K. P. Lloyd, O. A. Ojelabi, J. K. De Zutter and A. Carruthers, *J. Biol. Chem.*, 2017, **292**, 21035–21046.

12 A. Ballesta, F. Billy, J. P. C. Coverdale, J. I. Song, C. Sanchez-Cano, I. Romero-Canelón and P. J. Sadler, *Metallomics*, 2019, **11**, 1648–1656.

13 R. Bevernaegie, B. Doix, E. Bastien, A. Diman, A. Decottignies, O. Feron and B. Elias, *J. Am. Chem. Soc.*, 2019, **141**, 18486–18491.

14 X. Cui, Y. Hartanto and H. Zhang, *J. R. Soc. Interface*, 14: 20160877.

15 R. Leek, D. R. Grimes, A. L. Harris and A. McIntyre, in *Tumor Microenvironment. Advances in Experimental Medicine and Biology*, eds. C. Koumenis, L. Coussens, A. Giaccia and E. Hammond, Springer, Cham, 2016, vol. 899, pp. 167–196.

16 S. Zhao, J. Huang and J. Ye, *J. Exp. Clin. Cancer Res.*, 2015, **34**, 1–9.

17 K. Howe, M. D. Clark, C. F. Torroja, J. Torrance, C. Berthelot, M. Muffato, J. E. Collins, S. Humphray, K. McLaren, L. Matthews *et al.*, *Nature*, 2013, **496**, 498–503.

18 C. N. Ko, C. Yang, S. Lin, S. Li, Z. Dong, J. Liu, S. M. Y. Lee, C. H. Leung and D. L. Ma, *Biosens. Bioelectron.*, 2017, **94**, 575–583.

19 H. Høgset, C. C. Horgan, J. P. K. Armstrong, M. S. Bergholt, V. Torraca, Q. Chen, T. J. Keane, L. Bugeon, M. J. Dallman, S. Mostowy and M. M. Stevens, *Nat. Commun.*, 2020, **11**, 1–12.

20 V. Mugoni, A. Camporeale and M. M. Santoro, *J. Vis. Exp.*, 2014, 1–11.

21 C. Lackmann, M. Santos, S. Rainieri, A. Barranco, H. Hollert, P. Spirhanzlova, M. Velki and T. B. Seiler, *Chemosphere*, 2018, **197**, 200–209.

22 L. U. Sneddon, *ATLA*, 2018, **46**, 309–311.

23 Development of New Stereoisomeric Drugs, FDA Guidance Document, https://www.fda.gov/regulatory-information/search-fda-guidance-documents/development-new-stereoisomeric-drugs, (accessed 5 February 2023).

24 D. W. Armstrong, J. Yu, H. D. Cole, S. A. McFarland and J. Nafie, *J. Pharm. Biomed. Anal.*, 2021, **204**, 114233.

25 N. J. Farrer, G. Sharma, R. Sayers, E. Shaili and P. J. Sadler, *Dalton Trans.*, 2018, **47**, 10553–10560.

Chapter 7

Appendix

7 Appendix

7.1 Syntheses

Synthesis A1. Synthesis of osmium precursor $[Os(bpy)_2Cl_2]$

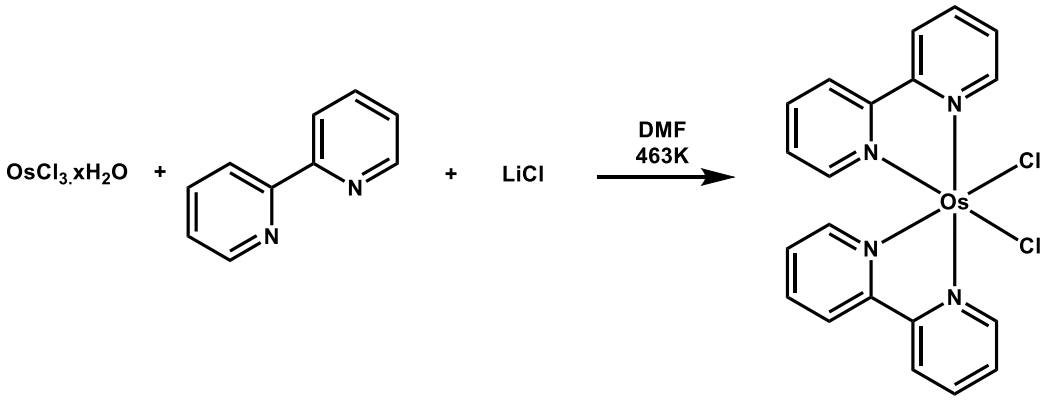

$[Os(bpy)_2Cl_2]$ was synthesised using a literature method.[1] Lithium chloride (0.913 g, 21.5 mmol, 12.7 eq), osmium trichloride hydrate (0.500 g, 1.7 mmol, 1 eq) and 2,2'-bipyridine (0.527 g, 3.37 mmol, 2 eq) were dissolved in 15 mL DMF and the reaction mixture was refluxed under nitrogen atmosphere at 463 K for 3 h. The solution was cooled to room temperature, triethylamine (960 µL, 6.89 mmol, 4.1 eq) was added, then the solution was refluxed again under nitrogen atmosphere at 463 K for a further 1.5 h. The reaction mixture was allowed to cool to room temperature and an excess of acetone (150 mL) was added, then put in the freezer for 72 h. Precipitate was filtered and washed with acetone to give a black solid. Yield = 0.4387 g (54%). ^{1}H NMR (400 MHz, DMSO) δ 9.16 – 9.01 (m, 8H), 8.36 (s, 4H), 8.18 (s, 4H). ESI-MS m/z calc. $[M+Na]^+$: 574.0, found: 574.0.

Synthesis A2. Attempted synthesis of osmium(II) glycoconjugate **11-Os**.

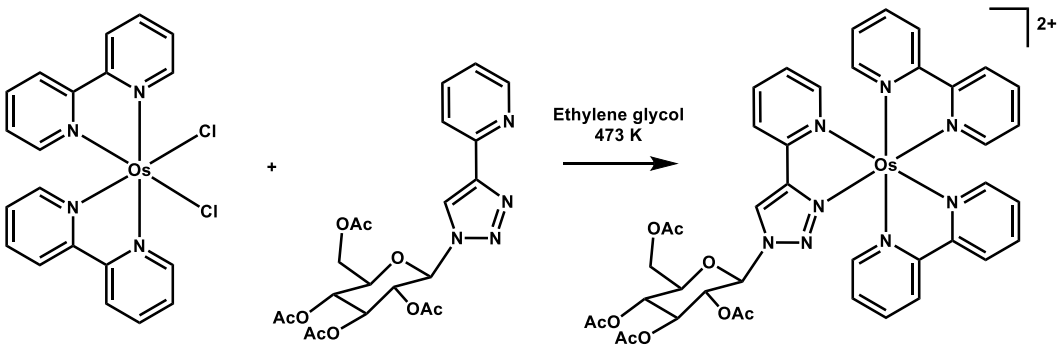

$[Os(bpy)_2Cl_2]$ (60 mg, 0.105 mmol, 1 eq.) and β-glucose ligand (50 mg, 0.105 mmol, 1 eq.) were dissolved in 10 mL nitrogen-purged ethylene glycol and refluxed for 4 h under nitrogen atmosphere. The reaction mixture was then cooled to room temperature and excess NH_4PF_6 was added, followed by stirring for 1 h at room temperature. Solution was then passed through a small silica column using 0-4% methanol in DCM. ESI-MS of eluent showed no product peak, but contained a peak at m/z = 649.1 potentially corresponding to $[OsC_{27}H_{21}N_8]^+$.

7.2 Tables

Table A1. Electron binding energy and XRF emission energy for endogenous elements and exogenous elements studied in Chapter 5.[2]

Element	Electron	Binding Energy (keV)	XRF Emission	Emission Energy (keV)
Ca	K_{1s}	4.04	$L_3\ (2p_{3/2}{}^{-1}) \rightarrow K\ (1s^{-1})$	3.69
Cl		2.82		2.62
Cu		8.98		8.05
Fe		7.11		6.40
K		3.61		3.31
Mg		1.31		1.25
Na		1.07		1.04
P		2.15		2.01
S		2.47		2.31
Zn		9.66		8.64
Ir	$L_3\ 2p_{3/2}$	11.22	$M_5\ (3d_{5/2}{}^{-1}) \rightarrow L_3\ (2p_{3/2}{}^{-1})$	9.18
Pt		11.56		9.44

Table A2. Fractional Atomic Coordinates ($\times 10^4$) and Equivalent Isotropic Displacement Parameters ($Å^2 \times 10^3$) for **α-Gal(OAc)$_4$-N$_3$**. U_{eq} is defined as 1/3 of the trace of the orthogonalized U_{IJ} tensor.

Atom	*x*	*y*	*z*	U(eq)
O4	5969.5(18)	4919(2)	2530.8(11)	22.7(4)
O2	1749.5(19)	2185(2)	3051.2(12)	24.7(4)
O3	4090.5(18)	4511(3)	3939.0(11)	23.5(3)
O5	3473.4(19)	4195(2)	964.7(11)	25.0(4)
O6	5616(2)	8413(3)	1112.1(13)	30.9(4)
O21	2469(2)	-562(3)	2562.8(14)	34.5(4)
O31	2328(2)	6191(3)	4655.0(14)	39.7(5)
O41	7009(2)	7096(3)	3532.4(17)	44.0(5)
O61	8152(3)	7587(3)	1104(2)	54.9(7)
N1	812(2)	4236(3)	1412.6(15)	28.1(4)
N2	-15(3)	4172(4)	627.8(16)	34.5(5)
C3	3314(3)	4829(3)	2983.4(15)	20.9(5)
C4	4469(3)	5868(3)	2421.9(16)	21.7(5)
C2	2923(3)	3013(3)	2513.4(17)	22.2(5)
C41	7118(3)	5642(4)	3165.4(18)	26.0(5)
C31	3562(3)	5381(3)	4702.7(17)	24.6(5)
C1	2323(3)	3256(4)	1443.7(17)	24.4(5)
C5	3869(3)	5958(3)	1356.5(17)	24.4(5)
C21	1671(3)	350(4)	3039.7(18)	26.7(5)
C32	4727(3)	5215(4)	5567.3(18)	31.6(6)
C61	7186(4)	8701(4)	1260(2)	37.0(7)
N3	-888(3)	4206(5)	-43(2)	58.1(9)
C6	5099(3)	6674(4)	731.9(19)	30.9(6)
C42	8487(3)	4392(4)	3338.1(19)	31.1(5)
C22	521(3)	-321(4)	3704(2)	40.9(7)
C62	7522(5)	10550(5)	1659(3)	53.5(9)

Table A3. Anisotropic Displacement Parameters ($Å^2 \times 10^3$) for **α-Gal(OAc)$_4$-N$_3$**. The anisotropic displacement factor exponent takes the form: $-2\pi^2[h^2a^{*2}U_{11}+2hka^*b^*U_{12}+\ldots]$.

Atom	U_{11}	U_{22}	U_{33}	U_{23}	U_{13}	U_{12}
O4	17.1(7)	25.9(9)	25.3(8)	-3.7(7)	3.3(6)	0.4(6)
O2	20.7(8)	24.2(9)	30.1(9)	3.6(7)	7.6(6)	1.4(7)
O3	20.6(7)	30.3(9)	19.4(7)	-0.5(7)	1.4(6)	3.8(7)
O5	25.3(8)	28.1(9)	22.3(8)	-4.0(7)	6.2(6)	-5.4(7)
O6	33.9(9)	33.6(10)	25.7(8)	1.0(8)	4.7(7)	-8.4(8)
O21	349(10)	26.4(9)	42.2(10)	-3.5(8)	4.5(8)	1.0(8)
O31	43.9(11)	48.9(12)	26.5(9)	-3.9(9)	5.0(8)	20.5(10)
O41	31.8(10)	36.7(12)	60.4(14)	-20.7(10)	-12.0(9)	4.4(9)
O61	34.1(11)	50.0(15)	79.3(18)	12.7(13)	-1.2(11)	-3.3(11)
N1	21.3(9)	38.0(12)	24.7(9)	0.3(9)	-0.1(7)	1.3(9)
N2	27.8(11)	44.2(14)	31.2(11)	-0.3(10)	0.6(9)	3.3(10)
C3	18.8(10)	25.1(12)	18.7(10)	-0.9(9)	1.9(8)	2.0(9)
C4	20.6(10)	23.0(12)	21.4(11)	-1.0(9)	1.9(8)	2.0(9)
C2	17.7(10)	25.9(12)	23.5(11)	0.1(9)	4.6(8)	0.1(9)
C41	21.6(11)	29.3(13)	27.4(11)	-2.7(10)	3.8(9)	-2.5(10)
C31	30.6(12)	21.3(11)	22.6(11)	0.3(9)	6.2(9)	-0.7(10)
C1	21.4(11)	27.4(12)	24.8(11)	-2.3(10)	4.5(9)	-3.0(10)
C5	26.7(11)	25.4(12)	21.5(11)	-1.6(9)	3.9(9)	-2.7(9)
C21	20.2(11)	26.7(13)	31.9(13)	5.1(10)	-3.4(9)	1.4(10)
C32	39.4(14)	31.9(14)	22.4(11)	-0.1(10)	-3.1(10)	-4.0(11)
C61	35.2(15)	41.4(17)	32.6(14)	10.4(12)	-5.4(11)	-10.4(12)
N3	50.9(16)	79(2)	40.1(14)	-8.2(15)	-16.4(12)	19.8(17)
C6	36.7(14)	33.1(14)	23.4(11)	-2.8(10)	6.1(10)	-9.1(11)
C42	21.9(11)	35.5(14)	35.7(13)	-0.8(12)	2.1(9)	0.9(11)
C22	28.1(13)	36.4(16)	59.0(18)	21.8(14)	9.0(12)	1.8(12)
C62	57(2)	48(2)	51.4(19)	5.0(16)	-13.3(15)	-21.7(17)

Table A4. Bond Lengths for **α-Gal(OAc)$_4$-N$_3$**.

Atom	Atom	Length/Å
O4	C4	1.450(3)
O4	C41	1.360(3)
O2	C2	1.439(3)
O2	C21	1.358(3)
O3	C3	1.443(3)
O3	C31	1.353(3)
O5	C1	1.416(3)
O5	C5	1.439(3)
O6	C61	1.347(3)
O6	C6	1.442(3)
O21	C21	1.200(3)
O31	C31	1.203(3)
O41	C41	1.197(3)
O61	C61	1.197(4)
N1	N2	1.239(3)
N1	C1	1.471(3)
N2	N3	1.133(3)
C3	C4	1.519(3)
C3	C2	1.515(3)
C4	C5	1.519(3)
C2	C1	1.533(3)
C41	C42	1.486(4)
C31	C32	1.485(3)
C5	C6	1.516(3)
C21	C22	1.491(4)
C61	C62	1.492(5)

Table A5. Bond Angles for **α-Gal(OAc)$_4$-N$_3$**.

Atom	Atom	Atom	Angle/°
C41	O4	C4	116.51(18)
C21	O2	C2	117.03(19)
C31	O3	C3	119.10(18)
C1	O5	C5	114.39(18)
C61	O6	C6	117.3(2)
N2	N1	C1	115.2(2)
N3	N2	N1	172.9(3)
O3	C3	C4	107.06(17)
O3	C3	C2	108.26(19)
C2	C3	C4	110.63(18)
O4	C4	C3	107.89(18)
O4	C4	C5	109.39(18)
C5	C4	C3	110.42(18)
O2	C2	C3	106.69(18)
O2	C2	C1	111.71(18)
C3	C2	C1	110.6(2)
O4	C41	C42	111.2(2)
O41	C41	O4	123.2(2)
O41	C41	C42	125.5(2)
O3	C31	C32	110.4(2)
O31	C31	O3	123.1(2)
O31	C31	C32	126.5(2)
O5	C1	N1	112.6(2)
O5	C1	C2	109.39(18)
N1	C1	C2	107.09(19)
O5	C5	C4	111.87(19)
O5	C5	C6	104.38(19)
C6	C5	C4	112.8(2)
O2	C21	C22	111.0(2)
O21	C21	O2	122.5(2)
O21	C21	C22	126.4(3)

O6	C61	C62	110.6(3)
O61	C61	O6	123.4(3)
O61	C61	C62	126.0(3)
O6	C6	C5	107.7(2)

Table A6. DFT-calculated transitions for iridium complex **4**.

	f	λ (nm)	ΔE (eV)	Contributions
T1	0.0	444	2.79	HOMO → LUMO+1 (17%), HOMO → LUMO+2 (45%)
T2	0.0	436	2.84	HOMO-1 → LUMO+1 (23%), HOMO → LUMO+1 (30%), HOMO → LUMO+2 (12%)
T3	0.0	428	2.90	HOMO → LUMO (89%)
S1	0.0018	428	2.95	HOMO → LUMO (96%)
S2	0.0286	381	3.24	HOMO → LUMO+1 (89%)

Table A7. DFT-calculated transitions for ruthenium complex **11**.

	f	λ (nm)	ΔE (eV)	Contributions
T1	0	509	2.44	HOMO → LUMO (50%), HOMO → LUMO+1 (31%)
T2	0	502	2.47	HOMO → LUMO (32%), HOMO → LUMO+1 (51%)
T3	0	498	2.49	HOMO-2 → LUMO+1 (11%), HOMO-1 → LUMO (31%), HOMO-1 → LUMO+1 (46%)
T4	0	482	2.57	HOMO-2 → LUMO (14%), HOMO-2 → LUMO+1 (46%), HOMO-1 → LUMO (33%)
S1	0.0014	476	2.60	HOMO → LUMO (92%)

S2	0.0004	467	2.65	HOMO → LUMO+1 (92%)
T5	0	465	2.66	HOMO-2 → LUMO (64%)
T6	0	458	2.70	HOMO-2 → LUMO+1 (28%), HOMO-1 → LUMO (21%), HOMO-1 → LUMO+1 (35%)
S3	0.0067	448	2.77	HOMO-2 → LUMO (61%), HOMO-2 → LUMO+1 (25%)
S4	0.0088	444.89	2.7861	HOMO-2 → LUMO (21%), HOMO-1 → LUMO (47%), HOMO-1 → LUMO+1 (29%)
T7	0	444.898	2.7868	HOMO-1 → LUMO+2 (24%), HOMO → LUMO+2 (57%)
S5	0.1234	428	2.90	HOMO-2 → LUMO+1 (27%), HOMO-1 → LUMO (41%), HOMO-1 → LUMO+1 (20%)

Table A8. DFT-calculated transitions for osmium complex **11-Os** (not synthesised).

	f	λ (nm)	ΔE (eV)	Contributions
T1	0	582	2.13	HOMO → LUMO (84%)
T2	0	568	2.18	HOMO → LUMO+1 (78%)
T3	0	554	2.23	HOMO-1 → LUMO (30%), HOMO-1 → LUMO+1 (48%)
S1	0.0038	543	2.28	HOMO → LUMO (98%)
T4	0	538	2.30	HOMO-2 → LUMO (30%), HOMO-2 → LUMO+1 (32%), HOMO-1 → LUMO (30%)
S2	0.0002	522	2.37	HOMO → LUMO+1 (98%)
T5	0	513	2.42	HOMO-2 → LUMO (54%), HOMO-2 → LUMO+1 (10%), HOMO-1 → LUMO (14%), HOMO-1 → LUMO+1 (12%)

T6	0	502	2.47	HOMO-2 → LUMO+1 (34%), HOMO-1 → LUMO (13%), HOMO-1 → LUMO+1 (20%), HOMO → LUMO+2 (14%)
T7	0	494	2.51	HOMO-1 → LUMO+1 (12%), HOMO → LUMO+2 (58%)
S3	0.0120	490	2.53	HOMO-2 → LUMO (81%), HOMO-2 → LUMO+1 (10%)
S4	0.0266	486	2.55	HOMO-2 → LUMO+1 (12%), HOMO-1 → LUMO (64%), HOMO-1 → LUMO+1 (21%)
T8	0	472	2.63	HOMO-2 → LUMO+2 (42%), HOMO-1 → LUMO+2 (27%), HOMO → LUMO+2 (14%)
S5	0.0818	460	2.69	HOMO-2 → LUMO+1 (24%), HOMO-1 → LUMO (17%), HOMO-1 → LUMO+1 (18%), HOMO → LUMO+2 (30%)

Table A9. Percentage of Pt(II) observed by LCF of XANES spectra in samples treated with 3×IC_{50} (10.5 μM) Pt-Ir without irradiation.

Sample	Pt(II) %
C14	53.5
C15	46.7
Average	50.1 ± 3.4

7.3 Spectra

Spectra A1: A) ^{1}H NMR (400 MHz) of complex **1** in d^{6}-DMSO with trifluoroacetic acid. B) ^{13}C APT NMR (176 MHz) of complex **1** in d^{6}-DMSO.

a)

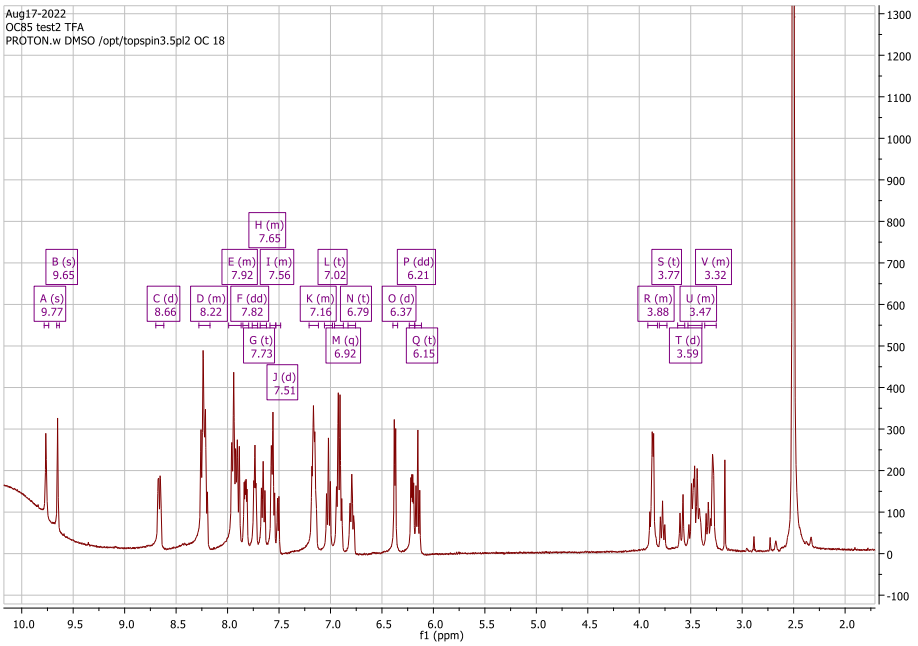

b)

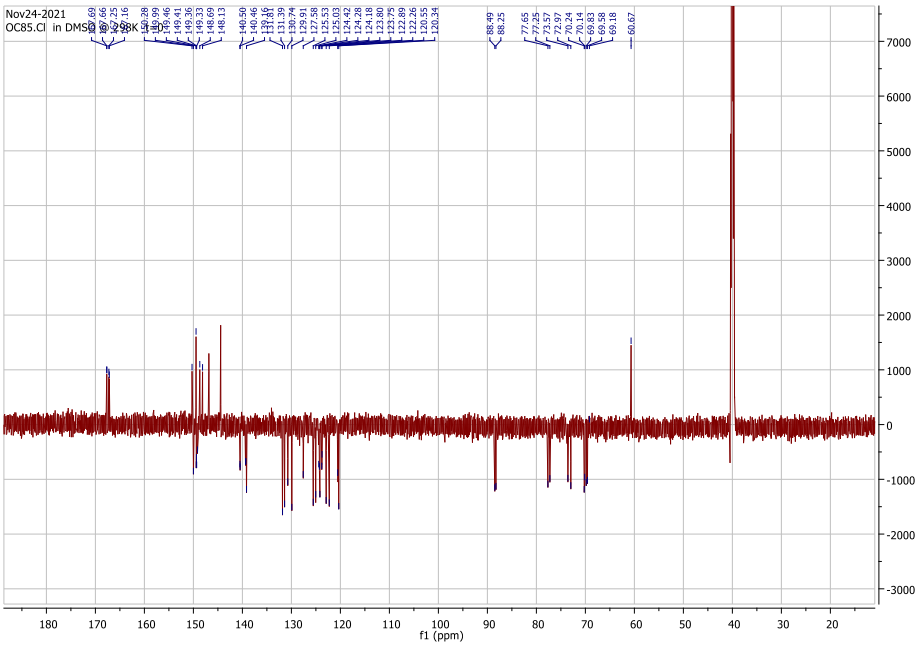

Spectra A2: A) ^{1}H NMR (400 MHz) of complex **2** in d^{6}-DMSO with trifluoroacetic acid. B) ^{13}C APT NMR (176 MHz) of complex **2** in d^{6}-DMSO.

a)

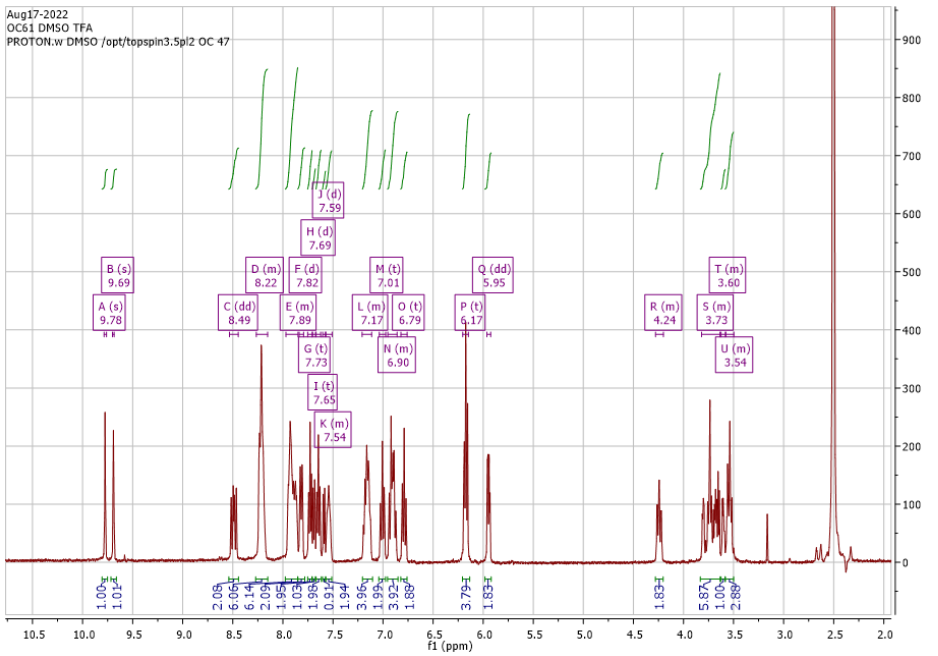

b)

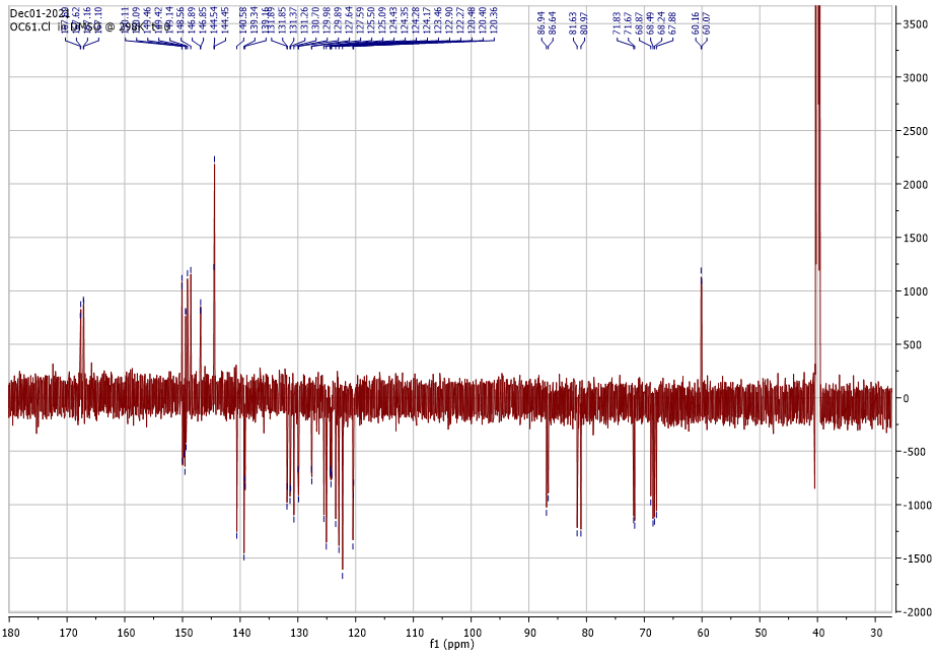

Spectra A3: A) ^{1}H NMR (400 MHz) of complex **3** in d^{6}-DMSO with trifluoroacetic acid. B) ^{13}C APT NMR (176 MHz) of complex **3** in d^{6}-DMSO.

a)

b)

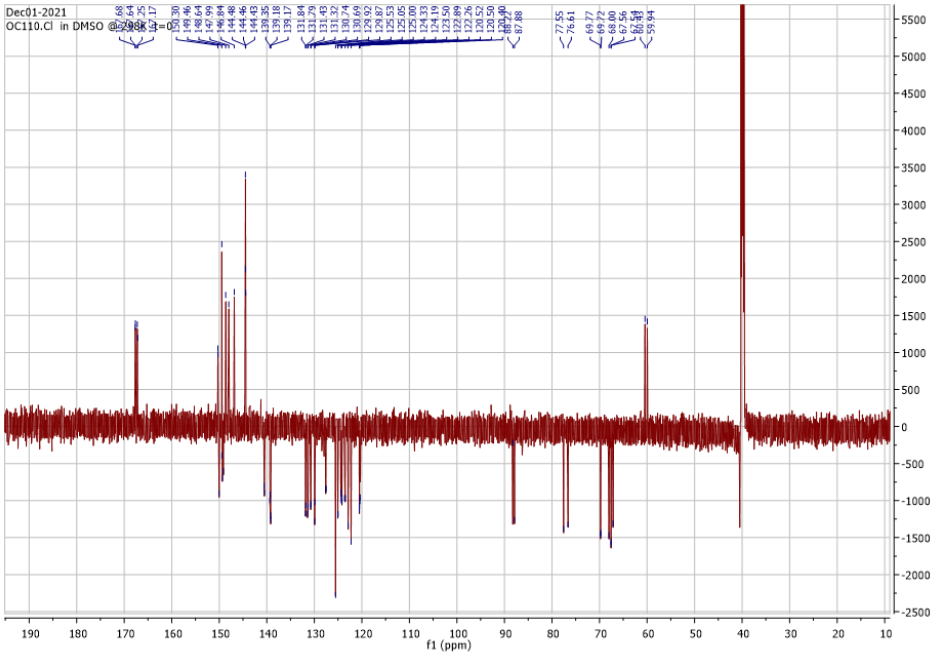

Spectra A4: A) ^{1}H NMR (400 MHz) of complex **4** in d^{6}-DMSO with trifluoroacetic acid. B) ^{13}C APT NMR (176 MHz) of complex **4** in d^{6}-DMSO.

a)

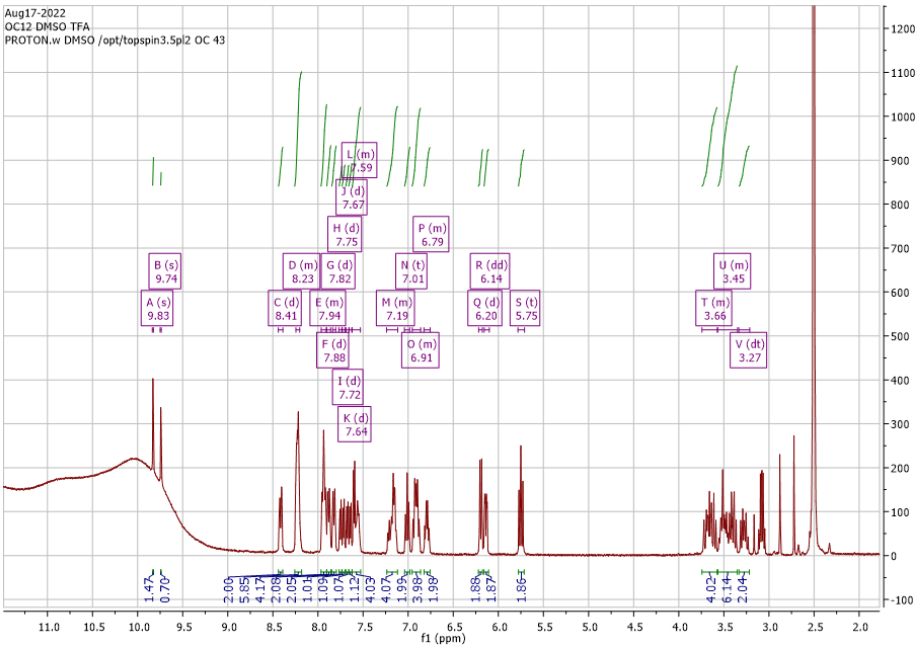

b)

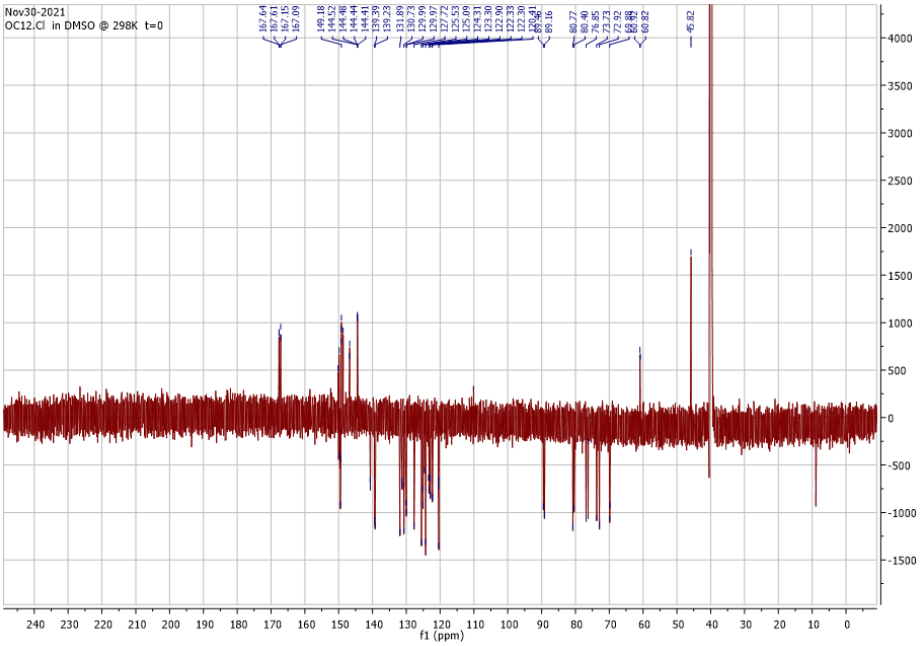

Spectra A5: A) ^{1}H NMR (400 MHz) of complex **5** in d^{6}-DMSO with trifluoroacetic acid. B) ^{13}C APT NMR (176 MHz) of complex **5** in d^{6}-DMSO.

a)

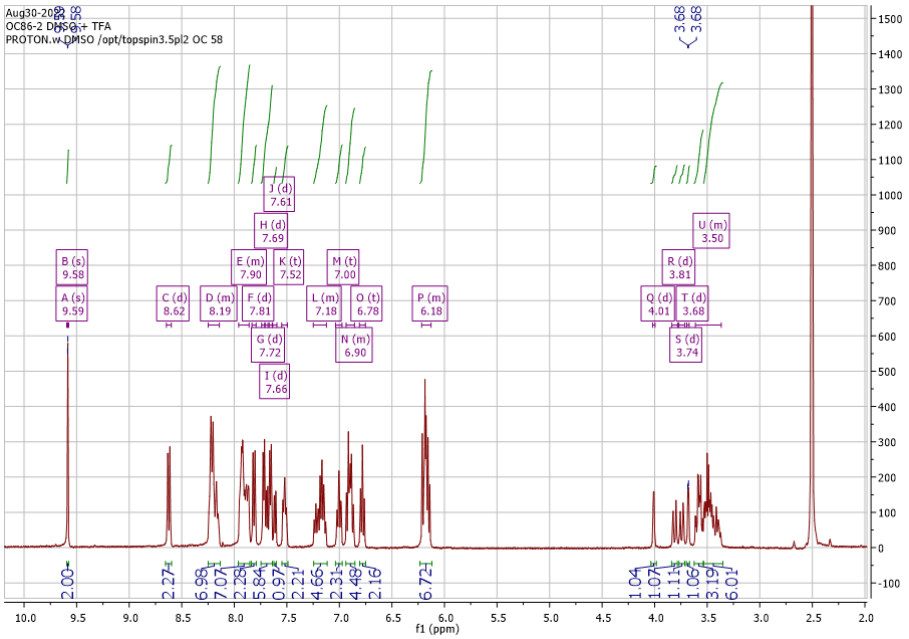

b)

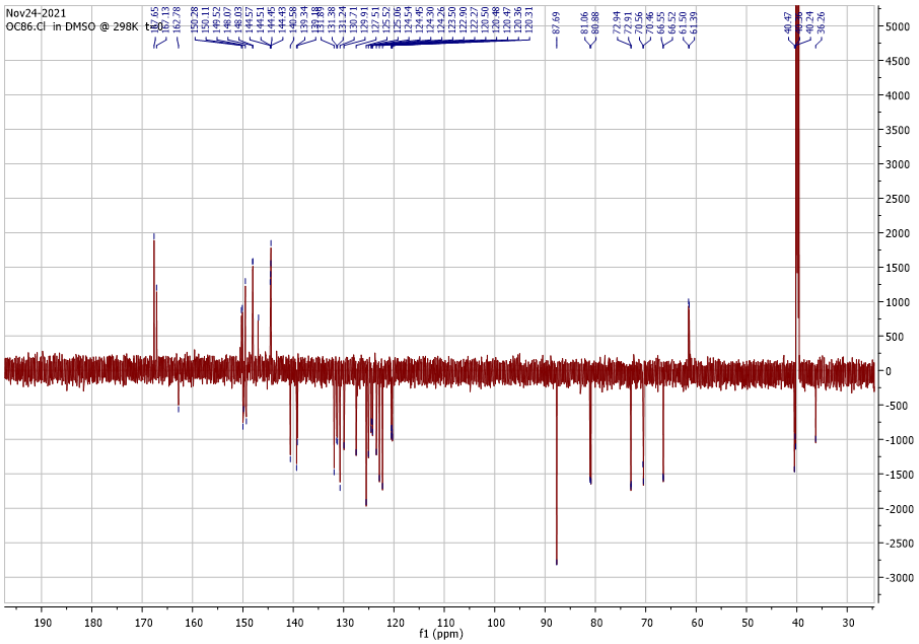

Spectra A6: A) ^{1}H NMR (400 MHz) of complex **6** in d^{6}-DMSO with trifluoroacetic acid. B) ^{13}C APT NMR (176 MHz) of complex **6** in d^{6}-DMSO.

a)

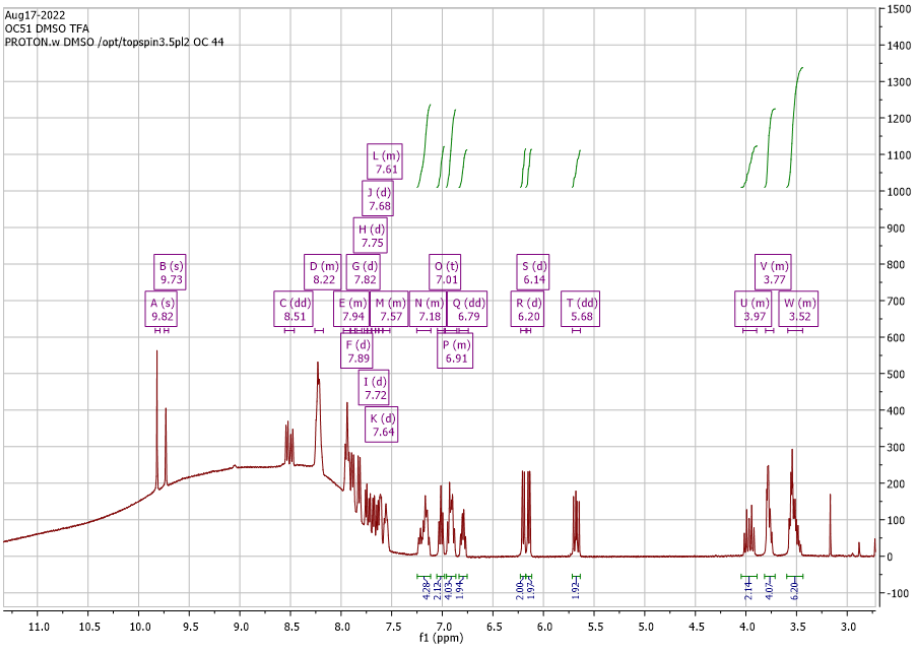

b)

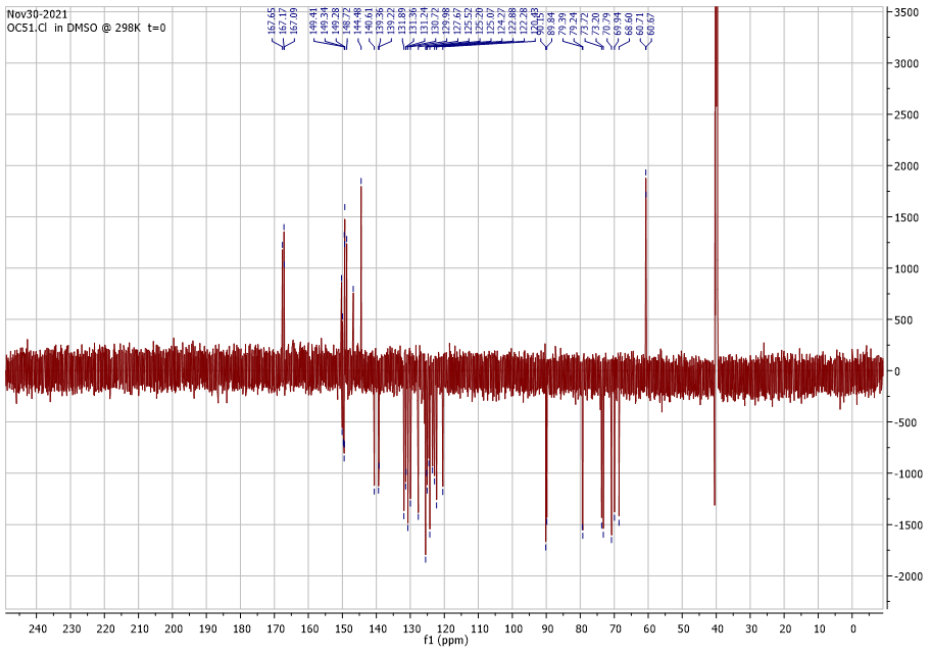

Spectra A7: A) ^{1}H NMR (400 MHz) of complex **7** in d^{6}-DMSO with trifluoroacetic acid. B) ^{13}C APT NMR (176 MHz) of complex **7** in d^{6}-DMSO.

a)

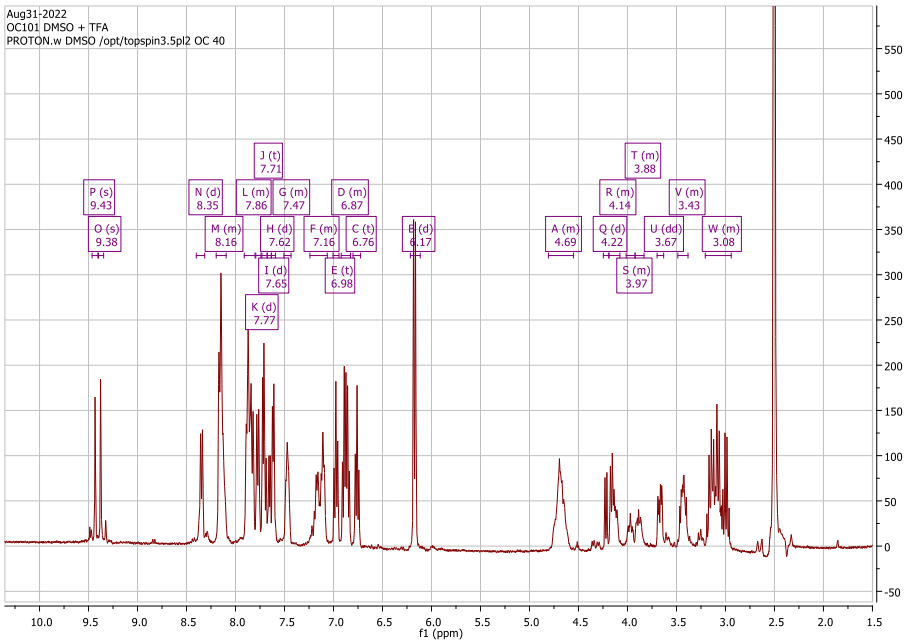

b)

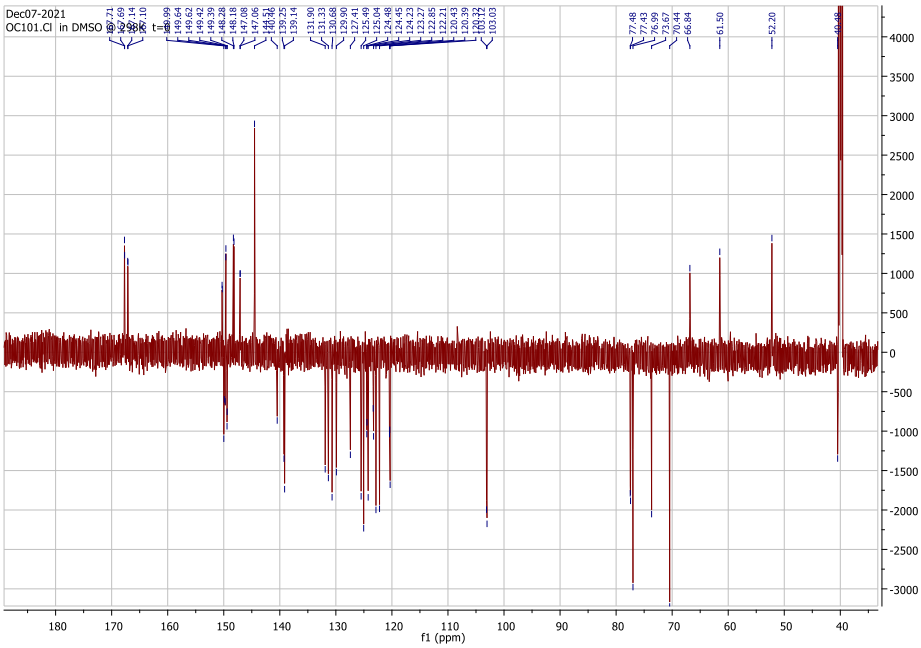

Spectra A8: A) ^{1}H NMR (400 MHz) of complex **8** in d^{6}-DMSO with trifluoroacetic acid. B) ^{13}C APT NMR (176 MHz) of complex **8** in d^{6}-DMSO.

a)

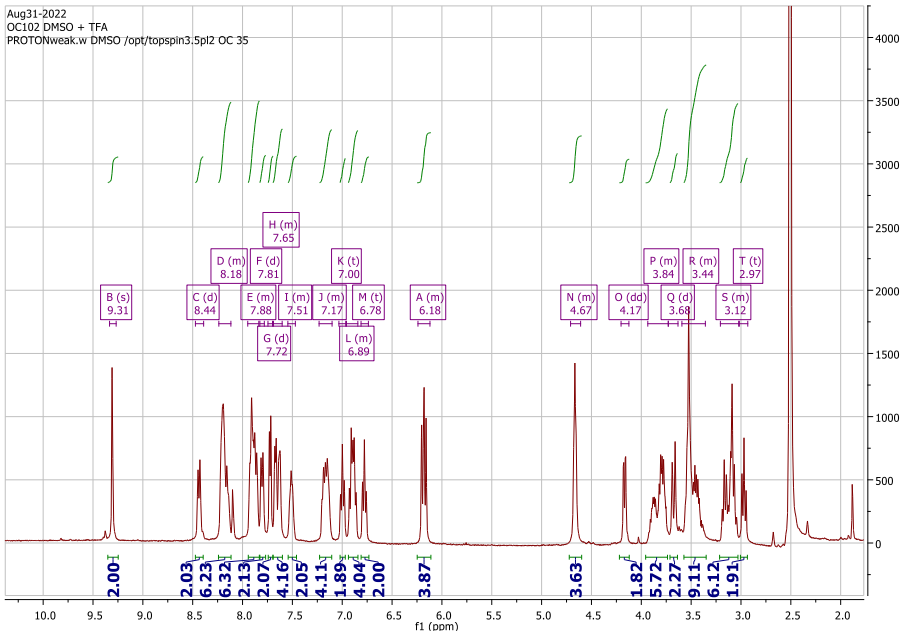

b)

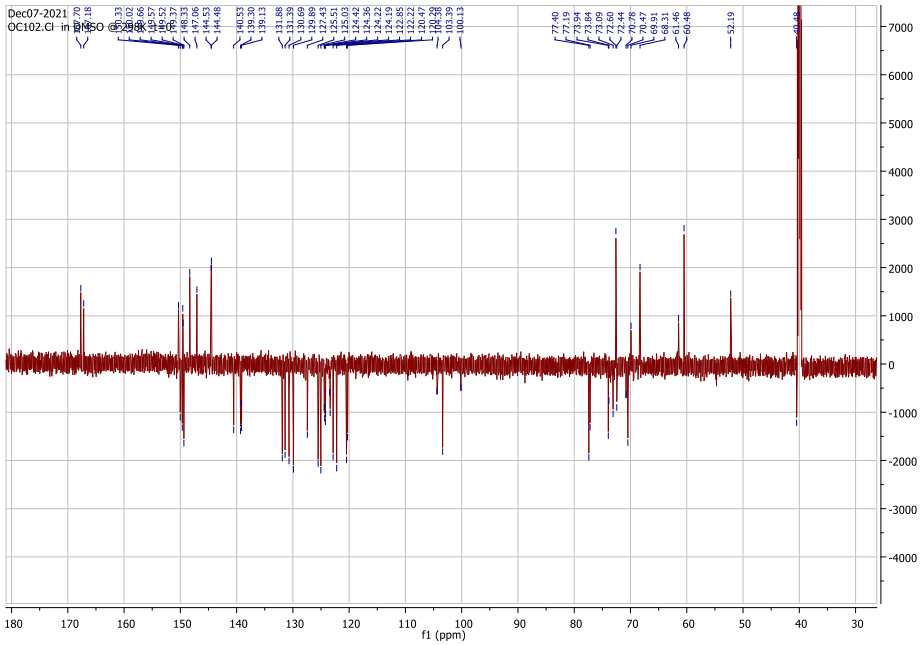

Spectra A9: A) ^{1}H NMR (400 MHz) of complex **9** in d^{6}-DMSO with trifluoroacetic acid. B) ^{13}C APT NMR (176 MHz) of complex **9** in d^{6}-DMSO.

a)

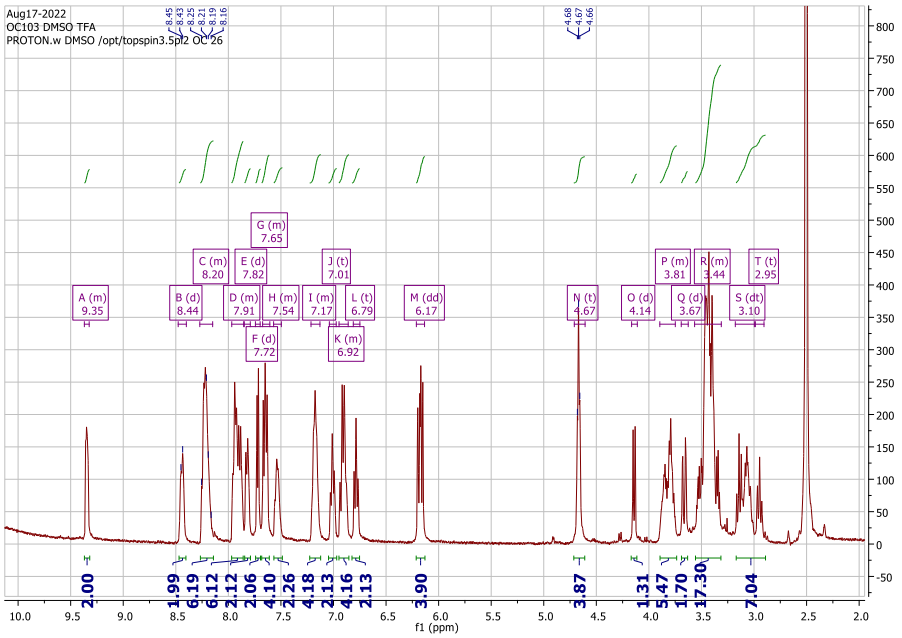

b)

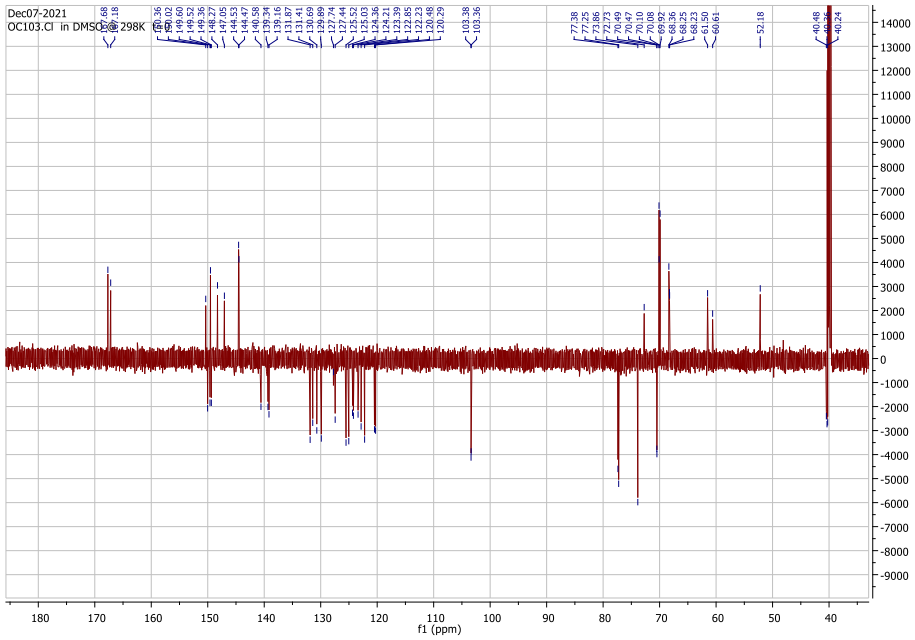

Spectra A10: A) ^{1}H NMR (400 MHz) of complex **10** in d^{6}-DMSO. B) ^{13}C APT NMR (176 MHz) of complex **10** in d^{6}-DMSO.

a)

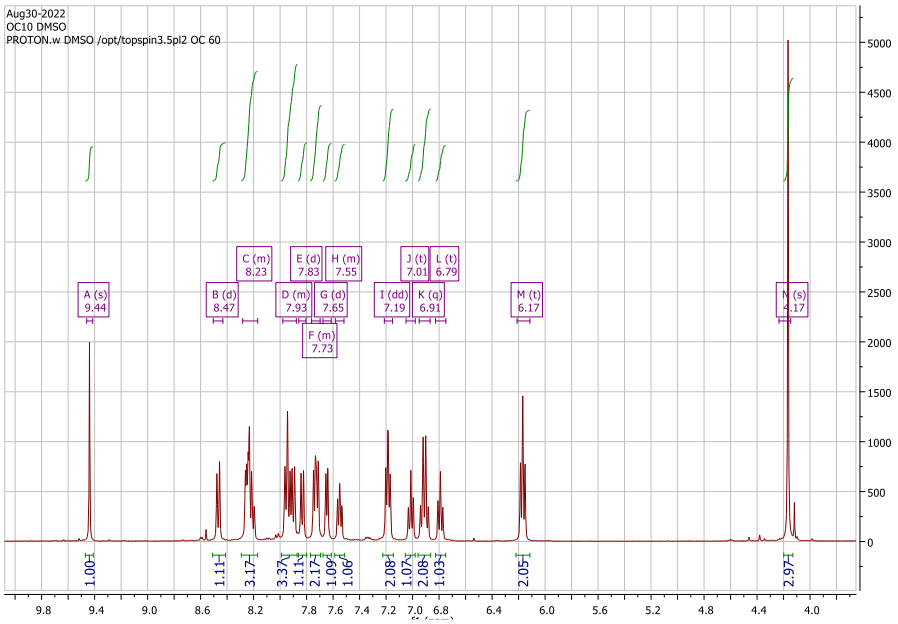

b)

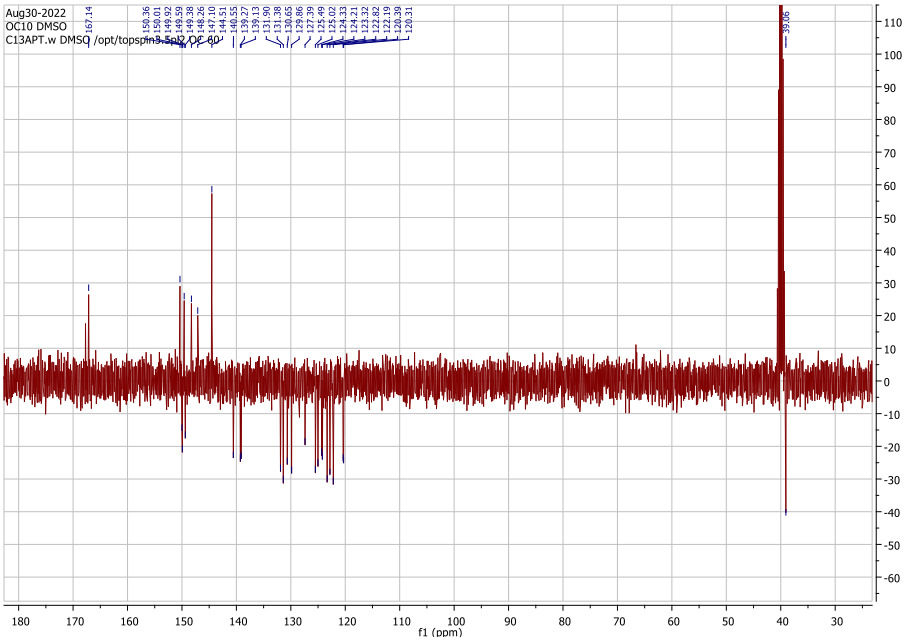

Spectra A11: A) ^{1}H NMR (400 MHz) of complex **11** in d^{6}-DMSO with trifluoroacetic acid. B) ^{13}C APT NMR (176 MHz) of complex **11** in d^{6}-DMSO.

a)

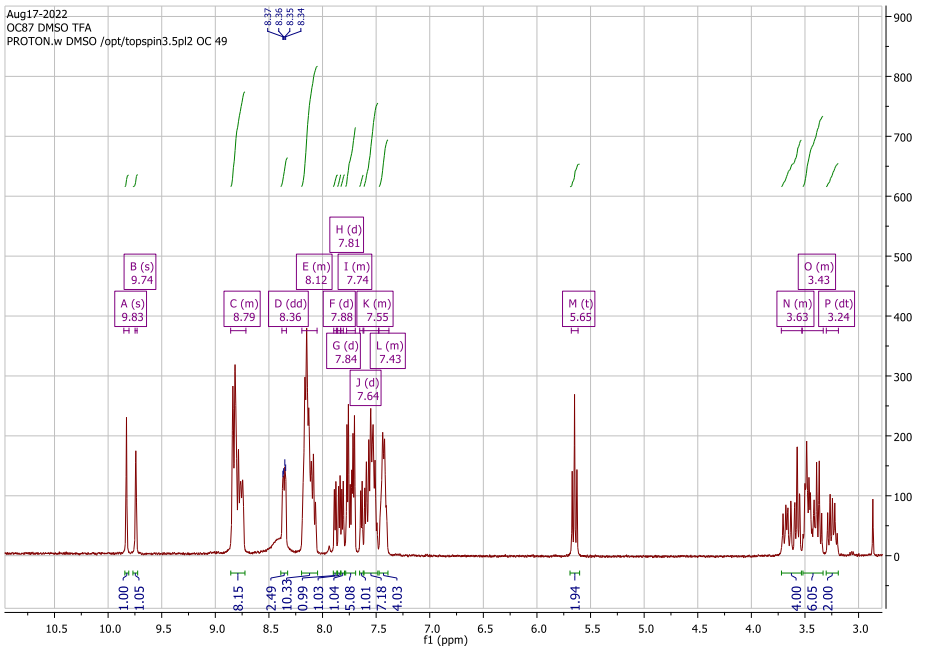

b)

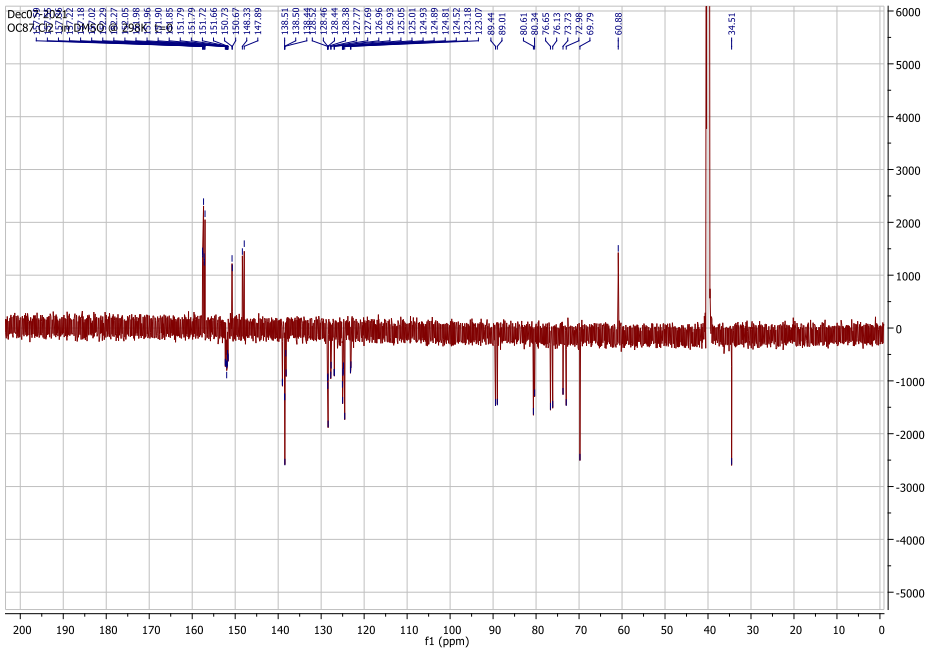

Spectra A12: A) ^{1}H NMR (400 MHz) of complex **12** in d^{6}-DMSO with trifluoroacetic acid. B) ^{13}C APT NMR (176 MHz) of complex **12** in d^{6}-DMSO.

a)

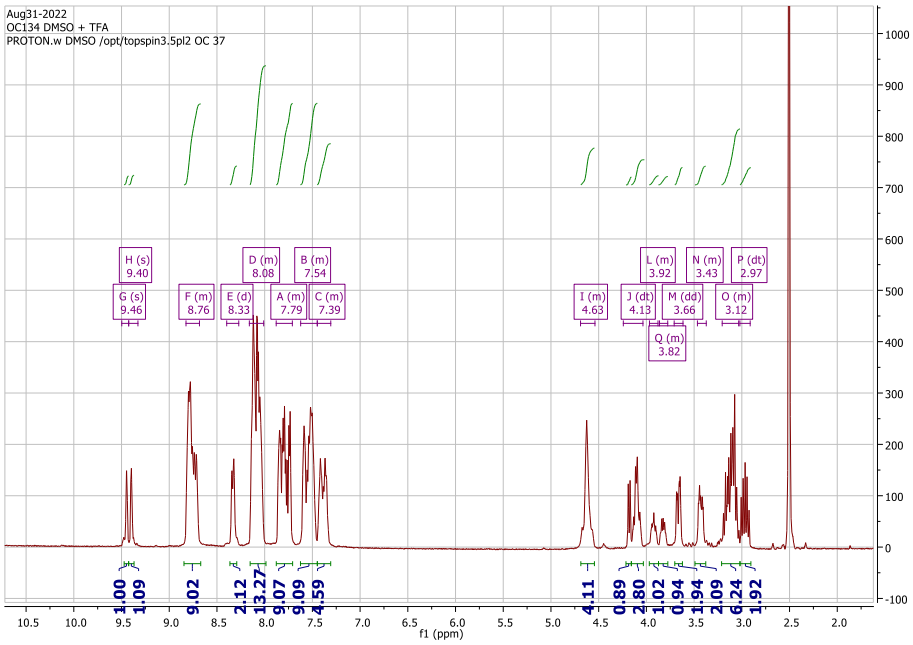

b)

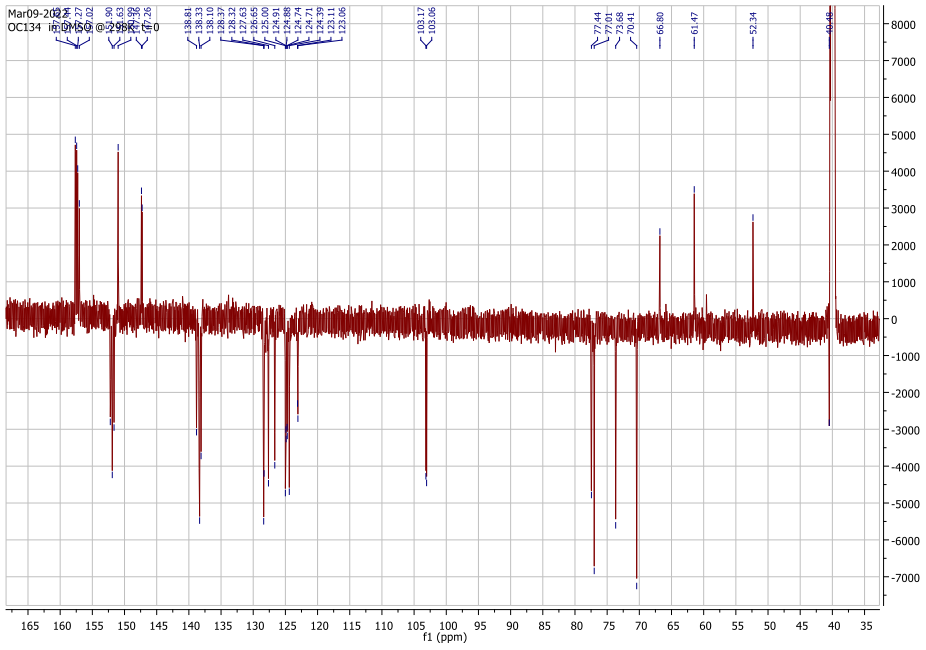

Spectra A13: A) ^{1}H NMR (400 MHz) of complex **13** in d^{6}-DMSO with trifluoroacetic acid. B) ^{13}C APT NMR (176 MHz) of complex **13** in d^{6}-DMSO.

a)

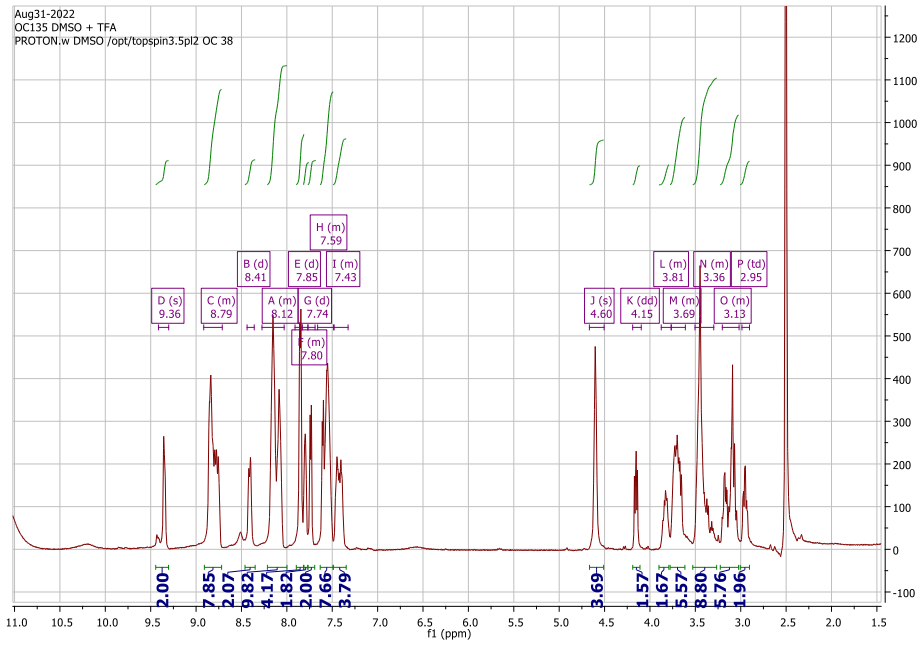

b)

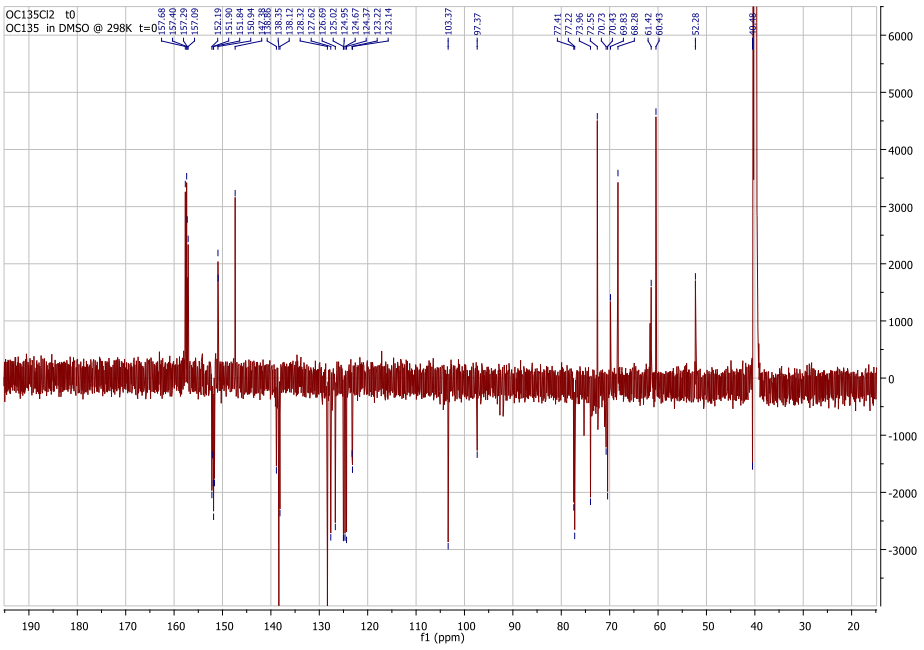

Spectra A14: A) ^{1}H NMR (400 MHz) of complex **14** in d^{6}-DMSO with trifluoroacetic acid. B) ^{13}C APT NMR (176 MHz) of complex **14** in d^{6}-DMSO.

a)

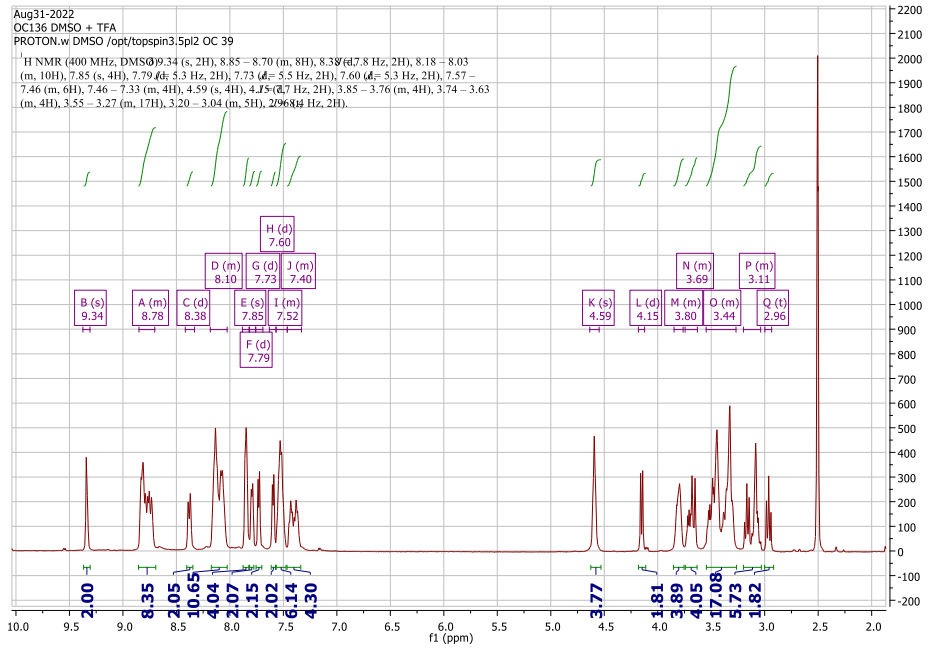

b)

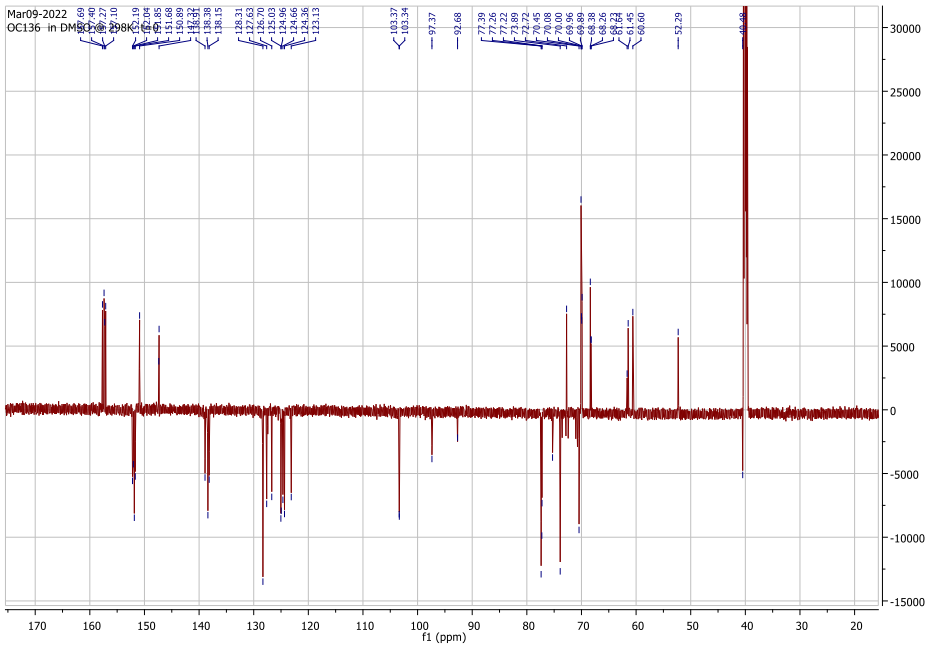

7.4 Figures

Figure A1. A) DPC and B) normalised phase gradient images of **C1**.

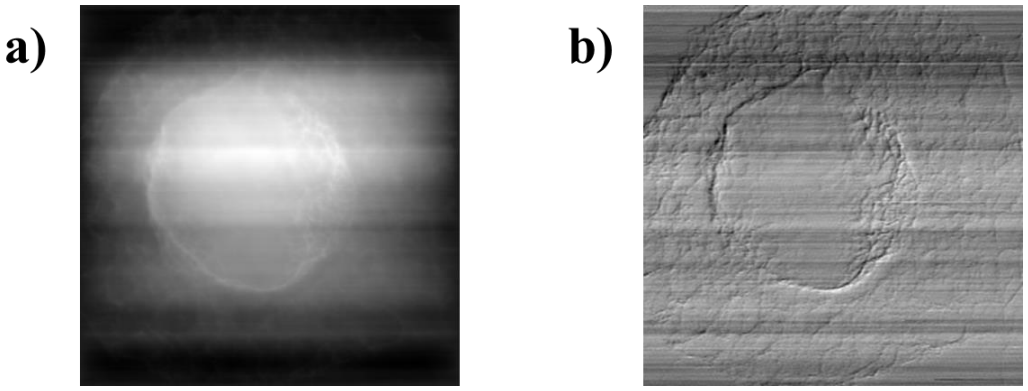

Figure A2. A) DPC and B) normalised phase gradient images of **C2**.

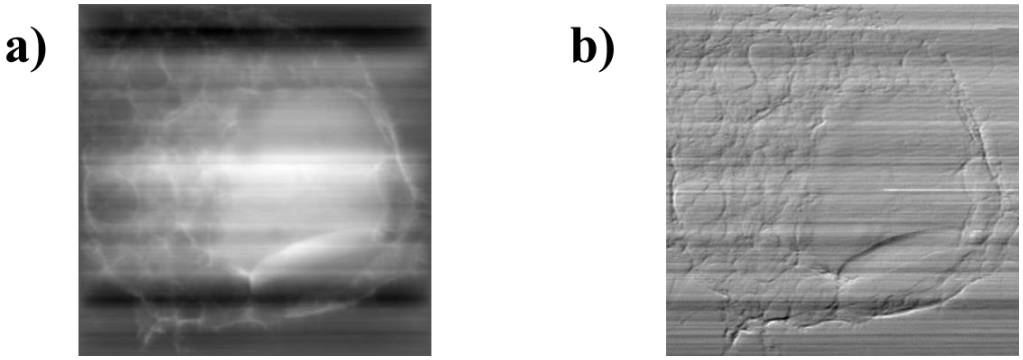

Figure A3. A) DPC and B) normalised phase gradient images of **C3**.

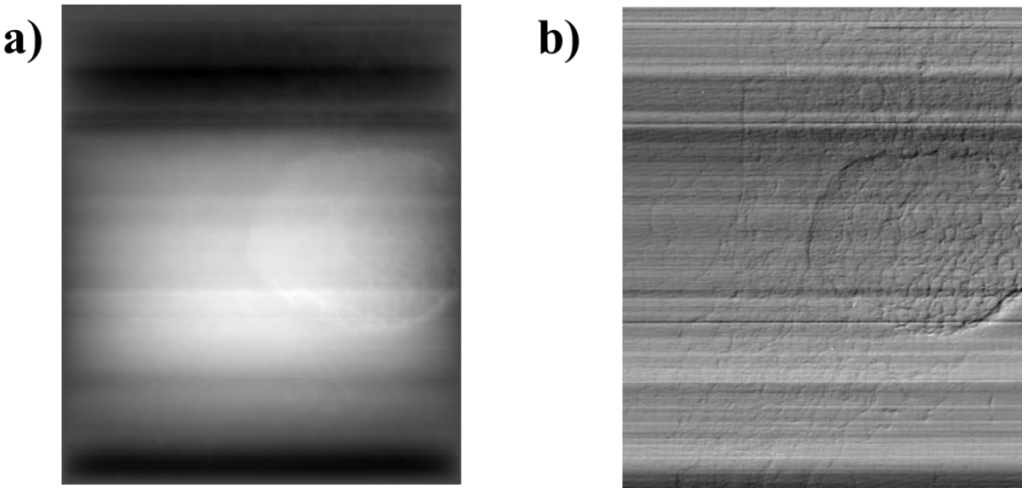

Figure A4. A) DPC and B) normalised phase gradient images of **C4**.

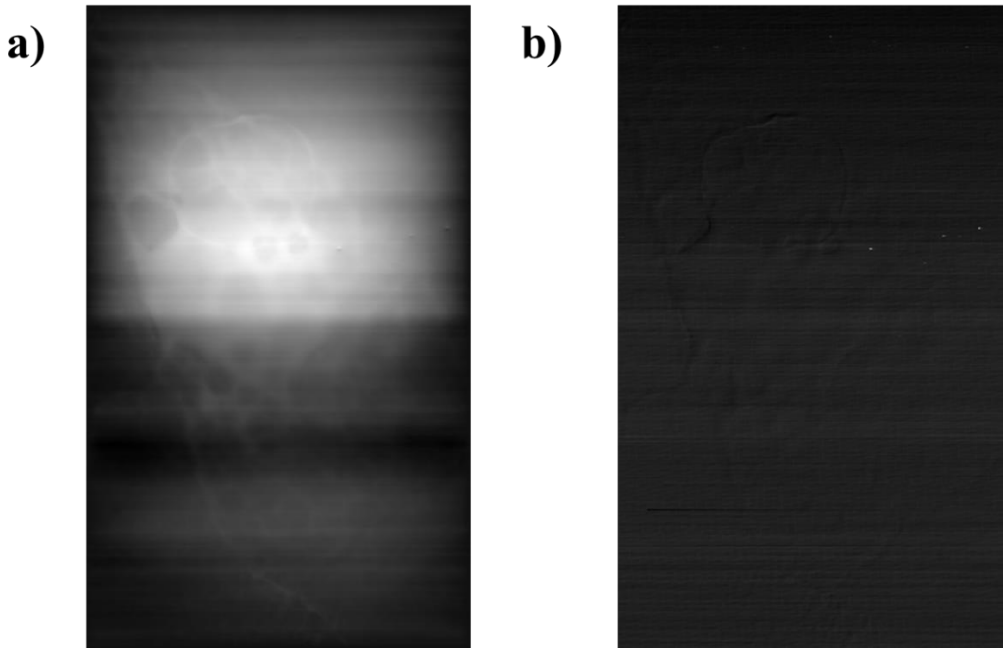

Figure A5. A) DPC and B) normalised phase gradient images of **C5**.

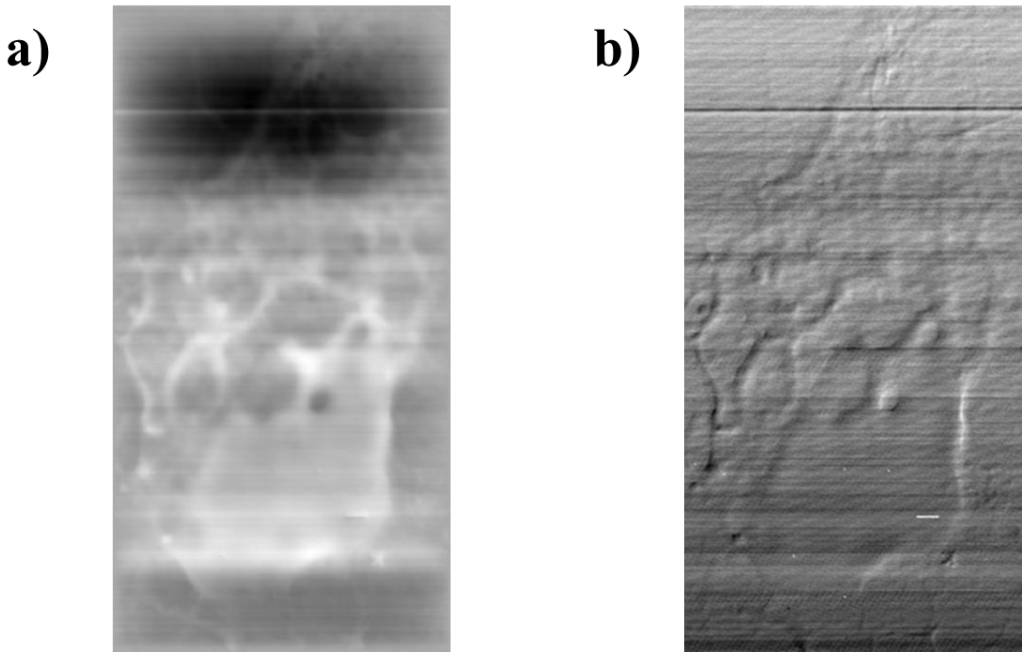

Figure A6. A) DPC and B) normalised phase gradient images of **C6**.

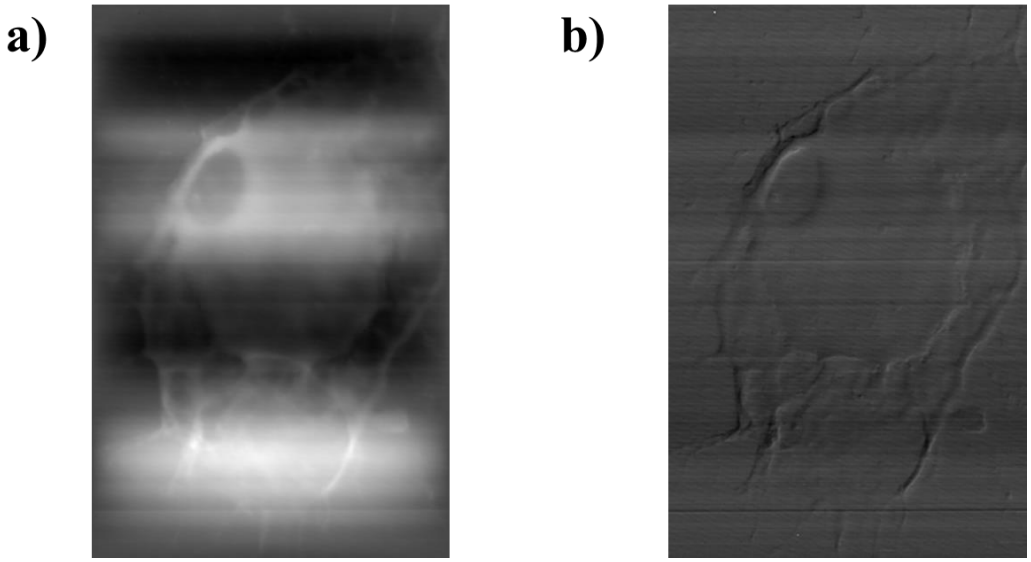

Figure A7. A) DPC and B) normalised phase gradient images of **C7**.

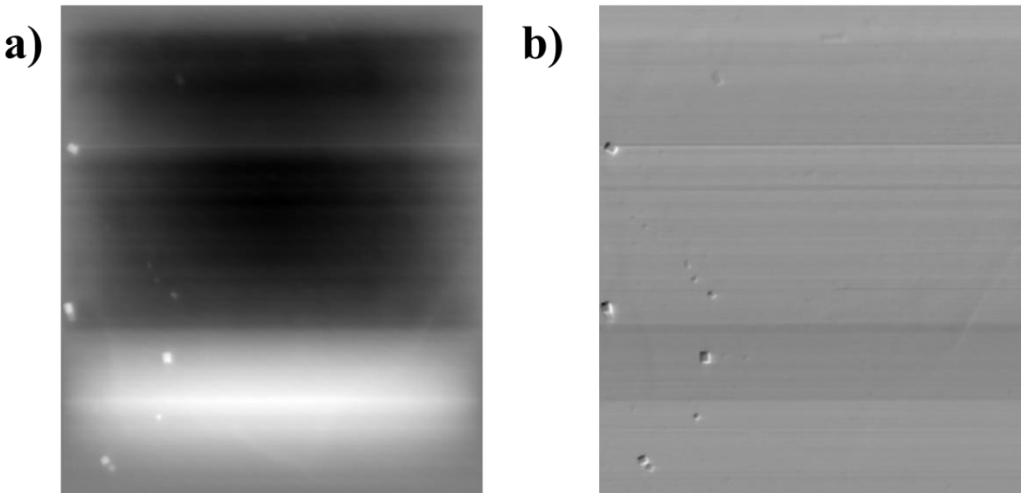

Figure A8. A) DPC and B) normalised phase gradient images of **C8**.

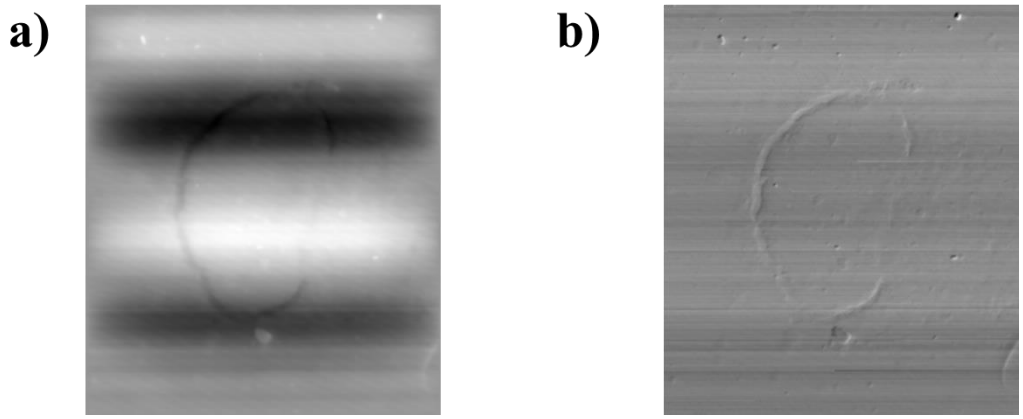

Figure A9. A) DPC and B) normalised phase gradient images of **C9**.

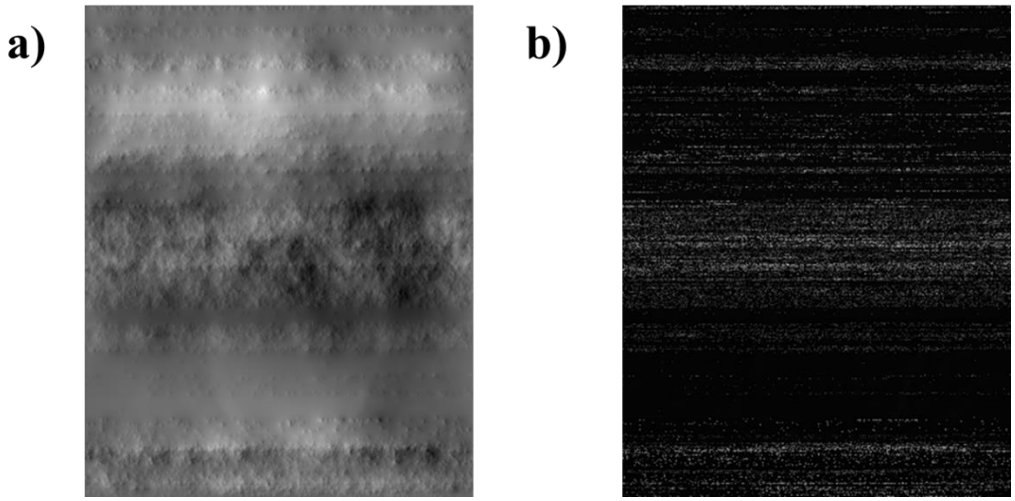

Figure A10. A) DPC and B) normalised phase gradient images of **C10**.

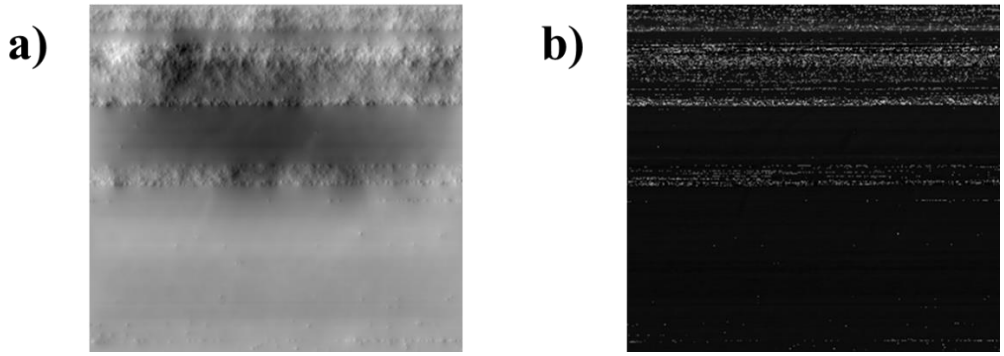

Figure A11. A) DPC and B) normalised phase gradient images of **C11**.

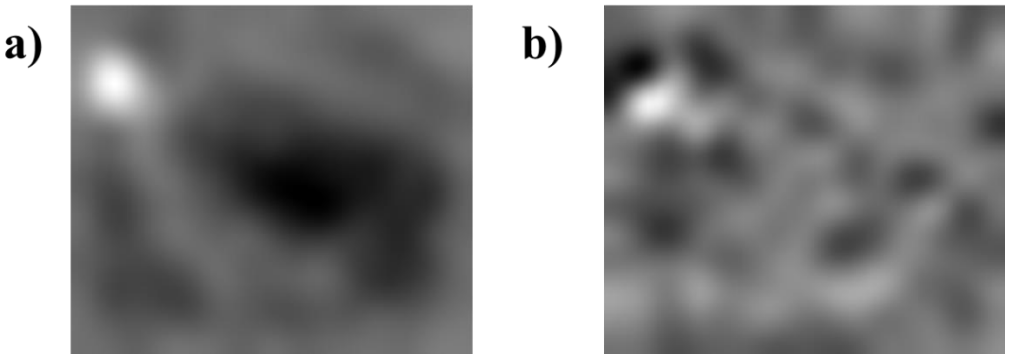

Figure A12. A) DPC and B) normalised phase gradient images of **C12**.

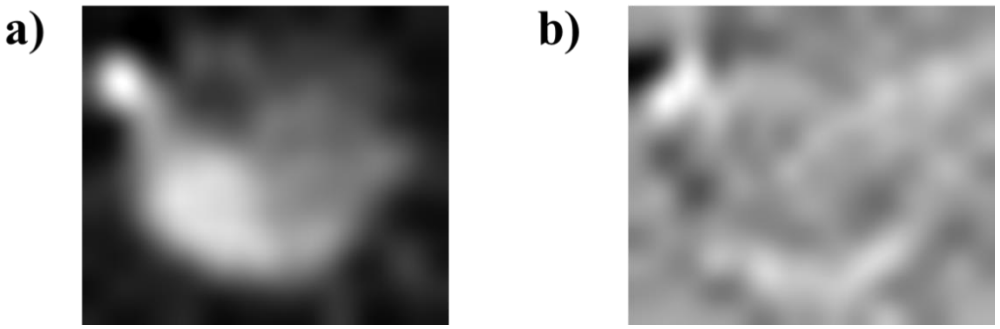

Figure A13. A) DPC and B) normalised phase gradient images of **C13**.

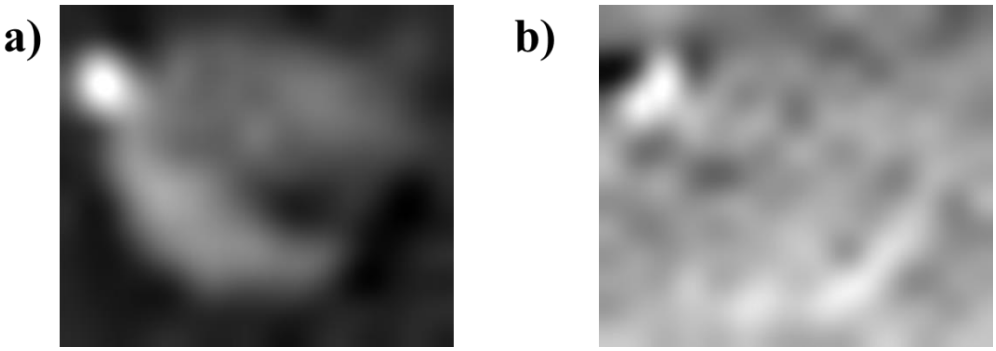

7.4 LED arrays

LED array A1. 425 nm LED array built in house by electronics technician Rod Wesson.

Power per LED: 4.8 mW·cm^{-2}

LED array A2. 465 nm LED array built in house by electronics technician Rod Wesson. Image reproduced from H. Shi PhD thesis.[3]

Power per LED: 4.8 mW·cm^{-2}

7.5 Light intensity

Light intensity A1

In use the LEDs are mounted in a black well plate as shown below.

This then sits on a second well plate that holds the sample.

The distance from the dome of the LED to the top of the sample well plate is 1.8 mm and to the bottom of the well is 13 mm.

Measurements of light intensity are made using a FDS1010 Si photodiode from ThorLabs mounted on a block of aluminium for heat sinking and an Agilent 34401A multimeter set to the low current range giving a shunt resistance of approximately 5.6 Ohms.

There are two LED holders made from black acetal with an opening of 6.5 mm which is the same diameter of the well giving a surface area of 0.332 cm^2. The lengths of the holders are 25.4 mm and 14.4 mm, this gives a difference of 11 mm which is the depth of the well. The holders are long enough to enclose individual LEDs so excluding light from adjacent LEDs.

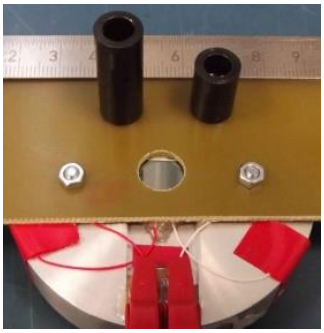

Measurements are made by placing the LED holder on the diode and then inserting the LED to be tested ensuring that the LED is aligned with the diode. The current is then taken from the multimeter and multiplied by the responsivity for the given wavelength which gives a result in mW per 0.332 cm^2.

Example: Wavelength 620 nm (Red) = 0.325 $A \cdot W^{-1}$ from FDS1010-CAL test calibration sheet

Device area = 9.7×9.7 mm = 94.09 mm^2 (0.9409 cm^2)

Exposed area = 0.332 cm^2 = 35%

0.325 x 35% = 0.114 $A \cdot W^{-1}$ so 1W of radiated power will deliver 0.114 A of current from the device.

A reading of 180 μA will equate to 180 μA / 0.114 $A \cdot W^{-1}$ = 1.58 mW.

7.6 References

1 A. Byrne, C. Dolan, R. D. Moriarty, A. Martin, U. Neugebauer, R. J. Forster, A. Davies, Y. Volkov and T. E. Keyes, *Dalton Trans.*, 2015, **44**, 14323–14332.

2 W. M. Haynes, *CRC Handbook of Chemistry and Physics*, CRC Press, 2014.

3 H. Shi, PhD Thesis, University of Warwick, 2019.